
Insights into the Acid-Base Properties of Functionalized Multiwall Carbon Nanotubes

Klaus Dieter Friedel Ortega



Berlin 2014

Insights into the Acid-Base Properties of Functionalized Multiwall Carbon Nanotubes

vorgelegt von
Diplom-Ingenieur
Klaus Dieter Friedel Ortega
aus Caracas, Venezuela

Von der Fakultät II - Mathematik und Naturwissenschaften
der Technischen Universität Berlin
zur Erlangung des akademischen Grades

Doktor der Ingenieurwissenschaften
- Dr.-Ing. -

genehmigte Dissertation

Promotionsausschuss:

Vorsitzender: Prof. Dr. Martin Lerch

Berichter/Gutachter: Prof. Dr. Robert Schlögl

Berichter/Gutachter: Prof. Dr. Peter Strasser

Berichter/Gutachter: Prof. Dr. Jaeyoung Lee

Tag der wissenschaftlichen Aussprache: 1. Juli 2014

Berlin 2014

D 83

La filosofía no puede sino beneficiarse de nuestras disputas, porque si nuestras concepciones se prueban verdaderas, se llegará a nuevos logros; y si se prueban falsas, su refutación confirmará aún más las doctrinas originales.

Philosophy itself cannot but benefit from our disputes because if our thoughts are true then we will make new gains, and if they are false then their refutation will confirm further the earlier doctrines.

Galileo Galilei

Acknowledgement

Once Sir William Lawrence Bragg stated: “The important thing in science is not so much to obtain new facts as to discover new ways of thinking about them”. Rational, practical, and theoretical knowledge combined with a substantial amount of creativity form altogether the fundamental basis necessary for gaining new perspectives about the macro- and microscopic world we intend to understand. This, in fact, is one the most important lessons I learned during my PhD thesis. However, reaching this status quo would have never been possible without the constant help and support of a long list of colleagues and advisors that accompanied me in the past years, who day by day taught me that cooperative and harmonic work is the only true key leading to success.

First and foremost, I would like to express my sincere gratitude to my advisor Prof. Dr. Robert Schlögl, Director of the Department of Inorganic Chemistry at the Fritz Haber Institute of Max Planck Society, for the faith he placed in me from the beginning until the end of my research stay, and for his unconditional support. Thanks to his patience, understanding, guidance, encouragement, and great knowledge I was able to accomplish my PhD project.

I would like to particularly acknowledge the members of the doctoral board, Prof. Dr. Peter Strasser and Prof. Dr. Jaeyoung Lee, who gladly accepted to invest their valuable time in reviewing this work. Additional gratitude goes to Prof. Dr. Martin Lerch for taking the chair of the examination board.

My special thanks and appreciation goes to my supervisor Dr. Annette Trunschke, leader of the Reactivity group, who warmly welcomed me from the very first day. Her recommendations and regular discussions helped me to develop a critical eye about my own work. Furthermore, I am truly grateful for the time invested in reviewing the extensive paper drafts, and for the resulting feedback. At this point I would like to express my gratitude to all the members of the Reactivity group, not only for the daily support in my research work, but also for the great moments we spent in conferences, after PhD days, during department trips, and in Christmas parties.

I am highly grateful and indebted to Dr. Benjamin Frank for providing me not only a comprehensive overview of the research topic, but also for introducing me into the utilization of the home-built TPD setup known as Reverend T. His continuous technical assistance and ideas in general were invaluable in the past years. In a similar manner, I thank my former colleague Pierre Kube for all the knowledge transfer in the field of gas chromatography and for his willingness to help with any kind of technical issue at any time.

Further acknowledgment goes to Dr. Benjamin Johnson for the XPS measurements performed over the NCNT samples. With this respect, I am truly grateful to the support

offered by Dr. Rosa Arrigo in the time-consuming evaluation of the various XP spectra. Similarly, I would like to express my gratitude to Dr. Sabine Wrabetz for all the efforts made in performing microcalorimetric measurements on various samples that helped me to gain a better understanding of their surface acid-base properties.

Herewith I would like to thank Dr. Olaf Timpe and Dr. Gregor Wowsnick for discussing my ideas related with the chemical modification strategies planned and applied to the CNT material. On top of that, I do not know how to express my gratitude for the outstanding and motivating office atmosphere. In a similar way, I would like to thank all my labmates, colleagues, and project partners for every piece of contribution that lead to the success of this work: Prof. Dr. Jean-Phillipe Tessonnier, Dr. Ali Rinaldi, Dr. Sylvia Reiche, Youngmi Yi, Dr. Stefanie Köhl, Mateusz Jastak, Pia Kjær Nielsen, Christian Heine, Dr. Johannes Noack, Pierre Schwach, Dr. Raoul Naumann d'Alnoncourt (Furnace), Dr. Zilai Xie (CarboKat), Jutta Kröhnert (ATR-FTIR), Elif Ider, Dr. Andrey Tarasov (TG-MS), Jasmin Allan (TG-MS), Dr. Marc Willinger, Dr. Thomas Lunkenbein, Dr. Ramzi Farra, Dr. Manfred Schuster (TEM), Norbert Pfänder (TEM), Wiebke Frandsen (SEM/EDX), Dr. Thomas Cotter, Dr. Neil Hamilton, Dr. Stefan Zander, Dr. Timur Kandemir, Maike Hashagen (BET), Dr. Raoul Blume (XPS/BESSY), Dr. Heiner Schwarz, Dr. Juan Velasco Vélez, Prof. Dr. Martin Muhler (CarboKat/Bochum), Dr. Wei Xia (CarboKat/Bochum), Jason Anderson.

Last but certainly not least important, I would like to thank my family who has supported me ever since I came to Germany for my university studies in 2005. Although the distance has not allowed us to share important moments, I know they have been there for me whenever I needed them. At this point, however, I would like to express my special love and gratitude to my mother by dedicating some words in my native language to her: “Gracias mamá por todo tu esfuerzo y dedicación. Este es el punto final de un largo viaje y el comienzo de una nueva etapa. Te estaré infinitamente agradecido por haber hecho de mi la persona que soy. Siempre te llevo en mi corazón”. Finally, I would like to deeply thank my girlfriend, Maria Natália Gabriele Moura, an outstanding lovely woman who has supported me every since I met her - muito obrigado pelo seu suporte incondicional.

Kurzfassung

Kohlenstoffnanoröhren (CNTs) werden aufgrund ihrer hohen spezifischen Oberfläche, ihrer einzigartigen geometrischen und elektronischen Struktur und der hohen chemischen Stabilität als vielversprechende Materialien zur Anwendung in der heterogenen Katalyse diskutiert. Struktur und intrinsische Eigenschaften ihrer Oberfläche können zudem durch Einbau von Defekten, insbesondere durch Funktionalisierung mit Heteroatomen, gesteuert werden. Durch verschiedenartige Funktionalisierungen lassen sich saure oder basische Zentren auf der Oberfläche generieren, wodurch CNTs als heterogene Säure-Base-Katalysatoren eingesetzt werden können, aber auch als Trägermaterial z.B. für katalytisch aktive Metalle, da durch gezielte Modifizierung der CNT-Oberfläche Metall-Träger-Wechselwirkungen beeinflusst werden können und damit veränderte katalytische Eigenschaften zu erwarten sind. Um Struktur-Aktivitäts-Korrelationen aufstellen zu können, bedarf es sowohl geeigneter Präparationen zum Erhalt möglichst homogen funktionalisierter Oberflächen als auch belastbarer Methoden zu deren Strukturaufklärung. Die komplexe, stark von den Syntheseparametern abhängige Oberflächenchemie der CNTs, erfordert dazu die gleichzeitige Anwendung komplementärer Charakterisierungsmethoden.

Ziel dieser Arbeit war der Einbau von S-, N- und P-haltigen funktionellen Gruppen auf mehrwandigen CNTs, um gezielt Oberflächen mit sauren und basischen Zentren zu generieren. Die Art, Menge und thermische Stabilität der funktionellen Gruppen wurde vorwiegend mittels TPD, XPS, Mikrokalorimetrie und Elementaranalyse aufgeklärt. Die Säure-Base-Eigenschaften der Oberflächen wurden komplementär sowohl mittels pH-Titration in wässriger Phase als auch durch die sauer- bzw. basisch katalysierte Umsetzung von 2-Propanol in der Gasphase als sensitive Sondenreaktion bestimmt. TPO gab Aufschluss über den Einfluss der Heteroatome auf die oxidative Beständigkeit der CNTs.

Zunächst gelang die Seitenwandfunktionalisierung der CNTs mit Sulfonsäuregruppen mit Hilfe einer Diazotierung von Sulfanilsäure in *o*-Dichlorbenzol und Wasser. TPD-Experimente bestätigen eine thermische Stabilität der Gruppen bis 250 °C. Sowohl die pH-Titration als auch eine hohe Propylenselektivität in der Umsetzung von 2-Propanol beweisen die sauren Oberflächeneigenschaften. Eine Desaktivierung kann bei Durchführung der Reaktion unterhalb von 200 °C vermieden werden. Die Menge an sauren Zentren korreliert hierbei mit der Konzentration an S in den Proben und es konnte herausgestellt werden, dass das Lösungsmittel Wasser gegenüber *o*-Dichlorbenzol einen höheren S-Einbau begünstigt.

Die Darstellung N-funktionalisierter CNTs gelang mittels Aminierung in 50% NH₃/Ar-Atmosphäre von O-funktionalisierten CNTs bei verschiedenen Temperaturen. TPD- und

XPS-Analysen ergaben die Anwesenheit von vorwiegend Imiden und Lactamen nach Behandlung bei 300 °C und pyrrolischen N nach Funktionalisierung bei 500 °C. Eine Aminierung bei 700 °C führt gezielt zu überwiegend pyridinischen N. Während der N-Gehalt mit zunehmender Behandlungstemperatur leicht sinkt, steigt die Basizität der Oberflächen drastisch an, was weniger durch die Menge als vielmehr durch die Art der funktionellen Gruppen bestimmt wird. Die bei 700 °C funktionalisierten CNTs erreichten nahezu Totalselektivität bezüglich Aceton in der Umsetzung von 2-Propanol. Innerhalb einer Periode von 12 h ist die Aktivität stabil, solange die Temperatur weniger als 250 °C beträgt. Die basischen CNTs wiesen eine mit dem Ausgangsmaterial vergleichbare oxidative Beständigkeit auf.

Die Modifikation mit P wurde durch Aktivierung mit H_3PO_4 im Temperaturbereich zwischen 400 und 700 °C erreicht. P wird hierbei in Form von Phosphaten kovalent an die CNTs gebunden wie anhand der CO-Bildung bei Temperaturen jenseits von 750 °C während der TPD nachgewiesen werden konnte. Die Ergebnisse der pH-Titration und die annähernde Totalselektivität zu Propylen in der Umsetzung von 2-Propanol bewiesen die sauren Eigenschaften der Oberfläche. Die hydrolyseempfindlichen Spezies zeigen ein stabiles Verhalten während der Reaktion bis zu einer Temperatur von 200°C. Mikrokalorimetrische Untersuchungen zeigten die Anwesenheit von zwei homogeneverteilten und energetisch äquivalenten Sauren-Zentren. Im Gegensatz zur Funktionalisierung mit anderen Heteroatomen konnte die oxidative Stabilität signifikant verbessert werden.

Zusammenfassend wurden in dieser Arbeit mehrwandige CNTs erfolgreich mit S-, N- und P-basierten Gruppen funktionalisiert, wobei systematisch der Einfluss verschiedener Syntheseparameter auf die resultierenden Säure-Base-Eigenschaften untersucht wurde. Die komplementäre Anwendung von spektroskopischen, titrimetrischen und kalorimetrischen Methoden sowie Reaktivitätsstudien erlaubten qualitative und quantitative Aussagen über die Natur und Eigenschaften der verschiedenen funktionellen Gruppen auf der CNT-Oberfläche. Dieser wissensbasierte Ansatz führte mit Erfolg zur Darstellung wohldefinierter, nachweislich vielversprechender Säure-Base-Katalysatoren.

Abstract

Carbon nanotubes (CNTs) are regarded as promising materials in the field of heterogeneous catalysis due to their high specific surface area, unique geometric and electronic structure as well as their chemical stability. In addition, the structure and intrinsic surface properties can be influenced by incorporation of defects and, certainly, *via* chemical modification with heteroatoms. Various functionalization techniques allow the generation of acid or basic sites, thus enabling the possibility of employing CNTs either as heterogeneous acid-base catalysts or as a support for catalytic active phases. Metal-support-interactions can be influenced through specific functionalization of the CNT surface, which in turn are expected to have an impact on the resulting catalytic properties. In order to establish structure-activity correlations, it is essential to find suitable preparation routines that lead to homogeneously functionalized surfaces, whose structure may be elucidated employing reliable techniques. In addition, the complex surface chemistry of CNTs, whose state strongly depends on the synthesis parameters, requires the application of complementary characterization techniques.

The aim of this work was the incorporation of S-, N-, and P-containing functional groups onto multiwall CNTs in order to purposefully generate surfaces with acid and basic centers. The nature, amount, and thermal stability of the functional groups were determined with the aid of TPD, XPS, microcalorimetry, and elemental analysis. Surface acid-base properties were elucidated by complementary techniques, namely pH titrations in aqueous phase and the catalytic transformation of 2-propanol performed in the gas-phase. TPO experiments provided information on the influence of heteroatoms on the oxidative resistance of CNTs.

First of all, a sidewall functionalization of CNTs with sulfonic acid groups was achieved through diazotization of sulfanilic acid in ODCB and water. TPD experiments confirm a thermal stability of the surface species up to 250 °C. Potentiometric pH titration results and a high propylene selectivity in the course of the transformation of 2-propanol confirm the acidic surface properties. A deactivation can be prevented by performing the reaction at temperatures below 200 °C. The amount of acid sites correlates with the S-content in the samples. In addition, the incorporation of sulfur could be enhanced when using water as a solvent instead of ODCB.

The synthesis of N-doped CNTs was accomplished by amination of O-containing CNTs at different temperatures in a 50 % NH₃/Ar atmosphere. TPD and XPS analyses showed that imides and lactams are predominantly present after treatment at 300 °C, while pyrrolic-N is preferentially formed upon functionalization at 500 °C. Amination at 700 °C mainly yields pyridinic-N species. Whereas the N-content slightly drops with rising

treatment temperature, the surface basicity is drastically increased, which is determined by the nature rather than the amount of functional groups. The CNTs modified at 700 °C almost achieved total selectivity towards acetone in the transformation of 2-propanol. The activity is stable within a period of 12 h, at least for reaction temperatures below 250 °C. The basic CNTs exhibit an oxidative resistance comparable to that of the pristine material.

The modification with P was carried out through chemical activation with H_3PO_4 in the temperature range between 400 and 700 °C. P in form of phosphate species is hereby covalently attached to the CNTs as evidenced by CO formation at temperatures beyond 750 °C during TPD experiments. Results derived from potentiometric pH titrations and the approximately total selectivity towards propylene in the transformation of 2-propanol confirm the acidic surface properties. The hydrolysis-sensitive species exhibit a stable behaviour during reaction to a temperature of around 200 °C. Microcalorimetric measurements further confirmed the presence of two homogeneously distributed and energetic equivalent acid sites. In contrast to the functionalization with other heteroatoms, it was possible to significantly enhance the oxidative stability.

In summary, in this work multiwall CNTs were successfully functionalized with S-, N-, and P-containing groups, whereby the influence of different synthesis parameters on the resulting acid-base properties was systematically investigated. The complementary employment of spectroscopic, titrimetric, and calorimetric methods as well as reactivity measurements allowed drawing conclusions on a qualitative and quantitative basis about the nature and properties of different functional groups present on the CNT surface. This knowledge based approach led to a successful synthesis of promising acid-base catalysts.

Table of Contents

List of Figures	iv
List of Schemes	viii
List of Tables	ix
List of Abbreviations	xi
1 Introduction	1
2 Carbon nanotubes: An overview	5
2.1 Atomic structure	5
2.2 Electronic properties	10
2.3 Reactivity of carbon nanotubes	13
2.4 Chemical derivatization approaches	14
2.4.1 Non-covalent exohedral functionalization	16
2.4.2 Endohedral functionalization	18
2.4.3 Defect site functionalization	21
2.4.4 Sidewall functionalization	24
2.5 Heteroatoms in carbon materials	26
2.6 Carbon as a catalyst	30
3 Motivation and outline of the work	35
4 Tailoring the acidity of carbon nanotubes through addition of <i>in situ</i> generated benzenesulfonic acid radicals	37
4.1 Introduction	38
4.2 Experimental section	39
4.2.1 Functionalization of CNTs	39
4.2.2 Analytical Techniques	40
4.3 Results and Discussion	42
4.3.1 Functionalization of MWCNTs in Organic and Aqueous Media	42
4.3.2 Textural properties of the functionalized MWCNTs	43

4.3.3	Characterization of Sulfonic Acid Groups by Thermal Analysis . . .	45
4.3.4	Spatial Distribution of Hetero-Elements Analyzed by SEM/EDX . .	48
4.3.5	ATR-FTIR spectroscopy	49
4.3.6	Acidity of S-modified CNTs in Aqueous Media	50
4.3.7	Catalytic Transformation of 2-Propanol	51
4.4	Conclusion.....	55
4.5	Supporting Information	57
5	Insights into the intrinsic acid-base properties of N-doped carbon nanotubes: a combined TPD, XPS and 2-propanol reaction investigation	59
5.1	Introduction	60
5.2	Experimental section	61
5.2.1	Functionalization of MWCNT	61
5.2.2	Nitrogen Adsorption	62
5.2.3	Potentiometric pH Titrations	62
5.2.4	Temperature Programmed Desorption	62
5.2.5	Temperature Programmed Oxidation	63
5.2.6	Elemental Analysis	63
5.2.7	X-Ray Photoelectron Spectroscopy	63
5.2.8	Catalytic transformation of 2-propanol	64
5.3	Results and Discussion	64
5.3.1	Textural properties and elemental composition	64
5.3.2	Thermal Stability and Nature of Surface Species	66
5.3.3	Surface Analysis by XPS	73
5.3.3.1	N1s Core-Level Spectrum	73
5.3.3.2	O1s Core-Level Spectrum	76
5.3.4	Acid-base properties in the Aqueous Phase	80
5.3.5	Catalytic Transformation of 2-Propanol	82
5.3.6	Oxidative Stability of N-Doped Carbon Nanotubes	85
5.4	Conclusion.....	87
5.5	Supporting Information	89
6	Influence of thermal treatment on surface and oxidation properties of P-modified carbon nanotubes	91
6.1	Introduction	92
6.2	Experimental section	93
6.2.1	Phosphorus modification of MWCNT	93

6.2.2	Characterization techniques	94
6.3	Results and Discussion	96
6.3.1	Textural properties and elemental composition	96
6.3.2	Analysis of functional groups by means of Temperature Programmed Desorption	98
6.3.3	Acidic properties of P-modified CNTs in the Aqueous Phase	100
6.3.4	Investigation of gas-phase acidity by NH ₃ microcalorimetry and NH ₃ -TPD	102
6.3.5	Catalytic Transformation of 2-propanol	108
6.3.6	Oxidation resistance of P-modified CNTs	111
6.4	Conclusions	113
6.5	Supporting Information	115
7	Conclusion and outlook	119
	Bibliography	123

List of Figures

1.1	Molecular model of the C_{60} fullerene (a) and of a single-walled carbon nanotube with fullerene-like ends (b).	2
2.1	Formation of a carbon nanotube starting from a graphene sheet.	5
2.2	Graphical representation of the geometrical parameters (\vec{C}_h , Θ , \vec{a}_1 , \vec{a}_2) of a single-wall carbon nanotube based on a 2D graphite sheet. The depicted case corresponds to the nanotube defined by the indices $n=4$ and $m=2$. . .	6
2.3	Schematic models of the three different types of single-wall carbon nanotubes: (a) armchair ($\Theta=30^\circ$), (b) zigzag ($\Theta=0^\circ$), and (c) chiral ($0^\circ < \Theta < 30^\circ$).	8
2.4	Reciprocal lattice with primitive reciprocal lattice vectors and unit cell (shaded).	8
2.5	Model of a multi-walled carbon nanotube.	10
2.6	Electronic band structure of graphene along the high symmetry points of the triangle ΓMK as shown in Figure 2.4.	11
2.7	Schematic representation of the first Brillouin zone of a (3,3) nanotube (a) and a (6,0) nanotube (b).	12
2.8	Density of states of a nanotube with the chiral indices $(n,m)=(5,5)$	12
2.9	Diagrams of (a) pyramidalization angle (Θ_P), and (b) the π -orbital misalignment angles (Φ) along the C1-C4 in a (5,5)-SWCNT and C_{60}	14
2.10	Derivatization strategies for carbon nanotubes.	15
2.11	Stages of carbon nanotube filling with fullerene C_{60} <i>via</i> the gas-phase mechanism.	19
2.12	Scanning tunneling spectra of a C_{60} peapod taken in between and on top of the peak-like features (STM image not shown) along the nanotube axis. . .	21
2.13	Schematic representation of CNT oxidative treatment and subsequent amidation of carboxylic acid groups using thionyl chloride.	22
2.14	Solvent-based sidewall arylation of SWCNTs.	25

2.15	Different types of oxygenated functionalities formed on carbon surfaces: (a) carboxylic acids groups, (b) lactone, (c) hydroxyl, (d) carbonyl, (e) quinone, (f) ether, (g) pyrone, (h) carboxylic anhydride, (i) chromene, (j) lactol, and (k) π electron density on carbon basal planes.	27
2.16	Nitrogen-containing functional groups on carbon materials: (a) pyrrole-like group; (b) nitrile; (c) secondary amine; (d) nitro group; (e) nitroso group; (f) tertiary (g) amine; (h) pyridine-like group; (i) imine; (j) amide; (k) lactam; (l) pyridone; (m) quaternary amine.	28
2.17	Dehydration (top) and dehydrogenation (bottom) mechanism of aliphatic alcohols.	33
4.1	(a) BET isotherms and (b) pore size distributions of pristine and functionalized carbon nanotubes.	44
4.2	Thermogravimetric curves depicting the simultaneous mass loss and SO ₂ evolution during heating in an inert gas atmosphere.	45
4.3	TPD profiles of S-functionalized carbon nanotubes obtained from heating the samples at 5 °C·min ⁻¹ in a He flow rate of 25 mL _n ·min ⁻¹	46
4.4	Top: SEM micrograph showing the elemental distribution (a) and corresponding EDX spectrum (b) of CNT-P. Bottom: Elemental mapping (c) with representative EDX spectrum (d) of CNT-W200.	48
4.5	ATR-FTIR spectra of as prepared carbon materials.	49
4.6	Potentiometric titration curves obtained with a 0.01 M sodium hydroxide solution.	50
4.7	Amount of acid sites derived from potentiometric pH titrations and sulfur content calculated from elemental analysis as a function of the sulfur concentration assessed by TPD.	51
4.8	Activities and selectivities as a function of time on stream at four different temperatures observed during the catalytic testing of samples (a) CNT-O150, (b) CNT-O200 and (c) CNT-W200 previously treated at 350 °C in N ₂ for 2h.	52
4.9	ATR-FTIR spectra of the investigated carbon catalysts after the decomposition of 2-propanol.	55
S4.1	TEM images of (a,c) CNT-P and (b,d) CNT-W200	57
5.1	Evolution of (a) CO ₂ , (b) CO, (c) HCN, (d) N ₂ , (e) H ₂ , (f) H ₂ O, (g) HNCO, and (h) C ₂ N ₂ during TPD analysis of oxygen and nitrogen modified carbon nanotubes.	67

5.2	Deconvoluted XP N1s spectra of (a) 300-NCNT, (b) 500-NCNT and (c) 700-NCNT obtained from ammonia treatment of O-CNT.	74
5.3	Area-to-nitrogen-content ratio derived from the N1s spectral features as a function of NH ₃ treatment temperature.	75
5.4	Deconvoluted XP O1s difference spectra (hatched areas) of (a) O-CNT/300-NCNT, (b) 300-NCNT/500-NCNT and (c) 500-NCNT/700-NCNT. Dotted lines represent the background corrected experimental data.	77
5.5	Conversions and selectivities as a function of time on stream obtained at five different temperatures during the catalytic decomposition of 2-propanol on (a) 300-NCNT, (b) 500-NCNT and (c) 700-NCNT. Samples were previously treated at 350 °C in N ₂ for 2h.	83
5.6	Thermogravimetric changes (a) and DSC signals (b) during temperature-programmed oxidation of pristine, oxidized and ammonia treated carbon nanotubes.	86
S5.1	(a) Nitrogen adsorption isotherms and (b) pore size distributions of pristine and functionalized CNTs.	89
S5.2	Potentiometric pH titration curves of (a) HP-CNT before and after HNO ₃ oxidation and (b) NCNTs obtained after NH ₃ treatment of O-CNT at 300, 500 and 700 °C.	89
S5.3	XP N1s difference spectra of (a) 300-NCNT/500-NCNT and (b) 500-NCNT/700-NCNT.	89
S5.4	Mass traces recorded during TPO experiments of HP-CNT, O-CNT and NCNTs. CO ₂ [m/z = 44] (a) and NO _x [m/z = 30] (b) were normalized with respect to Ar [m/z = 40] and the employed sample mass.	90
6.1	Evolution of (a) CO ₂ and (b) CO during TPD analysis of phosphorus containing carbon nanotubes.	99
6.2	Potentiometric pH-titration curves of the pristine and P-modified carbon nanotubes.	101
6.3	Potentiometric pH-titration curves of as-prepared 400-PCNT and after up to 3 cycles (W1, W2, and W3) of hydrothermal treatment.	103
6.4	Adsorption isotherms (a,c) and diff. heats as a function of coverage (b,d) derived from NH ₃ microcalorimetry carried out at 80 °C after 1 st and 2 nd cycle over 400-PCNT and 500-PCNT.	104

6.5	(a) Analysis of gas-phase acidity and estimation of process reversibility by NH_3 -TPD is shown for 400-PCNT. Arrows indicate regions with sites of different strength. (b) Deconvoluted profile of 1 st NH_3 adsorption cycle on 400-PCNT according to the identified regions.	107
6.6	Conversions and selectivities as a function of time on stream obtained at four different temperatures during the catalytic decomposition of 2-propanol on (a) 400-PCNT, (b) 500-PCNT, (c) 600-PCNT, and (d) 700-PCNT. Samples were previously treated at 350 °C in N_2 for 2h.	109
6.7	(a) Thermogravimetric changes during TPO of pristine and P-modified CNTs in synthetic air (b) Dependency of $-\Delta H_{\text{Oxidation}}$, T_{Onset} and T_{50} on phosphorus content.	112
S6.1	(a) BET isotherms and (b) pore size distributions of pristine and functionalized carbon nanotubes.	115
S6.2	Fit of adsorption isotherms obtained during 1 st and 2 nd ammonia adsorption at 80 °C over 400-PCNT. Langmuir, higher order Langmuir and Temkin models were applied in both cases.	115
S6.3	Elemental distribution with corresponding SEM micrograph of 400-PCNT (A) and SEM micrographs of C-CNT (B), 400-PCNT (C), 500-PCNT (D), 600-PCNT (E), and 700-PCNT (F).	116
S6.4	Thermosignals at low coverage obtained for the 1 st (a) and 2 nd (b) NH_3 adsorption cycle over 400-PCNT. The corresponding equilibrium pressures in addition to the sum of integral heats of adsorption and overall integral heat of desorption are also shown.	117

List of Schemes

4.1	Reaction pathways of 2-propanol transformation.	39
4.2	Aryl radical formation <i>via</i> diazotization of sulfanilic acid and subsequent addition of sulfonic acid entities to carbon nanotubes.	42
4.3	Sonolytical dissociation of water (left) and formation of hydroperoxy radical through reaction between hydrogen radical with molecular oxygen (right).	47
5.1	Reaction pathways associated with the catalytic transformation of 2-propanol.	61
5.2	Formation pathway of amides and imides through carboxylic acid neutralization respectively ring-opening of cyclic anhydrides.	68
5.3	Lactam formation <i>via</i> ring-opening of lactones.	68
5.4	Thermal induced decarbonylation of lactams into pyrrole-like nitrogen.	71
5.5	Pyridinic-N (1) exhibiting configuration of quaternary nitrogen (2) induced by H-bonding with adjacent phenolic group.	76
6.1	Reaction pathways associated with the catalytic transformation of 2-propanol.	93
6.2	Formation of P-containing species upon H ₃ PO ₄ activation of O-functionalized carbon nanotubes.	98

List of Tables

2.1	Binding energies of the most common nitrogen and oxygen containing functional groups.	30
4.1	Nomenclature, functionalization conditions and elemental analysis of as prepared carbon catalysts.	43
4.2	Porous structural parameters derived from nitrogen absorption of pristine and functionalized CNTs.	44
4.3	Evolved quantities of SO ₂ , CO ₂ and CO calculated from TPD profiles. . . .	47
4.4	Elemental analysis of samples pretreated in nitrogen atmosphere and after catalysis.	53
4.5	Product selectivity to propylene, acetone, and diisopropylether at iso-conversion and acidity (formation rate of propylene) of benzenesulfonic acid functionalized CNTs determined by the transformation of 2-propanol. . . .	53
5.1	Textural properties and elemental composition of pristine and functionalized CNTs.	65
5.2	Calculated amounts of CO ₂ , CO, N ₂ and HCN (GC peak areas) obtained from the TPD profiles.	72
5.3	Decomposition products, TPD temperature peak maxima and XP O1s/N1s contributions characteristic of O- and N-containing functional groups present on oxidized and N-doped CNTs.	79
5.4	Elemental composition as determined by XPS.	80
5.5	Quantities derived from potentiometric pH titrations.	81
5.6	Product selectivities at isoconversion, basicity (acetone-to-dehydration-products ratio) and acidity (formation rate of dehydration products) of NCNTs determined by the transformation of 2-propanol.	84
S5.1	Elemental composition of NCNTs after catalytic transformation of 2-propanol.	90
S5.2	Characteristic temperatures and heats of combustion derived from TG and DSC results.	90

6.1	Textural properties and elemental composition of pristine and P-modified CNTs.	96
6.2	Calculated amounts of CO ₂ and CO amounts calculated from TPD and characteristic quantities derived from potentiometric pH titrations.	100
6.3	Estimation of total acidity according to NH ₃ -TPD and NH ₃ microcalorimetry (re)adsorption results of 400-PCNT and 500-PCNT performed at 80 °C	108
6.4	Elemental composition of PCNTs after catalytic decomposition of 2-propanol.	111
S6.1	pK _a values of selected oxoacids of phosphorus.	115
S6.2	Fitting parameters obtained for three different adsorption models derived from NH ₃ microcalorimetry measurements performed over 400-PCNT at 80 °C.	116

List of Abbreviations

ATR-FTIR	Attenuated Total Reflectance Fourier Transform Infrared
BET	Brunauer Emmet Teller
BJH	Barrett Joyner Halenda
CNT	Carbon Nanotube
DMF	N,N-Dimethylformamide
DSC	Differential Scanning Calorimetry
EDX	Energy Dispersive X-Ray
FWHM	Full Width at Half Maximum
GC	Gas Chromatography
<i>i</i>-PrOH	Isopropanol
MS	Mass Spectroscopy
MWCNT	Multiwall Carbon Nanotube
ODCB	<i>o</i> -Dichlorobenzene
SEM	Scanning Electron Microscopy
SWCNT	Single-wall Carbon Nanotube
TEM	Transmission Electron Microscopy
TG(A)	Thermogravimetry (Analysis)
TPD	Temperature Programmed Desorption
TPO	Temperature Programmed Oxidation
XPS	X-Ray Photoelectron Spectroscopy

1. Introduction

Buckminsterfullerene, the first spherical carbon molecule ever reported, was discovered by Kroto, Curl, Smalley and co-workers during a joint research project at Rice University in 1985 [1]. In order to understand the origin of the peculiar naming of the C_{60} molecule, it is important to consider the following question: which feasible geometry yields the most stable structure when arranging sixty carbon atoms? Assuming either a planar or a tetrahedral configuration similar to a graphite respectively diamond fragment leads rapidly to the conclusion, that a high number of valences at the edges respectively at the surface would remain unsatisfied. The only plausible geometry that meets all requirements of satisfied sp^2 valences is that of a sphere. This symmetrical structure found for the C_{60} molecule is similar to the geodesic domes designed by the architect Richard Buckminster Fuller, whose work, in consequence, served as the source of inspiration for the name-giving of the new carbon allotrope.

The serendipitous synthesis of this stable nanocage (see Figure 1.1a) represented an important breakthrough in carbon research. In the following years after the discovery great efforts were made in order to explain the stability of the structure from a theoretical point of view. Hence, different physical properties, including the optical spectrum [2], the electronic structure and bonding [2–4], magnetic properties [5, 6] as well as vibrational modes [7–10] were analyzed by means of several calculation methods. In spite that the Buckminsterfullerene became the target of numerous studies, the main problem remained the vanishingly small quantities produced by the conventional laser vaporization method described in [1], thus hindering an experimental validation of the theoretically assessed macroscopic properties. In order to overcome this central problem, alternative production technologies had to be developed. The first process that achieved an output of some grams was the one described by Krätschmer and Huffman [11], in which two graphite electrodes were evaporated using a vacuum arc discharge in a noble gas atmosphere.

In 1991, only one year after the Krätschmer-Huffman arc process had been reported, Iijima presented interesting results about the synthesis of what he defined as “a new type of finite carbon structure consisting of needle-like tubules” [12], using a slight modification of the technique which until then had only been employed for the production of fullerenes. Although these tubular arrangements of sp^2 hybridized carbon atoms, which were mostly considered as filamentous carbons [13–16], had also been observed in the past, it was

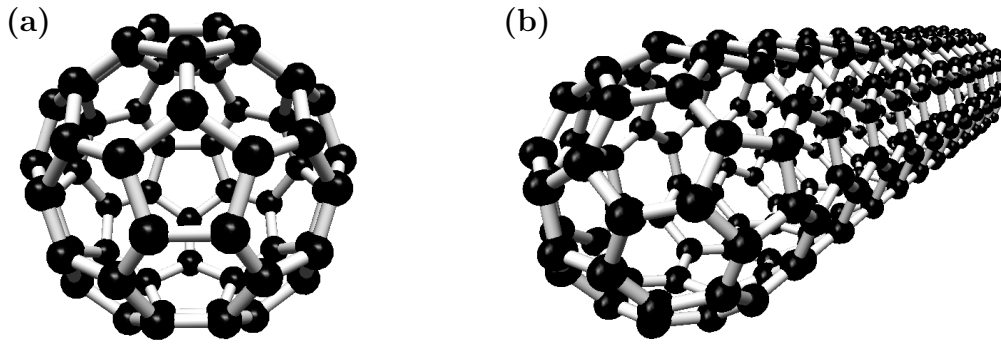


Figure 1.1.: Molecular model of the C_{60} fullerene (a) and of a single-walled carbon nanotube with fullerene-like ends (b).

Iijima who performed the first systematic study using a High-Resolution Transmission Electron Microscope. At this juncture it should be pointed out that the observed structures were what are nowadays called Multiwall Carbon Nanotubes (MWCNT), which consist of multiple concentrically arranged graphene sheets. Emphasizing this is all but trivial, because the only hollow filaments for which several predictive studies had been carried out were made up of one single graphene shell. For instance, Robertson et al. [17] used theoretical methods in order to examine both the lattice energetics and the elastic properties of Single-Wall Carbon Nanotubes (SWCNT) with radii smaller than 9 Å. Regarding the former property, the authors suggested a higher preference for tubular rather than for cage structures. As to the latter one, the results of the study implied that the tubules become softer as their radii decrease. Other theoretical analyses, which for instance focused on the electronic conductivity, predicted that a carbon nanotube may possess either metallic or semiconducting properties, depending on the geometrical constraints, that is to say the radius and the wrapping angle [18, 19]. Although a crucial step was reached when both Iijima and Ichihashi [20] as well as Bethune and co-workers [21] simultaneously reported about the existence of these type of nanotubes, six more years had to pass in order to prove on an experimental basis the topological dependency of the electronic structure [22, 23].

Figure 1.1 depicts an ideal representation of the Buckminsterfullerene as well as of a single-walled carbon nanotube. In contrast to the spheroidal structure of the C_{60} molecule, SWCNTs exhibit an elongated one-dimensional morphology consisting of a cylindrically wrapped graphene sheet, which, according to Geim and Novoselov's definition, is "a flat monolayer of carbon atoms tightly packed into a two-dimensional (2D) honeycomb lattice" [24]. Within this context it is worth mentioning that Smalley and other scientists held the view that a single wall carbon tubule might be the limiting case of a fullerene molecule. Actually, there is an indisputable relation between these nanostructures since the terminal sections of closed carbon nanotubes can be considered as fullerene-like caps or hemispheres

(see Figure 1.1b). A curious fact regarding the geometry of fullerenes and carbon nanotubes is that in the latter case the smallest diameter ever reported corresponds to the diameter of the C_{60} molecule, which is the smallest fullerene cage that satisfies the isolated pentagon rule [25]. According to this principle, fullerenes consisting of pentagons and hexagons are thermodynamically more stable if no two pentagons are adjacent to one another.

Based on the aforepresented historical background there should be no doubt that the discovery of fullerenes and naturally of the carbon nanotubes changed radically the view about the science of carbon, which until then had dealt with the physics and chemistry of graphite, diamond and amorphous carbons. Moreover, the initial excitement in the scientific community triggered by Iijima's observations in 1991 accelerated the research towards a better understanding of the constitution and functionality of carbon based nanostructures, which on the one hand made it possible to substantially improve well-established applications and on the other opened a wide range of potential usages that became possible thanks to the remarkable and unique properties of these compounds [26].

2. Carbon nanotubes: An overview

2.1. Atomic structure

Conceptually, a single-walled carbon nanotube can be imagined as a seamless hollow cylinder constituted by an arrangement of sp^2 hybridized carbon atoms located on the vertices of a rolled-up honeycomb lattice (Figure 2.1). These nanostructured materials can be produced using several techniques including laser ablation, arc-discharge and high-pressure CO conversion (HiPCO), which in general lead to a Gaussian distribution of diameters with mean values between 1.0 and 1.5 nm [28]. As a consequence of the intramolecular van der Waal's forces, single-walled tubes tend to form hexagonal-packed bundles during the growth process. Interestingly, the wall-to-wall distance between two neighboring nanotubes equals the interlayer distance in graphite, which is about 3.41 Å [28]. In spite of the improvements that have been achieved with regard to the synthesis of carbon nanotubes, a remaining problem lies in the fact that the current understanding of the growing mechanisms is far from unambiguous and complete, which in consequence hinders the precise control of the structure. This aspect is of eminent importance as the physical properties of a nanostructured tubule depend on the way the graphene sheet is wrapped (see section 2.2). Each nanotube is specified by a pair of parameters, namely the tube diameter d_t and the chiral or wrapping angle Θ . The chiral vector \vec{C}_h , which connects two crystallographically equivalent sites on the graphene sheet, describes mathematically

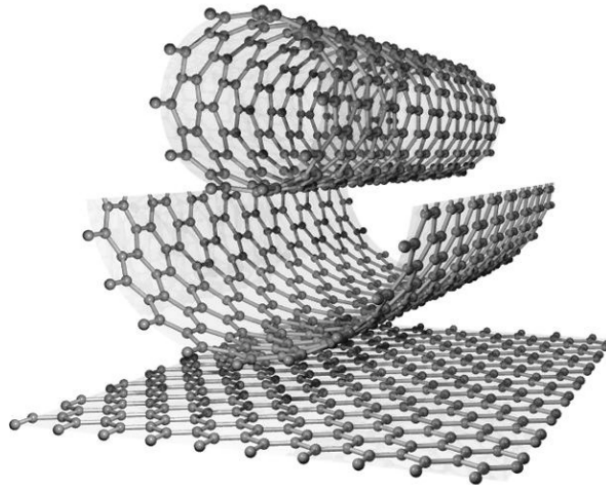


Figure 2.1.: Formation of a carbon nanotube starting from a graphene sheet [27].

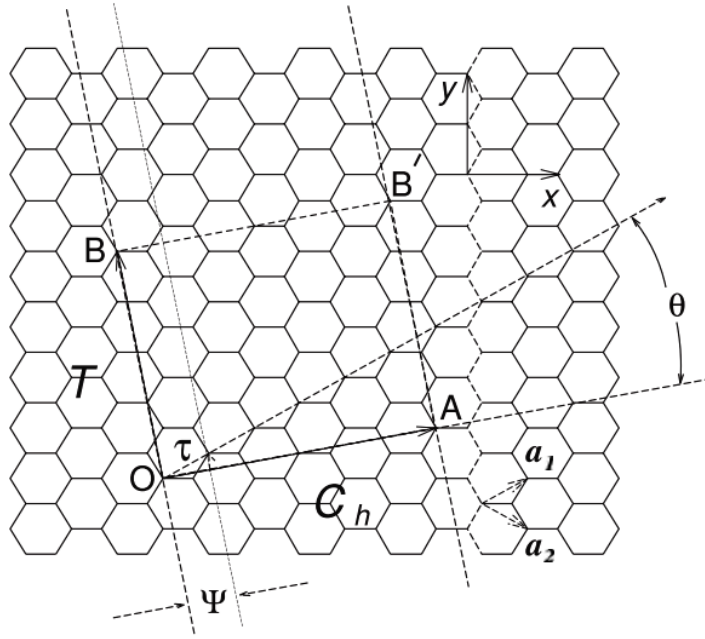


Figure 2.2.: Graphical representation of the geometrical parameters (\vec{C}_h , Θ , \vec{a}_1 , \vec{a}_2) of a single-wall carbon nanotube based on a 2D graphite sheet. The depicted case corresponds to the nanotube defined by the indices $n=4$ and $m=2$ [25].

the circumference of the tube. This quantity is defined by means of the relation

$$\vec{C}_h = n\vec{a}_1 + m\vec{a}_2 \quad 0 \leq |m| \leq n \quad (2.1)$$

with the natural numbers (n,m) and the basis vectors \vec{a}_1 and \vec{a}_2 . In terms of rectangular Cartesian coordinates, these unit vectors can be written as follows:

$$\vec{a}_1 = \left(\frac{\sqrt{3}}{2}, \frac{1}{2} \right) a \quad \vec{a}_2 = \left(\frac{\sqrt{3}}{2}, -\frac{1}{2} \right) a \quad (2.2)$$

In equation 2.2, a stands for the length of the unit vector, which is defined as the square root of three times the distance between two adjacent carbon atoms in the honeycomb lattice ($a = \sqrt{3}a_{C-C}$). This constant has a value of approximately 2.46 Å.

In order to describe the unit cell of a carbon nanotube, it is necessary to introduce a second geometrical object denominated as the translational vector \vec{T} , which lies perpendicular to the chiral vector \vec{C}_h and runs parallel to the tube axis. As can be seen out of Figure 2.2, vector \vec{T} ranges from the origin O to the first lattice point B in the graphene sheet. In general, this quantity is determined in terms of the indices (n,m) by

$$\vec{T} = \frac{2m+n}{d_R}\vec{a}_1 - \frac{2n+m}{d_R}\vec{a}_2 \quad (2.3)$$

where

$$d_R = \begin{cases} d, & \text{if } n - m \text{ not a multiple of } 3d \\ 3d, & \text{if } n - m \text{ a multiple of } 3d \end{cases} \quad (2.4)$$

with d as the highest common divisor of (n,m) . Given the above parameters, the length of the translational vector \vec{T} can be calculated using the expression

$$t = |\vec{T}| = a \frac{\sqrt{3(n^2 + m^2 + nm)}}{d_R}, \quad (2.5)$$

whereas the tube diameter is determined by

$$d_t = \frac{|\vec{C}_h|}{\pi} = a \frac{\sqrt{n^2 + m^2 + nm}}{\pi} \quad (2.6)$$

An important aspect regarding the calculation of d_t using equation 2.6 is that it neglects the effects of the graphene sheet curvature on the C-C bond. For this reason, the application of the aforementioned relation is valid for nanotubes with diameters greater than 1 nm [29]. The chiral angle Θ , defined as the angle between \vec{a}_1 and \vec{C}_h , can be also obtained from the natural numbers (n,m) by means of the following equation:

$$\Theta = \cos^{-1} \left(\frac{n + m/2}{\sqrt{n^2 + m^2 + nm}} \right) \quad (2.7)$$

Furthermore, the amount N of hexagons in the unit cell of a nanotube can be determined by setting the area $S_c = \vec{T} \cdot \vec{C}_h$ of the cylinder surface in relation to the area S_g of the hexagonal graphene unit cell. The calculation of this ratio can be performed based on the following relation:

$$N = \frac{S_c}{S_g} = \frac{2(n^2 + m^2 + nm)}{d_R} \quad (2.8)$$

At this juncture it is necessary to distinguish between three different types of nanotube structures, depending on the values of the wrapping angle. A schematic representation is shown in Figure 2.3. When the absolute value of Θ lies between 0° and 30° , the nanotube is denominated as chiral. In case that the wrapping angle equals the lower boundary, than this type of achiral nanotube is referred to as “zig-zag” $(n,0)$. On the contrary, when Θ reaches the value of 30° , the pattern observed along the circumference corresponds to that of a so-called “armchair” nanotube (n,n) .

After having described the unit cell of a carbon nanotube in the real space, it is now important to define its corresponding Brillouin zone. As shown in Figure 2.4, the Brillouin zone of 2D graphite, which is defined as the Wigner-Seitz primitive cell in the reciprocal lattice, is represented by a shaded hexagon.

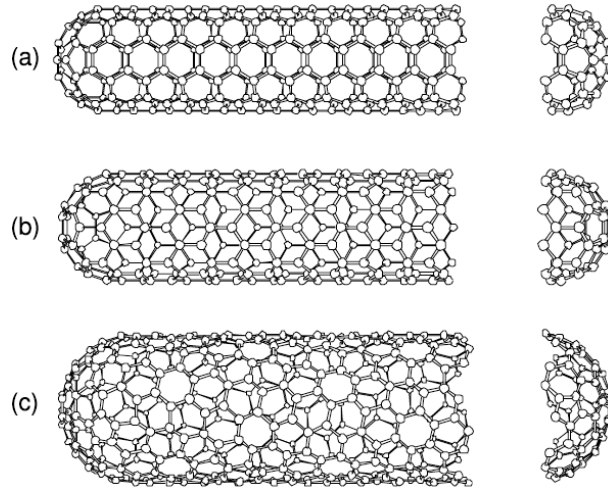


Figure 2.3.: Schematic models of the three different types of single-wall carbon nanotubes: (a) armchair ($\Theta=30^\circ$), (b) zigzag ($\Theta=0^\circ$), and (c) chiral ($0^\circ < |\Theta| < 30^\circ$) [25].

The unit vectors \vec{b}_1 and \vec{b}_2 of the reciprocal lattice are given by the following coordinates:

$$\vec{b}_1 = \left(\frac{2\pi}{\sqrt{3}a}, \frac{2\pi}{a} \right) \quad \vec{b}_2 = \left(\frac{2\pi}{\sqrt{3}a}, -\frac{2\pi}{a} \right) \quad (2.9)$$

In analogy to the vectors \vec{C}_h and \vec{T} , which span the unit cell of a carbon nanotube with the indices (n,m) in the real space, the Brillouin zone is defined by \vec{k}_z in the direction of the tube axis and \vec{k}_\perp along the circumference of the tube. These reciprocal vectors are given by the following relations:

$$\begin{aligned} \vec{k}_\perp \cdot \vec{C}_h &= 2\pi & \vec{k}_\perp \cdot \vec{T} &= 0 \\ \vec{k}_z \cdot \vec{C}_h &= 0 & \vec{k}_z \cdot \vec{T} &= 2\pi \end{aligned} \quad (2.10)$$

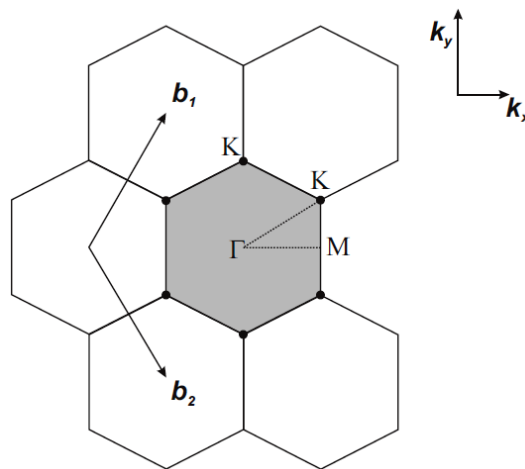


Figure 2.4.: Reciprocal lattice with primitive reciprocal lattice vectors and unit cell (shaded) [27].

As a consequence of the high aspect ratio of a SWCNT, the tube can be regarded as infinitely long, wherefore the wave vector \vec{k}_z is continuous. The first Brillouin zone in the z-direction encompasses the interval $-\pi/t < \vec{k}_z \leq \pi/t$. However, along the circumference of the tube, the wave vector \vec{k}_\perp is quantized. Following boundary condition must be fulfilled

$$\mu \cdot \lambda = |\vec{C}_h| = \pi \cdot d \quad \Leftrightarrow \quad \vec{k}_{\perp,\mu} = \frac{2\pi}{\lambda} = \frac{2\pi}{|\vec{C}_h|} \cdot \mu = \frac{2}{d} \cdot \mu, \quad (2.11)$$

where μ is an integer that can assume values according to the sequence $-N/2, -N/2+1, \dots, 0, 1, \dots, +N/2$. According to equation 2.11 the wave function of a quasi-particle in a nanotube, such as an electron or a phonon, must undergo a phase shift of an integer of 2π around the circumference in order to prevent a cancellation due to destructive interference.

On the basis of the mathematical model presented above, which can be found in more detail elsewhere [30], it is evident that the atomic structure of a single shell nanotube is quite well understood. On the contrary, the geometry of multi-walled carbon nanotubes continues to be an issue of debate, especially because their structure vary depending on the production method applied. In addition, structural discrepancies can be observed even within one single batch, suggesting that the determination of the final structure of the carbon nanotubes is somewhat stochastically driven [31].

A multi-walled carbon nanotube may be constituted by several graphene sheets with different helicities. Intertestingly, it has been reported that the diversity of chiral angles represents about 20 to 50% of the observed number of graphene sheets, implying that some sheets are characterized by the same chirality. An explanation for this finding may be found therein, that the tube helicity needs to be properly changed in order to accommodate tubules with increasing diameters in a coaxial way, prevailing at the same time the wall-to-wall distance of about 3.4 Å, which is similar to the interlayer spacing in turbostratic graphite [32].

For certain multishell nanotubes there is evidence that they possess an asymmetric structure defined by non-uniform fringes. In other words, when taking a closer look at the cross section of the tubules, one can observe that the distance between successive walls is different depending on which side of the tube is being analyzed. In HRTEM images, the fringes of the smaller and regular spacings are usually of higher contrast, whereas the side with the thicker walls is rather weak and irregular [33]. From these observations a concept based on a polygonal form of the cross-sections was proposed. This model has also been applied to explain the coaxial accommodation of tubules with increasing circumferences.

Even though a great number of publications have dealt with multi-walled carbon nanotubes, insofar there is no uniform definition for this type of tubules. On the one hand, based on Iijima's observations [12], MWCNTs are constituted by a coaxial arrangement

of singleshell carbon nanotubes with increasing diameters (Figure 2.5). On the other hand, indications exist that multi-walled nanotubes may be constructed by scrolling a single graphene sheet. Starting from the predominant definitions found in the literature, MWCNTs are described either from a morphological or a structural point of view. Whereas in the former case a carbon nanotube is referred to as any kind of carbonaceous hollow cylinder, in the latter one, the definition is based on the nested model reported by Iijima. This discrepancies make it difficult to unambiguously speak about multi-walled nanotubes, wherefore Tessonnier et al. [34] suggest to generalize the structural definition.

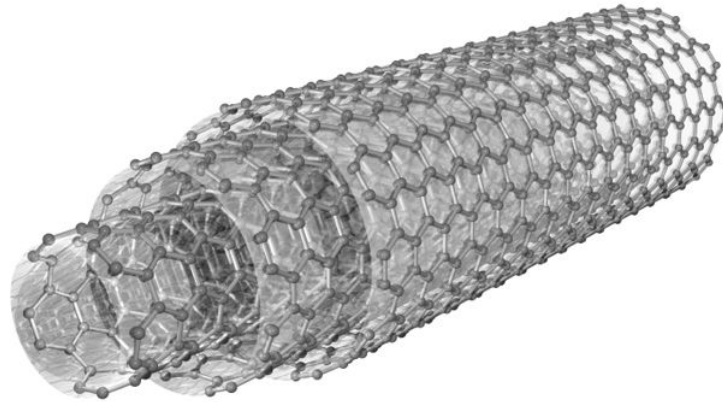


Figure 2.5.: Model of a multi-walled carbon nanotube [27].

2.2. Electronic properties

As has been mentioned before, the physical properties of carbon nanotubes depend not only on the amount of graphene shells from which they are constituted, but also on the chirality and diameter of the wrapped sheets. In this section, only the electronic properties will be highlighted and presented. The aim hereby is to give a theoretical background that explains both the metallic and semiconducting behavior of carbon nanotubes.

To gain an insight into the electronic properties of a SWCNT, it is convenient to start analyzing the band structure of graphene. In this material, the carbon atoms exhibit a trigonal sp^2 hybridization resulting from the linear combination of one 2s and two 2p orbitals. This leads to the formation of the bonding and anti-bonding σ orbitals, which are in-plane with the graphene sheet. Although one might expect that the σ bonds determine the electronic properties, in fact their energy values are too far away from the Fermi level in order to play a significant role. This can be seen clearly in Figure 2.6, where the energy dispersion relations of graphene along the border of the triangle defined by the high symmetry points ΓMK are shown. The smallest band gap between the bonding and

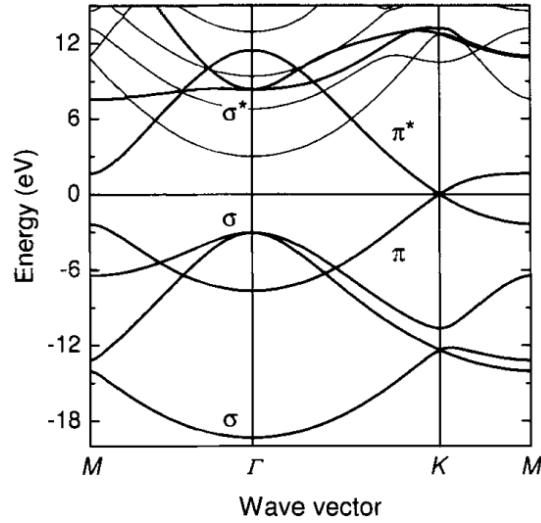


Figure 2.6.: Electronic band structure of graphene along the high symmetry points of the triangle ΓMK as shown in Figure 2.4 [28].

anti-bonding states is about 11 eV and can be found at the Γ point. As a consequence of the large energy difference, these bonds have a neglectable influence on the electrical conductivity of graphene. The second type of bond found in graphene is the π bond, which is formed by the overlapping $2p_z$ orbitals of adjacent carbon atoms. Each sp^2 hybridized carbon atom has one π electron, which can be found with a high probability either above or below a graphene layer. Therefore, the π electrons are not stationary, but are delocalized within neighboring π orbitals. As can be further seen in Figure 2.6, the π valence and π^* conduction bands degenerate near the Fermi level at the K point of the hexagonal Brillouin zone. For this reason, graphene is referred to as a zero-gap semiconductor, characterized by a Fermi surface consisting of six different points.

At this juncture it is important to remember that, whereas the wave vectors around the nanotube circumference only take discrete values, those along the tube axis are continuous. If the electronic states along the \vec{k}_z direction are plotted onto the Brillouin zone of graphene, a series of parallel lines formed by the allowed wave vectors of a nanotube can be found. The nature of these lines, namely the length, position and orientation, depends on the helicity of a particular nanotube. An exemplification is given in Figure 2.7, showing the first Brillouin zone of an armchair and a zig-zag nanotube.

In order to determine whether a carbon nanotube is a semiconductor or a metal as a function of its geometrical constraints, it is necessary to interrelate the allowed k lines of a nanotube along its circumference with the Fermi surface of graphene. Among others we know that the degeneration of the valence and conduction bands of graphene takes place at the K point of the Brillouin zone. A carbon nanotube only exhibits metallic properties when the allowed k lines pass through this high symmetry point. As the quantization of

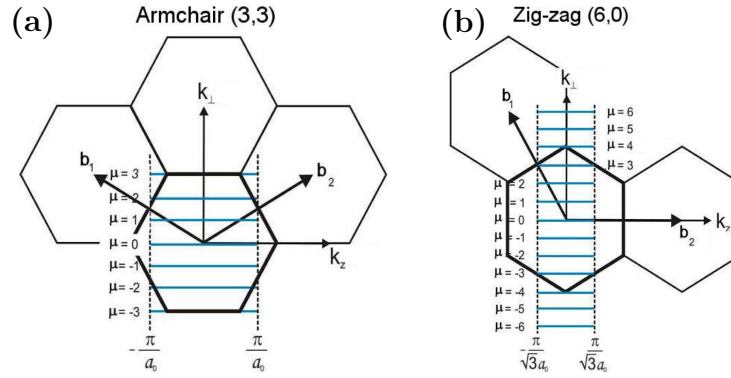


Figure 2.7.: Schematic representation of the first Brillouin zone of a (3,3) nanotube (a) and a (6,0) nanotube (b) [35].

the wave vectors along the circumference is given by equation 2.11 and the location of the K point in the Brillouin zone is described by the vector $\vec{K} = \frac{1}{3}(\vec{b}_1 - \vec{b}_2)$, then the following should apply to a metallic nanotube:

$$\vec{K} \cdot \vec{C}_h = 2\pi\mu \frac{1}{3}(\vec{b}_1 - \vec{b}_2) \cdot (n\vec{a}_1 + m\vec{a}_2) = \frac{2\pi}{3}(n - m) \quad (2.12)$$

A further simplification of equation 2.12 leads finally to the well known relation

$$3\mu = n - m, \quad (2.13)$$

which implies that whenever $n-m$ becomes a multiple of three, a single-walled carbon nanotube shows metallic properties with a non-zero density of states at the Fermi level as shown in Figure 2.8.

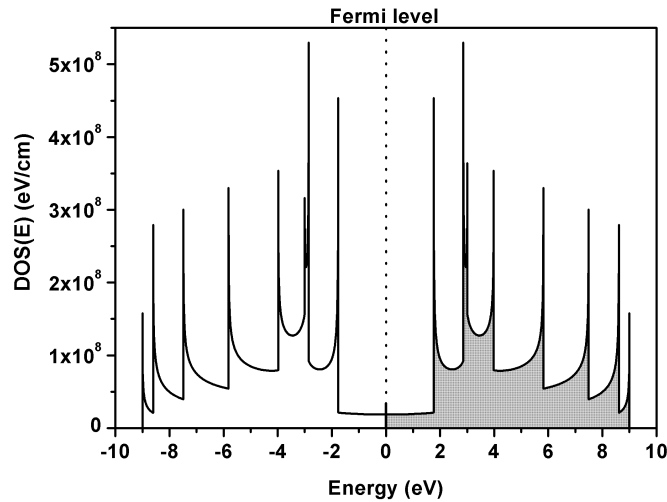


Figure 2.8.: Density of states of a nanotube with the chiral indices $(n,m)=(5,5)$.

2.3. Reactivity of carbon nanotubes

The chemical reactivity of carbon nanotubes can be better understood when studied together with that of their closest sp^2 -hybridized relatives, namely graphite and fullerenes. Graphene and therefore graphite can be regarded as carbonaceous materials with a high degree of chemical inertness, which is a natural consequence of their planar, aromatic structure. Merely a handful of greatly reactive compounds, including fluorine, possess the ability of derivatizing such flat conjugated π -surfaces [36]. As opposed to this, performing the functionalization of a curved π -surface as available in fullerenes is a less complex task, which can be confirmed by the wide range of derivatization strategies successfully applied to these compounds [37]. At this point it is evident that bending a graphene sheet in a three-dimensional manner introduces strain into the carbon framework, resulting in an increased reactivity. The following two determining factors have to be taken into account whenever the different behavior of the aforementioned carbon allotropes towards a chemical modification needs to be described [38]:

- (i) **Curvature-induced pyramidalization:** sp^2 -hybridized carbon atoms are characterized by a trigonal planar shape, implying that the pyramidalization angle Θ_P equals 0° . In the case of a tetragonal sp^3 -hybridized carbon atom, the angle between the σ and π orbitals is larger than 90° , which in turn leads to a pyramidalization angle of 19.47° (see Figure 2.9a). For all the carbon atoms in the buckminsterfullerene it was found that $\Theta_P=11.6^\circ$, suggesting that the hybridization of the carbon atoms tends to be more tetragonal rather than trigonal. From this it follows that the chemical modification of any carbon atom in the C_{60} molecule leads to a relaxation of the entire structure, reducing the strain originally induced by the curvature of the geometry.
- (ii) **π -orbital misalignment:** as can be observed from Figure 2.9b, the π -orbitals located at the carbon atoms 1 and 4 of the C_{60} molecule are perfectly aligned with respect to each other, leading to a misalignment angle Φ of 0° . In the case of CNTs it is necessary to distinguish between two different types of bonds: whereas the C-C bond lying normal to the nanotube axis shows again no π -orbital misalignment, the other is slightly rotated with respect to the circumference, exhibiting a misalignment angle Φ of 21.3° as a consequence of the curvature. This effect is responsible for the torsional strain in carbon nanotubes, which is released whenever the sidewall of a nanotube undergoes an addition reaction.

From a chemical point of view it is convenient to divide a carbon nanotube in two different zones: the end caps and the sidewall. The former region is similar to a hemispherical fullerene, whereas the latter one corresponds to a one dimensional folded graphene sheet.

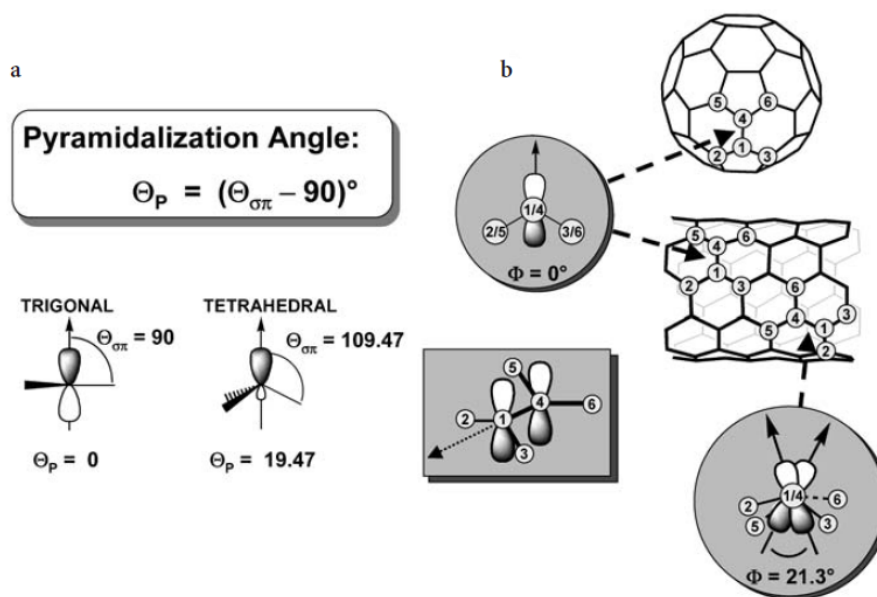


Figure 2.9.: Diagrams of (a) pyramidalization angle (Θ_P), and (b) the π -orbital misalignment angles (Φ) along the C1-C4 in a (5,5)-SWCNT and C₆₀ [39].

As it is already known from the curvature-induced pyramidalization, the highest reactivity can be found at the end caps, where the chemical modification is driven by the release of strain energy. This is ensured for any nanotube irrespective of its diameter as shown by Haddon et al. [40], who reported that the maximum pyramidalization angle of a fullerene with icosahedral symmetry cannot take values below 9.7° . With respect to the sidewall and the corresponding chemistry it must be said that although the pyramidalization angle assumes nonzero values, the observed reactivity is rather ascribed to the more pronounced misalignment of the π -orbitals located at the carbon-carbon bonds tilted to the nanotube axis. Furthermore, both Θ_P and Φ exhibit an inverse dependency on the diameter, which has been theoretically studied by means of DFT calculations [41] and experimentally observed on the ground of Raman spectroscopy [42].

Both Θ_P and Φ are useful quantities with which the chemical inertness of graphene and graphite can be explained. In the case of planar conjugated π -surfaces no pyramidalization at any carbon atom as well as no π -orbital misalignment between adjacent pairs of carbon atoms exists, meaning that no strain energy is stored within the framework of these carbon allotropes. As a consequence, any kind of addition reaction would build up strain energy instead of releasing it as opposed to their curved sp^2 -hybridized relatives [36].

2.4. Chemical derivatization approaches

Although it is indisputable that carbon nanotubes are promising macromolecules for a wide range of nanotechnological applications, including electrically conducting composite

materials [43], field electron emission sources [44, 45], electrochemical devices such as supercapacitors [46], assemblies for hydrogen storage [47], chemical gas sensors [48], and scanning tips for atomic probe microscopes [49], there are still some drawbacks that need to be overcome before reaching a large-scale commercial use. For instance, it is necessary to enhance the low solubility of as-produced nanotubes both in organic and aqueous solvents, which is necessary for a proper handling of these compounds [50]. Moreover, some meaningful problems related to the production of CNTs need to be solved, as so far no technique is capable of yielding large amounts of nanotubes with homogeneous properties, that is to say with uniform diameter, chirality and length [26]. In other words, until now there is no possibility to selectively produce either metallic or semiconducting SWCNTs, which in turn hinders their entry into the world of nanosized electronic devices [39].

One of the solutions that addresses the solubility issue is the chemical functionalization of the nanotubes, which enables the structural alteration of the carbon framework, and thus the tailoring of the physico-chemical properties. For instance, introducing moieties of different kinds may be used in order to adjust the interaction of the nanotubes with other entities, such as solvents, polymers or simply other nanotubes. A functionalized nanotube may even exhibit mechanical as well as electrical properties that are not present in the pristine sample [39]. Due to the fact that many studies have dealt with this topic in the past, nowadays a wide range of derivatization strategies is available. A benefit related to

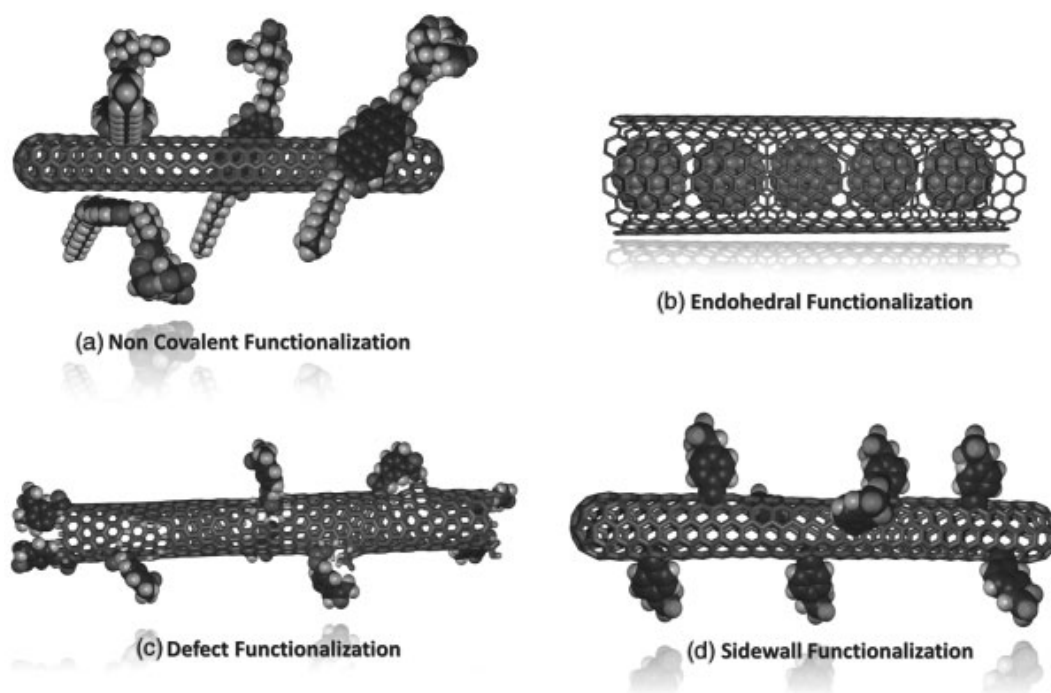


Figure 2.10.: Derivatization strategies for carbon nanotubes [36].

this development is the possibility of using nanotubes as solid acid or base catalysts as well as a support for an active phase. Both aspects will be discussed in more detail in section 2.6.

In order to deal with the vast amount of derivatization approaches that have been successfully applied in the past, it is reasonable to discuss the topic based upon the following categories: non-covalent, endohedral, defect site and sidewall functionalization (Figure 2.10). At this juncture it is important to mention that the upcoming overview should not be perceived as an attempt to review the existing literature, but rather as an effort to give the reader an insight into the different ways of tuning the chemical properties of carbon nanotubes.

2.4.1. Non-covalent exohedral functionalization

Supramolecular derivatization approaches offer the great advantage of attaching organic as well as inorganic moieties to the outer surface of carbon nanotubes, while preserving their intrinsic electronic and mechanical properties [36, 51]. The driving force behind this kind of modification strategy is the non-covalent interaction between the nanotube skeleton and the adsorbate of interest. Some of the interactions involved in the process are charge transfers, π - π -stacking interactions, and van der Waal as well as electrostatic forces.

Several publications have focused on finding a way to improve the dissolution of CNTs in water as these compounds tend to form insoluble agglomerates *via* intermolecular van der Waal interactions, which are strengthened by their large specific surface area [52]. Breaking a bundle by means of ultrasonication is not enough as individual nanotubes rebundle again with time. Nevertheless, the agglomeration process can be inhibited if suitable surfactants are introduced into the suspension. While the lipidic chain interacts with the surface of the nanotubes, the polar end ensures their solubility in the aqueous medium. Up to date, sodium dodecyl sulfate (SDS) has been the most widely used surfactant [53–57]. By means of TEM analysis it was shown that SDS forms supramolecular assemblies consisting of rolled-up half-cylinders in which the alkyl rests point towards the nanotube framework. Depending on the symmetry and the diameter of the nanotubes, different types of arrangements, including rings, helices, and double helices have been observed. [57].

Surfactants with aromatic groups are physisorbed on the graphitic surface of the nanotubes through more specific and more directional π - π -stacking interactions [58]. In a comparative study performed by Islam et al. [59] using single-walled carbon nanotubes and surfactants of different types, it was stated that the superior dispersing capability of sodium dodecylbenzene sulfonate (SDBS) as well as of Triton-X-100 compared to that of

SDS arises from a π -like stacking of aromatic moieties onto the surface of CNTs. Other factors influencing the graphite-surfactant interactions are the hydrophobic chain length, headgroup size, and charge. Atomic force microscopy measurements demonstrated that even at nanotube concentrations as high as 20 mg/mL, more than 60% of the agglomerates exfoliated into isolated tubes [59].

In the field of materials science the utilization of carbon nanotubes as functional fillers in polymer nanocomposites has gained increasing attention, because this application has opened up the possibility to greatly enhance the physical properties of the materials in question. Different noncovalent modification strategies have been developed for this purpose, including physical mixing in solution, *in situ* polymerization of monomers in the presence of nanotubes, surfactant-assisted processing of composites, as well as chemical functionalization of the incorporated nanotubes [60]. In the following paragraphs the focus will be set on hydrocarbon and conjugated polymers.

Carbon nanotubes have been used as reinforcement elements in hydrocarbon polymers, such as polystyrene, polypropylene, and polyethylene. The blending results in a composite material with improved strength and stiffness characteristics. Using a simple solution-evaporation method, Qian et al. [61] dispersed multiwalled carbon nanotubes throughout polystyrene matrices. Tensile tests performed on composite films containing 1 wt% of CNTs evidenced increases of the Young's modulus and break stress by around 40% and 25%, respectively. In addition, *in situ* TEM observations confirmed that the external load is effectively transferred to the nanotubes, a finding that may be ascribed to the high aspect ratio of the carbon nanostructure. Similar conclusions, but with regard to polypropylene-based composites, were made in a study by López Manchado et al. [62]. The authors investigated the tensile mechanical properties of isotactic polypropylene blended with SWCNTs containing different amounts of the carbon material. One of the core statements was that both the Young's modulus and the tensile strength considerably increased in the presence of the nanotubes, showing maximum values for a mass fraction of 0.75%. Furthermore, a comparison with carbon black used as a filler evidenced the superiority of the nanostructured material, which again, was ascribed to its high aspect ratio.

Among the polymer composites attracting the attention of researchers, conjugated polymers such as poly(phenylenevinylene) (PPV) are of special interest. One of the first polymers to be studied within this context was poly(phenylacetylene) (PPA), a soluble photoconductive compound [60]. The synergistic effects that arise from its combination with carbon nanotubes are reflected in two different features. On the one hand, the helically wrapped polymer induces solubility of the blend in organic solvents. On the other hand, whenever the composite is exposed to harsh laser irradiation, the nanotubes stabilize

the polymer, protecting it from photodegradation [63]. Another eye-catching example comprises the enhancement of the electrical conductivity of poly(m-phenylenevinylene-co-2,5-dioctoxy-p-phenylenevinylene) (PmPV). This polymer is known to be poorly electrically conductive, but highly luminescent. Although doping a polymer results in an increasing conductivity, it is detrimental for the optical properties as it reduces the bandgap of the material. A solution for this trade-off proposed by Curran et al. [64] consists in using small amounts of MWCNTs as physical "dopants" and mixing them up with the luminescent polymer by means of ultrasonication. This simple approach made it possible to increase the electrical conductivity of PmPV by a factor of 8, preserving thereby the luminescence properties of the pure polymer.

A further application worth mentioning is the employment of carbon nanotubes as a host material for the immobilization of biomolecules. Using noncovalent functionalization methods it has been possible to combine the superior electro-conducting properties of CNTs with the specific recognition capabilities of the immobilized biosystems, resulting in supramolecular assemblies that are suitable for being used as miniaturized sensors [39]. In an investigation performed by Besteman et al. [65] it was shown that semiconducting SWCNTs coated with the redox enzyme glucose oxidase act as reversible pH sensors and at the same time show a response towards the addition of glucose, which make them ideal for monitoring the enzymatic activity. Agüí et al. [66] reported about a lactate biosensor constructed by immobilizing the enzyme lactate dehydrogenase (LDH) on glassy carbon modified with a conducting polymer and combined with MWCNTs. The sensor was used for the recognition of NADH, which is generated during the enzyme-catalytic conversion of lactate to pyruvate. It was shown that the bioelectrode was able to operate at low potential values without any redox mediator and without losing its analytical performance. Finally, it should be mentioned that DNA biosensors are being developed at a fast pace with the aim of finding a rapid, simple and inexpensive way to test genetic and infectious diseases. As expected, performance improvements have been achieved in the presence of CNTs. Wang and coworkers [67], for instance, demonstrated that carbon-nanotube modified glassy-carbon electrodes facilitate the adsorptive accumulation of guanine as compared to the bare glassy carbon, which in turn enhances the oxidation signal of the nucleobase.

2.4.2. Endohedral functionalization

Filling the inner cavities of carbon nanotubes with foreign species such as fullerenes or nanoparticles has become an important tool for studying the chemistry and physics of molecules encapsulated in a quasi one dimensional channel. In fact, the structural and

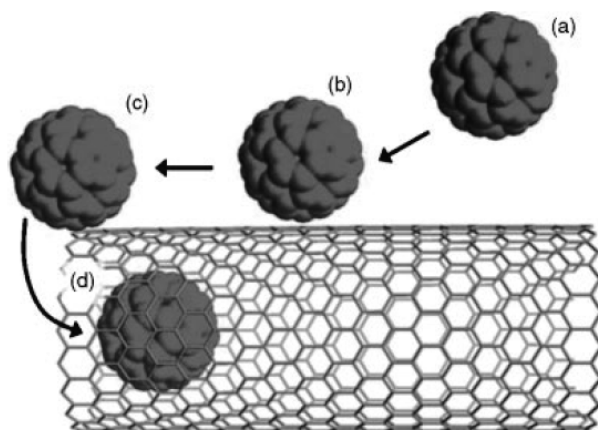


Figure 2.11.: Stages of carbon nanotube filling with fullerene C_{60} *via* the gas-phase mechanism [68].

dynamic properties of some compounds change dramatically as a result of the confinement-induced arrangements achieved inside the nanotubes. At the very beginning, the fact that CNTs could serve as nanosized containers was considered an unusual peculiarity of the nanoworld. Over time, researchers were able to broaden their knowledge about this special feature, not least because of the discovery of some important rules regarding host-guest interactions. Nevertheless, the effects that the encapsulated compounds have on the physicochemical properties of nanotubes are far from being completely understood, probably a consequence of CNT polydispersity and/or of their complex intrinsic properties. [68].

Since the C_{60} molecule is the most abundant among the higher fullerenes and at the same time the less complex to encapsulate, it has become the guest species most widely studied. In the seminal work of Smith and co-workers [69], it was shown for the first time that the buckminsterfullerene could be hosted inside the channels of single-walled carbon nanotubes. These so-called peapods were produced during the purification of raw nanotubes using the pulsed laser vaporization method. Similar observations were reported for nanotubes synthesized by the arc evaporation of carbon in the presence of nickel-yttrium catalysts [70, 71]. Both methods have low production quantities in common. Nevertheless, a controlled synthesis procedure based upon the vacuum-annealing of previously oxidized SWCNTs in the presence of fullerenes has shown to be the method of choice when large amounts of peapods are required [72, 73]. Not only the low sublimation temperature of the fullerenes, but also the thermal stability of these compounds make the latter procedure suitable for a large-scale production [60].

One important question concerns the filling mechanism of nanotubes with buckyballs. Two different pathways have been proposed in order to explain the formation of peapods [74]: (1) direct encapsulation of C_{60} from the gas phase into the channel either through

open ends or defects present in the sidewall or (2) diffusion of adsorbed buckyballs from the external surface into the nanotube interior (see Figure 2.11). With respect to the latter route, it is necessary to point out that even though the guest species become adsorbed onto the outer surface of the carbon framework (Figure 2.11b), they are able to freely migrate along the tube and consequently to reach an open cavity (Figure 2.11c). Before entering the channel, the adsorbates must overcome a specific activation barrier - around 0.3 eV for C_{60} - which is overcompensated upon encapsulation (Figure 2.11d) by stronger host-guest van der Waals interactions [68]. This enhancement evidently results from the larger contact surface area between the nanotube and the confined molecules.

After the discovery of fullerene-filled nanotubes, several publications focused on studying their structural, vibrational and electronic properties. Transmission electron microscopy studies revealed the periodic linear arrangement of the guest molecules inside the nanotubes and electron diffraction measurements served as a basis for assessing the inter-fullerene distance, which in the case of the C_{60} molecule was estimated to be around 0.95-0.97 nm [75, 76]. Interestingly, it was found that the intermolecular spacings of fullerenes in peapods were smaller compared to those of the corresponding crystalline bulk sample, suggesting a competition between two kinds of interactions, namely, the fullerene-fullerene and fullerene-tube interactions [75].

Concerning the vibrational properties it is known that fullerene-filled nanotubes exhibit characteristic features of their constituent components [77]. For the C_{60} and C_{70} peapods, the RBM frequency has been found to undergo a downshift by up to 5 cm^{-1} in relation to the empty nanotubes, while the G-band seems to remain unaffected despite the functionalization. The former observation has been considered as an evidence for the weak electron transfer to the fullerenes, which is additionally supported by the existence of a peak centered at 1465 cm^{-1} , probably ascribable to the pentagonal pinch mode of the buckminsterfullerene. In view of the fact that the frequency value is 4 cm^{-1} lower than the one found for the corresponding bulk material, being the former one too largely downshifted in order to be explained solely in terms of electron transfer, other explanations have been proposed for this finding: For instance, the downshift could be related to an increase of the tube diameter arising from the confinement of foreign molecules or to the reduction of intertube interactions as a result of fullerene intercalations into the bundles [78].

A deeper insight into the local electronic structure of individual peapods has been gained using sophisticated techniques like scanning tunneling spectroscopy [79]. Besides finding a semiconducting behaviour for all studied peapods, significant differences between the valence and conduction states were further observed. As depicted in Figure 2.12, a pronounced bimodal peak evolves in the conduction band only when the spectrum is taken

on top of an encapsulated C_{60} molecule, whereas the occupied DOS (negative bias) remains rather unchanged regardless of the axial position at which the spectroscopical analysis is performed. This asymmetric finding is consistent with the corresponding spatial mapping along the nanotube axis (not shown), as only the unoccupied electronic states display periodic features at a distance of around 1 nm. This value resembles the one obtained from electron diffraction measurements [75, 76], which supports the statement that the spatial modulations indeed arise from the confined molecules.

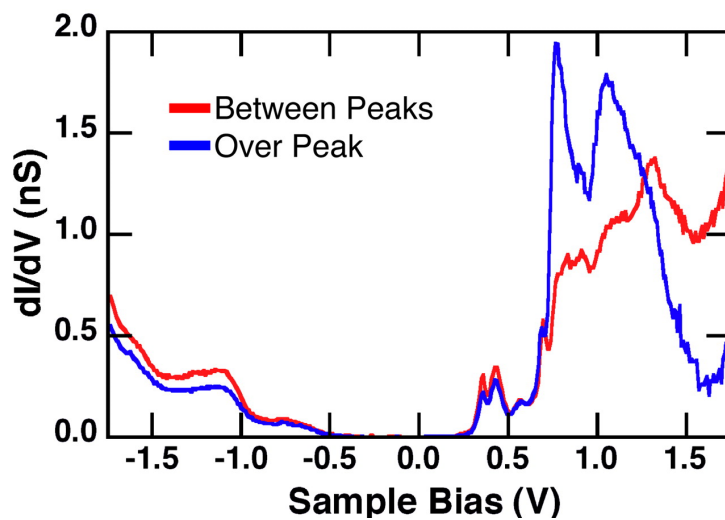


Figure 2.12.: Scanning tunneling spectra of a C_{60} peapod taken in between and on top of the peak-like features (STM image not shown) along the nanotube axis [79].

2.4.3. Defect site functionalization

Even though carbon nanotubes are often assumed to be perfect structures without distortions in the lattice, research has brought to evidence that this is very seldom the case. Several types of defects and dislocated carbon atoms are known to be already generated during the production step, especially at the ends of the nanotubes. In these areas of disorder it is not uncommon to find enclosed catalyst particles that originally serve as starting points for initiating the growth process of the material. Defects can also be present in the sidewalls of the nanostructure: pentagon-heptagon pairs called Stone-Wales defects, sp^3 -hybridized defects, and vacancies are some examples [36].

A common way of introducing defects into the structure of carbon nanotubes involves exposing the material to different kinds of oxidizing agents, including nitric and sulfuric acids as well as potassium permanganate and hydrogen peroxide, among others [80]. This approach is in many cases unavoidable owing to the necessity of removing up to several layers of the highly reactive pyrolytic carbon that covers the outer surface of

as grown nanotubes. Furthermore, only under rather harsh conditions it is possible to drastically reduce the amount of catalyst residues present in the pristine specimens, which are reported to lower the decomposition temperature and increase the decomposition rate [81]. A widely known side effect of such liquid-phase oxidative treatments is the inevitable introduction of oxygen functional groups at the ends and defect sites of the material in question. Actually, one of the most critical aspects related to this kind of surface modification is that the nature of the created moieties cannot be controlled in a selective way, meaning in turn that the acid-basic properties of the starting material are changed in a rather arbitrarily manner. At this juncture it is necessary to point out that the development of non-destructive purification strategies, which are capable of removing impurities without affecting the carbon framework, has turned out to be one of the most challenging tasks [36].

In spite of the structural degradation suffered by CNTs upon contact to strong oxidizing agents, one great advantage offered by the liquid-phase purification procedures is the fact that carboxylic acid functionalities are widely created, and precisely their existence is of paramount importance as these sites serve as starting points for numerous types of functionalization sequences [36]. Therefore it is not surprising that the achievable final state of a specific modification procedure directly depends on the surface density of carboxylic acid groups.

One of the most widely applied derivatization approaches within this context, referred to as the oxidation-amidation procedure, was developed by Liu et al. [82] in 1998. In

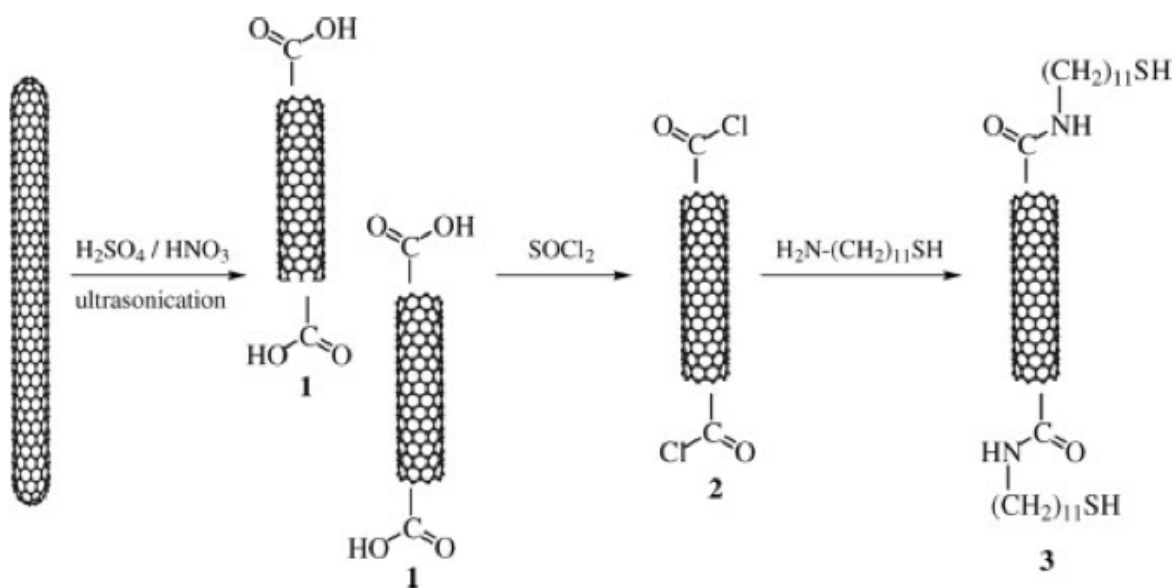


Figure 2.13.: Schematic representation of CNT oxidative treatment and subsequent amidation of carboxylic acid groups using thionyl chloride [36].

their seminal work, the authors described an ultrasonic cutting method for SWCNTs using a mixture of concentrated sulfuric and nitric acid that lead to shorter, carboxylated specimens. The oxygen functionalities were subsequently treated with SOCl_2 (2) and $\text{NH}_2\text{-(CH}_2\text{)}_{11}\text{-SH}_2$ (3) in order to yield alkanethiol chains coupled to the nanostructure through amide linkers (Figure 2.13). In a further step they were able to attach gold nanoparticles to the free thiol groups, a fact that was confirmed by means of AFM. This functionalization approach was also applied by Haddon and co-workers [83], who derivatized both metallic and semiconducting SWCNTs as described previously, but using octadecylamine (ODA) after the formation of the acyl chloride, with the aim of improving the solubility of the material in organic media. Further investigations performed by the same research group showed that even though the use of para-substituted alkyl aryl amines could also give soluble materials, the targeted physical property was not enhanced to the same extent as it was by the derivatization with long chain alkanes [84]. In the same study they demonstrated that an acid-base reaction between the carboxylated nanotubes and a long chain alkyl amine was also a suitable strategy for enhancing the solubility of the material. However, in the latter case the organic moieties instead of being covalently bonded to the nanostructure, they remained attached by ionic forces.

Esterification of immobilized carboxylic acid groups as a further defect-based derivatization route leading to soluble carbon nanotubes, has been extensively investigated, for instance, by Sun and co-workers [85–88]. One of their earlier studies dealt with the functionalization of SWCNTs and MWCNTs using various types of lipophilic and hydrophilic dendrimers in association with the modification step involving the formation of acyl chlorides. The resulting materials, which were fully characterized by means of NMR and electron microscopy, showed in dependence of the used substrates enhanced solubility in both organic solvents and water [85]. Further evidence confirming the existence of ester linkages was gathered by defunctionalizing the modified carbon nanotubes under based-catalyzed hydrolysis reaction conditions. Using this approach, the authors were able to recover the starting CNTs that were again insoluble in any solvent [86]. An interesting report from the same research group demonstrated that carbon nanotubes could be deuterated using ethanol- d_6 as a co-reactant together with 3,5-dihexadecyloxybenzyl alcohol in esterification reactions [87]. Later investigations dealing with the attachment of pyrene moieties to the surface of nanotubes showed that the carbon material efficiently quenched the pyrene photoexcited states. This observation was explained in terms of a process involving energy transfers from the bonded molecules to the CNTs [88].

As has been previously stated, amidation and esterification strategies have been widely implemented whenever soluble carbon nanotubes were needed. This can be also observed in the work of Gu and co-workers [89], who were able to perform a solid-state reaction

between oxidized nanotubes and 2-aminoethanesulfonic acid yielding a material with enhanced water solubility. An improvement was also achieved by Pompeo et al. through covalent grafting of glucosamine to the surface of single-walled carbon nanotubes, while the group of Chen et al. [90] attained excellent results by simply attaching the amino acid lysine to acyl chloride modified MWCNTs. Interestingly, in the latter mentioned study it was stated that stable concentrations of around 10 mg/mL could be obtained in deionized water, which is a value nearly 2 orders of magnitude higher than the one achieved for the acidified material. Of special interest are solvent-free processes since, on the one hand they are environmentally friendly, while on the other they render the possibility to simplify the scale-up of the synthesis from laboratory to industrial dimensions. Within this context, Ford et al. [91] presented a method whereby acid-purified carbon nanotubes are treated with molten urea, which in this case is used as both a solvent and reactant. NMR and XPS measurements confirmed that ureido functionalities were indeed attached to the water soluble material.

2.4.4. Sidewall functionalization

In order to understand the importance of direct sidewall derivatization approaches it is necessary to have in mind that carbon nanotubes possess a high aspect ratio. Since the previous described defect-based functionalization techniques require the existence of carboxylic acid groups, which are preferentially created at the tips of the nanotubes, suggesting that only a small portion of the carbon material participates in the chemical modification, it is not surprising that the overall derivatization degree is relatively low. This in turn implies that the sidewalls are hardly involved in the transformation sequence. For this reason, the availability of direct sidewall functionalization approaches offer the opportunity to tether a great amount of functional entities onto the nanotube framework, meaning that a higher functionalization degree is theoretically achievable. Nevertheless, two important drawbacks are directly linked to the direct sidewall functionalization. As opposed to the defect-mediated derivatization approaches, the straight modification of the sidewalls always leads to a rehybridization of a sp^2 carbon atom into a sp^3 configuration, which is a requirement for the formation of a covalent bond between an attacking substrate and a carbon atom with aromatic character. The main consequence is that the π -system of the carbon nanotube is disrupted, which is known to have a negative effect on the electronic and mechanical properties of the material. The other issue concerns the lower reactivity of the sidewall, which arises from the similarity between the CNTs and a planar π -system in terms of chemical inertness. In spite of the aforementioned problems, the direct chemical derivatization of carbon nanotube sidewalls is indeed an interesting possibility

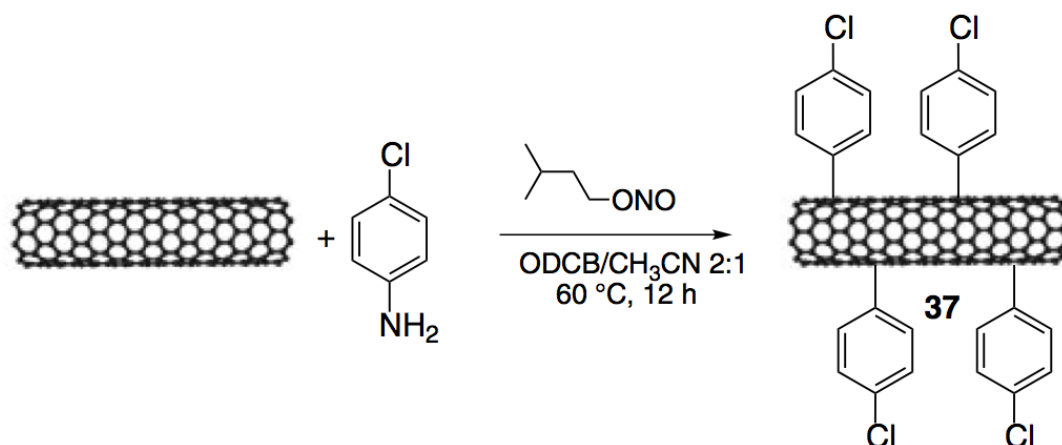


Figure 2.14.: Solvent-based sidewall arylation of SWCNTs.

of introducing heteratoms into the framework, which is strongly evidenced by the great amount of transformation sequences that have been developed for this purpose [36]. In view of the different ways to perform this task, only the diazotization as a potential selective route will be highlighted in detail.

In 2001, the research group of Tour and co-workers reported about a method to functionalize the sidewall of carbon nanotubes *via* an electrochemical reaction, in which several types of aryl diazonium salts were used together with SWCNTs, yielding water-soluble specimens characterized by a high derivatization degree. The generation of the aromatic radical was done *in situ* through a one-electron reduction. Furthermore, the solvent-based process as depicted in Figure 2.14, consisting in a thermally induced generation of the aryl radical by reacting a para-substituted aniline with isoamyl nitrite, was carried out shortly after. The high versatility of the approach can be found therein, that the process can be also used without employing any type of solvent [36].

Another related route consisting in exfoliating as well as derivatizing individual SWCNTs can be achieved by simply grinding a sample at room temperature with aryl diazonium salts in the presence of ionic liquids and potassium carbonate. This fast and environmentally friendly procedure can be even performed on the basis of water as a solvent. Hereby, disentangled SWCNTs are functionalized by vigorous stirring in water under the presence of a substituted aniline and an oxidizing agent. It should be mentioned that type of solvent can be further extended to a mixture of 96 % sulfuric acid and ammonium persulfate. By using this mixture it is possible to substitute the solvent oleum, which generally leads to a sulfonation of the pyrolytic aromatic hydrocarbons present on the nanotube surface. Currently, it was shown that the *in situ* generation of aryl diazonium compounds in the presence of ammonium persulfate leads to an efficient, scalable and solvent-free functionalization of multiwalled nanotubes. Furthermore, organic compounds

like triazene are stable precursors of diazonium salts for using them in the functionalization of SWCNTs in aqueous media. As can be inferred from the aforementioned, this approach is especially of interest whenever the molecules to be immobilized do not survive the common diazotization conditions. With respect to the employment of azomethine ylides in association with diazonium precursors for the functionalization of CNTs it must be said that the reaction can be appreciably speed up by employing microwaves. For instance, using *o*-dichlorobenzene as a solvent and accompanying the experiment with microwaves, it is possible to achieve a high modification degree while simultaneously shortening the reaction times during the diazotization of single walled nanotubes with 4-chloroaniline and isoamyl nitrite. A further derivatization step with which the chloro substituent is transformed into a thiol functionality giving a material soluble in DMSO [36].

2.5. Heteroatoms in carbon materials

Surface oxygen-containing groups are by far the most common type of functionalities bound to the surface of carbon materials [92]. Ever since the first studies in the 19th century, it is known that, as opposed to other kinds of adsorbed gases, the removal of oxygen only occurs at relative high temperatures. In fact, the amount of adsorbed oxygen augments when the temperature is moderately elevated, showing maximum concentrations in the range between 400 and 500 °C. Among the pioneering studies, the one carried out by Bartell and Miller is worth mentioning. The results showed that charcoals oxidized by air at low temperatures yielded basic functionalities, whereas acidic groups were preferentially formed when the carbon was allowed to cool down before exposing it air.

The high diversity of oxygenated surface groups is shown in Figure 2.15. It should be noted that not only carboxylic, phenolic and ketonic functional groups are considered to be chemically active, but also the π -electron density of the carbon basal planes. In general, oxygen functionalities are classified according to their properties into either acidic or basic ones [92]. The former are created when a carbon material is treated preferentially with oxidizing agents in the liquid phase, while the latter can be obtained when a previously oxidized surface is annealed at high temperatures. Actually the heat treatment itself does not yield basic groups, but rather the exposure of the material to air after cooling it in an inert gas atmosphere. This arises from the fact that the acid groups are decomposed at elevated temperatures, which results in the formation of active edge sites that bind the oxygen in form of basic functionalities such as chromene or pyrone.

Even though a general agreement exists with respect to those types of oxygen surface species responsible for the acidic character of a carbon compound, the origin of the basic properties is still a subject of debate. In an investigation performed by León y León et

al. [93] it was proposed that the overall basicity is defined by both pyrone-like groups and oxygen-free carbon sites localized at basal plane areas with a high π -electron density, that is away from the surface edges. In spite of this consensus, up to date one of the most critical problems when dealing with this property lies in the difficulty of assessing the basic strength of the aforementioned types of sites. In addition, there is still no much information concerning the extent to which both oxygen functionalities and π -electrons contribute to the global carbon basicity. As a matter of fact, León y León et al. [93] observed a strong correlation between the overall basicity and the oxygen content present in a carbon material. Accordingly, this property is determined by pyronic and related groups in samples with large amounts of O_2 , whereas delocalized π -electrons are important when oxygen is scarcely available. The so far mentioned aspects were further discussed by Montes-Morán et al. [94], who on the basis of experimental and theoretical approaches generalized the idea that pyrones present on the carbon edges are responsible for the overall basicity, assigning π -electrons only a negligible role.

A major difference concerning the formation of oxygen- and nitrogen-containing functional groups is that, as opposed to the former, the latter are not created spontaneously when a carbon material is exposed to air. In general, the amount of nitrogen found in carbons is rather small unless the element is part of the precursor used in the carbonization process. Some of the most common compounds employed for this purpose are carbazole,

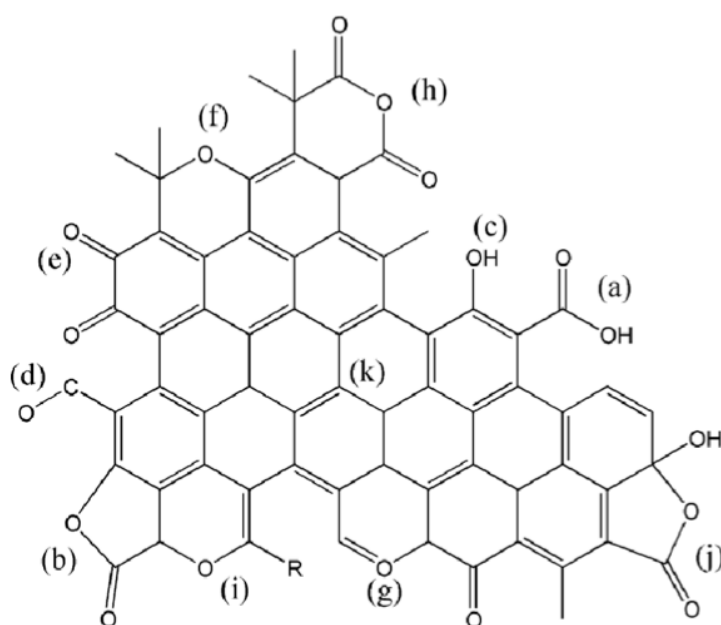


Figure 2.15.: Different types of oxygenated functionalities formed on carbon surfaces: (a) carboxylic acids groups, (b) lactone, (c) hydroxyl, (d) carbonyl, (e) quinone, (f) ether, (g) pyrone, (h) carboxylic anhydride, (i) chromene, (j) lactol, and (k) π electron density on carbon basal planes [92].

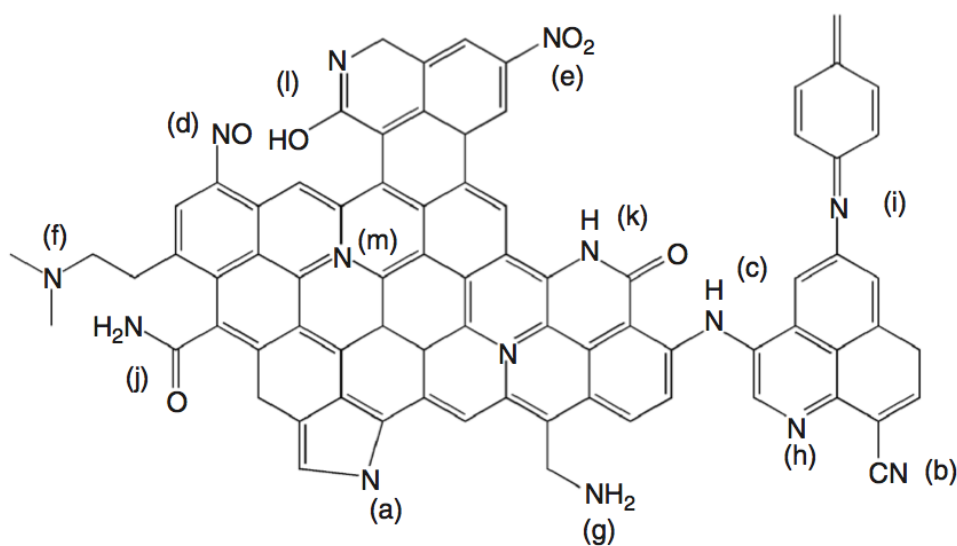


Figure 2.16.: Nitrogen-containing functional groups on carbon materials: (a) pyrrole-like group; (b) nitrile; (c) secondary amine; (d) nitro group; (e) nitroso group; (f) tertiary (g) amine; (h) pyridine-like group; (i) imine; (j) amide; (k) lactam; (l) pyridone; (m) quaternary amine [92].

acridine and melamine. Within this context is important to mention that the type of nitrogen functionality found in carbons strongly depends on the way the material is pretreated. Besides the type of nitrogen-containing precursor, the properties of the carbon surface and the chosen treatment temperature also play an important role. In view of the fact that the N-containing species present in the precursor material exhibit a different thermal stability, it is obvious that the temperature is the parameter which determines the type of chemistry that takes place. Consequently, the range of nitrogen surface species present on a carbon material can be as diverse as shown in Figure 2.16. Other common synthesis routes are magnetron sputtering, laser ablation and catalytic chemical vapor deposition (CCVD) of nitrogen-containing hydrocarbons [95]. A further possibility of binding nitrogen to a carbon structure is by exposing it to an N-containing reagent such as ammonia [96, 97], urea or hydrogen cyanide.

As one would expect, nitrogen functional groups are responsible for the acidic and basic properties of a carbon surface and consequently for both its chemical reactivity as well as catalytic behaviour. Lactams, imides and amines, which are considered to be weakly acidic, can be formed when carbon materials are treated with suitable precursors at temperatures lower than 530 °C [92]. As opposed to this, the amount of quaternary nitrogen, pyridinic and pyrrole-like groups substantially increases when high temperatures are chosen. These groups account for the basicity of the material. Against the background of the aforementioned, it is evident that global acid-basic properties is the defined by the concentration and distribution of surface functionalities present in carbon materials.

Generally, one of the most demanding tasks when dealing with carbon materials and their physicochemical properties is the quantification of the surface functionalities. This challenge applies equally to all types of functionalities, regardless of the elements from which they are constituted and arises from the fact that many of these groups coexist and therefore interact with each other, making it nearly impossible to unambiguously discern between them, even when several complementary characterization techniques are applied.

In spite of the above, valuable information can be still extracted from experimental data obtained from methods such as Boehm titration, potentiometric titration, XPS and TPD. The first mentioned technique was developed to neutralize the surface functionalities according to their acid strength using organic bases with different pK_a values [98]. The assumptions contemplated hereby are the following: carboxylic acid groups are deprotonated by sodium bicarbonate, sodium carbonate neutralizes carboxylic acids and lactones, and sodium hydroxide is employed for titrating the aforementioned groups and phenols. When using the potentiometric titration it is necessary to know that the data analysis is somewhat complicated as quite often the first derivatives obtained exhibit a large amount of maxima, which can hardly be assigned to a specific type of functionality. Nevertheless, theoretical models describing the acid-basic mechanisms on the carbon surface have been developed, which can be used in order to simulate the run of experimental curves. Although this quantitative approach results in a distribution of pK_a values, it is rather impossible to assign them to a certain species, which originates from the fact that several heteroatom combinations can lead to similar acid dissociation constants.

A more complicated approach is the analysis of the carbon material by means of XPS. This surface sensitive technique can be briefly described as follows: X-rays photons directed to a sample are absorbed by the constituent atoms, exciting and ejecting hereby a core electron, which possesses a kinetic energy that depends on its binding energy, the energy of the incoming photon and the work function of the spectrometer. When this process takes place, the inner-shell hole is filled by an outer electron. Consequently, either a photon or an Auger electron is emitted. This technique, as one would expect, has been employed numerous times in order to assess the binding energies of the C1s, N1s and O1s photoelectrons. One important aspect in association with the identification and quantification of the groups containing heteroatoms is that for a proper analysis a deconvolution of the obtained spectra needs to be carried out. As an example, the results obtained for aminated nanocarbons in a study carried out by Arrigo et al. [97] are presented in Table 2.1.

TPD is another common technique used for quantification purposes. This is done by heating a carbon sample in an inert gas atmosphere at a specific rate, inducing a gradual thermal decomposition of the surface functionalities. The hereby evolved gases, which are generally analysed by mass spectroscopy or gas chromatography, can be used for

estimating the oxygen content. Moreover, the deconvolution of the corresponding profiles may provide information about the amount of each type of functionality. Such a disputable approach assumes that CO₂ is created when carboxylic acids, lactones and anhydrides are decomposed, whereas CO evolves from anhydrides, phenols, ethers and ketones.

Table 2.1.: Binding energies of the most common nitrogen and oxygen containing functional groups [97].

Type of N	Pyridine	Amine / Amide	Pyrrol / Pyridone	Quarternary N		N-oxide / Nitro
BE [eV]	398.4±0.1	399.4±0.1	400.1±0.1	401.1±0.1		406±0.1
Type of O	Quinones	C=O	COOH	C-O	NO ₂	H ₂ O
BE [eV]	530.7±0.1	531.4±0.1	532.41±0.1	533.7±0.1	533.2±0.1	535±0.1

2.6. Carbon as a catalyst

A wide range of carbonaceous materials including graphite, carbon black and active carbon, amongst others, have been used over a long period of time in heterogeneous catalysis. The reason for this may be found in the fact that the carbon allotropes possess remarkable physicochemical properties, as for instance high chemical inertness, great stability in oxygen-free atmospheres, outstanding mechanical resistance, large surface area as well as an optimum porosity, which make them suitable for the use as a catalyst support [99]. In addition, it is possible to attach a series of functional groups containing different heteroatoms like oxygen and chlorine onto the carbon surface, enabling the possibility to employ them directly as catalysts in distinct reactions [100]. Still, it should be pointed out that a mismatch exists between the outstanding suitability of carbon to serve as an adequate support for a considerable amount of reactions and the small number of large-volume processes that indeed use carbon-based catalytic systems. This contradiction does not seem to be plausible at a first glance; however, the explanation for this lies in the fact that the interplay of the textural and chemical properties are yet not fully understood and even less the way the aforementioned properties influence the catalytic behavior of these materials [101]. Another aspect which intensifies the outlined problem is the missing reproducibility of the catalytic results caused in particular by the batch-to-batch production applied by manufacturers, leading to a varying quality of the carbons [102].

It is well known that carbon is mainly used as a catalyst support. Nevertheless, the employment of this material as a catalyst of its own should also be taken into account as there are distinct industrial reactions such as the production of phosgene [103] and sulfur halides [104] as well as the desulfurization of gases [105] which use carbon catalysts. Regarding the latter case, there are several examples of industrial applications working

effectively with flue gases containing small amounts of sulphur dioxide, e.g. the Sulfacid and the Bergbau-Forschung-Uhde processes. Both of them were developed on the basis of the adsorptive/catalytic properties of active carbon and designed for the purpose of converting the hazardous contaminant into products with a commercial value [105].

In addition to the previously mentioned, well established manufacturing processes, a great number of carbon-catalyzed reactions have been intensively investigated. According to the excellent review of Radovic and Rodríguez-Reinoso, “the group of reactions that has attracted the most attention is [the] oxidative dehydrogenation of alkylbenzenes” [102]. In this context, Figueiredo and Pereira mention that Alkhazov et al. [106] were the first scientific group to investigate the oxidative dehydrogenation of ethylbenzene over activated carbons [107]. In the ensuing years, several analyses were carried out in order to associate the textural properties of the carbons employed with the corresponding activities achieved in the ODH of ethylbenzene. In addition to the carbon surface physics, which comprises the effects of the total surface area and of the pore size distribution on the catalytic performance, it was also necessary to study the influence of the surface chemistry on the styrene yields [102, 107]. Investigations concerning this aspect were carried out with diverse carbonaceous materials including charcoal [108], activated carbon [109], mesoporous carbon [110], carbon nanofibers [111] and carbon molecular sieves [112]. In general, a broad agreement with respect to the nature of the active site exists as it has been stated that the turn over of the aromatic hydrocarbon takes place at the surface carbonyl/quinone groups, which have been identified as such using methods like TPD [109, 111] and XPS [110]. Although empirical correlations do not necessarily give an insight deep enough in order to understand the phenomena underlying macroscopic observations, they can still be viewed as a simplified way to explain the responses of a complex system evoked by defined stimulations. Thus, it is important to mention that Pereira et al. [109] found a linear relation between the catalytic activity in the ODH of ethylbenzene and the assessed concentrations of the quinone groups present on the investigated samples. Furthermore, the results of the same study showed that regardless of the initial state of oxidation, all tested activated carbons behaved similarly as the reaction proceeded. This finding was ascribed to the formation of coke.

As evidenced by the work of Su et al. [110], the catalytic performance and stability of a carbon material is strongly influenced by its microstructure. For instance, the yield towards the formation of styrene positively correlated with the basal plane to edge site ratio, a result which was obtained based on the performance of onion-like carbons, carbon nanotubes and graphite. In addition, a high stability was observed for the previously mentioned materials, whereas in the case of carbon black the overall yield steadily decreased. The effects of the microstructure were further investigated by Delgado et al. [113] for carbon nanotubes.

In this study, commercial CNTs were heat treated at different temperatures and tested in the ODH of ethylbenzene. Differences in styrene yields were explained in terms of oxygen content and graphization degree: at high annealing temperatures lower amounts of functionalities are available and at the same time a structure with less defects is obtained, which leads to a low reactive surface and therefore to lower activities. Similar results were reflected in a study performed by Rinaldi and co-workers [114], who investigated the impact of the purification of carbon nanotubes on their catalytic performance in the ODH of ethylbenzene and propane. It was shown that a mild oxidation treatment lead to an incrementation of the surface functionalities as well as to an improved graphitic character of the carbon material, which was not only confirmed by means of TPD and Raman spectroscopy, but also by the evident changes in the catalytic activities and selectivities. Furthermore, the effects of a subsequent annealing step at different temperatures confirmed the behaviour observed by Delgado et al [113].

Another critical aspect deserving attention concerns the possibilities of improving the catalytic performance of nanocarbons in ODH reactions. As was shown by Frank et al [115], higher selectivities towards olefins can be achieved by simply modifying the surface of carbon nanotubes with electron-attracting heteroatoms. In that study the authors demonstrated that the presence of borates and phosphates enhances the oxidation resistance of the investigated material. Not only the results of TPO experiments served as a basis for confirming the aforementioned effect, but also the calculated activation energy of O₂ conversion in the oxidative dehydrogenation of propane, which increased after the functionalization by approximately one third of the values obtained for the pristine and oxidized samples. Interestingly, the activation energy of the alkane was similar for all studied specimens. In addition, SSITKA experiments using ¹⁶O₂ and ¹⁸O₂ evidenced the lower isotope exchange capability of boron doped CNTs in contrast to oxidized ones, which is a behaviour comparable to that of a low-loaded VO_x/Al₂O₃ catalyst. As opposed to the enhanced selectivities towards propylene, the improvements achieved in the case of ethylene under comparable reaction conditions were rather moderate [116]. Unfortunately, significantly higher selectivities could only be reached under an alkane-lean flow and at high temperatures. Moreover, based on an analysis of the formal kinetics, the authors showed that the rate order of oxygen increased by a factor of two to three after the modification, which was interpreted in terms of a slower catalyst reoxidation. In other words, the presence of heteroatoms restrained the formation of highly reactive oxygen intermediates that are known to favour the total oxidation of the hydrocarbon.

A further type of reaction that has received notable attention in literature is the decomposition of alcohols [118–136]. In the early nineties, Szymański performed a series of studies dealing with the conversion of isopropanol [119, 120], 2-butanol [118] and

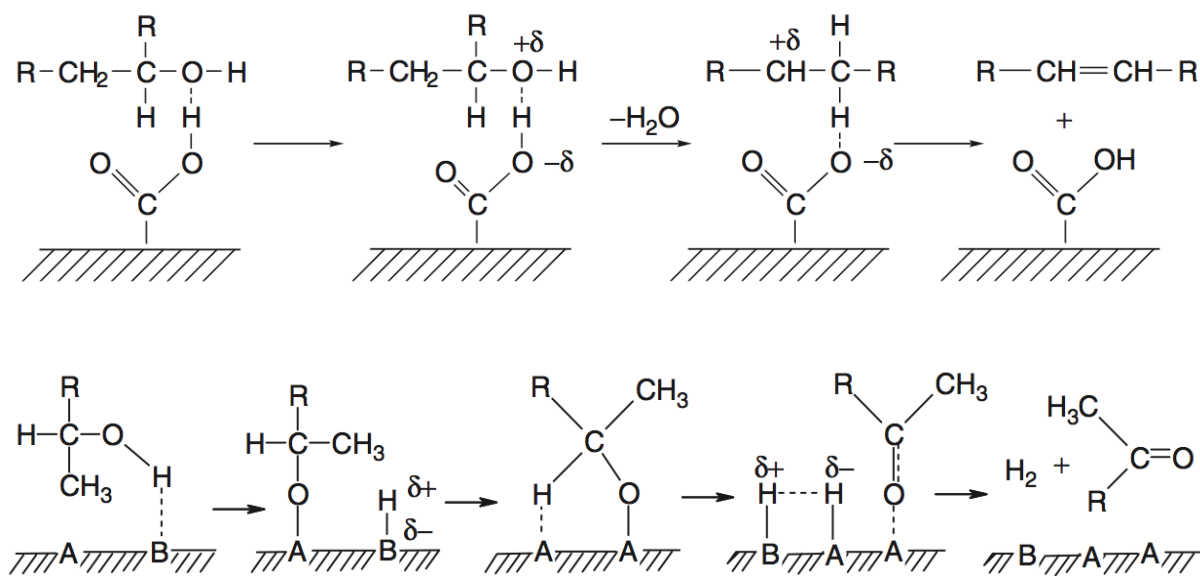


Figure 2.17.: Dehydration (top) and dehydrogenation (bottom) mechanism of aliphatic alcohols [117].

ethanol [121] over oxidized activated carbons. These investigations revealed that two different pathways may take place on the carbon surface, namely the dehydration and dehydrogenation of the aliphatic alcohol. While the former occurs on acidic centres, the latter only takes place when Lewis acid and basic sites are simultaneously present on the surface of the carbon catalyst [120]. A schematic representation of the corresponding mechanisms is given in Figure 2.17. Moreover, it was shown that the introduction of oxygen functionalities into the carbon structure through an oxidative treatment considerably enhanced the overall catalytic activity. Using a wide range of metal cations, Szymański was able to demonstrate that their presence improved the dehydrogenation activity, thereby suppressing to some extent the dehydration step [118, 119, 121]. This effect was strong for cations with high Lewis acidity, which was in agreement with results obtained in other studies for zeolites and ion-exchange resins [118]. Some interesting observations were made concerning the optimal amount of surface acid sites necessary to maximize the dehydration activity [120, 126]. First of all, it was concluded that as opposed to the dehydration, which only occurs on the outer surface of the carbon catalyst, the dehydrogenation also takes place within its pores. Taking the aforementioned finding into account as well as the fact that the acidic active centres can be formed either inside or outside the catalyst, an incrementation of their concentration only leads to an enhancement of the dehydration activity as long as the maximum amount that can be formed on the outer surface is not reached. After surpassing a certain threshold value, the rate of reaction at which dehydration products are formed may even decrease [120]. Moreover, steric hindrances

rising from a too large amount of acidic centres were also considered to be responsible for a decrease in the dehydration activity [126]. It is plausible to think that the interactions between adjacent polar groups become stronger with increasing concentration, which in turn hampers their interactions with the alcohol molecules necessary for a successful turnover.

Some studies dealing with the dehydration of methanol over oxidized carbon catalysts to produce dimethyl ether (DME) have also been carried out [123, 124]. Using different types of oxidizing agents (HNO_3 , H_2O_2 , $(\text{NH}_4)_2\text{S}_2\text{O}_8$) and analysing their impact on the acid-basic properties of the employed activated carbons by means of TPD, XPS, potentiometric titration and point of zero charge determinations, Moreno-Castilla et al. [124] empirically derived a relationship between the DME rate of formation [in $\mu\text{mol}\cdot\text{g}^{-1}\cdot\text{min}^{-1}$ at 453 K] and the proton concentration at the point of zero charge:

$$r_{DME} = (2759 \pm 97) \cdot [H^+] + (0.53 \pm 0.25) \quad (2.14)$$

Extensive kinetic investigations based on the decomposition of isopropanol [131] and 2-butanol [132] over phosphoric acid treated activated carbons have been performed by Bedia and co-workers. In view of the high surface acidity induced by the phosphorous groups, the conversion of the secondary alcohols yielded mainly dehydration products. Therefore, the kinetic analysis focused on this pathway. The authors suggested that the reaction can occur *via* two different types of elimination mechanisms. According to the proposed E1 model, the initial rate-determining step involves the protonation of the OH group, followed by the cleavage of the C-O bond giving a carbocation and a water molecule. Subsequently, the carbocation is rapidly deprotonated and a propylene molecule is formed. On the contrary, the E2 mechanism only includes a single surface reaction, which consists of a simultaneous departure of the OH group and the β hydrogen. Based on the obtained values for the kinetic parameters of the rate determining steps established in the E1 and E2 models, namely the pre-exponential constant and the activation energy, the main conclusion drawn was that probably both mechanisms occur simultaneously. In the study of the decomposition of isopropanol [131], this statement was supported by features found in the FTIR spectrum of the used catalyst. It suggested that two adsorbed species coexist, identified as an undissociated 2-propanol molecule and an isopropoxide-carbocation surface complex.

3. Motivation and outline of the work

Acid-base catalytic processes are commonly used in the petrochemical [137] and fine chemical industries [138]. Not only large scale processes, as for instance cracking, isomerization and alkylation, but also typical organic reactions, including hydrogenation and esterification [139], play in this context an important role. Numerous advantages of heterogeneous catalysts over homogeneous ones, including easy separation from the reaction mixture, reusability whenever stable and leaching-resistant, and suitability for being used in continuous processes, have triggered a transition towards heterogenization of homogeneously catalyzed processes [140]. Furthermore, heterogeneous catalysts are often environmentally benign and safe to handle owing to the fact that the active species is immobilized on a support material. In view of this, great efforts are being made in order to develop new solid acids and bases that are suitable for replacing conventional homogeneous catalysts.

In contrast to conventional metal oxides, CNT agglomerates are distinguished by their predominantly mesoporous structure, which is a desirable textural property from a macrokinetical point of view as the mass transport of reactants to the active sites located at the carbon surface is strongly facilitated. On top of this, the physicochemical surface properties can be adapted to meet the specific catalytic requirements. While numerous types of carbonaceous materials have been tested in oxidative dehydrogenation reactions, the acid-base catalyzed transformation of alcohols has been mainly performed over highly microporous activated carbons. In contrast, mesoporous carbon materials have received considerably less attention [136]. As a matter of fact, carbon nanotubes have never been used as catalysts in the dehydration-dehydrogenation of alcohols. Furthermore, despite various types of modification strategies that are nowadays available for the generation of functional groups on CNT surfaces, many of these methods have been carried out only using small amounts of the pristine material. Because larger batches are required in the field of heterogeneous catalysis, it is absolutely necessary to explore the possibility of up-scaling the synthetic approaches. In consequence, following aspects are addressed in the scope of this work:

1. How do the acid-base properties and oxidative characteristics of MWCNTs change upon generation of surface species containing various types of heteroatoms?
2. To what extent can the acid-base properties of carbon nanotubes be changed following controlled synthesis routes like the diazonium-based method [141]?

3. What are the determining factors that define the surface acidity and basicity of MWCNTs modified by amination in the gas phase?
4. Can the physicochemical surface properties of carbon nanotubes be properly tailored by phosphorus incorporation?

A valuable possibility to investigate the effects of different sorts of functionalization strategies on the surface properties of CNTs is by comparing the activities and selectivities yielded by the modified samples during the transformation of 2-propanol under the same reaction conditions. In addition, it is essential to apply further techniques such as potentiometric pH titration, TPD, XPS, microcalorimetry, TGA as well as FTIR spectroscopy in order to gain a deeper insight into the complex surface chemical properties of the functionalized CNTs. The findings thus obtained are described in detail in the three main chapters:

Chapter 4 deals with the generation of benzenesulfonic acid entities on the surface of CNTs *via* diazotization of sulfalinic acid with isoamyl nitrite in ODCB and water. An integral characterization of the acid sites by thermal analysis, liquid phase titration, ATR-FTIR spectroscopy, and the transformation of 2-propanol is presented.

Chapter 5 focuses on the incorporation of N-containing functionalities into the surface of oxidized MWCNTs by gas-phase amination. XPS and TPD analysis provide fundamental information about the amount and nature of oxygen and nitrogen species. Acid-base properties investigated by potentiometric pH titration and the catalytic transformation of 2-propanol as well as the oxidative characteristics studied by TPO are discussed in detail.

Chapter 6 provides details on the analysis of the acid-base and oxidative properties of MWCNTs modified with phosphate species obtained by chemical activation in phosphoric acid. Results obtained by TPD, liquid-phase titration, the gas-phase transformation of 2-propanol, NH_3 -microcalorimetry, and TPO are presented.

Chapter 7 summarizes the obtained results from a general and critical point of view. A compact outlook discusses important aspects to be considered for future investigations.

4. Tailoring the acidity of carbon nanotubes through addition of *in situ* generated benzenesulfonic acid radicals

Klaus Friedel Ortega, Benjamin Frank, Annette Trunschke, and Robert Schlögl

Abstract

A direct sidewall functionalization approach based on the diazotization of sulfanilic acid with isoamyl nitrite in either *o*-dichlorobenzene (ODCB) or water as solvents was used in order to modify the surface of multiwalled carbon nanotubes (MWCNTs) (Baytubes C150 HP[®]) with benzenesulfonic acid entities. The use of water proved to be significantly more efficient than ODCB since a larger number of functional groups was attached to the carbon backbone despite lower sulfanilic-acid-to-carbon ratios. Temperature programmed desorption (TPD) experiments revealed that the covalently attached surface species are thermally stable up to 250 °C forming SO₂ and H₂O upon decomposition. The sulfur content ranged between 0.1 and 1.6 wt% according to elemental analysis and TPD. Elemental mapping by SEM-EDX proved that the modification protocol is suitable for introducing sulfur-containing species in a homogeneous way. In addition, the presence of benzenesulfonic acid groups was confirmed based on ATR-FTIR spectroscopy. Potentiometric pH titrations revealed the acidic character of the functionalized materials. The number of acid sites correlates with the sulfur content. Surface acidity was further verified by high selectivity to dehydration products in the transformation of 2-propanol. Propylene formation rates have been used as a measure of acidity.

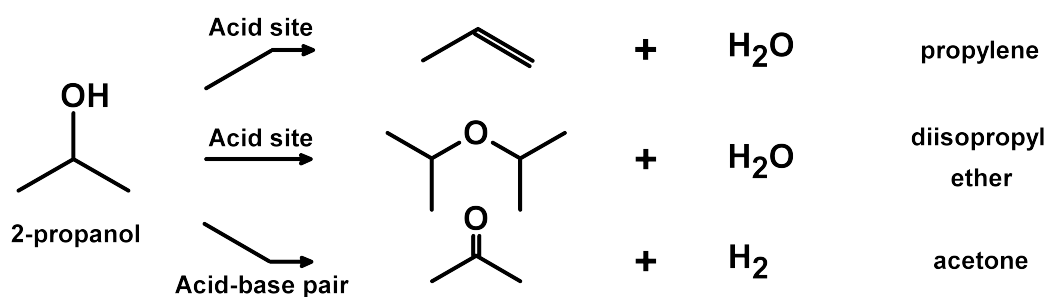
4.1. Introduction

Carbon nanotubes have attracted much attention due to their outstanding electronic, thermal and mechanical properties, thus making them valuable and suitable for numerous technological applications. One major drawback, however, is the difficult processability of the nanostructured material arising from a poor solubility in aqueous and organic media [142], which is related to the inherent surface hydrophobicity. This aspect is likewise crucial when CNTs are employed as a catalyst on their own and as a support [107]. In spite of their high specific surface area, a homogeneous dispersion of an active phase is not possible as long as proper anchoring sites are not available on the graphitic sheets. In order to overcome these hurdles, several covalent functionalization approaches allowing a chemical modification of the CNT surface have been applied [143]. Oxidative treatments either in nitric acid [144–146] or using gaseous compounds (e.g. oxygen [147, 148] or ozone [9,10]) belong without doubt to the most common methods for generating O-containing functional groups. Sulfur incorporation is generally achieved through functionalization of the CNT material in the presence of H₂SO₄ alone [149] or in a mixture with nitric acid [149–152]. Even though substantial amounts of the heteroatoms can be introduced by these methods, a common undesired side effect is the structural degradation of the carbon framework promoted by the strong oxidative environment to which the CNT material is exposed. In order to avoid this, it is desirable to apply functionalization techniques capable of modifying the surface without altering the morphology. A synthesis that fulfills both requisites is the diazonium-based modification strategy proposed by Bahr and Tour [141]. Para-substituted anilines can be converted *in situ* into the corresponding diazo compound, followed by a subsequent decomposition into molecular nitrogen and a highly reactive aryl radical. The latter is capable of breaking the aromatic bonds of the nanotubes sidewalls, thereby generating a covalent bond with the carbon structure. An ensuing work shows that the coupling reaction can also be performed “on water” as an alternative to the less environmentally friendly o-dichlorobenzene (ODCB) [153].

Sulfonation of mesoporous carbon nanocages *via* the aforementioned diazonium-based derivatization approach using sulfanilic acid results in a solid acid catalyst that is active in the cross-Aldol condensation of ketones with aromatic aldehydes [154]. Similarly, benzenesulfonic acid species generated either in water, dimethylacetamide, or dioxane by the previous method can be immobilized on the backbone of carbon nanofibers, thereby yielding nanostructured materials capable of catalyzing the transesterification of triolein and methanol [155]. Whereas in the former study 120 mg of catalyst were prepared employing a sulfanilic-acid-to-carbon molar ratio of 280:1000, the latter reports an eight times higher amount of processed carbon material, however, using a molar ratio of 100:1000.

Evidently, both the precursor-to-carbon molar ratio and the solvent are suitable parameters for tuning the surface density of desired functional groups. However, no investigation addressing this important aspect of the diazonium-based functionalization has been yet reported.

In this study, multiwalled carbon nanotubes (CNTs) were modified with sulfonic acid entities in a systematic way based on the *in situ* diazotization of sulfanilic acid both in ODBC and water. Samples thus obtained were subjected to various characterization techniques, which undoubtedly affirm the presence of highly acidic surface functionalities. Furthermore, the catalytic transformation of 2-propanol serving as a probe reaction was carried out in order to characterize the acidic properties of sulfonated carbon nanotubes in the gas phase. As depicted in Scheme 4.1, the secondary alcohol dehydrogenates to acetone over an acid-base pair, while the dehydration step yielding propylene or diisopropyl ether occurs on acidic centers.



Scheme 4.1: Reaction pathways of 2-propanol transformation [120].

4.2. Experimental section

4.2.1. Functionalization of CNTs

Functionalization experiments were performed using purified CNTs (Baytubes C150 HP[®], Bayer Material Science, carbon purity > 99 wt%, outer mean diameter ~ 13 nm, bulk density 140–230 kg·m⁻³) according to an up-scaled procedure based on the method previously described by Bahr and Tour [141]. Typically, 4 g of pristine CNTs were immersed in 400 mL of ODBC (Emsure from VWR) together with the corresponding amount of 4-aminobenzenesulfonic acid (ACS from VWR). The suspension was ultrasonically homogenized for approximately 20 minutes in a Bandelin Sonorex RK 510 sonication bath (640 W peak output power). After heating the mixture to 60 °C under vigorous magnetic stirring in Ar atmosphere, the reaction was started by adding drop-wise 2

equivalents of isoamyl nitrite (96 % from Sigma Aldrich) per mol of sulfanilic acid using a dropping funnel. After performing the reaction for 4 or 16 h and subsequent cooling to ambient temperature, the suspension was vacuum filtered over a 0.45 μm Nylon membrane. Unreacted organic matter was removed by sonicating the solid material in 100 mL dimethylformamide (DMF, GPR Rectapur from VWR) under Ar for 20 min, followed by a filtration step. This procedure was repeated until a colourless filtrate was obtained. The functionalized material was resuspended and stirred in 0.5 L HCl (0.5 M) for 16 hours. Subsequent filtration, neutralization, and drying in Ar at 200 $^{\circ}\text{C}$ for 24 h yielded S-containing CNTs. Functionalization in water was performed following the same steps, but deviating from the previous description as follows: first, no ultrasonic dispersion prior to functionalization was performed and second, 4-aminobenzenesulfonic acid was dissolved in a sodium hydroxide solution resulting in $\text{pH} = 7$ before carbon modification. The functionalized materials are labeled as follows: CNT-(solvent)-(amount of sulfanilic acid). The shortcuts O and W correspond to o-dichlorobenzene or water, respectively, used as solvent during functionalization. The amount of sulfanilic acid is given relative to 1000 moles of carbon (Table 4.1).

4.2.2. Analytical Techniques

Carbon materials were characterized by N_2 adsorption at liquid nitrogen temperature (-196°C) using a Quantachrome Autosorb-6B KR instrument. Analyses were performed on 70 mg of powdered substance, which were degassed for 2 h at 200 $^{\circ}\text{C}$ before measurement. Surface area calculations were undertaken using the BET equation [156], pore size distributions were derived from the desorption branches of the isotherms according to the BJH method [157], and total pore volumes were determined at a relative pressure of $p/p_0 = 0.97$. Micropore surface area S_{Micro} and volume V_{Micro} were respectively obtained on the basis of the MP-method proposed by Mikhail, Brunauer and Bodor using a statistical thickness interval of 0.05 [158].

Samples were investigated by potentiometric pH titrations carried out with a Mettler DL 77 autotitrator monitored by a Mettler Toledo DGi114-SC electrode. In a typical experiment, 100 mg of powdered sample were suspended in 50 mL of 0.1 M NaCl solution. Equilibration was achieved by vigorously mixing the suspension over night. In order to minimize side effects from dissolved CO_2 , the mixture was degassed under Ar for 30 min prior to starting a measurement. The titrant used was a 0.01 M NaOH solution, diluted from a 1 M Titrisol standard (Merck Millipore).

Temperature programmed desorption was carried out in a home-built setup equipped with a gas chromatograph (Varian CP-4900 Micro-GC) and a mass spectrometer (Pfeiffer

Omnistar) for on-line product analysis. Typically, weighted amounts of sample were loaded into a fixed-bed quartz reactor, which was heated to 100 °C in a He stream at a flow rate of 25 mL_n·min⁻¹. Weakly adsorbed water was removed at this temperature within 1 h. Experiments were started thereafter by linearly heating the reactor at 5 °C·min⁻¹ to 850 °C. This temperature was maintained for 1 h before cooling to room temperature. TG-MS experiments were performed in a Netzsch STA 449C Jupiter thermobalance coupled to a Pfeiffer Omnistar mass spectrometer for simultaneous gas analysis. In a typical run, 10 mg of sample were loaded in an Al₂O₃ crucible, which was heated at 5 °C·min⁻¹ from room temperature to 1000 °C in Ar at a flow rate of 100 mL_n·min⁻¹.

Elemental analyses (CHNS) were conducted applying a Thermo FlashEA 1112 NC Analyzer. Scanning electron microscopy was employed for the investigation of elemental distribution using a Hitachi S-4800 (FEG) equipped with an energy dispersive X-ray sapphire detector, type EDAX Genesis 4000 system. Elemental maps were collected for a time frame of 1 h applying an acceleration voltage of 10 kV. Quantitative analysis of C, O and S were carried out based on the respective K_α lines.

FTIR spectra were recorded in the range between 675 and 5500 cm⁻¹ with a Perkin Elmer PE100 spectrometer equipped with a MCT detector cooled with liquid nitrogen. An ATR accessory with a Ge internal reflection element was used. In general, 1024 scans were collected for every sample at a resolution of 2 cm⁻¹. A single beam spectrum of the pristine compound served as the background for the measurements. This technique was also applied in order to investigate the changes after the catalytic testing.

For the transformation of 2-propanol, a nitrogen stream of 22.7 mL_n·min⁻¹ was passed through a saturator maintained at 20 °C (4.2 % isopropanol, ≥ 99.5 from Carl Roth) before reaching a U-shaped quartz reactor (i.d. 6 mm) containing 25 mg of catalyst material (250-355 μm). Under these conditions the space-time corresponds to 0.035 g·s·mol⁻¹. Prior to the measurements, the samples were heated in N₂ to 350 °C at 5 °C·min⁻¹ for 2 h. Temperatures were varied in 25 °C steps from 175 to 250 °C at constant inlet flow rate, whereby every set of parameters remained unchanged for a period of 12 h. The conversion of 2-propanol was calculated based on the ratio of product concentration to amount of secondary alcohol fed into the reactor.

$$X_{i\text{-PrOH}} = \frac{\chi_{\text{Propylene}} + \chi_{\text{Acetone}} + \chi_{\text{Diisopropyl ether}}}{\chi_{i\text{-PrOH}}}$$

Carbon balances of at least 97 % have been achieved. Selectivity is defined in molarity terms as the concentration of a given product to the sum of all detected products.

$$S_{\text{Product}, i} = \frac{\nu_i \cdot \chi_{\text{Product}, i}}{\nu_i \cdot \chi_{\text{Product}, i} + \sum \nu_j \cdot \chi_{\text{Product}, j}}$$

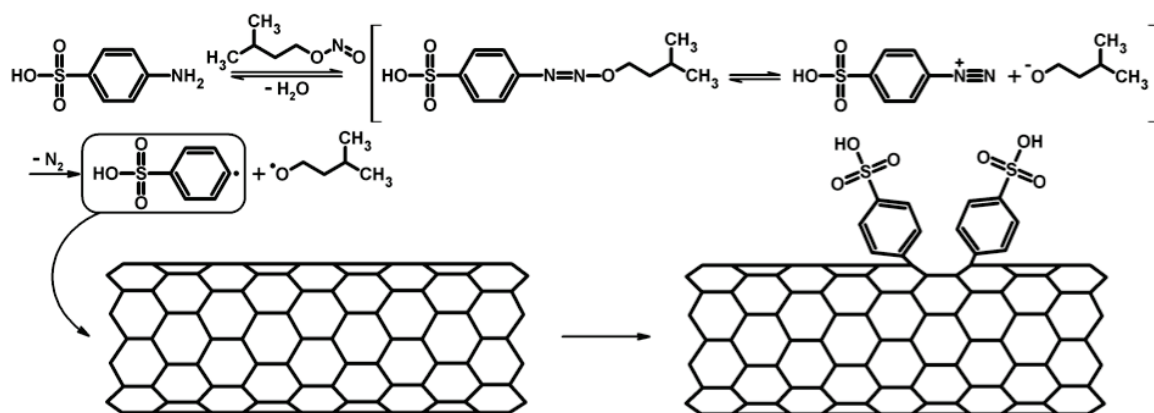
4.3. Results and Discussion

4.3.1. Functionalization of MWCNTs in Organic and Aqueous Media

Sulfonated CNTs were synthesized as displayed in Scheme 4.2 by the modification of commercial CNTs with *in situ* generated aryl radicals containing sulfonic acid entities *via* diazotization of sulfanilic acid. The diazonium compound formed is unstable and decomposes at room temperature immediately according to Scheme 4.2. The resulting highly reactive radical intermediates were shown to successfully attack the bent basal plane of the outer CNT surface, breaking up the sp^2 hybridized aromatic system to yield a covalent bond between the sidewall of the nanocarbon and the benzenesulfonic acid functionality [159]. As compared to previous investigations using SWCNTs in milligram scale [160–166], in this work 4 g CNTs were used per batch, since the materials were functionalized to investigate them as heterogeneous catalysts. In view of this scale-up, it was necessary to strongly reduce the molar ratio of functionalizing agent to carbon support. In this way, the lower limit sufficient for significantly changing the acid-base properties of the CNTs could be explored. The molar ratios applied are listed in Table 4.1.

With respect to the carbon material, *o*-dichlorobenzene is an attractive solvent since CNTs can be highly dispersed in this medium [142]. However, high concentration of radical precursors is difficult to achieve since sulfanilic acid is insoluble in most solvents due to its zwitterionic nature, which gives rise to a very stable crystal lattice in the solid state. In aqueous alkaline media deprotonation of the NH_3^+ moiety takes place and the solubility strongly increases [167]. Thus, the impact of the solvent on the degree of functionalization was investigated by using water as an alternative solvent Table 4.1.

Elemental analysis (Table 4.1) reveals that sulfur can be attached to the carbon backbone despite the low solubility of sulfanilic acid in the organic medium. An increase of the sulfanilic-acid-to-carbon ratio leads to higher sulfur concentration in the prepared carbon



Scheme 4.2: Aryl radical formation *via* diazotization of sulfanilic acid and subsequent addition of sulfonic acid entities to carbon nanotubes.

materials. Although the highest applied ratio lies far below the values often employed in literature, it is still adequate for introducing considerable amounts of sulfur. In presence of ODCB, the sulfur content approaches an upper value near 0.4 wt %, which might be related to the limited solubility of sulfanilic acid in ODCB as previously discussed. In contrast, dissolving the radical precursor in an alkaline aqueous solution significantly enhances the sulfur content in the CNTs. By using water as solvent, the sulfur content in CNT-W200 was increased by a factor of four compared to CNT-O200 (Table 4.1).

The superiority of the aqueous medium is further revealed by the S-content of CNT-W50, which is almost three times higher than in CNT-O200, despite a substantially lower molarity of sulfanilic acid and shorter reaction time, respectively. Moreover, trace amounts of N found in the product obtained in ODCB are indicative for residual sulfanilic acid strongly adsorbed on the CNTs, which cannot be efficiently removed in spite of the subsequent extensive washing step. The absence of N in the materials functionalized in water suggests that the sulfur in these materials is present in form of benzenesulfonic acid groups.

Table 4.1.: Nomenclature, functionalization conditions and elemental analysis of as prepared carbon catalysts.

Entry	Sample	$n_C : n_{SA}$	Solvent	Reaction Time [h]	Elemental analysis [wt %]			
					C	H	N	S
12832	CNT-P	-	-	0	97.2	0	0	0
13742	CNT-O100	1000 : 100	ODCB	16	96.4	0	0.04	0.09
14002	CNT-O150	1000 : 150	ODCB	16	93.9	0	0.02	0.35
14017	CNT-O200	1000 : 200	ODCB	16	94.5	0	0.03	0.39
14177	CNT-W50	1000:50:00	Water	4	91.7	0.24	0	1.07
14215	CNT-W200	1000:200	Water	16	90	0.31	0	1.57

4.3.2. Textural properties of the functionalized MWCNTs

Specific surface areas calculated for the pristine and functionalized materials are summarized in Table 2. The absorption isotherms are classified as type III showing a H3 hysteresis (Figure 4.1a) [168]. These results are indicative for weak interaction of nitrogen with the carbon and significant adsorbate-adsorbate interactions as sometimes observed for organic polymers and carbonaceous systems with slit-shaped pores. BET surface area and total pore volume of the carbonaceous products strongly drop after functionalization. While the micropore surface area and volume remain unchanged for the samples prepared in ODCB, a slight increase is observed for those functionalized in water, in particular for CNT-W200 (Table 4.2). This observation might be associated with the formation of branched chains on the carbon surface. From a structural point of view, they might be comparable to

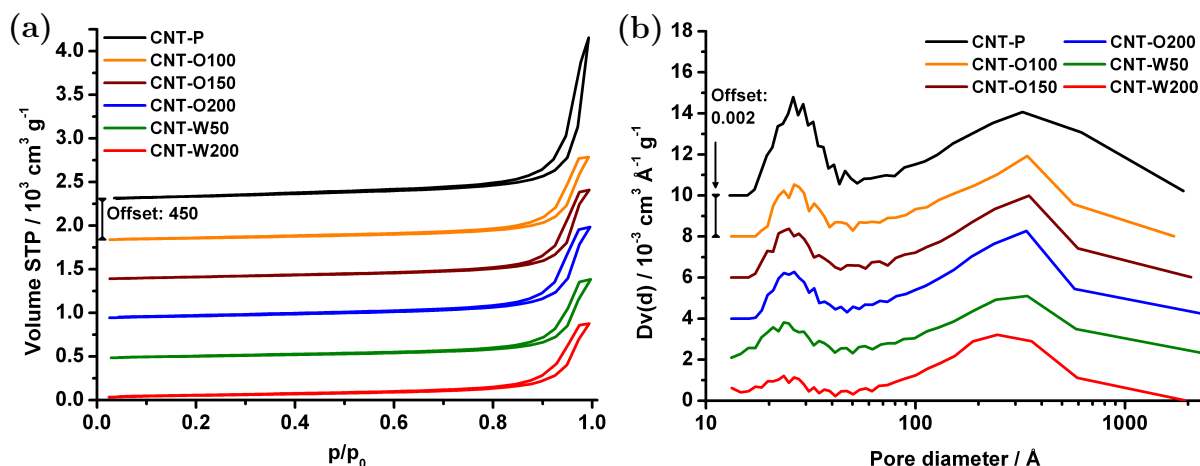


Figure 4.1.: (a) BET isotherms and (b) pore size distributions of pristine and functionalized carbon nanotubes.

microporous dendrimers that can be synthesized *via* C-C coupling chemistry [169, 170]. Furthermore, the bimodal pore size distributions depicted in Figure 4.1b derived from the desorption branch of the sorption isotherms reflect a loss in mesopore volume. In addition to small mesopores, the samples possess mesopores of a diameter between 20 and 30 nm, which can be ascribed to the voids formed between entangled nanotubes [34]. The volumes of the large mesopores are almost unaffected by the functionalization, but decrease slightly for CNT-W50 and CNT-W200. Similar observations have been reported by Giambastiani et al. [171] after introduction of cyclic nitrene functionalities onto the surface of multiwalled CNTs. N₂ molecules do not exclusively physisorb on the exterior basal planes of the nanocarbon, but also fill hollow regions, e.g., formed between entangled CNTs and bundles thereof. Thus, the loss of mesoporosity in the range from 2 to 5 nm and the concomitant reduction of BET surface area could be related to changes in the agglomeration of the CNTs due to stirring during the functionalization. This is evidenced by the structural differences observed in the TEM micrographs in Figure S4.1a and b. While CNT-P is arranged in a compact fashion, bigger voids are formed between entangled nanotubes after the functionalization step.

Table 4.2.: Porous structural parameters derived from nitrogen absorption of pristine and functionalized CNTs.

Sample	S _{BET} [m ² /g]	S _{Micro} [m ² /g]	V _{Tot} [cm ³ /g]	V _{Micro} [mm ³ /g]
CNT-P	304	0	2.96	0
CNT-O100	203	0	1.53	0
CNT-O150	224	0	1.64	0
CNT-O200	233	0	1.68	0
CNT-W50	190	1	1.45	10
CNT-W200	191	11	1.36	60

4.3.3. Characterization of Sulfonic Acid Groups by Thermal Analysis

Thermogravimetric analyses (TGA) carried out under inert gas conditions were undertaken in order to analyse the thermal stability of sulfur containing functional groups. As can be inferred from Figure 4.2 together with results obtained by elemental analysis (Table 4.1), mass loss becomes more pronounced with higher sulfur content. The mass loss is mainly due to the evolution of SO_2 ($m/z = 64$), which evolves as a result of the thermal decomposition of sulfonic acid entities. In addition to SO_2 other gaseous compounds identified by m/z traces 18, 28, and 44 were monitored, which could be attributed to H_2O , CO , N_2 , and CO_2 . The onset of decomposition reveals that the sulfur-containing functional groups introduced by the diazotization approach are stable up to 250 °C. Thus, the benzenesulphonic acid groups withstand thermal treatments to a higher extent in contrast to carboxylic acid entities commonly introduced by wet oxidation treatments. It has been reported that the latter decompose at temperatures as low as 100 °C [172].

Another noteworthy aspect to be considered is that SO_3H groups introduced by sulfuric acid treatments exhibit a slightly lower thermal stability compared to their homologues generated *via* diazotization of sulfanilic acid [173, 174]. Specifically, the onset of decomposition in the former case is nearly 40 °C lower. Furthermore, attaching acidic species to the exposed graphitic planes of carbon materials using mineral acids with high oxidation power can lead to undesired structural degradation. As shown in Figure S4.1c and d, the surface modification using sulfanilic acid is rather mild, which in consequence prevents damaging the nanostructure. Neither etching nor drilling of the outer graphitic sheets is observed for CNT-W200. In addition, the herein applied functionalization approach has a

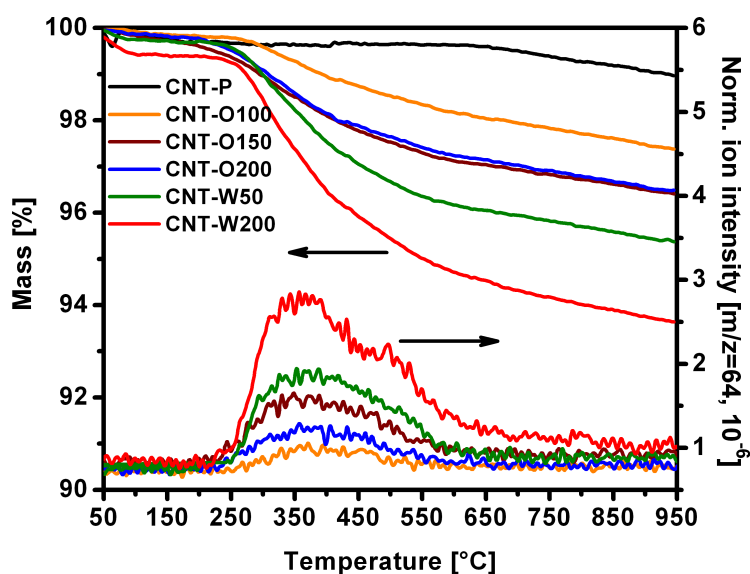


Figure 4.2.: Thermogravimetric curves depicting the simultaneous mass loss and SO_2 evolution during heating in an inert gas atmosphere.

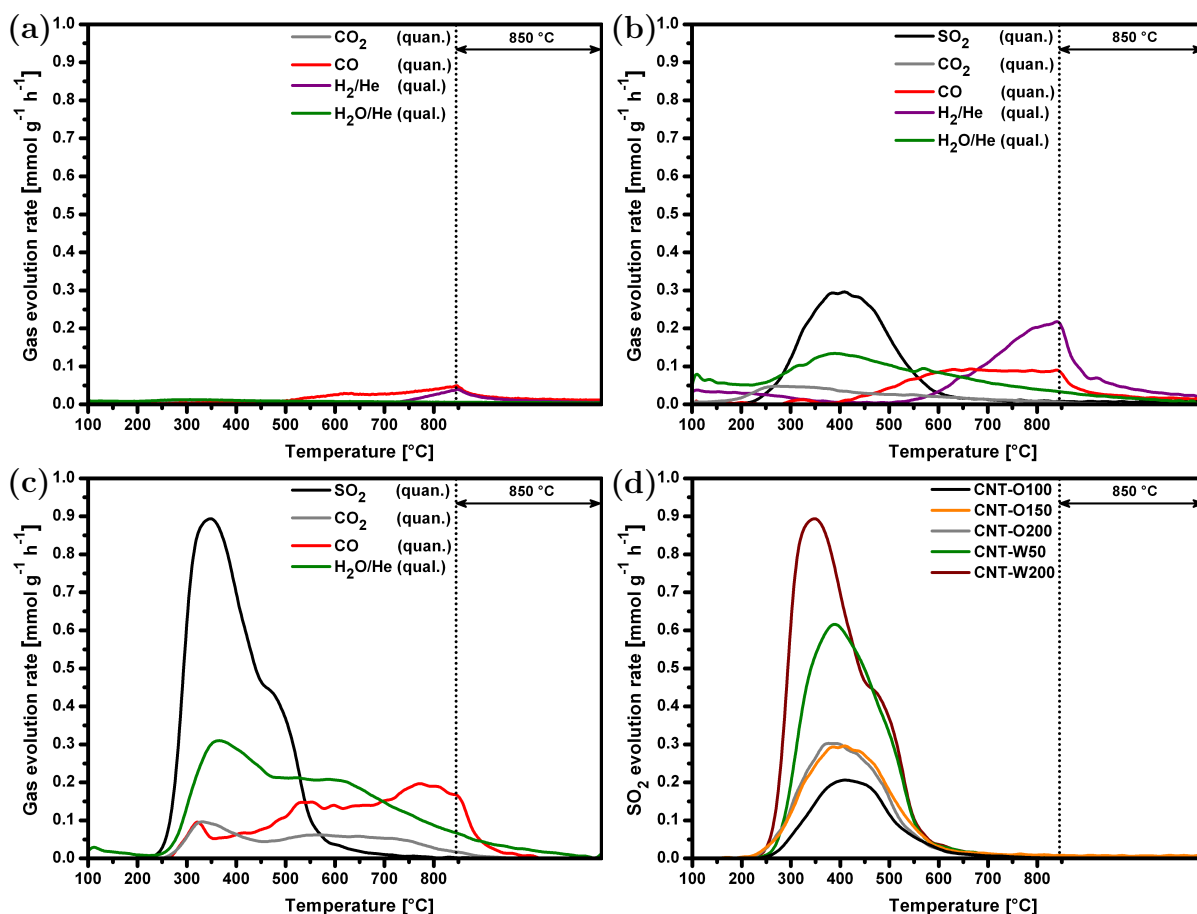


Figure 4.3.: TPD profiles of S-functionalized carbon nanotubes obtained from heating the samples at $5\text{ }^{\circ}\text{C}\cdot\text{min}^{-1}$ in a He flow rate of $25\text{ mL}_{\text{N}}\cdot\text{min}^{-1}$.

positive impact on the crystallinity of the carbon material. CNT-P contains amorphous carbon domains (Figure S4.1c) that are not present on the neat surface of CNT-W200. Thus, the graphitic character is notoriously improved after chemical modification.

Quantification of the surface functional groups was performed by temperature-programmed desorption coupled with GC analysis (Figure 4.3). Pristine CNTs are poorly decorated with oxygen-containing functional groups. However, the surface has notoriously changed upon functionalization. Here, larger amounts of CO and CO₂ are observed. Since no oxidizing agent was used in the course of the modification approach, the occurrence of oxygen-containing functional groups may arise from the washing cycles performed in DMF using ultrasonication. Although Ar was flown through the system during this step, the dissolved O₂ and/or H₂O present in the solvent seems to be sufficient for the generation of O-containing functional groups [175]. Water residues in the organic solvent can be sonolytically dissociated into hydrogen and hydroxyl radicals [176]. The former species can further react with dissolved O₂ present in DMF leading to the formation of hydroperoxy radicals (Scheme 4.3). This assumption is reflected in similar specific molar concentrations



Scheme 4.3: Sonolytical dissociation of water (left) and formation of hydroperoxy radical through reaction between hydrogen radical with molecular oxygen (right).

of CO and CO₂ (Table 4.3) among the as-prepared samples. However, slightly higher amounts of CO were released during TPD of CNT-W200. This might be associated with the addition of OH radicals onto the CNT surface that are formed in the course of the chemical modification between benzenesulfonic acid radicals and water molecules.

TPD experiments reveal that SO₂ and H₂O are concomitantly released, which is related to the thermal decomposition of sulfonic acid entities. This method confirms that the use of water as a solvent increases the amount of S-containing functionalities significantly. According to the results shown in Table 4.3, the amounts of SO₂ range from 70 to 488 $\mu\text{mol}\cdot\text{g}_{\text{Sample}}^{-1}$, demonstrating that a factor of almost 4 lies between the lowest (CNT-O100) and the highest (CNT-W200) functionalized sample. All the SO₂ desorption profiles show the same onset of decomposition, starting at around 250 °C, which coincides with the temperature determined by TGA (Figure 4.2). Consequently, the surface functional groups introduced through the radical based modification approach possess a moderately high thermal stability. It should be noted that, as opposed to the other materials, only the profile of sample CNT-W200 shows a shoulder centered at around 500 °C in the thermogravimetric experiment (Figure 4.2) suggesting that at least two types of sulfur containing functional groups are present. We assume sulfonic acid entities located at different sites, making them unequal in terms of thermal stability, e.g., grafted on basal plane or prismatic edges, inside or outside CNTs. Furthermore, generated radicals can not only bind to the carbon surface, but also to a benzene ring already attached to the sidewall. Therefore it cannot be excluded that dendrimer-like structures are created in the course of the modification, making the branched structures less stable than simple moieties. Either of these considerations, or even both, may be the origin for the relatively broad SO₂ peaks in the TPD profiles. In none of the experiments SO₃ was found, since no changes in the mass trace $m/z = 80$ were observed.

Table 4.3.: Evolved quantities of SO₂, CO₂ and CO calculated from TPD profiles.

Sample	CO ₂	CO	SO ₂
	[$\mu\text{mol}\cdot\text{g}_{\text{CNT}}^{-1}$]		
CNT-P	14	70	-
CNT-O100	25	87	70
CNT-O150	53	116	195
CNT-O200	53	110	193
CNT-W50	71	120	351
CNT-W200	93	222	488

4.3.4. Spatial Distribution of Hetero-Elements Analyzed by SEM/EDX

Figure 4.4a shows an SEM micrograph together with the corresponding elemental maps of carbon and oxygen obtained for pristine CNTs. Oxygen is homogeneously distributed along the CNT agglomerates. No catalyst residues from the synthesis of the CNTs were found due to the high purity grade of the commercial CNTs with a residual metal content below the EDX detection limit. According to the EDX spectrum in Figure 4.4b, the carbon content amounts to 93.27 wt%, whereas oxygen is present to an extent of about 6.73 wt%.

Carbon, oxygen, and sulfur are evenly distributed in the functionalized sample CNT-W200 (Figure 4.4c) indicating that the modification protocol is suitable for introducing sulfur-containing moieties in a homogeneous way within the resolution of SEM-EDX. Based on the EDX spectrum displayed in Figure 4.4d, a quantitative analysis was performed, from which it can be stated that the concentrations of carbon, oxygen and sulfur amount to 91.51 wt%, 6.86 wt% and 1.64 wt%, respectively, which is consistent with elemental analysis.

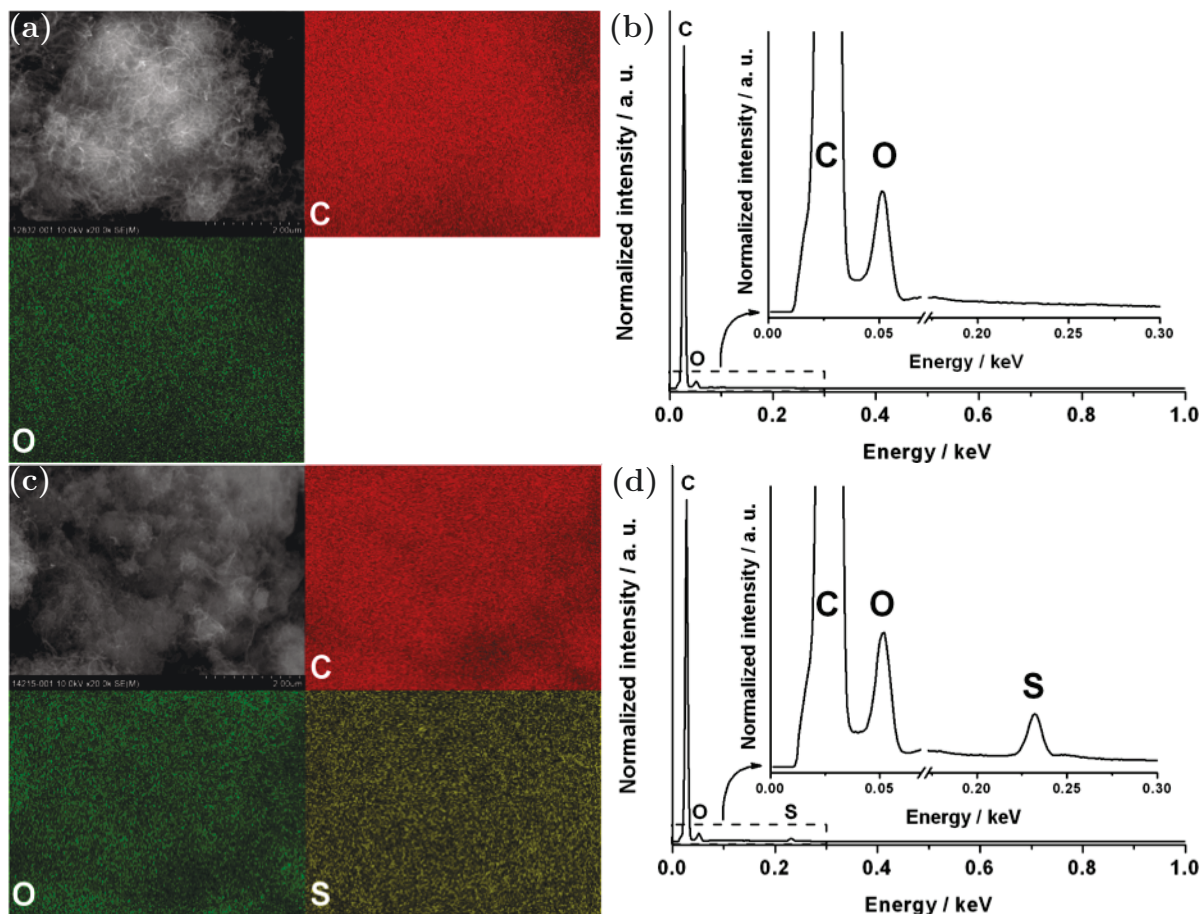


Figure 4.4.: Top: SEM micrograph showing the elemental distribution (a) and corresponding EDX spectrum (b) of CNT-P. Bottom: Elemental mapping (c) with representative EDX spectrum (d) of CNT-W200.

4.3.5. ATR-FTIR spectroscopy

ATR-FTIR spectra shown in Figure 4.5 reflect the differences between the functionalized samples and the pristine material, since the single beam spectrum of the latter one was used as a background. Spectra of the as-prepared samples show features ascribable to benzenesulfonic acid entities. Absorption peaks centered at 1610 cm^{-1} , 1584 cm^{-1} and 1461 cm^{-1} are attributed to C=C stretching vibrations, which may arise both from the aromatic nature of the CNTs and the phenyl ring serving as a linker between the sidewall of the nanostructure and the sulfonic acid functionality. Further indications for the existence of phenyl rings are the =C-H vibrations appearing at 1009 cm^{-1} [177]. The presence of SO_3H groups is evidenced by the features observed at 1376 cm^{-1} and 1183 cm^{-1} , which emerge from the $-\text{SO}_2$ antisymmetric and symmetric stretching modes, respectively. In addition, these bands are downshifted to lower wavenumbers whenever water interacts in a physisorbed state with the sulfonic acid entities [154]. This effect, which is more pronounced for CNT-W50 and CNT-W200 due to their enhanced surface hydrophilicity, can be confirmed by the appearance of bands centered at 1122 cm^{-1} and 1031 cm^{-1} . Sulfonic acid groups can be further identified by the broad absorption band between 3520 and 3080 cm^{-1} arising from the $-\text{OH}$ stretching vibrations of the surface moiety, as well as of adsorbed water. Finally, the feature found at 830 cm^{-1} can be regarded as a proof for the covalent attachment of phenylsulfonic acid groups to the carbon surface, which can be attributed to the C-H out-of-plane vibrations characteristic of para-substituted aromatic compounds [177].

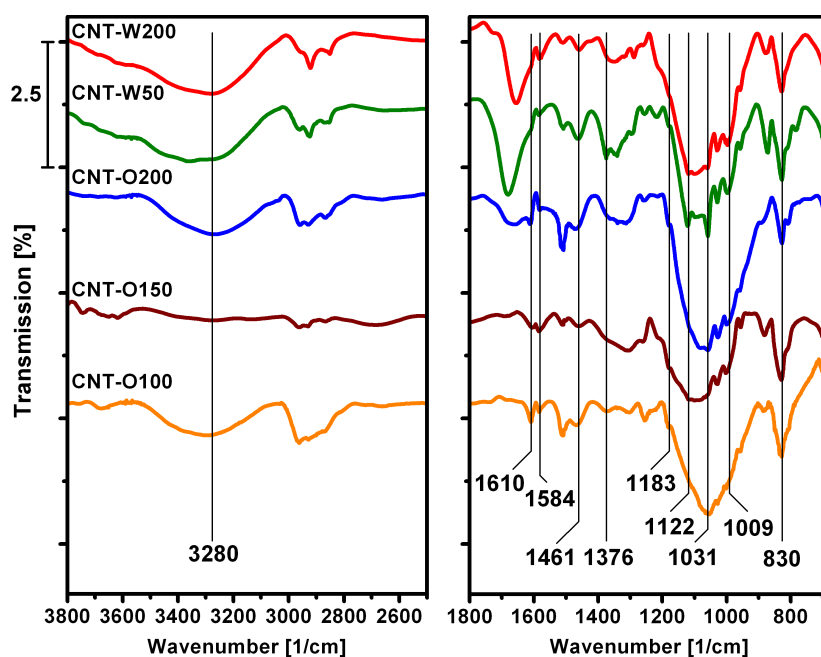


Figure 4.5.: ATR-FTIR spectra of as prepared carbon materials.

4.3.6. Acidity of S-modified CNTs in Aqueous Media

The obtained titration curves are compared in Figure 4.6. As can be expected from the very low amounts of CO and CO₂ evolved during TPD experiments, the pristine material shows a rather neutral behavior in aqueous media. Besides exhibiting a starting pH of about 7, there is no evidence for an inflection point of the curve, implying that only a negligible quantity of acid sites is available on the pristine material. On the contrary, as soon as sulfur is present in the sample the pH begins to drop, reaching its lowest value at 3.2 for CNT-W200, which is accompanied by a progressive right-shift of the curves towards larger volumes. A closer look at the first derivative of the titration curve corresponding to CNT-W200 reveals that two types of acid centers are available. This observation is in agreement with the TG-MS (Figure 4.2) and TPD (Figure 4.3) profile of SO₂ evolution that show a shoulder suggesting the presence of two types of S-containing surface functionalities.

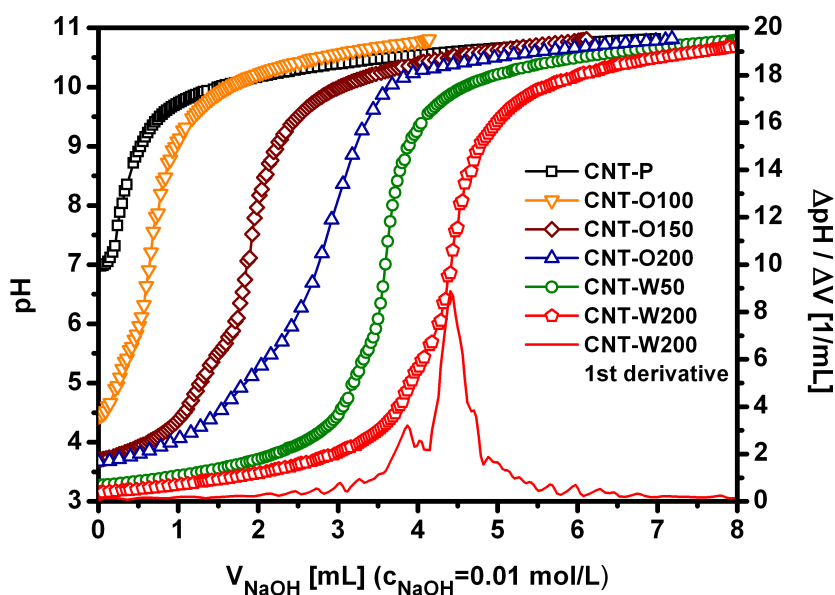


Figure 4.6.: Potentiometric titration curves obtained with a 0.01 M sodium hydroxide solution.

Evidently, the herein employed functionalization approach enables the possibility of controlling the surface acidity, which in this case solely depends on the extent to which the heteroatom is attached to the CNT framework. This assumption is supported by the linear correlation that has been found between the specific concentration of titratable sites and the sulfur content assessed by TPD as depicted in Figure 4.7. It is noteworthy to mention that carboxylic acid species are scarcely present on the surface of the nanostructure, which is evident from the comparably low CO₂ amounts derived from TPD experiments. Thus, their contribution to the overall acidity is negligible. A similar linear relationship can be

established between the sulfur concentration determined by TPD and elemental analysis, respectively. From this result it can be deduced that sulfur as a constituent element of benzenesulfonic acid species is not present in the bulk of the material, but is in fact distributed along the CNT surface.

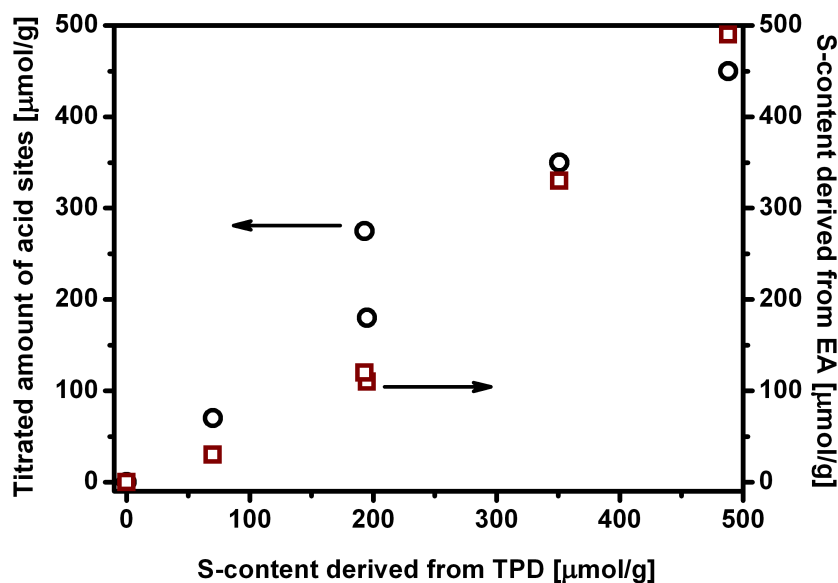


Figure 4.7.: Amount of acid sites derived from potentiometric pH titrations and sulfur content calculated from elemental analysis as a function of the sulfur concentration assessed by TPD.

4.3.7. Catalytic Transformation of 2-Propanol

Sulfonic acid modified CNTs have been prepared with the primary aim to explore their catalytic properties in gas-phase acid-base catalysis, like isomerization reactions. The decomposition of 2-propanol was carried out as a probe reaction to analyze the residual acid-base character of the functionalized materials after typical catalyst pretreatment and under reaction conditions (T, p, gas phase) close to a catalytic test. The turnover of 2-propanol on Brønsted acid centers yields both propylene and diisopropyl ether together with water as a couple product. Surface basicity is indicated by the formation of acetone and hydrogen (Scheme 4.1).

Pretreatment in N_2 were performed prior to the test reaction at 350 °C since this is a typical temperature at which common catalytic gas-phase reactions are carried out. For instance, various types of nanocarbons including CNTs have been tested in the ODH of ethane [116], propane [115], n-butane [178] and ethylbenzene [179] in the range between 350 and 450 °C. As displayed in Table 4.4, the pretreated CNTs contain nearly a third of the original sulfur amount present in the as prepared samples.

Figure 4.8 represents the conversion of isopropanol and the selectivity observed at different reaction temperatures over three different materials pretreated at 350°C in inert gas. As can be clearly observed, the conversion of the secondary alcohol over CNT-O150 and CNT-O200 is similar, which indicates that the number of active sites at the surface is comparable (Figure 4.8a and b). In contrast, the number of active sites is much higher at the surface of CNT-W200, which is reflected in higher conversion at the same reaction temperature (Figure 4.8c).

As outlined above, the selectivity of the reaction contains information about the nature of active sites. All three materials display acid as well as basic character, while acidity is generally the predominating feature of these bifunctional catalysts. The selectivity to propylene, i.e., the acidic character decreases in the order CNT-O150 > CNT-W200 > CNT-O200 when the catalysts are compared at iso-conversion of approximately 2% (Figure 4.8, Table 4.4). Studies have shown that the surface acidity of cation exchanged

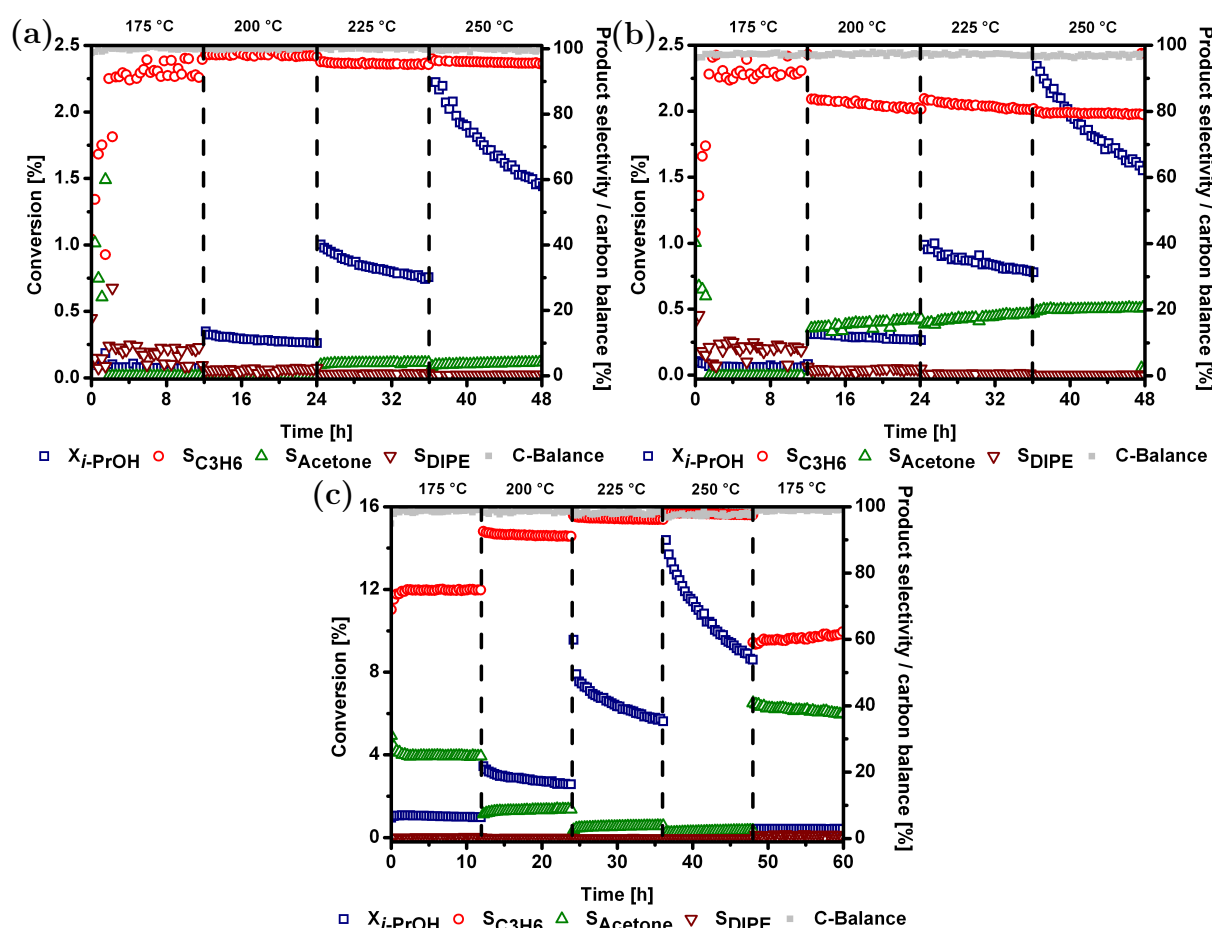


Figure 4.8.: Activities and selectivities as a function of time on stream at four different temperatures observed during the catalytic testing of samples (a) CNT-O150, (b) CNT-O200 and (c) CNT-W200 previously treated at 350 °C in N₂ for 2h.

Table 4.4.: Elemental analysis of samples pretreated in nitrogen atmosphere and after catalysis.

Entry	Sample	Description	Elemental analysis				
			[wt %]				
			C	H	N	S	O
17764	CNT-O150-N2	CNT-O150, N2, 350 °C, 2h	97.8	0.1	0.06	0.06	2
17765	CNT-O200-N2	CNT-O200, N2, 350 °C, 2h	97.2	0.1	0.09	0.06	2.6
17766	CNT-W200-N2	CNT-W200, N2, 350 °C, 2h	94.8	0.2	0.03	0.46	4.5
17767	CNT-O150-IPA	CNT-O150, after reaction	98.4	0.1	0.03	0	1.5
17768	CNT-O200-IPA	CNT-O200, after reaction	97.6	0.2	0.2	0	2
17769	CNT-W200-IPA	CNT-W200, after reaction	94.8	0.3	0.08	0.57	4.3

molecular sieves correlates with the rate of formation towards dehydration products [180]. Propylene formation rates are used to estimate the strength of acidity by normalizing to the sulfur content (Table 4.5). According to the values thus obtained, CNT-O150 and CNT-O200 are similarly capable of catalyzing the transformation of a 2-propanol molecule, while CNT-W200 is less efficient as evidenced by a 4-fold lower propylene formation rate per mole sulfur.

However, the catalyst surface is changed in particular at the high reaction temperatures, which is reflected in a decreased conversion when the reaction temperature is lowered again to the initial temperature of 175°C after probing the catalysts at 250°C (Figure 4.8). This clearly shows that time on stream or deactivation studies are absolutely necessary when the decomposition of 2-propanol is applied as a reaction to probe acidity or basicity of functional materials. The drop in activity is mainly due to the loss of sulfur during the catalytic probe reaction (Table 4.4). Sulfur-containing functional groups could be reduced by formation of hydrogen in the probe reaction. Another deactivation scenario could be hydrolysis due to the water formed in the reaction.

To further explore this, changes induced by the test reaction on the carbon surface were investigated by ATR-FTIR spectroscopy. As has been previously discussed, the acidic sites generated on the carbon surface dehydrate the secondary alcohol to almost exclusively propylene. Figure 4.9 shows the appearance of a broad intense band within the range 3390 and 3260 cm^{-1} , which can be attributed to stretching vibrations of OH groups [125].

Table 4.5.: Product selectivity to propylene, acetone, and diisopropylether at iso-conversion and acidity (formation rate of propylene) of benzenesulfonic acid functionalized CNTs determined by the transformation of 2-propanol.

Sample	T ¹ [K]	X _{i-PrOH} [%]	S _P ² [%]	S _A ³ [%]	S _{DIPE} ⁴ [%]	r _P 10 ⁻³ [mol·mol _S ⁻¹ ·s ⁻¹]
CNT-O150	250	1.44	95.4	4.2	0.3	0.20
CNT-O200	250	1.55	79	20.6	0.3	0.17
CNT-W200	200	2.58	91.1	8.8	0.1	0.05

¹ Temperature of isoconversion ² P: Propylene ³ A: Acetone

⁴ DIPE: Diisopropyl ether

Hydrolysis of benzenesulfonic acid species with water results in the formation of phenolic species that, despite their lower acidic strength, are still able to catalyze the secondary alcohol dehydration towards propylene. This might be the origin of the deactivation that can be observed with increasing reaction temperature. Bands showing the presence of SO_3H groups disappear, whereas the band at 820 cm^{-1} remains unchanged suggesting that the phenyl linker stays covalently attached to the carbon backbone, while the C–S bond is broken by hydrolysis. This assumption is further supported by the elemental analysis of CNT-O150 and CNT-O200 after reaction, which confirms the absence of sulfur (Table 4.4). It is interesting that the S-content in CNT-W200 is not decreasing. Most likely, a large fraction of phenylsulfonic acid radicals generated during the sidewall modification of CNT-W200 reacted with the aromatic ring of species previously formed on the carbon surface. As has been previously stated, this facilitates the development of dendrimer-like structures. Under these circumstances, it becomes evident that a significant amount of acid sites is not accessible to the relatively large 2-propanol molecule due to steric hindrance. In addition, benzenesulfonic acid anhydride groups could have been formed during the pretreatment at $350\text{ }^\circ\text{C}$, resulting in a reduced amount of active sites. This also explains why CNT-W200 produces less amount of propylene per mole sulfur compared to CNT-O150 and CNT-O200. Steric effects, however, have no impact on the amount of acid sites that can be determined by potentiometric pH titration experiments. This is because the ion mobility is not affected by the branched structure of the acid sites in the liquid phase. Thus, it could be that a significant portion of S-atoms remains inactive on the surface since is not exposed to water. An IR study performed by Zawadzki et al. on carbon films revealed that bands at 1161 and 949 cm^{-1} can be ascribed to the skeletal stretching and C–O stretching/ CH_3 rocking vibrations of adsorbed 2-propanol, respectively [125]. ATR-FTIR spectra of the samples after reaction show bands at 1183 and 955 cm^{-1} supporting the presence of an adsorbed species.

The loss in activity as well as the deactivation observed at temperatures beyond $200\text{ }^\circ\text{C}$ is related to the hydrothermal decomposition of sulfonic acid entities. Nevertheless, the acid character of the samples after functionalization could be unambiguously confirmed, making these surfaces suitable for catalytic applications under milder conditions as in the case of esterification [181] and etherification [182] reactions. Such catalytic liquid phase reactions are performed at temperatures below $100\text{ }^\circ\text{C}$. Furthermore, highly acidic systems as presented in this study show an increase in hydrophilicity, which consequently enhances the dispersion of functionalized carbon materials. This aspect is of great importance for composite materials. In such applications, symbiotic effects originating from the interaction between the reinforcement compound and the host matrix notably affect the properties of the resulting material. For instance, the electrical conductivity of a PHET/CNT

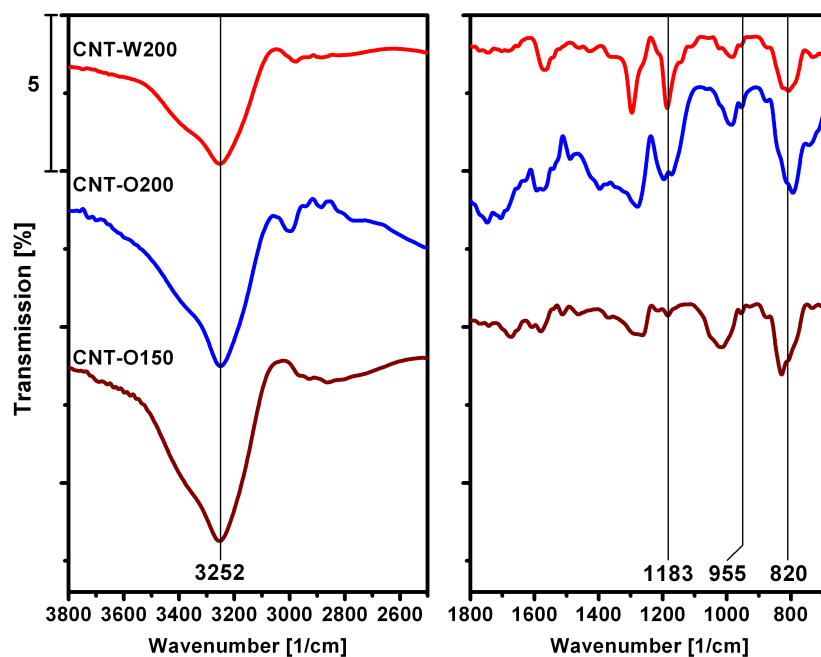


Figure 4.9.: ATR-FTIR spectra of the investigated carbon catalysts after the decomposition of 2-propanol.

nanocomposite prepared by covalently attaching the polymer to the carbon framework was $38.5 \text{ S}\cdot\text{cm}^{-1}$ [183]. In contrast, a physical mixture between PHET and the pristine CNT material led to a 28-fold lower value. In either case, the improvement is drastic considering that PHET is non-conducting ($< 10^{-8} \text{ S}\cdot\text{cm}^{-1}$). Mechanical properties can be likewise improved by addition of carbon nanotubes to the host material. An example thereof is the enhancement of the tensile strength and tensile modulus of polyamide 6 by 16 % and 13 %, respectively, due to the incorporation of 1.5 wt% MWCNT into the composite material obtained by *in situ* anionic ring-opening polymerization [184]. For these applications highly dispersed suspensions are needed, which can be certainly achieved by applying the functionalization approach presented in this investigation.

4.4. Conclusion

Multiwalled CNTs modified with benzenesulfonic acid entities *via* the *in situ* generation of aryl radicals through the thermal decomposition of diazo compounds yielded nanostructured materials possessing a well-defined Brønsted acidity. These surface functionalities are further characterized by a moderately high thermal stability up to 250 °C, making them suitable for applications where carboxylic acids created by conventional methods are already decomposed. Undoubtedly, the success of functionalization strongly depends on the ability of the radical precursor to dissolve in the liquid phase. Therefore, water revealed to be more efficient as solvent compared to *o*-dichlorobenzene, since much lower

sulfanilic-acid-to-carbon ratios are necessary to introduce the same number of acid sites in aqueous medium. According to the results obtained by infrared spectroscopy the functional groups are in fact benzenesulfonic acid entities.

The decomposition of 2-propanol was applied as a test reaction for probing the acid-base character of S-modified multiwalled carbon nanotubes. These are bifunctional materials, containing mainly acid, but also basic sites. However, although the materials were pretreated at temperatures above the reaction temperature, they all show the same deactivation pattern in 2-propanol decomposition. This means that 2-propanol transformation cannot *a priori* be considered as a non-destructive probe reaction for acid-base properties, but the stability in the test reaction has to be confirmed. The sulfonic acid modified CNTs are stable in the test reaction at 175°C, but deactivate rapidly at higher temperatures. The deactivation is attributed to hydrothermal decomposition of the benzenesulfonic acid functionalities.

4.5. Supporting Information

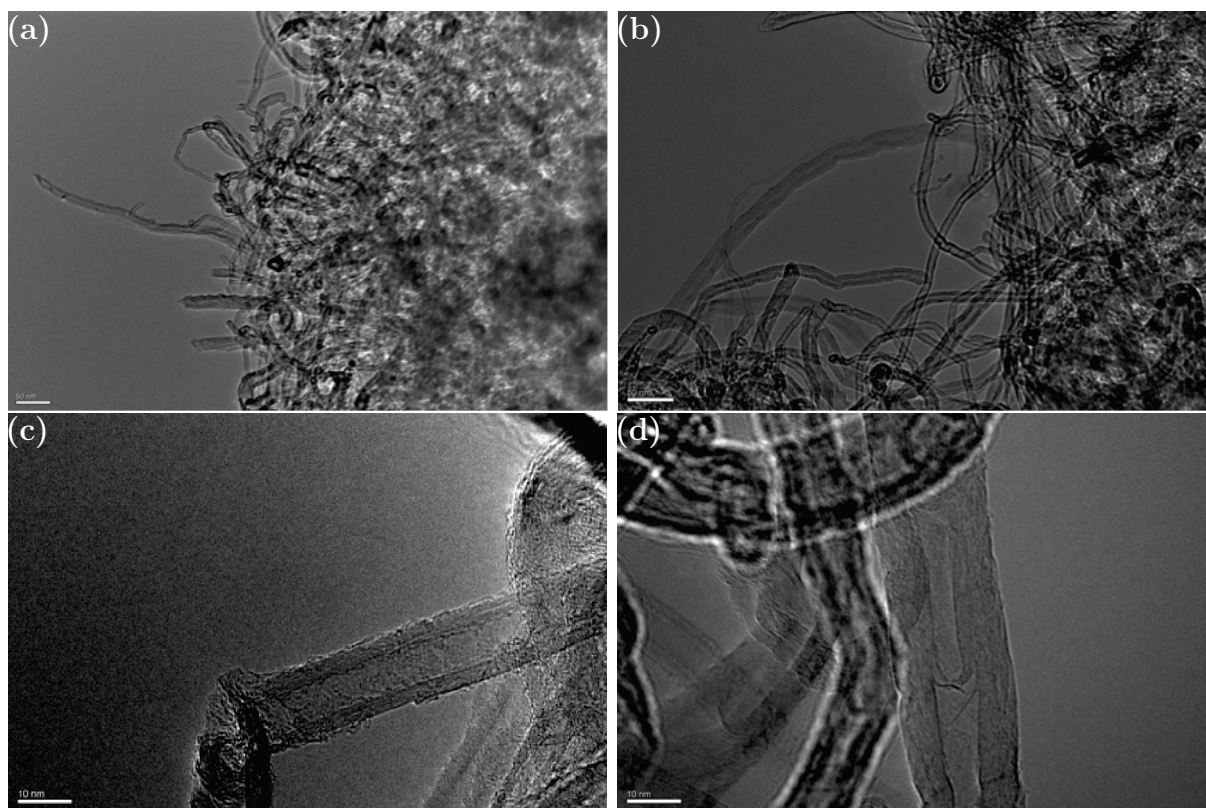


Figure S4.1.: TEM images of (a,c) CNT-P and (b,d) CNT-W200

5. Insights into the intrinsic acid-base properties of N-doped carbon nanotubes: a combined TPD, XPS and 2-propanol reaction investigation

Klaus Friedel Ortega, Rosa Arrigo, Benjamin Frank, Robert Schlögl, and Annette Trunschke

Abstract

Chemical and electronic properties of nitrogen-doped multiwalled carbon nanotubes (Baytubes C150 HP[®]) synthesized by NH₃ treatment of preoxidized CNTs at three different temperatures have been investigated by a set of surface sensitive techniques. Temperature programmed desorption (TPD) provides information about the nature and thermal stability of nitrogen and oxygen containing functional groups. X-ray photoelectron spectroscopy (XPS) serves as a complementary tool allowing to understand the binding state of the investigated heteroatoms present on the carbon surface. Acid-base properties in aqueous phase were analyzed by potentiometric pH titration, while the catalytic transformation of 2-propanol provided insights into the acid-base behavior of the modified systems in the gas phase. NH₃ treatment at 300 °C leads to an acid-base bifunctional surface, predominantly decorated with imide species. Pyrrole-like nitrogen was the most abundant moiety present on the sample modified at 500 °C. Only a small fraction is ascribed to lactam groups and pyridinic species. This shift of the nitrogen distribution already creates a surface with basic properties as evidenced by a selectivity to acetone of at least 80 %. Nitrogen incorporation at 700 °C leads to a carbon surface with a well-defined basicity. Pyridinic nitrogen serving as a Lewis basic site was identified as part of the acid-base pair necessary for the formation of dehydrogenation products. The oxidative stability of NCNTs strongly depends on the NH₃ treatment temperature. NCNTs obtained at 700 °C exhibit a combustion resistance comparable to that of the pristine CNT material. In contrast, lower NH₃ treatment temperatures are detrimental for the oxidative stability.

5.1. Introduction

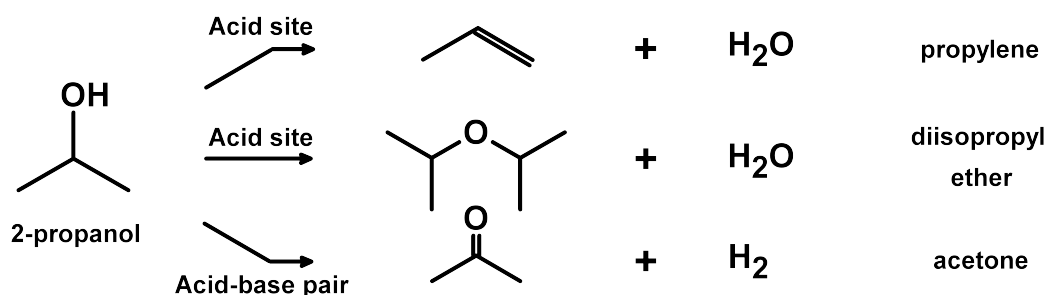
Nitrogen doped carbon nanotubes (NCNTs) have gained considerable attention due to their tunable acid-base properties along with their specific electronic structure induced by the incorporation of electron-rich nitrogen surface species into the carbon framework. In the context of metal-free catalysis, NCNTs have been successfully employed as solid-base catalysts in the Knoevenagel condensation of benzaldehyde with ethylcyanoacetate [185]. The initial activity correlates with the amount of pyridinic nitrogen species present in the carbon nanostructure. Beneficial effects have also been observed when nitrogen doped carbons are used in redox catalysis [186] or electrochemistry [187]. Regarding the support function for metal nanoparticles *via* a strong metal-heteroatom interaction, N-containing species stabilize small nanoparticles consequently leading to a high degree of dispersion. Arrigo et al. [188] showed that the morphology of Pd nanoparticles depends not only on the kind of heteroatom present on the carbon, namely oxygen and nitrogen, but also on the type of surface functionality. NCNTs generated by post-treatment of OCNTs with NH_3 at 600 °C (N-CNT873K) yield Pd nanoparticles with an enhanced wetting at the carbon surface and an average diameter of 2.7 nm, being smaller in size than those formed on N-doped CNTs modified at 200 and 400 °C. Pd/N-CNT873K leads to the highest turnover frequency in the liquid phase oxidation of benzyl alcohol to benzaldehyde, which is 2-fold times larger than the value obtained for Pd supported on OCNTs. Villa et al. observed similar differences in terms of catalytic activity during the same reaction among O- and N-doped CNTs loaded with Au-Pd nanoparticles [189].

The complexity of nitrogen incorporation into a carbon framework becomes evident when attempts are made in order to understand the underlying formation mechanisms of the corresponding functionalities. For instance, when carbon is modified by a post functionalization method as it is the case when an oxygenated specimen is subjected to amination *via* ammonia treatment, several reactions take place between the oxygen species and the nitrogen precursor. The nature and abundance of functional groups characterizing the final state of a given graphitic surface is strongly affected by the amination temperature, but also by the thermally induced dynamic rearrangement as well as decomposition of existing surface species. As reported by Kundu et al. [190], below 300 °C the N-containing functional groups are mainly created by a dehydration mechanism. Upon neutralization of carboxylic acids with NH_3 , the resulting ammonium salts are thermally decomposed to amides, which can be further converted into nitrile groups [191]. In an analogue way, preexisting anhydrides react with ammonia to imides, which subsequently decarboxylate to pyridinic nitrogen at 300 - 500 °C. Similarly, lactones undergo a dehydration reaction with the nitrogen precursor leading to lactams, which decarboxylate to pyrrolic nitrogen above

500 °C. These reaction sequences make evident that several formation and decomposition reactions overlap at low temperatures in a rather narrow frame, which consequently leads to the coexistence of various types of nitrogen surface species, differing among each other not only in terms of structure, but most importantly, with respect to their electronic and acid-base properties.

Studies dealing with the characterization of N-containing carbons have contributed to the understanding of the interrelation between type of functional group and acid-basic properties. On the basis of XPS and CO₂ microcalorimetry, Arrigo et al. [97] showed that an amination at 600 °C leads to a strongly basic surface decorated by mainly pyridine-like and pyrrolic species. Instead, low treatment temperatures result in amide-like functional groups accompanied by thermally stable oxygenated species, yielding an acid-base bifunctional material.

The present contribution provides further insights into the physicochemical properties of NCNTs by a comparative study of temperature programmed desorption (TPD), XPS and the catalytic transformation of 2-propanol as a probe reaction. The reaction occurs *via* the conversion of the secondary alcohol to dehydration products on acid centers and to acetone over an acid-base pair (Scheme 5.1).



Scheme 5.1: Reaction pathways associated with the catalytic transformation of 2-propanol [120].

5.2. Experimental section

5.2.1. Functionalization of MWCNT

Purified carbon nanotubes (Baytubes C150 HP[®], carbon content > 99 wt%, bulk density 140-230 kg·m⁻³) with 13 nm outer diameter and 4 nm inner diameter in average were obtained from Bayer Material Science (HP-CNT). 20 g of HP-CNT were treated in 1 L concentrated nitric acid (Carl Roth, 65 wt.%, p.a.) under reflux for a period of 4 h. After cooling down to ambient temperature, the oxidized sample was thoroughly washed and filtrated with Millipore water until neutral pH. Finally, the resulting carbon was dried at

110 °C in static air for 3 days (O-CNT). Nitrogen incorporation was performed by flowing a gas stream containing 50 % NH₃ in Ar at 150 mL_n·min⁻¹ through a tubular quartz reactor (40 mm inner diameter and 740 mm in length) previously loaded with 4 g O-CNT. In order to minimize concentration and temperature gradients, the reactor was placed in a swinging furnace. The functionalization was carried out by heating the oxidized sample at 5 °C·min⁻¹ to 300 °C, 500 °C and 700 °C, respectively, and maintained at the target temperature for a period of 6 h. Thereafter, the samples were cooled down to ambient temperature in the NH₃/Ar mixture. Nomenclature of nitrogen functionalized carbons is composed by the functionalization temperature followed by NCNT (Table 5.1).

5.2.2. Nitrogen Adsorption

Carbon materials were characterized by N₂ adsorption at liquid nitrogen temperature (-196 °C) using a Quantachrome Autosorb-6B KR instrument. Analyses were performed on 30 mg of powdered substance, which were degassed for 2 h at 200 °C before measurement. Surface area calculations were undertaken using the BET equation [156], pore size distributions were derived from the desorption branches of the isotherms according to the BJH method [157], and total pore volumes were determined at a relative pressure of $p/p_0 = 0.97$. Micropore analysis was performed by applying the MP-method proposed by Mikhail, Brunauer and Bodor using a statistical thickness interval of 0.05 [158].

5.2.3. Potentiometric pH Titrations

Samples were investigated by potentiometric pH titrations carried out with a Mettler DL 77 autotitrator monitored by a Mettler Toledo DGi114-SC electrode. In a typical experiment, 100 mg of powdered sample were suspended in 50 mL of 0.1 M NaCl solution. Equilibration was achieved by vigorously mixing the suspension overnight. In order to minimize side effects from dissolved CO₂, the mixture was degassed under Ar for 30 min prior to starting a measurement. The titrants used were 0.01 M NaOH and 0.01 M HCl solutions, depending on the samples to be investigated, respectively diluted from 1 M Titrisol standards (Merck Millipore).

5.2.4. Temperature Programmed Desorption

Temperature-programmed desorption (TPD) was carried out in a home-built setup equipped with a gas chromatograph (Varian CP-4900 Micro-GC) and a mass spectrometer (Pfeiffer Omnistar) for on-line product analysis. Typically, weighted amounts of sample were loaded into a fixed-bed quartz reactor (9 mm i.d.), which was placed in a self-constructed furnace with an isothermal zone of 4 cm at the upper temperature limit.

Weakly adsorbed water was removed within 1 h at 100 °C in a He stream passed at a flow rate of 25 mL_n·min⁻¹. Experiments were started thereafter by linearly heating the reactor by 5 °C·min⁻¹ to 1035 °C. This temperature was maintained for 30 min before cooling down to ambient temperature.

5.2.5. Temperature Programmed Oxidation

Temperature-programmed oxidation (TPO) experiments were performed in a TG-DSC Netzsch STA 449C Jupiter thermobalance coupled to a Pfeiffer Omnistar mass spectrometer for simultaneous gas analysis. DSC curves recorded during TPO gave the enthalpies associated with the thermal oxidation of the carbon samples. In a typical run, 10 mg of sample were loaded in an Al₂O₃ crucible, which was heated at 5 °C·min⁻¹ from room temperature to 950 °C in synthetic air (21 % O₂ in Ar) at a flow rate of 100 mL_n·min⁻¹. The maximum temperature was maintained for 30 min before cooling down the system to room temperature.

5.2.6. Elemental Analysis

Elemental analyses (CHNS) were conducted applying a Thermo FlashEA 1112 NC Analyzer.

5.2.7. X-Ray Photoelectron Spectroscopy

X-ray photoelectron spectroscopy (XPS) measurements were performed at ambient temperature under UHV conditions (base pressure < 3·10⁻¹⁰ mbar) employing non-monochromated Al K_α radiation source (1486.6 eV). Spectra were acquired using a hemispherical analyzer (Phoibos 150, SPECS) operated in fixed analyzer transmission mode at pass energy of 20 eV. The binding energy scale of the system was calibrated using Au 4f_{7/2} = 84.0 eV and Cu 2p_{3/2} = 932.7 eV from foil samples. Carbon samples were evenly distributed and densely packed over a conductive adhesive tape fixed on a stainless-steel holder. For each sample, a survey spectrum (0-1000 eV) and the C1s (280-300 eV), O1s (520-540 eV) and N1s (390-410 eV) core level spectra were recorded. Fitting of the core level peaks was performed using Casa XPS software [192]. The number of components included in the fitting was determined by applying the difference method [193, 194]. In the case of the N1s, after subtraction of a Shirley background [195], the peaks were fitted using a nonlinear, least squares routine with mixed Gauss-Lorentz functions. For this purpose, peak maxima were fixed within ± 0.1 eV and the full-width at half maximum (FWHM) applied for all spectra was set to 1.6 eV. Due to the high complexity of the broad O1s spectrum, the fitting was performed on the plot resulting from the difference between

the O1s spectra relative to samples functionalized at different temperature: this represents the O1s spectrum of the relatively less thermally stable species. Oxygen and nitrogen contents were assessed with the aid of theoretical cross sections [196].

5.2.8. Catalytic transformation of 2-propanol

For the transformation of 2-propanol, 50 mL_n·min⁻¹ N₂ was passed through a saturator at 20 °C (4.2 % isopropanol) before reaching a U-shaped quartz reactor with an inner diameter of 9 mm containing 150 mg of catalyst material previously sieved to a fraction between 250 and 355 μm. Prior to the measurements, the samples were heated in N₂ to 350 °C at 5 °C·min⁻¹ for 2 h. Temperatures were varied in 25 °C steps from 200 to 300 °C at constant inlet flow rate, whereby every set of parameters remained unchanged for a period of 12 h. The conversion of 2-propanol was calculated based on the ratio of product concentrations to amount of secondary alcohol fed into the reactor.

$$X_{i\text{-PrOH}} = \frac{\chi_{\text{Propylene}} + \chi_{\text{Acetone}} + \chi_{\text{Diisopropyl ether}}}{\chi_{i\text{-PrOH}}}$$

Propylene, acetone, and diisopropyl ether were the only carbon containing products detected. Carbon balances obtained for each measured catalyst reaching values of at least 98 % were calculated as follows:

$$\text{C-balance} = \frac{\chi_{i\text{-PrOH,out}} + \chi_{\text{Propylene}} + \chi_{\text{Acetone}} + \chi_{\text{Diisopropyl ether}}}{\chi_{i\text{-PrOH,in}}}$$

Selectivity is defined in molarity terms as the concentration of a given product to the sum of all detected products.

$$S_{\text{Product, i}} = \frac{\nu_i \cdot \chi_{\text{Product, i}}}{\nu_i \cdot \chi_{\text{Product, i}} + \sum \nu_j \cdot \chi_{\text{Product, j}}}$$

5.3. Results and Discussion

5.3.1. Textural properties and elemental composition

Structural parameters derived from N₂ adsorption-desorption experiments for the pristine and modified samples are summarized in Table 5.1. The isotherms identified as type III are indicative for weak adsorbent-adsorbate and typical for significant adsorbate-adsorbate interactions. CNTs form entangled agglomerates due to strong noncovalent interactions rising from their high aspect ratio. The observed H3 hysteresis has been often encountered in carbonaceous systems with slit-shaped pores (Figure S5.1a) [168]. BET surface areas

Table 5.1.: Textural properties and elemental composition of pristine and functionalized CNTs.

ID ^a	Sample	S_{BET} [m ² g ⁻¹]	S_{Micro} [m ² g ⁻¹]	V_{Tot} [cm ³ g ⁻¹]	V_{Micro} [mm ³ g ⁻¹]	Elemental analysis [wt %]				
						C	H	N	O ^b	N/O ^c
12832	HP-CNT	304	0	1.37	0	97.2	0	0	2.8	0
16603	O-CNT	338	34	1.34	20	92.0	0.03	0	8	0
16646	300-NCNT	323	15	1.31	10	94.8	0.02	1.3	3.9	0.38
16645	500-NCNT	324	14	1.35	10	96.4	0.03	1.2	2.4	0.57
16644	700-NCNT	350	39	1.51	30	97.4	0.02	1	1.6	0.71

^a Internal sample number to distinguish reproductions of sample preparation

^b Oxygen is calculated as a difference to 100 % ^c Ratio is determined on a molar

increase after oxygen and subsequent nitrogen functionalization, in contrast to the total pore volume that remains constant, increasing only for 700-NCNT (Table 5.1).

Micropore surface areas exhibit a different trend. Oxidation is known to open the caps of nanotubes, making the inner channels accessible. However, introduction of oxygen species has an evident impact on surface roughness reflected by an increase in micropore surface area from initially zero to 34 m²·g⁻¹. In contrast, NH₃ treatment at 300 °C and 500 °C reduces the BET surface area by the same extent as the micropore surface area, lowering S_{Micro} by more than 50 %. Decomposition of oxygen functional groups and thermal effects might be the origin of this observation. The treatment temperature of sample 700-NCNT is high enough to produce H₂ and aggressive species like H atoms, NH₂ and NH radicals through thermal decomposition of NH₃ [197]. In the presence of hydrogen, the thermal stability of functional groups is significantly decreased [198]. Most important, the radical species serve as etching agents that upon reacting with the carbon surface enhance the development of microporosity [199]. As shown in Figure S5.1b, the peak centered at 2.6 nm, representing small mesopores, becomes broader towards the micropore region after oxidation of HP-CNT and the subsequent NH₃ treatment of O-CNT. The micropore volumes change in a similar manner as the micropore surface area, but the total pore volume remains unaffected. This implies that mesoporosity is the governing structural factor. Large mesopores, as evidenced by the feature centered at 32 nm, are attributable to the voids between agglomerates of entangled individual nanotubes [34].

The elemental composition of the pristine and modified carbon nanotubes is listed in Table 5.1. HP-CNT already contains up to 3 wt% oxygen. After HNO₃ oxidation the corresponding value is more than doubled to about 8 wt%. Subjecting O-CNT to NH₃ treatment leads to nitrogen incorporation. Its concentration slightly decreases from 1.3 to 1.0 wt% with increasing modification temperature. A significantly higher impact is observed for the calculated amounts of oxygen, which progressively decrease from 3.9 to 1.6 wt% with increasing temperature. The rise of the N/O molar ratio from 0.4 to 0.7 indicates that oxygen is not exclusively a constituent element of nitrogen containing functional groups at higher temperatures.

5.3.2. Thermal Stability and Nature of Surface Species

Based on the characteristic profiles of the volatile compounds detected in the course of the TPD experiments, it becomes evident that the modified samples possess different types of surface species. In particular, the discussion of N-containing functionalities refers to characteristic pyrolysis products of organic reference compounds including pyrrole, pyridine, benzonitrile, and 2-pyridone.

Wet oxidation treatments confer the system acidic properties by introducing carboxylic acid entities, which degrade to CO₂ at low temperatures as evidenced in Figure 5.1a by the peak located at 275 °C. When the temperature is further increased, a second step representing the thermal degradation of anhydrides is observed (453 °C). Finally, the decomposition stage at 650 °C belongs to the depletion of lactones [172].

In general, oxygen functional groups decomposing to CO have a higher thermal stability (Figure 5.1b). However, a small amount is already released at 300 °C. In this temperature regime, water is detected most likely due to a condensation reaction between adjacent carboxylic acids yielding anhydride groups, which subsequently decompose to equimolar amounts of CO and CO₂. A contribution to water evolution may also arise from the dehydration of neighbouring phenolic species [200]. The second step observed at 460 °C stems from the CO contribution of anhydrides. Compared to the corresponding CO₂ peak, the maximum rate of CO evolution is shifted by 25 °C towards higher temperatures, which might be an indication for a sequential decomposition mechanism. Some evidence was provided by Fields and Meyerson on the pyrolysis of phthalic anhydride [201]. Besides biphenyl and naphthalene, the detection of fluorenone allowed the authors to conclude that CO is formed after CO₂ elimination. In the region between 600 and 850 °C a broad peak evolves due to the degradation of phenols and ethers [172]. Two small features were found above 850 °C, which can be ascribed to carbonyls and quinonic groups [172]. In this high temperature regime, concisely starting at around 900 °C, dehydrogenation of the carbon backbone begins as a consequence of homolytic C–H bond cleavage, leading to radicals that subsequently recombine to H₂ (Figure 5.1e).

Drastic changes on the carbon surface become evident after treating O-CNT in NH₃ at 300 °C. The CO₂ profile is characterized by the complete disappearance of the carboxylic acid groups and a strong reduction of the anhydride feature (Figure 5.1a). The CO intensity loss at 460 °C further confirms the decomposition of cyclic anhydrides (Figure 5.1b). In addition, lower amounts of phenols, ethers, carbonyl species and quinone groups are present on the surface of 300-NCNT as evidenced by the reduced intensity of the CO profile in the range between 600 and 950 °C. Moreover, in contrast to the oxidized carbon sample, 300-NCNT possesses surface features that upon heating lead to the formation of HCN and N₂. Carboxylic acids are known to react with ammonia, forming amides *via* dehydration

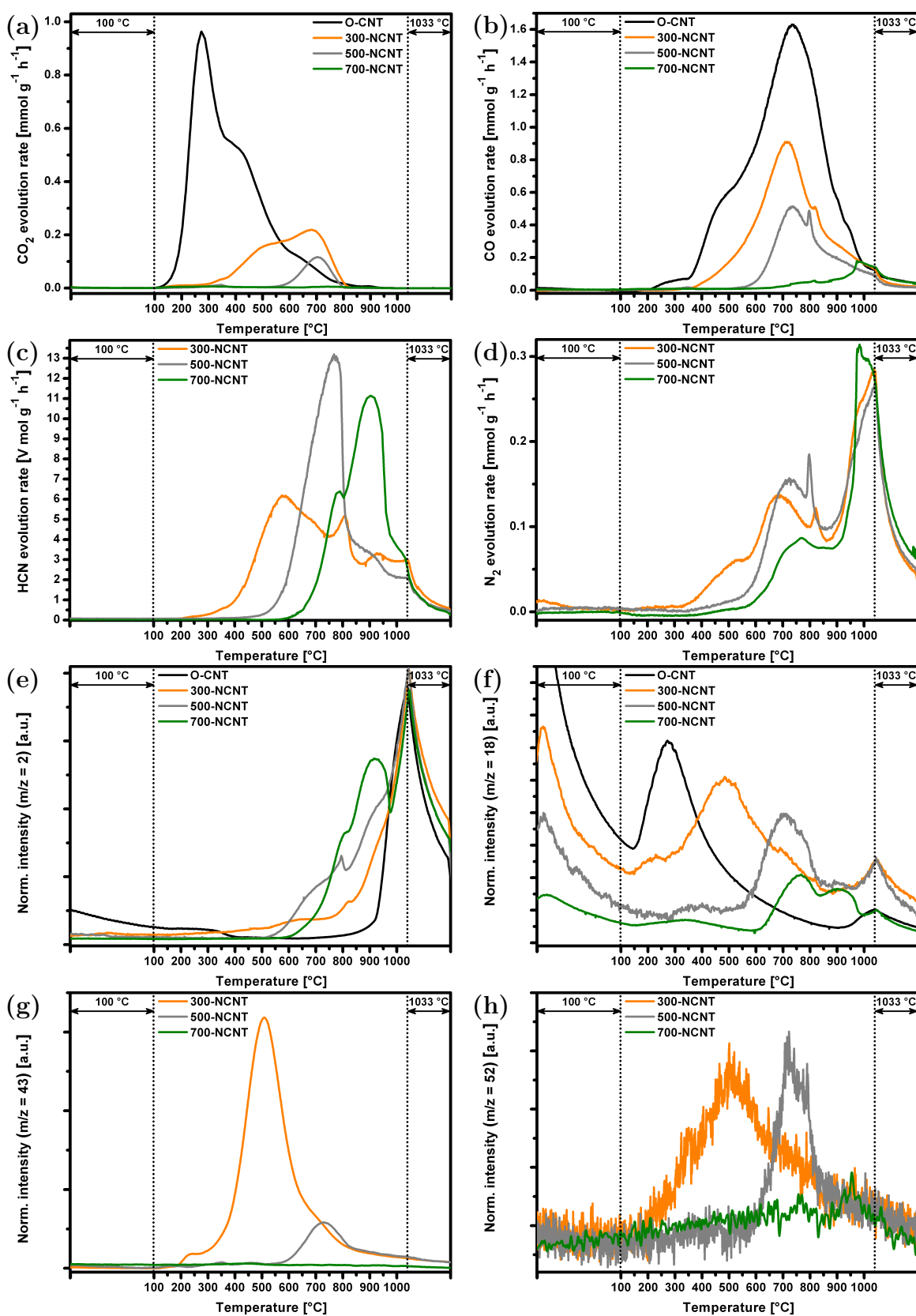
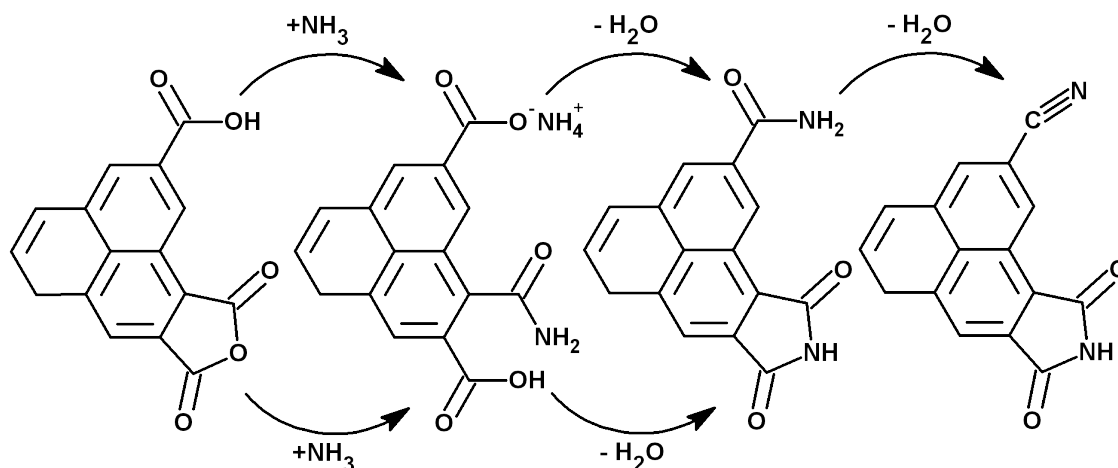


Figure 5.1.: Evolution of (a) CO_2 , (b) CO , (c) HCN , (d) N_2 , (e) H_2 , (f) H_2O , (g) HNCO , and (h) C_2N_2 during TPD analysis of oxygen and nitrogen modified carbon nanotubes.

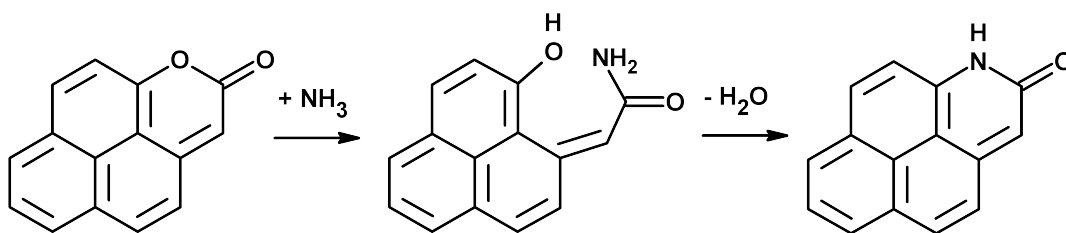


Scheme 5.2: Formation pathway of amides and imides through carboxylic acid neutralization respectively ring-opening of cyclic anhydrides.

of ammonium salts [191], whereas imides are generated through ring opening accompanied by subsequent water elimination (Scheme 5.2).

According to Kundu et al. [190] the interconversion of amides into nitrile groups *via* water elimination (Scheme 5.2) takes place at around 200 °C, which is 100 °C below the treatment temperature of 300-NCNT. Consequently, the presence of amides on this sample is questionable. As shown in Figure 5.1f, a small H₂O peak evolves between 145 and 260 °C. The low intensity compared to the dominating feature centered at 485 °C suggests that only a small fraction of the formed nitrogen species are in the amide configuration. A small shoulder between 200 and 300 °C in Figure 5.1c serves as a further indication for the low amount of amide species, which degrade to HCN upon rearrangement into nitrile groups.

As evidenced by the HCN and HNCO evolution depicted in Figure 5.1c and g, the decomposition of N-containing functional groups present on 300-NCNT begins at 200 °C. Theoretical calculations on the decomposition pathway of phthalimide [202] suggest a decarboxylation route involving four transition states leading to the formation of benzonitrile, which further degrades to HCN *via* a free radical mechanism [203]. In view of



Scheme 5.3: Lactam formation *via* ring-opening of lactones.

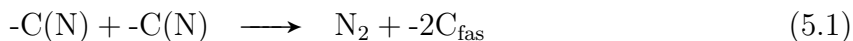
this, the evolution of CO₂ between 350 and 550 °C may correspond to the superimposed decomposition of anhydrides and imides. Thus, HCN formation between 400 and 600 °C is related to the thermal degradation of imide species. Following the results obtained by Choudhary et al. [204] on the pyrolysis of succinimide, an alternative decarboxylation mechanism should be considered. In a similar way, a four-center cyclic transition state generates CO₂ followed by the scission of a C–C bond resulting in the formation of HCN. In addition, the thermal decomposition of succinimide generates isocyanic acid (HNCO). Since the major contributions to the mass spectrum of HNCO arise from $m/z = 42$ and 43 [205], these traces were also recorded during TPD experiments. According to Figure 5.1c and g, HNCO is located in the same regime of the broad low temperature HCN peak. This observation is a further indication for the presence of imide species.

Likewise, the decomposition of lactams that are formed through ring-opening of lactones (Scheme 5.3) yields HCN and HNCO as known from the pyrolysis of 2-pyridone [206]. Since both cyclic functionalities decompose to the same volatile compounds, it is not possible to discern between them based on the TPD results. However, the low temperature peak in the HCN profile is too broad in order to be explained only in terms of one functional group (Figure 5.1c). This is further supported by the HNCO profile of 300-NCNT (Figure 5.1g), which shows a peak located at 510 °C that precedes a small shoulder at 700 °C. The latter is centered at the same temperature as the HNCO peak in 500-NCNT. These observations suggest that imides and lactams are present on 300-NCNT, although to a different extent, whereas the former are absent on the surface of the carbon modified at 500 °C. Based on the knowledge of O-containing functional groups, an analogous assignment can be done for these nitrogen species. Imides decompose at lower temperatures since they exhibit a structural correspondence to anhydrides, whereas lactams are thermally more stable as they show a similarity to lactones.

At temperatures exceeding 700 °C, the HCN profile of 300-NCNT exhibits two more features. In the pyrolysis of pyrrole and pyridine several major decomposition products have been identified, including HCN and H₂ [207, 208]. Although the mechanisms are strictly valid for the model compounds, similar decomposition pathways might govern the depletion of analogous functionalities on carbon materials. As depicted in Figure 5.1e, H₂ evolution already starts at 400 °C. The presence of two peaks centered in a similar position as the high temperature features in the HCN profile suggest that two more species with different thermal stability exist on the carbon surface. The first feature is tentatively assigned to pyrrolic nitrogen whereas the second to pyridinic species [209].

As observed in Figure 5.1d, N-containing functional groups may also decompose to N₂. In contrast to other volatile compounds, pathways explaining the formation of molecular nitrogen are not straightforward. This decomposition product is not directly linked to a

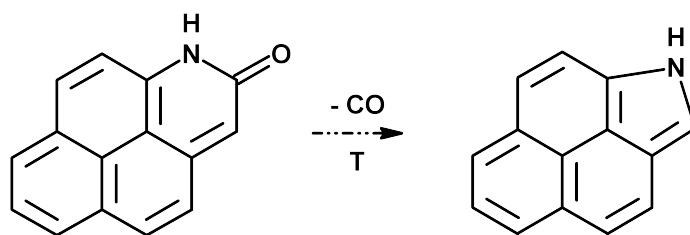
certain kind of species, but it rather implies that surface diffusion plays an important role [210]. This phenomenon is reflected by the following surface reaction:



In order that reaction 5.1 takes place, one surface species needs to be mobile yielding N_2 upon recombination with another N-containing functionality, leaving two free active sites (fas) $-C_{\text{fas}}$ on the surface. Cyanogen (C_2N_2) evolution in the course of the TPO of N-containing carbons serves as an evidence for the mobility of surface species [210]. Although it has been stated that C_2N_2 cannot be detected during TPD experiments as a consequence of thermal decomposition [209], our study shows that a compound with an m/z value of 52 is released. This mass-to-charge-ratio corresponds to the most intense contribution of the cyanogen mass spectrum [211]. Figure 5.1h shows that the C_2N_2 evolution for 300-NCNT takes place already at low temperatures. Probably a large fraction is decomposed to N_2 over the active surface and only a small amount goes into the gas phase, which is suggested by the poor signal-to-noise ratio of trace 52. The ability of detecting this minor compound most likely arises from the fact that sample amounts in the range of 300 mg were employed. In addition, the fluid dynamic conditions are better defined in a fixed bed reactor compared to studies in which TPD experiments are performed in a thermobalance.

Besides the discussed reaction pathways between ammonia and oxygen-containing functional groups, the dynamic character of the carbon surface has to be taken into consideration. This is insofar important as thermally induced rearrangements of surface entities change the state of the starting material by altering the distribution of functionalities. A comparison between the CO profile of 300-NCNT and O-CNT clearly shows that the overall intensity decreases after ammonia treatment and the feature arising from the anhydride decomposition is strongly reduced (Figure 5.1b). However, the TPD spectrum of 300-NCNT has a sharp CO feature at 800 °C, which is not present in O-CNT. The narrow peak width suggests that the underlying process occurs fast. This observation is probably linked to the decarbonylation of lactam groups into pyrrolic-like nitrogen species as depicted in Scheme 5.4.

In comparison to 300-NCNT, the CO_2 profile of 500-NCNT is characterized by the complete absence of the anhydride peak and the presence of a minor contribution due to lactone decomposition at 650 °C. Since the functionalization was performed at 500 °C, anhydrides were converted to imides in the presence of ammonia. In consequence of the treating temperature and the so far discussed thermal stability, it is probable that a large fraction of these groups was already decomposed during amination. This is supported by



Scheme 5.4: Thermal induced decarboxylation of lactams into pyrrole-like nitrogen.

the absence of the HNCO and HCN peaks in the temperature regime between 600 and 750 °C as shown in Figure 5.1c and g. Since the presence of imides cannot be fully excluded, CO₂ evolving between 600 and 750 °C may partly arise due to the decomposition of this species. However, this is not predominant as their HCN contribution is also strongly reduced. The absence of anhydrides is further supported by the complete disappearance of the tailing observed in the CO profile of 300-NCNT between 350 and 600 °C (Figure 5.1b). On the contrary, the sharp CO feature at 800 °C is still present after modification at 500 °C, which was ascribed to the interconversion of lactams into pyrrolic species. This observation strengthens the concept that lactams possess a higher thermal stability than imides.

Changes are also observed in the evolution of HCN as shown in Figure 5.1c. Not only the low temperature peak is absent, but in particular the intensity of the feature belonging to pyrrolic species strongly increases. The asymmetry in the range between 600 and 700 °C might be indicative for the presence of another species, which in view of the thermal stability may be ascribed to lactams. Pyridinic nitrogen was likewise generated as evidenced by the feature centered at 900 °C. However, the low intensity suggests that only a small fraction belongs to this kind of functionality. As has been discussed so far, H₂ evolution observed at temperatures below the dehydrogenation of the carbon backbone is due to the thermal depletion of pyrrolic and pyridinic species (Figure 5.1e). Although the N₂ profile is similar to sample 300-NCNT, the low temperature contribution in 500-NCNT is completely absent (Figure 5.1d). This leads to the question whether the generation of N₂ at low temperatures is also linked to imides. Within this context, C₂N₂ is only observed at higher temperatures. If this high temperature peak arises from the decomposition of lactams is likewise debatable.

As can be seen in Figure 5.1a amination at 700 °C leads to a full disappearance of all CO₂ contributions thus far observed. Hence, carboxylic acids, anhydrides and lactones fully reacted with NH₃, which upon generating N-containing surface species rearranged to other functional groups or totally decomposed. Similarly, only a small amount of CO at 980 °C evolves (Figure 5.1b), suggesting at most the presence of carbonyl species. The corresponding HCN profile displays two features that fulfill the so far presented systematics.

While the amount of pyrrolic species decreases, the concentration of pyridinic nitrogen substantially increases. Additionally, the peaks observed in the H₂ profile are centered at the same temperature as the features identified in the HCN profile. In contrast to the samples functionalized at 300 °C and 500 °C, no HNCO evolves in the course of the TPD of 700-NCNT, which is indicative for the absence of imides and lactams. Interestingly, similar to the sharp CO peak identified in 300-NCNT and 500-NCNT, the N₂ profile of both samples exhibit a sharp feature located exactly at the same temperature (Figure 5.1d). This peak completely vanishes when the chemical modification is performed at 700 °C. An implication of this finding might be that lactam decomposition gives also rise to N₂ formation. Furthermore, 700-NCNT does not show any contribution of C₂N₂.

From the TPD investigation it is possible to derive the quantities of different evolving gases linked to the thermal decomposition of surface species (Table 5.2). For this purpose, calibration factors for CO₂, CO, and N₂ were determined with the aid of certified calibration gases upon identification of the corresponding peaks in the Micro-GC. The total amount of CO₂ desorbed drops by a factor of 70 from 919 μmol·g_{CNT}⁻¹ for O-CNT to 13 μmol·g_{CNT}⁻¹ for 700-NCNT. Although the specific molar concentrations of CO are significantly larger than the corresponding CO₂ amounts, a similar downward trend is observed as evidenced by the reduction from 1836 μmol·g_{CNT}⁻¹ to 137 μmol·g_{CNT}⁻¹ for O-CNT and 700-NCNT, respectively. Oxygen functional groups like phenols, ethers and carbonyls are scarcely present on 700-NCNT. The availability of O-containing surface species strongly depends on the temperature of the NH₃ treatment. On the contrary, comparable quantities of N-containing gases formed as a consequence of the thermal degradation of lactam/imide, pyrrole and pyridine species were obtained. The total amount of N₂ only drops slightly from 294 μmol·g_{CNT}⁻¹ to 239 μmol·g_{CNT}⁻¹ for 300-NCNT and 700-NCNT, respectively. Similarly, HCN concentrations calculated only on the basis of GC areas without determination of calibration factors remain comparably high since the values obtained change from 9.4 V·mol·g_{CNT}⁻¹ to 8.4 V·mol·g_{CNT}⁻¹. The overall amount of nitrogen dispersed on the surface remains unaffected by the functionalization. This is in line with results obtained by elemental analysis (Table 5.1). Nevertheless, TPD clearly shows that the amination temperature determines the nature of N-containing species.

Table 5.2.: Calculated amounts of CO₂, CO, N₂ and HCN (GC peak areas) obtained from the TPD profiles.

Sample	CO ₂ [μmol·g _{CNT} ⁻¹]	CO [μmol·g _{CNT} ⁻¹]	N ₂ [μmol·g _{CNT} ⁻¹]	HCN [V·mol·g _{CNT} ⁻¹]
O-CNT	919	1836	-	-
300-NCNT	263	847	294	9.4
500-NCNT	87	410	271	9.5
700-NCNT	13	137	239	8.4

5.3.3. Surface Analysis by XPS

Oxygen and nitrogen functional groups introduced through chemical modification into carbonaceous com-pounds can be analyzed by the respective O1s and N1s inner-shell photoelectrons. As previously shown by TPD, a large number of species decomposing at different temperatures are bound to the CNT framework, which were identified on the basis of reference compounds. In spite of the consistent results, thermally induced rearrangements of functional groups that could change the initial state of the surface should be taken into account [96]. Therefore, with the aid of XPS, information about the bonding state of the heteroatoms can be obtained together with the surface elemental composition of the sample under investigation. Chemical bonds and environments can be identified since the electronic structure of the photoemitting atoms as the constituent elements of surface species give rise to characteristic chemical shifts [188]. However, several functional groups with comparable electronic configurations differ from each other in terms of thermal and chemical properties. Hence, a combination of both techniques is essential in order to gain a more comprehensive insight into the overall surface properties.

5.3.3.1. N1s Core-Level Spectrum

Depending on the chemical configuration, three different BE regions can be found in N1s core level spectra of carbonaceous materials [96, 212]. A region between 398 and 399 eV, generally ascribed to N atoms bound to two C atoms that are located on the edge of graphene layers, is characteristic for pyridine-like nitrogen (N1). This moiety contributes to the π -system with one p-electron. The zone at 400.3 eV is usually attributed to nitrogen atoms at edge sites that are bound to two C atoms and one H atom. This is typical for structures arranged in the pyrrole-like fashion (N2). In this case the N atom contributes to the aromatic system with two p-electrons. Similar configurations are found in lactam as well as imide species both located at a BE around 399.7 eV [213]. In the high BE zone ranging from 401 to 403 eV, shifts are originated by the presence of quaternary nitrogen (N3). This type of species substitutes a carbon atom in the graphene layer forming three σ -bonds with vicinal C atoms. In terms of electronic structure, the “graphitic nitrogen” contributes to the π -system with two p-electrons. The presence of nitrogen-oxygen bonds can be confirmed by the appearance of spectral features in the BE range between 403 and 406 eV [97]. Surface functional groups like pyridine-oxide [190] and NO₂ [214] haven been identified in this regime.

Figure 5.2 displays the deconvoluted N1s photoelectron spectra of the nitrogen-functionalized CNTs obtained by NH₃ treatment of O-CNT at 300, 500 and 700 °C, respectively. Pyridinic nitrogen (N1) gives rise to the lowest BE at 398.3 eV. The relative intensities

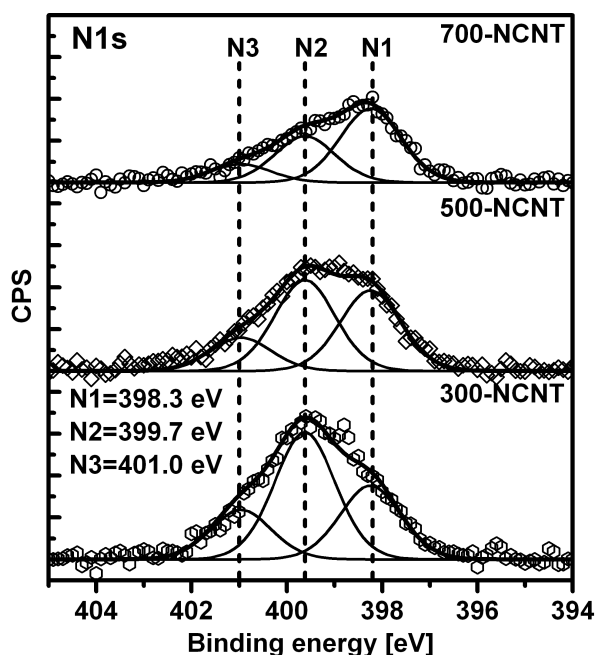


Figure 5.2.: Deconvoluted XP N1s spectra of (a) 300-NCNT, (b) 500-NCNT and (c) 700-NCNT obtained from ammonia treatment of O-CNT.

between N1, N2 and N3 indicate that the former is the most abundant species dominating the N1s spectrum of 700-NCNT. As the treatment temperature is lowered, the relative contribution of N1 progressively decreases. Figure 5.3 shows the area-to-nitrogen-content ratio calculated for the features employed in the deconvolution of the N1s spectra as a function of the NH_3 treatment temperature. This quantity increases for the N1 signal with the amination temperature. Since pyridinic nitrogen exhibits the highest thermal stability compared to the remaining detected surface species during TPD, the HCN feature located at 900 °C was attributed to the thermal depletion of this functional group. A significantly lower contribution in this high temperature regime is found for 500-NCNT and 300-NCNT. Both methods show a correspondence between the spectral features attributed to pyridinic nitrogen, indicating that in either case a plausible identification is possible.

The interpretation of the N2 signal is certainly more complex. A component at 399.8 eV was detected on the basis of the difference N1s spectrum obtained by subtraction of 500-NCNT from 300-NCNT (Figure S5.3a). According to the results obtained by TPD, imides are the dominant species present in 300-NCNT, which decompose between 400 and 600 °C evolving as HCN and HNCO. As the functionalization treatment temperature is incremented to 500 °C, the broad low temperature HCN peak in 300-NCNT vanishes yielding an asymmetric feature at 700 °C. Furthermore, the low temperature shoulder at 530 °C of the N_2 profile most likely arising from the decomposition of imides disappears. Moreover, larger quantities of isocyanic acid are detected at earlier stages in comparison to

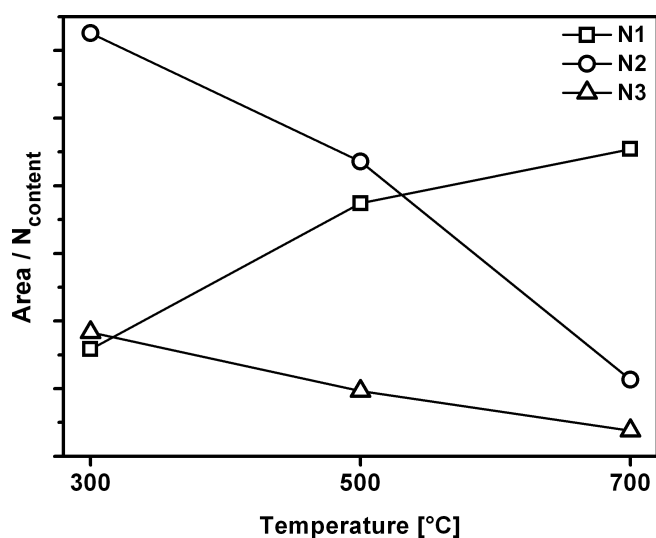
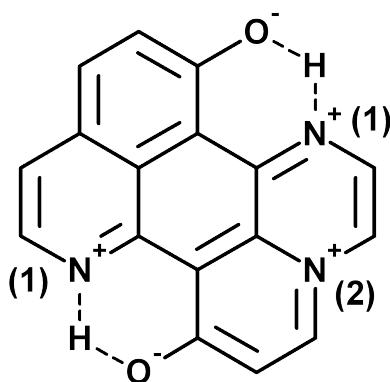


Figure 5.3.: Area-to-nitrogen-content ratio derived from the N1s spectral features as a function of NH_3 treatment temperature.

500-NCNT. These observations suggest that the component obtained at a BE of 399.8 eV resulting from the difference spectrum analysis is strongly related to the presence of imide species. The same approach applied to 500-NCNT with respect to 700-NCNT resulted in the identification of a component with a BE at 399.7 eV. As evidenced by the absence of features below 750 °C in the HCN profile of 700-NCNT in addition to the nonappearance of HNCO, it can be stated that neither imides nor lactams are present in the high temperature modified sample. Moreover, isocyanic acid evolves in the same regime of the dominating asymmetric HCN feature during the TPD of 500-NCNT, while no HNCO was found in the imide region. In view of the previous discussion the feature obtained from the difference spectrum between 500-NCNT and 700-NCNT at 399.7 eV as shown in Figure S5.3b is tentatively assigned to lactams. For the sake of completeness, an isolated analysis of the 700-NCNT N1s spectrum suggests that pyrrole-like N is the dominating surface species contributing to the N2 feature. The thus far discussed differentiation is insofar important since Figure 2 suggests that N2 abounds on the surface of 300-NCNT. As opposed to N1, which is ascribable to pyridinic-N, this feature embraces a set of surface species. In general it can be stated that all identified functional groups during TPD having a N–H bond in common give rise to the N2 signal observed in the N1s spectrum of the NCNTs.

A peak at 401 eV in Figure 5.2 confirms the presence of quaternary nitrogen (N3) species. As evidenced by Figure 5.3, the N3 signal progressively decreases with increasing NH_3 treatment temperature. In a combined TP-XPS study performed by Arrigo et al. [96] it was shown that the maximum concentration of N3 species is reached at 300 °C, which corresponds to the NH_3 treatment temperature applied for the preparation of 300-NCNT. Accordingly, quaternary nitrogen (N3) is formed at the expense of pyridinic

(N1) species. In view of this, an increase of the N1 signal accompanied by a decrease of the N3 feature as observed in Figure 5.3 seems to be contradictory. However, the presence of O-containing functionalities like carboxylic acids or phenolic groups that are capable of forming hydrogen bridges with pyridinic-N forming pyridinium species induce a quaternary-N type of arrangement (Scheme 5.5) [215]. TPD experiments confirmed a gradual removal of phenolic groups from 300-NCNT to 700-NCNT, consequently decreasing the amount of potential sites capable of creating hydrogen bonds. Thus, the amount of pyridinic-N increases to the same extent as the concentration of pyridinium species decreases. Therefore, the N3 signal contains information about substitutional nitrogen and protonated pyridinic-N.



Scheme 5.5: Pyridinic-N (1) exhibiting configuration of quaternary nitrogen (2) induced by H-bonding with adjacent phenolic group.

As evidenced by the absence of spectral features in Figure 5.2 above 403 eV, no species containing nitrogen-oxygen bonds like pyridine-oxide or nitro groups are present on any of the NCNTs. In contrast to observations made by other investigations [97, 214], no nitrogen-functional groups were incorporated into the carbon backbone of HP-CNT in the course of the liquid phase oxidation *via* nitric acid treatment (N1s spectrum not shown).

5.3.3.2. O1s Core-Level Spectrum

Assignments of the chemical bonds constituting the O1s core-level spectrum are not as straightforward as in the nitrogen case. In spite of the reigning controversy, the following BE regions will be considered for the ongoing discussion [97]: C=O bonds in a highly conjugated form as in pyridone species (O1) is found at 530.7 eV; C=O bonds (O2) are located in the range between 531.1 and 531.8 eV; C–O bonds in ether-like oxygen (O3, O4) give rise to a signal near 532.6 eV; C–O bonds in hydroxyl groups (O5, O6) are considered as the origin of a peak at 533.5 eV. The BE range between 532 and 533 eV has been likewise attributed to carboxylic acid species (O3, O4) owing to their intermediate

nature oscillating between a single and a double bond [216]. Marchon et al. [217] have shown that adsorbed water on oxidized carbon materials gives rise to a broad O1s peak centered at 533 eV. Adsorbed water and/or oxygen (O7) being responsible for a spectral feature near 535.2 eV is a debatable assignment. Shifts towards high binding energies can be alternatively explained in terms of differential charging [218]. This phenomenon is observed in functionalized samples without sufficient metallic conductivity that are capable of transporting the photoelectrons over the entire sample avoiding the formation of potential drops [100].

Figure 5.4 displays the deconvoluted O1s difference photoelectron spectra of the oxygen and nitrogen modified carbon nanotubes. The application of this analytic method is insofar advantageous since it can be related to changes observed in the CO₂ and CO profile of the samples in the course of the TPD investigations.

The difference spectrum derived between O-CNT and 300-NCNT can be mathematically fitted with four different peaks. According to the previous BE considerations, one type of carbon-oxygen double bond (O2 – 531.4 eV) and two types of carbon-oxygen single bonds (O4 – 532.6 eV, O6 – 533.6 eV) are detected in a 1:2 ratio. According to the TPD experiments, carboxylic acids completely disappear after functionalization at 300 °C, whereas anhydrides and lactones are partly removed. Likewise, the amount of ketone/quinone species is reduced as evidenced by the intensity decrease in the high

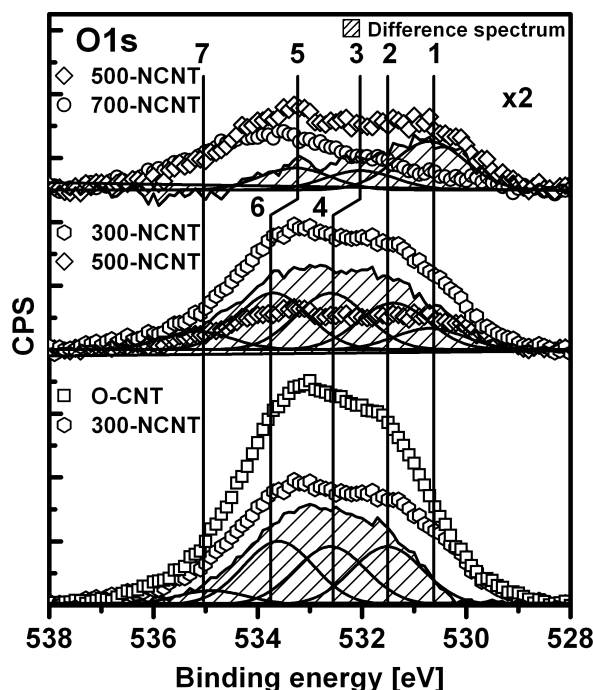


Figure 5.4.: Deconvoluted XP O1s difference spectra (hatched areas) of (a) O-CNT/300-NCNT, (b) 300-NCNT/500-NCNT and (c) 500-NCNT/700-NCNT. Dotted lines represent the background corrected experimental data.

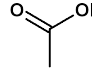
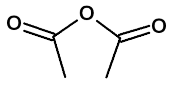
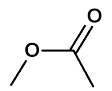
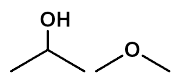
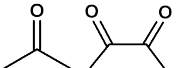
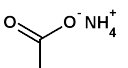
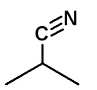
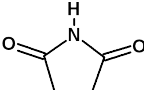
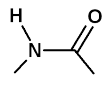
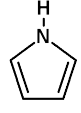
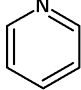
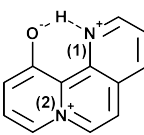
temperature regime of the CO profile. Chemical shifts in conjugated carbonyl compounds range between 531.0 and 531.9 eV [219, 220], supporting the assignment of 531.4 eV to ketone moieties. All afore-mentioned surface functionalities contribute to the O2 signal. Phenolic species (O6) and ether-like oxygen (O4) are present on O-CNT to a significant higher extent than on 300-NCNT as reflected by the intense peaks in the difference XP O1s spectrum, which is consistent with the larger amounts of CO evolving in the range between 600 and 800 °C during TPD. Carboxylic acids should be considered as an important component contributing to the O4 signal. This is supported by the full disappearance of the feature in the corresponding CO₂ profile of 300-NCNT. Furthermore, it has to be taken into account that a lower amount of ether-like oxygen (O4) is present on 300-NCNT compared to O-CNT since the NH₃ treatment leading to the formation of nitrogen species like lactams and imides strongly reduces its availability on the carbon surface.

In addition to the features discussed before, one more component is needed to deconvolute the difference spectrum between 300-NCNT and 500-NCNT. O1 (530.7 eV) is assigned to C=O double bonds that are constituent elements of lactam/pyridone or quinone species. As discussed for the N2 signal in the N1s core-level spectrum, imide species are the dominant functional groups in 300-NCNT. Since O1 scales with the N2 feature, it is assumed that the component at 530.7 eV is likewise a C=O vicinal to a nitrogen atom in imides. As expected from the different intensities in the CO TPD profiles, 300-NCNT contains more phenolic (O6) and ether-like (O4) species compared to 500-NCNT. In consequence to the complete absence of carboxylic acid groups, the contribution to the O2 signal arises from the larger amounts of anhydrides and lactones on 300-NCNT.

According to the third difference spectrum in Figure 5.4, only three components are needed for a proper description. As confirmed by the presence of O1, lactams are present on 500-NCNT. This could be related to the sharp CO peak at 800 °C. In contrast, O2 is not observed even though the CO₂ profile of 500-NCNT shows a contribution in the lactone regime. This might be an indication for a decarboxylation rearrangement reaction. One interesting finding is the respective shift of O4 to O3 and O6 to O5 towards lower binding energies. O3 (532.0 eV) has been attributed to ether-like oxygen and O5 (533.3 eV) to OH species that are arranged in a more thermally stable configuration due to the increased graphitic character of the carbon surface.

As displayed in the XP O1s difference spectra, the intensity of O7 decreases until no contribution is observed. This is in conformity with the concentration reduction of heteroatoms on the carbon samples as a function of temperature in addition to the thermally induced improvement of the graphitic character and the changes of the electronic properties associated with the presence of “graphitic” nitrogen species. This reduces the formation of potential drops arising from differential charging.

Table 5.3.: Decomposition products, TPD temperature peak maxima and XP O1s/N1s contributions characteristic of O- and N-containing functional groups present on oxidized and N-doped CNTs.

Functional group		TPD		Comments	XPS
Structure	Name	Products	T _{Max} [°C]		
	Carboxylic acid	CO ₂	275	-	O2 & O4
		H ₂ O	275	Recombination of neighboring -COOH groups	
	Cyclic anhydride	CO ₂	435	Subsequent decomposition mechanism	O2
		CO	460		
	Lactone	CO ₂	661	-	O2
	Phenol, Ether	CO ₂	735	Temperature range: 600-850 °C Recombination of adjacent -OH species	O6 (O5), O4 (O3)
		H ₂ O	275		
	Ketone, Quinone	CO	920	-	O1 & O2
	Ammonium salt	H ₂ O	200	Dehydration leading to nitrile groups	-
	Nitrile	HCN	250	Pyrolysis product of benzonitrile	-
	Imide	CO ₂	450	Decarboxylation of phthalimide to benzonitrile with subsequent decomposition to HCN	N2
		H ₂ O	500		
		HNCO	510	Pyrolysis product of succinimide	
	Lactam (Pyridone)	HCN	680	Pyrolysis products of 2-pyridone	N2 & O1
		HNCO	725		
		CO	800	Decarbonylation to pyrrole	
	Pyrrole	HCN	785	Pyrolysis products of pyrrole	N2
		H ₂	805		
	Pyridine	HCN	905	Pyrolysis products of pyridine	N1
		H ₂	920		
	Quaternary nitrogen	-	-	Substitutional N (2) and protonated pyridinic species (1) formed <i>via</i> H-bonding with nearby located OH groups	N3

Decomposition products detected during TPD investigation and signals applied for the deconvolution of XP spectra required for the identification of nitrogen and oxygen functional groups present on the surfaces of oxidized and N-modified CNTs are summarized in Table 5.3. Since various types of surface species decompose to the same volatile compound, it is imperative to have knowledge of the respective temperature peak maxima.

Similarly, XPS data has to be interpreted with care since one binding energy can be attributed to more than one type of functional group.

The elemental composition of the modified carbon nanotubes as determined by XPS is summarized in Table 5.4. Whereas the liquid phase oxidation in refluxing nitric acid yields an oxygen concentration of around 13 at.%, this value is drastically reduced to about 2.0 at.% after NH_3 treatment at 700 °C. On the contrary, the amount of nitrogen ranging between 2.6 and 3.4 at.% is nearly independent from the functionalization temperature. These results are in line with those obtained from elemental analysis (Table 5.1). Similarly, the increasing N/O ratio as a function of treatment temperature indicates a progressive increment of the nitrogen fraction that is directly bound to the carbon backbone. This is reflected by the dominating presence of pyrrolic, pyridinic, and quaternary N-species in 700-NCNT in contrast to the samples modified at lower temperatures.

Table 5.4.: Elemental composition as determined by XPS.

Sample	N [at %]	O [at %]	C [at %]	N/O
O-CNT	-	13.0	87.0	0.00
300-NCNT	3.4	7.1	89.5	0.48
500-NCNT	3.3	3.0	93.8	1.10
700-NCNT	2.6	2.0	95.4	1.30

5.3.4. Acid-base properties in the Aqueous Phase

Titration curves were recorded for the pristine, oxidized and ammonia treated samples in order to investigate the impact of chemical modification on the acid-base properties. Figure S5.2a shows the state of the pristine carbon nanotubes and the effect arising from oxidation in concentrated nitric acid. The starting pH of HP-CNT is around 7, which is indicative for the neutral character of the surface. Furthermore, the lack of an inflection point serves as an evidence for the negligible concentration of acidic species. In agreement with the steps observed in the CO_2 profile obtained in the course of the TPD experiment, a large amount of carboxylic acid entities and cyclic anhydrides are present on the surface of O-CNT. This is in line with the strong increase in acidity after nitric acid treatment, which is reflected in a low initial pH of about 3.5. According to the 1st derivative of O-CNT shown in Figure S5.2a, at least two different types of acid sites are neutralized. Acid dissociation constants (pK_a) were experimentally derived from the titration curves by determining the pH at the corresponding half-equivalent points. Both species exhibit a middle-strong acidity as reflected by pK_a values of 4.0 and 6.2, respectively (Table 5.5). The total amount of sites calculated at the equivalent point equals $630 \mu\text{mol}\cdot\text{g}_{\text{Sample}}^{-1}$. This value is clearly lower than the amount of CO_2 released during TPD

experiments. However, a more convenient comparison can only be performed if the CO_2 molarity is related to the sample mass before rather than after the TPD experiment. The aforementioned consideration leads to a specific molar concentration of $705 \mu\text{mol}\cdot\text{g}_{\text{Sample}}^{-1}$. Both values are in excellent agreement with each other, indicating that the acidic character is predominantly determined by carboxylic acids and cyclic anhydrides.

As depicted in Figure S5.2b, the acid-base properties are reverted after nitrogen incorporation *via* ammonia treatment. In spite of the significant differences observed between the nitrogen doped samples in the TPD experiments, the corresponding titration curves are rather similar. This is especially applicable for 300-NCNT and 500-NCNT. In both cases the initial pH is around 7.3, which is similar to the value obtained for HP-CNT. Contrary to the pristine carbon nanotubes, the titration curves belonging to these samples exhibit an inflection point, from where the amount of neutralizable sites can be derived. The values thus obtained are respectively in the range of $110\text{--}120 \mu\text{mol}\cdot\text{g}_{\text{Sample}}^{-1}$. Slightly increased basicity can be appreciated in the case of 700-NCNT as evidenced by an initial pH close to 8. This observation is in line with the results obtained in the TPD experiments. Most of the nitrogen present is in form of pyridinic species, being in nature the most basic type of N-containing functional groups. In contrast to 300-NCNT and 500-NCNT, the inflection point of this sample has the largest shift towards higher volumes. The amount of titratable surface species is about $160 \mu\text{mol}\cdot\text{g}_{\text{Sample}}^{-1}$, corresponding to the highest value obtained for the nitrogen-doped samples. However, the pK_b values derived from the half-equivalent points slightly differ from each other, lying between 7.2 and 7.5. This similarity is most likely due to the variety of surface species present on the carbon surface. Whereas imides and lactams prevail on 300-NCNT, pyrrolic and pyridinic nitrogen dominate to different extents on the samples treated in ammonia at higher temperatures. The acid-base character of these functional groups strongly differ among each other, wherefore the overall behavior of the nanostructured material in aqueous phase is determined by the extent to which nitrogen in different configurations is attached to or incorporated into the carbon framework. It is noteworthy to mention that solvation effects have a strong influence on the behavior of surface species, wherefore a discrepancy between liquid and gas phase can be expected.

Table 5.5.: Quantities derived from potentiometric pH titrations.

Sample	Initial pH	Acid sites [$\mu\text{mol}\cdot\text{g}_{\text{Sample}}^{-1}$]	Basic sites	pK^1
O-CNT	3.5	630	-	4.0, 6.2
300-NCNT	7.3	-	110	7.2
500-NCNT	7.4	-	120	7.3
700-NCNT	7.7	-	160	7.5

¹ pK_a in case of O-CNT and pK_b for NCNT samples

5.3.5. Catalytic Transformation of 2-Propanol

Catalytic experiments based on the conversion of 2-propanol were performed over the N-modified CNTs in order to elucidate their differences in terms of acid-base properties. The sensitivity of this approach is associated with the specificity of the reaction pathways. Isopropanol is converted to propylene and diisopropyl ether over Brønsted acid centers, whereas its dehydrogenation takes place on Lewis acid-base pairs yielding acetone [120].

Figure 5.5 displays the conversions, selectivities and carbon balances obtained during the conduction of the probe reaction over the NCNT samples. 300-NCNT exhibits an acid-base bifunctional surface as evidenced by selectivities towards dehydration and dehydrogenation products in a 1:1 ratio at 200 °C (Figure 5.5a). With increasing temperature the dehydration pathway is favored since the acetone selectivity falls from 50 % at 200 °C to 5 % at 300 °C. Differences are also observed with respect to the olefin and ether formation. Propylene is preferentially produced instead of diisopropyl ether. Whereas the selectivity of the latter drops from initially 10 % at 200 °C to nearly zero percent at 300 °C, the former is obtained with more than 90 % at the highest reaction temperature. Based on the results obtained by TPD and XPS, imides are the dominating species in 300-NCNT, whereas pyridinic nitrogen is present to a lower extent. In view of the free electron pair, the latter can act as a Lewis base. Such sites are needed in order to dehydrogenate the secondary alcohol to acetone [119]. Since the amount of oxygen is about 7 at.% according to XPS, the Lewis basicity of surface oxo (O^-) and superoxo (O^{2-}) ions present on the carbon surface should be considered [120]. Imides species possess an enhanced N–H acidity associated with the negative inductive effect of the carbonyl groups next to the nitrogen atom. Thus, the dehydration activity of 300-NCNT most likely arises from the acidic character of these species.

A drastic change is observed when the transformation of 2-propanol is carried out over 500-NCNT (Figure 5.5b). Although the selectivity towards propylene increases with temperature reaching a maximum value of 15 %, the major product is acetone. No diisopropyl ether was detected indicating a change in the distribution of Brønsted acid centers. The nature of the surface differs from that of 300-NCNT since lactam/pyridone species as well as pyrrolic-like nitrogen are attached to the carbon backbone. In terms of conversion, 300-NCNT is about five to six times more active than 500-NCNT in spite of comparable nitrogen concentrations detected on both samples. This could be related to differences in the number of active centers and/or changes of their intrinsic activities. Certainly, 300-NCNT contains more oxygen functional groups than 500-NCNT. Cyclic anhydrides, which are hydrolyzed in the presence of H_2O , can further contribute to the acidic character of 300-NCNT. Thus, in case of 500-NCNT, the dehydration activity

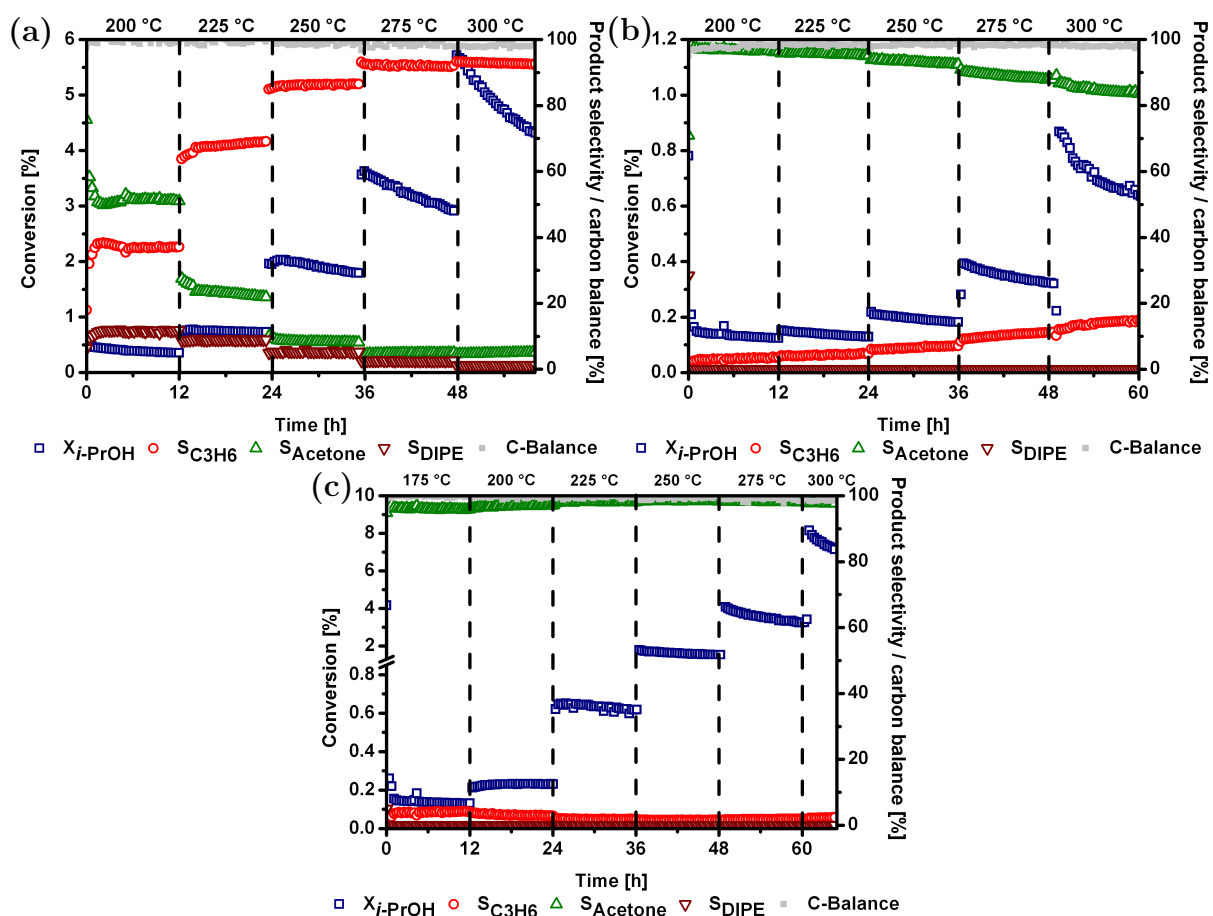


Figure 5.5.: Conversions and selectivities as a function of time on stream obtained at five different temperatures during the catalytic decomposition of 2-propanol on (a) 300-NCNT, (b) 500-NCNT and (c) 700-NCNT. Samples were previously treated at 350 °C in N_2 for 2h.

yielding propylene might be ascribed to the presence of lactams, while the dehydrogenation of 2-propanol most likely takes place over pyridinic species.

As derived from TPD and XPS investigations, 700-NCNT exhibits the highest abundance of pyridinic species. Complemented by the results obtained by elemental analysis, the amount of oxygen is strongly reduced to around 1.6 wt%. According to TPD, practically no CO_2 is detected while only a low amount of CO is observed. Figure 5.5c displays the time-on-stream conversions and selectivities of 700-NCNT. In contrast to the samples functionalized at 300 and 500 °C, the carbon surface of this material exhibits the most defined basic properties as reflected by acetone selectivities of at least 95 %. Similar to 500-NCNT, the only dehydration product formed was propylene. Interestingly, 300-NCNT being the only sample containing imide species produces diisopropyl ether.

Correlations between the acid-base characteristics of strontium based oxide catalysts derived from adsorption experiments employing basic probe molecules and the

dehydrogenation-to-dehydration-ratio in the catalytic transformation of 2-propanol suggest that the aforementioned ratio can be used as a measure for the basicity of a catalytic system [221]. In contrast, acidity correlates with the activity of 2-propanol towards dehydration products[180]. These quantities, which are summarized in Table 5.6, have been derived for the N-doped CNTs at isoconversion. Areal formation rates of propylene and diisopropyl ether decrease by a factor of 50 from $5.52 \cdot 10^{-10}$ to $0.11 \cdot 10^{-10}$ $\text{mol} \cdot \text{m}^{-2} \cdot \text{s}^{-1}$ with increasing NH_3 treatment temperature, indicating a strong decrease in surface acidity. Consistently, the ratio r_A/r_{P+DIPE} used as a measure for the basicity significantly increases from 0.28 to 54.41. These trends are evidently in line with the nature of species dominating the surfaces of the investigated samples. As has been stated before, pyridinic nitrogen acting as Lewis basic centers necessary for the acetone formation are the dominating species present on 700-NCNT, whereas imides being more acidic in nature prevail on 300-NCNT.

As can be observed in Figure 5.5, the conversion of 2-propanol decreases with time on stream at higher reaction temperatures. This deactivation phenomenon is generally related to the depletion of active sites in the course of the reaction and/or the irreversible adsorption of species on catalytic centers. Samples were investigated by elemental analysis after reaction in order to address this issue. The corresponding results are listed in Table S5.1. A comparison to the elemental composition after modification reveals that only 300-NCNT has 0.3 wt% less nitrogen after the catalytic transformation of 2-propanol. This reduction is most likely related to the pretreatment in N_2 at 350 °C, which is slightly higher than the functionalization temperature. In line with the thermal stability of the functional groups as reflected by the TPD results, 500-NCNT and 700-NCNT exhibit the same nitrogen amounts. Within the deactivation context it becomes evident that the reigning phenomenon is the irreversible adsorption of molecules on the carbon surface. This is further supported by the increased amount of oxygen after reaction. Besides the adsorption of 2-propanol in form of an isopropoxide species, acetone may be likewise irreversibly bound to nitrogen species. The oxygen present in both compounds might be the origin for the increased concentration. Consistently, between three to five times more hydrogen is found on the samples after reaction. Either C–H bonds as constituent fractions of

Table 5.6.: Product selectivities at isoconversion, basicity (acetone-to-dehydration-products ratio) and acidity (formation rate of dehydration products) of NCNTs determined by the transformation of 2-propanol.

Sample	T ¹ [K]	X _{i-PrOH} [%]	S _P ² [%]	S _A ³ [%]	S _{DIPE} ⁴ [%]	r _{P+DIPE} 10 ⁻¹⁰ [mol·m ⁻² ·s ⁻¹]	r _A 10 ⁻¹⁰ [mol·m ⁻² ·s ⁻¹]	$\frac{r_A}{r_{P+DIPE}}$
300-NCNT	225	0.73	69.1	21.9	9	5.52	1.55	0.28
500-NCNT	300	0.63	14.9	83.6	0	0.9	5.07	5.61
700-NCNT	225	0.62	1.8	98.2	0	0.11	5.87	54.41

¹ Temperature of isoconversion ² P: Propylene ³ A: Acetone ⁴ DIPE: Diisopropyl ether

adsorbed species or irreversibly bound H_2 resulting from the 2-propanol dehydrogenation might be reasons for this observation.

5.3.6. Oxidative Stability of N-Doped Carbon Nanotubes

Insights into the degree of graphitization and availability of defect sites serving as centers at which the combustion is preferably initiated can be obtained by subjecting the material to temperature-programmed oxidation (TPO) experiments. Thermogravimetry (TG) is a suitable technique for understanding the combustion stages and differential-scanning calorimetry (DSC) provides integral heats released in the course of the carbon oxidation. Coupling these methods with online gas analysis permits to monitor the combustion products evolving during the experiments.

Figure 5.6 displays the TG curves and DSC signals of the pristine, oxidized and nitrogen-doped carbon nanotubes obtained during TPO in synthetic air. From this experimental data, information about the (extrapolated) onset oxidation temperature, the T_{50} value representing the temperature at which 50 % of the initial mass has undergone combustion and the overall heat of oxidation can be derived. The determined values are summarized in Table S5.2. As indicated by the extrapolated onset temperatures, HP-CNT and 700-NCNT possess the highest stability against thermal oxidation. After the pristine material is oxidized in nitric acid, the corresponding value is lowered by 26 °C. XPS, TPD and elemental analysis showed that the amount of oxygen significantly increases after the wet chemical treatment introducing various types of surface species strongly differing from each other in terms of thermal stability. In fact, the TG curve of O-CNT begins to drop already at around 200 °C, which is far before the carbon oxidation begins. This mass reduction is associated with the thermal decomposition of the functional groups. In case of 300-NCNT, the extrapolated onset temperature is similar to the value encountered for the oxidized sample. However, the T_{50} value is lowered by 10 °C, indicating that the combustion occurs faster after nitrogen incorporation despite a comparable stability against oxidation. The properties of the carbon surface are further deteriorated when the ammonia treatment is performed at 500 °C. Both T_{Onset} and T_{50} determined for 500-NCNT are lower by almost 20 °C compared to 300-NCNT. However, a significant improvement is observed for 700-NCNT, which exhibits the highest extrapolated onset temperature of the series reaching almost 570 °C. No difference is found between the T_{50} values of HP-CNT and 700-NCNT

A good agreement is found between the T_{50} values and the position of the peak maximum in the DSC curves ($T_{Max,DSC}$). This result can be expected since the maximum rate of combustion represented in the mass consumption by the inflection point (T_{50} value) should

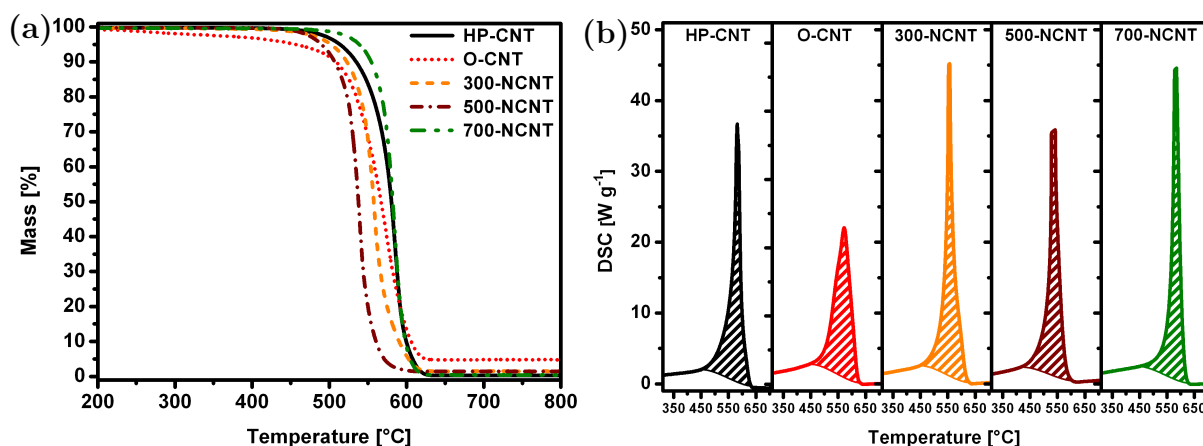


Figure 5.6.: Thermogravimetric changes (a) and DSC signals (b) during temperature-programmed oxidation of pristine, oxidized and ammonia treated carbon nanotubes.

be in correspondence with the maximum rate of heat evolution. The integral heats of combustion of the carbon nanotubes calculated from the DSC range between -294 and -352 $\text{kJ}\cdot\text{mol}_\text{C}^{-1}$, which are in good agreement with those obtained for charcoals [222, 223] and soots [224]. For comparison, a heat of combustion of -394 $\text{kJ}\cdot\text{mol}_\text{C}^{-1}$ has been determined for the oxidation of graphite [225]. An interesting value is the full-width at half maximum (FWHM_{DSC}) of the combustion peak in the DSC curves. The steeper the mass loss in the TG curves, the lower the value of FWHM_{DSC}. Based on this observation, it can be stated that the combustion of HP-CNT, 300-NCNT and 700-NCNT occurs faster than in the remaining samples. While 500-NCNT oxidizes slower, the combustion of O-CNT requires a longer period of time. The observations in the latter case suggest that the lower oxidative stability is related to the introduction of defects, which is also reflected in the increase in micropore area (Table 5.1), whereas the slow combustion originates from the oxygen species serving as a passivation layer.

For a better understanding in the case of the nitrogen-doped samples, it is important to analyze the differences in the profiles of volatile combustion products. Figure S5.4 shows the recorded CO_2 ($m/z=44$) and NO_x ($m/z=30$) traces obtained during the TPO experiments. The first evident result is that carbon dioxide is by two orders of magnitude the major product. No NO_x evolution was observed for HP-CNT and O-CNT. The small contributions seen in the corresponding profiles are rather attributed to an overlap arising from $m/z=29$, which is a fraction in the MS pattern of CO_2 that may partially overlap with $m/z=30$. With respect to the nitrogen-doped carbon nanotubes, the mass traces ascribed to NO_x significantly differ from the CO_2 profiles, wherefore an overlap can be discarded. The values determined for T_{50} and $T_{\text{Max.DSC}}$ are in excellent correspondence with the temperatures of the maxima determined in the CO_2 curves. This is likewise applicable for the NO_x traces. An interesting finding is the shoulder observed in 300-NCNT

and 500-NCNT located at 490 °C. A corresponding feature is neither found in the CO₂ profiles nor in the NO_x evolution of 700-NCNT. The main difference observed between the synthesized NCNTs in terms of N-containing functional groups is that 700-NCNT only contains nitrogen atoms incorporated into the carbon lattice in form of substitutional species or at the edges as pyrrolic and pyridine-like N, whereas 300-NCNT and 500-NCNT also contain nitrogen atoms that are part of a structure that is attached to the carbon backbone. As has been so far discussed, these species are imides and lactams, both exhibiting a thermal stability below 750 °C. Hence, the shoulder characterized by an onset near 450 °C is associated with the decomposition of these species. This leads to an increase in the defect density lowering the (extrapolated) onset temperature. In addition, less oxygen is present on these samples compared to O-CNT, eliminating thereby the passivation effect, which consequently accelerates the carbon combustion. In line with this argument, the exclusive presence of structurally more stable nitrogen species in 700-NCNT lowers the amount of defect sites, consequently increasing the onset temperature to a value comparable to that of the pristine material. In fact, a superposition of the CO₂ and NO_x profiles indicate that these compounds evolve at the same time, indirectly confirming the XPS and TPD results.

5.4. Conclusion

Nitrogen functionalized CNTs synthesized by posttreatment of OCNTs in ammonia at 300, 500, and 700 °C have been investigated with a set of complementary surface sensitive characterization techniques. Both abundance and type of oxygen and nitrogen functional groups were assessed by TPD and XPS. Profiles of volatile compounds like CO₂ and CO clearly confirm the presence of carboxylic acids, acid anhydrides and lactones in addition to phenols, esters and carbonyl species. Their availability on a carbon surface is a key factor since they serve as reaction centers for NH₃ leading to successful nitrogen incorporation. Imides, which are formed by ring-opening of cyclic anhydrides in the presence of ammonia, have been identified as the major N-containing species at a treatment temperature of 300 °C. This is indicated by the evolution of HCN and HNCO at low temperatures. The assignment is additionally supported by the strong intensity of the N₂ signal at 399.8 eV and O₁ feature at 530.7 eV assigned to the C=O of pyridone-like species. A further increase in the functionalization temperature to 500 °C incorporates lactams and pyrrole-like nitrogen to a larger extent. The HCN profile is characterized by the evanescence of the imide contribution and appearance of an asymmetric peak at higher temperatures. A modification at 700 °C yields a surface containing pyrrole-like and pyridinic nitrogen, which was confirmed by the characteristic peaks in the HCN profile as well as the respective N₂

(399.7 eV) and N1 (398.4 eV) signals of N1s XP core level spectrum. Quaternary N-atoms already formed at low functionalization temperatures give rise to the N1s spectral feature at 401 eV (N3). Substitutional nitrogen and protonated pyridinic N-species formed *via* hydrogen bonding with nearby located OH groups contribute to the N3 signal.

While the acid-base properties of NCNTs seemed to be similar in the aqueous phase, significant differences were obtained in the gas phase as evidenced by the results derived from the catalytic transformation of 2-propanol. The ratio between the rates of formation of dehydrogenation and dehydration products used as a quantity to assess the basicity increased from 0.3 to 54.4 as a function of NH₃ treatment temperature. Furthermore, the parallel formation of dehydration and dehydrogenation products reflects the acid-base bifunctional surface of 300-NCNT. On the contrary, an acetone selectivity of almost 100 % regardless of the reaction temperature for the sample obtained at 700 °C is characteristic for a carbon material with a defined surface basicity. Pyridinic species serving as Lewis basic sites were identified as part the active acid-base pair necessary for the 2-propanol turnover towards dehydrogenation products.

The resistance of NCNTs towards thermal oxidation strongly depends on the functionalization temperature. OCNTs, which serve as the starting material for nitrogen incorporation, are less stable than the pristine material. Similar properties were found for 300-NCNT. A surface modification at 500 °C is detrimental. In contrast, nitrogen incorporation at 700 °C yields a CNT material with a stability similar to that of the pristine carbon. This is related to the presence of nitrogen atoms that are incorporated into the carbon lattice.

The analytical approach presented in this work is suitable for linking the structural information of nitrogen species with the acid-base and oxidation properties of the modified surface resulting from the superimposed properties of the individual functional groups. Undoubtedly, these results allow a better understanding of the complex surface characteristics, which are important within the scopes of supported catalysts, acid-base and redox catalysis. Furthermore, this integral concept can be applied in order to investigate the impact of nitrogen incorporation on different types of carbon nanostructures including active carbon, carbon nanofibers, graphite or graphene.

5.5. Supporting Information

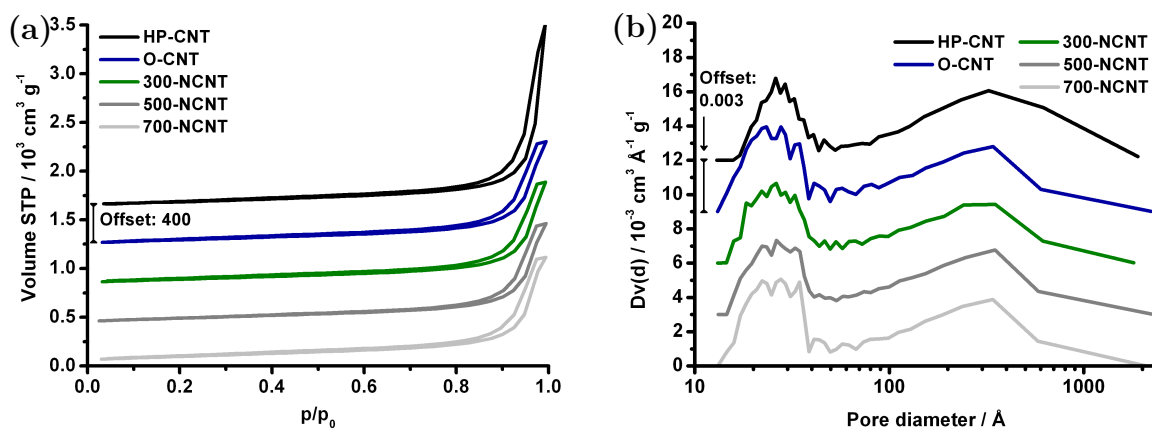


Figure S5.1.: (a) Nitrogen adsorption isotherms and (b) pore size distributions of pristine and functionalized CNTs.

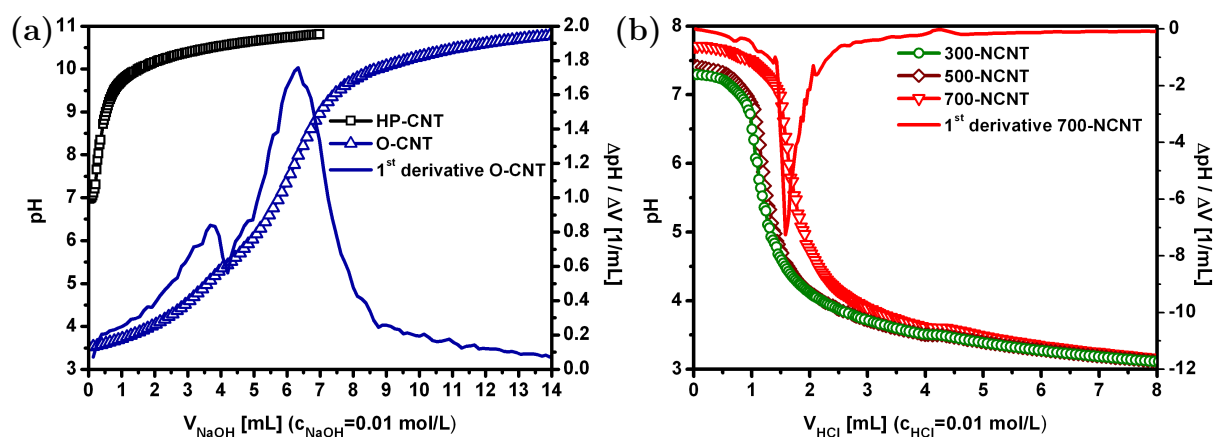


Figure S5.2.: Potentiometric pH titration curves of (a) HP-CNT before and after HNO_3 oxidation and (b) NCNTs obtained after NH_3 treatment of O-CNT at 300, 500 and 700 $^\circ\text{C}$.

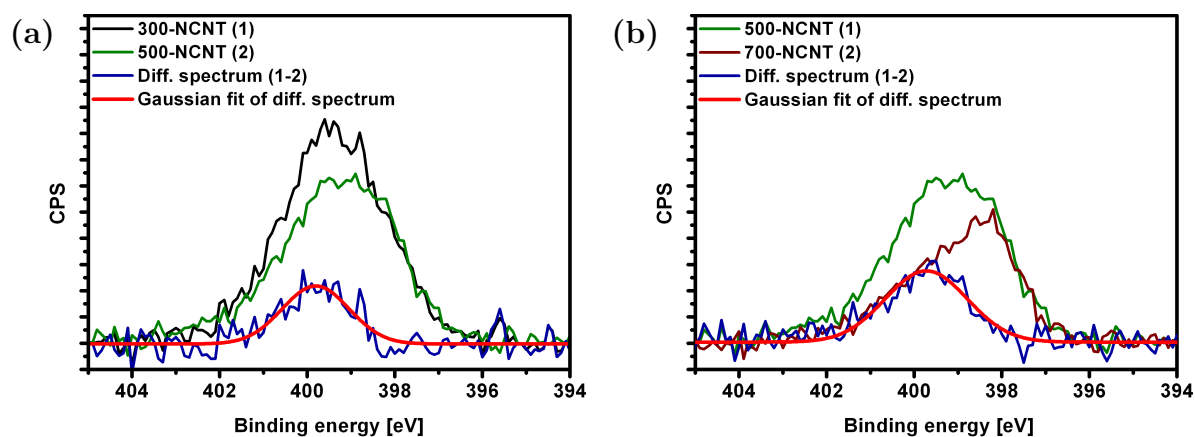


Figure S5.3.: XP N1s difference spectra of (a) 300-NCNT/500-NCNT and (b) 500-NCNT/700-NCNT.

Table S5.1.: Elemental composition of NCNTs after catalytic transformation of 2-propanol.

ID ^a	Sample	Description	Elemental analysis [wt%]			
			C	H	N	O ^b
17773	300-NCNT-A-ar	300-NCNT, after reaction	96.9	0.1	1.0	2.0
17772	500-NCNT-A-ar	500-NCNT, after reaction	96.0	0.1	1.2	2.7
17771	700-NCNT-A-ar	700-NCNT, after reaction	95.5	0.1	1.1	3.3

^a Internal sample number to distinguish reproductions of sample preparation

^b Oxygen is calculated as a difference to 100 %

Table S5.2.: Characteristic temperatures and heats of combustion derived from TG and DSC results.

Sample	T _{Onset} [°C]	T ₅₀ [°C]	T _{Max.DSC} [°C]	FWHM _{DSC} [°C]	ΔH _C [kJ/mol _C]
HP-CNT	564	580	582	25	-294
O-CNT	538	567	571	68	-352
300-NCNT	542	557	557	23	-349
500-NCNT	525	538	541	32	-322
700-NCNT	569	582	584	26	-331

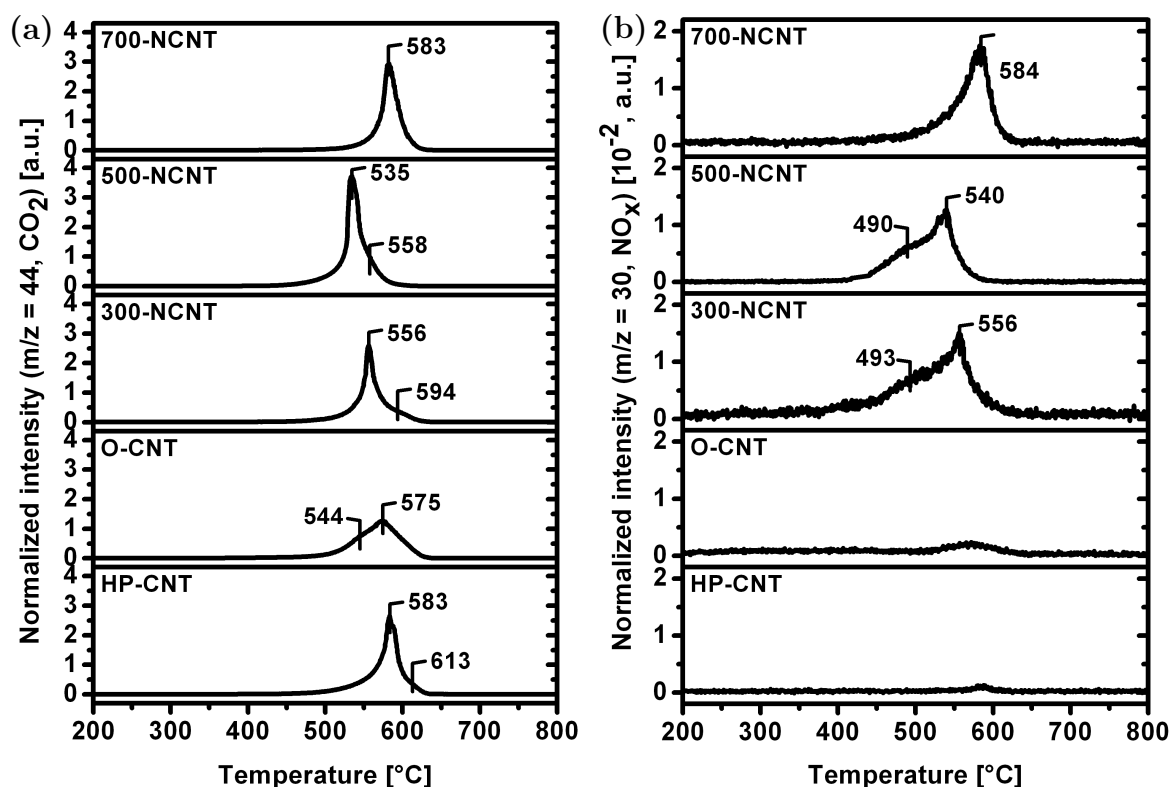


Figure S5.4.: Mass traces recorded during TPO experiments of HP-CNT, O-CNT and NCNTs. CO₂ [m/z = 44] (a) and NO_x [m/z = 30] (b) were normalized with respect to Ar [m/z = 40] and the employed sample mass.

6. Influence of thermal treatment on surface and oxidation properties of P-modified carbon nanotubes

K. Friedel Ortega, S. Wrabetz, A. Trunschke, and R. Schlögl

Abstract

Phosphorus doping of mesoporous nanocarbons has been scarcely reported in literature. Thus, P-modified CNTs obtained *via* postsynthesis activation with H_3PO_4 and subsequent thermal treatment at 400, 500, 600, and 700 °C in Ar were analyzed in terms of their chemical properties. Two types of phosphate species with different thermal stabilities were proven to be present on the CNTs by means of TPD. Their decomposition was pronounced at temperatures above 750 °C. Two characteristic pK_a values (3.3 and 6.8) comparable to those of phosphorus oxoacids were experimentally derived from potentiometric pH titrations. NH_3 -microcalorimetry evidenced the existence of two types of homogeneously distributed and energetically uniform acid sites reflected in the development of two plateaus with distinct differential heats of NH_3 adsorption. Increasing the treatment temperature from 400 to 500 °C reduces the overall amount of centers and simultaneously changes their acid strength. The initial differential heat of NH_3 -adsorption is lowered from 117 to 103 $\text{kJ}\cdot\text{mol}^{-1}$. Partial irreversible adsorption of ammonia is also confirmed by NH_3 -TPD. A selectivity of nearly 100 % towards propylene during the catalytic transformation of 2-propanol further confirmed the highly acidic character of P-CNTs prepared at 400 and 500 °C. Phosphorus incorporation enhances the oxidative stability as evidenced by a shift of the extrapolated T_{Onset} and the T_{50} value towards higher temperatures, simultaneously decreasing the specific heat of combustion. The well-defined acidity and the enhanced oxidative resistance enable the potential of using P-doped CNTs as solid adsorbents, as catalyst in ODH reactions and as electrode material in electrochemical applications.

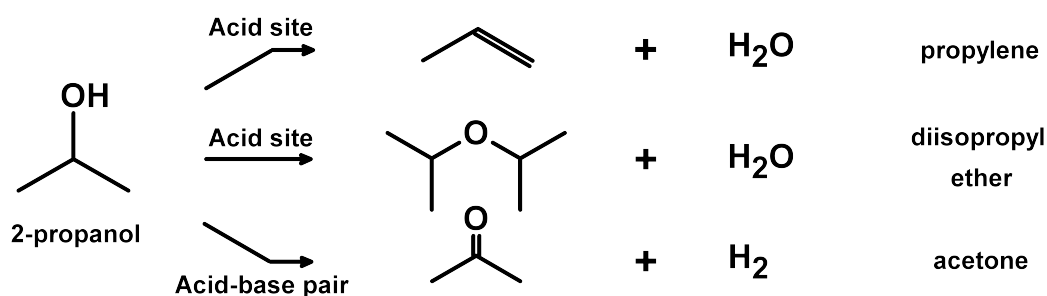
6.1. Introduction

Incorporation of heteroatoms into the framework of nanocarbons notably affects their physicochemical surface properties. Nitrogen functionalization changes the electronic structure by inducing a localized charge accumulation [97]. Furthermore, the presence of N-containing species alters the acid-base properties of the carbon material. Boron doping has attracted much attention in redox catalysis due to the particular electron-attracting nature of the element. For instance, boron species strongly reduce the formation of highly reactive oxygen intermediates like peroxide (O_2^{2-}) and superoxide (O_2^-) anions in the course of O_2 activation that favor the total oxidation of light alkanes during oxidative dehydrogenation (ODH) reactions [226]. In addition, boron-modified carbons exhibit an enhanced resistance towards oxidation since the heteroatom effectively blocks defect sites at which the combustion is preferably initiated [226–230]. Similar effects have been reported for phosphorus-modified carbons [227–229, 231–235]. XPS investigations carried out on materials obtained by activation of carbon precursors impregnated with H_3PO_4 [232, 234]. or $POCl_3$ [233] suggest that C–O– PO_3 and C– PO_3 surface species suppress the activation of O_2 towards electrophilic intermediates. Furthermore, the availability of phosphorus on nanocarbons induces a surface acidity associated with the presence of highly thermally stable phosphonic acids ($-PO_3H_2$), phosphonous acids ($-PO_2H_2$) and phosphine moieties [236].

P-modified carbons are often inexpensive and therefore attractive materials for water treatment since they exhibit an enhanced cation exchange capability towards heavy metals [237, 238]. Moreover, hydrogen can be effectively stored in phosphorus modified nanostructured carbons due to their high specific uptake capacity [239]. The adsorption properties are associated with the tunability of the porous structure and the chemical nature of the active surface [240]. Several synthesis methods have been applied for the production of phosphorylated carbon materials. A widespread technique involves the impregnation of a suitable carbon precursor, e.g. fruit stones [238], olive stones [130], and white oak [241] with a specific amount of phosphoric acid followed by a carbonization step at a given temperature either in air or in an inert gas atmosphere. Increasing the treatment temperature from 400 to 1000 °C leads to a volcano-type dependency of the phosphorus content in the prepared carbons reaching a maximum concentration of the heteroatom in the range between 7–9 % at 800 °C [242–244]. This is of particular interest since a linear correlation between the specific molar concentration of titratable sites and the phosphorus amount has been considered as indicative for the acidic nature of the surface arising from the phosphate structure of the anchored species [240]. Microporous carbons obtained by chemical activation of lignocellulosic waste with H_3PO_4 at 450 °C and 500 °C exhibit

a strong acidity as evidenced by NH_3 -TPD and a high selectivity towards propylene in the catalytic transformation of 2-propanol [130, 131]. However, studies dealing with the characterization of phosphorus modified mesoporous carbons have received considerably less attention [136]. To our knowledge, no systematic investigation exists involving the surface analysis of P-functionalized carbon nanotubes.

The aim of this work is to study the incorporation of phosphorus into the backbone of carbon nanotubes (CNTs) by activation with H_3PO_4 as a function of thermal treatment in the temperature range between 400 °C and 700 °C. Since the presence of the aforementioned heteroatom affects the acidity and oxidative stability of CNTs, a set of characterization techniques involving potentiometric pH titration, NH_3 -TPD, NH_3 -microcalorimetry, TPD, and TPO has been chosen in order to elucidate the surface properties of the modified samples. Furthermore, the employment of the catalytic transformation of 2-propanol is necessary since it shows a high sensitivity towards changes of the specific acid-base properties. According to Scheme 6.1, the secondary alcohol dehydrates to propylene and diisopropyl ether over Brønsted acid sites, whereas the presence of acid-base pairs leads to the dehydrogenation of the reactive molecule towards acetone.



Scheme 6.1: Reaction pathways associated with the catalytic transformation of 2-propanol [120].

6.2. Experimental section

6.2.1. Phosphorus modification of MWCNT

Multiwall carbon nanotubes (carbon content > 97 wt%) with 12.9 nm outer diameter and 4.7 nm inner diameter in average were obtained from Shangdong Dazhang Nano Materials Co., Ltd (C-CNT). 20 g of C-CNTs were pretreated in 1 L 30 % H_2O_2 solution at 60 °C for 4 h. After cooling down to room temperature, the oxidized sample was thoroughly washed and filtrated with Millipore water. Finally, the resulting carbon was dried at 110 °C in static air overnight (O-CNT). Phosphorus incorporation was carried out in two steps: O-CNTs were immersed and stirred in 1 L concentrated phosphoric acid (85 wt%) at

125 °C for 4 h. After cooling down to ambient temperature, the suspension was diluted with 1 L Millipore water and subsequently filtrated without further washing. 4 g of the impregnated powder were dried under reduced pressure at 100 °C prior to heat treatment in an inert gas stream. The vacuum-dried sample was transferred to a static tube furnace with an isothermal zone of nearly 15 cm determined at 1300 °C. Annealing was carried out respectively at 400, 500, 600, and 700 °C by passing an Ar stream at $100 \text{ mL}_n \cdot \text{min}^{-1}$ over a corundum crucible containing the carbon material. After flushing the furnace at ambient temperature for 30 min, the target temperature was reached at a heating rate of $10 \text{ }^\circ\text{C} \cdot \text{min}^{-1}$ and maintained for 4 h before cooling back to ambient temperature. Adsorbed species were removed by thoroughly washing the sample with Millipore water until achieving pH neutrality of the aliquot. After filtration, the modified sample was dried in static air at 110 °C overnight. P-functionalized carbons are labeled with the annealing temperature followed by the acronym PCNT.

6.2.2. Characterization techniques

Carbon materials were characterized by N_2 adsorption at liquid nitrogen temperature (-196 °C) using a Quantachrome Autosorb-6B KR instrument. Analyses were performed on 20 mg of powdered substance, which were degassed for 2 h at 200 °C before measurement. Surface area calculations were undertaken using the BET equation [156], pore size distributions were derived from the desorption branches of the isotherms according to the BJH method [157], and total pore volumes were determined at a relative pressure of $p/p_0 = 0.97$. Micropore analysis was performed by applying the MP-method proposed by Mikhail, Brunauer and Bodor using a statistical thickness interval of 0.05 [158].

Samples were investigated by potentiometric pH titrations carried out with a Mettler DL 77 autotitrator monitored by a Mettler Toledo DGi114-SC electrode. In a typical experiment, 100 mg of powdered sample were suspended in 50 mL of 0.1 M NaCl solution. Equilibration was achieved by vigorously mixing the suspension overnight. In order to minimize side effects from dissolved CO_2 , the mixture was degassed under Ar for 30 min prior to starting a measurement. The titrants used were 0.01 M NaOH and 0.01 M HCl solutions, depending on the samples to be investigated, respectively diluted from 1 M Titrisol standards (Merck Millipore).

Temperature-programmed desorption (TPD) and NH_3 -TPD were carried out in a home-built setup equipped with a gas chromatograph (Varian CP-4900 Micro-GC) and a mass spectrometer (Pfeiffer Omnistar) for on-line product analysis. Experiments were performed using a fixed-bed quartz reactor (9 mm i.d.), which was placed in a self-constructed furnace with an isothermal zone of 4 cm at the upper temperature limit. Weakly adsorbed water

was removed within 1 h at 100 °C in a He stream passed at a flow rate of 25 mL_n·min⁻¹. TPD investigations using 150 mg of functionalized samples were initiated by linearly heating the reactor at 5 °C·min⁻¹ to 1035 °C. This temperature was maintained for 30 min before cooling down to room temperature. NH₃-TPD analyses were performed as follows: the reactor loaded with 80 mg of carbon material was heated to 100 °C as previously described and subsequently cooled down to 80 °C. After stabilization of the adsorption temperature, a gas stream containing 1% NH₃ in Ar was passed for 15 min through the sample at flow rate of 25 mL_n·min⁻¹. Weakly bound ammonia was isothermally desorbed in a He flow until no NH₃ was detected by GC and MS analysis. Thereafter, the reactor was heated at 5 °C·min⁻¹ to 500 °C in a He stream of 25 mL_n·min⁻¹ and maintained at the target temperature for 30 min before cool down. Ammonia readsorption was performed using the same protocol as described before. Quantification of evolved NH₃ was achieved by calibration of the Micro-GC using a certified gas mixture containing 1% of the probe molecule in Ar.

For calorimetric measurements, a Calvet calorimeter (MS70 SETARAM) has been combined with a house-designed high vacuum system, which enables the dosage of probe molecules within a range of 0.02 μmol, described in detail elsewhere [245]. The pressure-controlled dosing systems with calibrated volume allows for the detection of the amount of adsorbed molecules (adsorption isotherm) as well as differential heat of adsorption and gives the possibility to elucidate the distribution of the adsorption sites along the range of adsorption heats. The samples were degassed (pretreated and activated under mild conditions to minimize thermal and mechanical stress) under vacuum at 80 °C overnight. The final pressure in the degassed cell was approximately 10⁻⁷ mbar. NH₃ was stepwise introduced into the evacuated cell at 80 °C, and the pressure evolution and heat signal were recorded for each dosing step. After reaching the saturation concentration the adsorbed NH₃ molecules were desorbed by evacuation at adsorption temperature 80 °C. Subsequently, a 2nd adsorption cycle was performed under identical conditions in order to evaluate the reversibility of the adsorbed NH₃ molecules. We have adopted the calorimetric sign criterion (positive energetic quantity for an exo-thermic process).

Temperature-programmed oxidation (TPO) experiments were performed in a TG-DSC Netzsch STA 449C Jupiter thermobalance coupled to a Pfeiffer Omnistar mass spectrometer for simultaneous gas analysis. DSC curves recorded during TPO gave the enthalpies associated with the thermal oxidation of the carbon samples. In a typical run, 5 mg of sample were loaded in an Al₂O₃ crucible, which was heated at 5 °C·min⁻¹ from room temperature to 950 °C in synthetic air (21 % O₂ in Ar) at a flow rate of 100 mL_n·min⁻¹. The maximum temperature was maintained for 30 min before cooling down the system to room temperature.

Scanning electron microscopy was employed for analyzing the elemental distribution using a Hitachi S-4800 (FEG) equipped with an energy dispersive X-ray sapphire detector, type EDAX Genesis 4000 system. Elemental maps were collected for a time frame of 1 h applying an acceleration voltage of 10 kV. Quantitative analysis of C, O and P were carried out based on the respective K_{α} lines.

For the transformation of 2-propanol, $100 \text{ mL}_{\text{n}} \cdot \text{min}^{-1} \text{ N}_2$ was passed through a saturator at $20 \text{ }^{\circ}\text{C}$ (4.2 % isopropanol) before reaching a U-shaped quartz reactor with an inner diameter of 9 mm containing 50 mg of catalyst material previously sieved to a fraction between 250 and 355 μm . Prior to the measurements, the samples were heated in N_2 to $350 \text{ }^{\circ}\text{C}$ at $5 \text{ }^{\circ}\text{C} \cdot \text{min}^{-1}$ for 2 h. Temperatures were varied in $25 \text{ }^{\circ}\text{C}$ steps from 200 to $275 \text{ }^{\circ}\text{C}$ at constant inlet flow rate, whereby every set of parameters remained unchanged for a period of 12 h. The conversion of 2-propanol was calculated based on the ratio of product concentrations to amount of secondary alcohol fed into the reactor.

$$X_{i\text{-PrOH}} = \frac{\chi_{\text{Propylene}} + \chi_{\text{Acetone}} + \chi_{\text{Diisopropyl ether}}}{\chi_{i\text{-PrOH}}}$$

Selectivity is defined in molarity terms as the concentration of a given product to the sum of all detected products.

$$S_{\text{Product, i}} = \frac{\nu_i \cdot \chi_{\text{Product, i}}}{\nu_i \cdot \chi_{\text{Product, i}} + \sum \nu_j \cdot \chi_{\text{Product, j}}}$$

6.3. Results and Discussion

6.3.1. Textural properties and elemental composition

Pristine and P-modified CNTs were characterized in terms of their structural properties by N_2 adsorption-desorption experiments. Parameters deduced by this method are listed in Table 1. All isotherms are type III according to the IUPAC classification, which arise due to weak adsorbent-adsorbate and significant adsorbate-adsorbate interactions [168]. Evolution of a type H3 hysteresis loop associated with capillary condensation is indicative for the

Table 6.1.: Textural properties and elemental composition of pristine and P-modified CNTs.

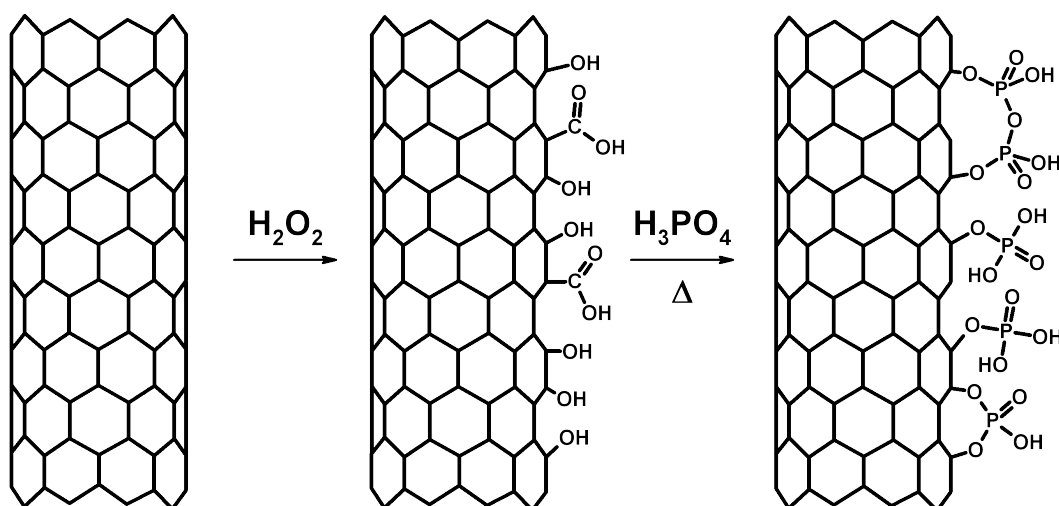
ID ^a	Sample	S_{BET} [$\text{m}^2 \text{ g}^{-1}$]	S_{Micro} [$\text{m}^2 \text{ g}^{-1}$]	V_{Tot} [$\text{cm}^3 \text{ g}^{-1}$]	V_{Micro} [$\text{mm}^3 \text{ g}^{-1}$]	Elemental analysis [wt %] ^b		
						C	O	P
14563	C-CNT	195	0	2.61	0	97	3	0
17182	400-PCNT	199	0	1.73	0	92 ± 3.1	6.3 ± 1.2	1.4 ± 0.6
17183	500-PCNT	256	0	1.81	0	93.5 ± 0.2	5.6 ± 0.2	0.9 ± 0.0
17184	600-PCNT	275	0	2.00	0	95.7 ± 0.4	4.1 ± 0.4	0.2 ± 0.0
17185	700-PCNT	273	0	2.15	0	95.4 ± 0.2	4.0 ± 0.2	0.7 ± 0.0

^a Internal sample number to distinguish reproductions of sample preparation

^b Elemental composition is the average of 7 measured EDX spectra

mesoporous structure of CNTs (Figure S6.1a). BET surface areas significantly increase from 195 up to 270 $\text{m}^2\cdot\text{g}^{-1}$ upon carbon activation. As depicted in Scheme 6.2, C-CNT was initially subjected to H_2O_2 oxidation aiming a preferential generation of phenolic species. Such wet chemical treatments are known to open the CNTs by oxidizing their tips, which is typically reflected in an increase of specific BET surface area [246, 247]. However, the subsequent phosphorus incorporation has an opposite effect. 400-PCNT exhibits a value similar to the one determined for C-CNT, suggesting that surface functional groups created at the ends of the nanotubes hinder the transport of N_2 into the open cavities. They become accessible as the phosphorus content decreases, leading to higher BET surface areas. It should be pointed out that the performed phosphoric acid treatment has no effect on microporosity. Both micropore volume and surface area remain unchanged (Table 6.1). Nevertheless, total pore volumes are reduced upon carbon modification. While a value of 2.61 $\text{cm}^3\cdot\text{g}^{-1}$ was determined for C-CNT, 400-PCNT shows a significant reduction by more than 30 %. A progressive increase, resembling the changes of the BET surface area, is observed for this parameter. The bimodal pore size distributions calculated with the BJH method applied on the desorption branch of the isotherms are presented in Figure S6.1b. The feature centered at 2.7 nm is related to the inner channel of the nanotubes. The volume of these smaller pores increases from 0.03 to 0.1 $\text{cm}^3\cdot\text{g}^{-1}$. This trend supports the opening of the inner cavities as a consequence of the oxidative treatment. V_{Tot} is, however, primarily affected by the decrease of volume corresponding to the larger pores that are represented by the peak located at around 39 nm. This fraction of mesopores has been ascribed to the presence of voids in agglomerates formed between entangled CNTs [34]. Accordingly to the phosphorus content, the presence of phosphate species increases the interaction between nanotubes leading to a closer packing, consequently reducing the pore volume in the formed particles. This is further evidenced by the differences observed in the SEM micrographs presented in Figure S6.3B-F.

Upon hydrolysis of phenolic species with phosphoric acid molecules, various types of phosphates can be formed (Scheme 6.2). Possible configurations are hydrogen and dihydrogen phosphates as well as pyrophosphoric-like species. The latter may be created through recombination of neighbouring phosphates groups leading to H_2O elimination. In contrast to observations made on activated carbons obtained by carbonization of a precursor previously impregnated with phosphoric acid [134, 238, 244, 248], our results reveal that the P-content decreases with increasing temperature (Table 6.1). This tentatively suggests a superposition of two effects, namely phosphorus incorporation into the structure and modification of the exposed graphitic layers has been observed in literature during carbonization. As opposed to this, the activation of a preformed nanostructured carbons solely leads to a surface functionalization. Irrespective of this essential difference, H_3PO_4



Scheme 6.2: Formation of P-containing species upon H_3PO_4 activation of O-functionalized carbon nanotubes.

activation of CNTs results in a homogeneous phosphorus modification as evidenced by the energy disperse X-ray (EDX) elemental distribution obtained for 400-PCNT, shown in Figure S6.3A.

6.3.2. Analysis of functional groups by means of Temperature Programmed Desorption

The existence of phosphates covalently attached to the surface of the P-modified CNTs can be confirmed and discussed particularly in terms of CO evolution during TPD experiments. Microporous carbons obtained through activation of carbonaceous precursors in the presence of phosphorus compounds leads to the creation of highly stable surface species, which upon thermal decomposition yield CO with a maximum observed at around 830-930 °C [130, 233, 234, 249]. As displayed in Figure 6.1, the same pattern is encountered for P-containing CNTs prepared *via* postsynthesis activation with H_3PO_4 . Irrespective of the treatment temperature, CO starts to evolve at a slow rate beyond 500 °C. A shoulder located at 890 °C precedes the emergence of a distinctive and sharp feature centered at 940 °C, which is dominant in every profile. This finding is indicative for two types of functional groups differing among each other in terms of their thermal stability. According to previous studies [130, 233], the intense CO formation originates from the cleavage of C–O– PO_3 moieties, which may be arranged in various configurations as shown in Scheme 6.2. Pyrophosphoric-like structures as well as phosphates attached to the carbon backbone *via* two independent C–O bonds are expected to exhibit a higher thermal stability. Wu and Radovic [233] have stated that metaphosphates and C– PO_3 species, being stable up to 1000 °C, also exist on the carbon surface upon activation with a

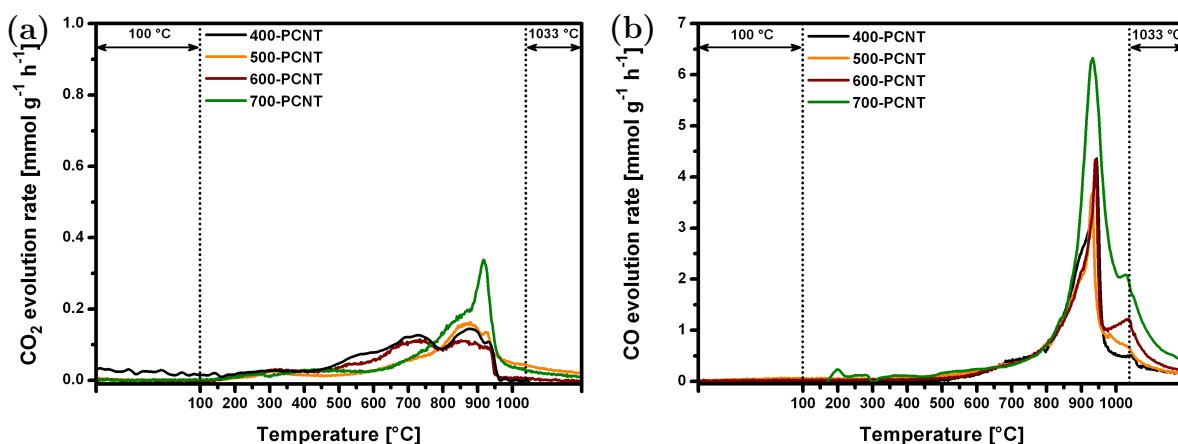
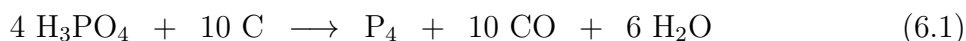


Figure 6.1.: Evolution of (a) CO₂ and (b) CO during TPD analysis of phosphorus containing carbon nanotubes.

phosphorus precursor.

As shown in Figure 6.1a, the presence of carboxylic acid species and cyclic anhydrides can be excluded owing to the absence of characteristic features in the CO₂ profiles located at 250 and 430 °C, respectively [172]. However, CO₂ evolution is observed beyond 800 °C, which is a considerably high and unexpected temperature. This might be a consequence of the thermal decomposition of stable $-\text{COO}-\text{PO}_3$ species [130]. Their existence is plausible considering the pretreatment of CNTs in H₂O₂, during which highly reactive peroxy radicals are formed that react with the carbon surface. Another source of CO₂ formation at high temperatures can be related to secondary reactions between CO evolving from the decomposition of phosphates and stable oxygen surface complexes [250].

Interestingly, 700-PCNT exhibits the most intense and broadest CO peak within the prepared series. Certain thermodynamic considerations have to be made in order to plausibly explain this encountered difference. The integral free Gibbs energy of reactions 6.1 - 6.3, which may occur during the functionalization step, decrease with increasing temperature [240]. The reduction of phosphoric acid in the presence of carbon resulting in the formation of elemental phosphorus 6.1 becomes exergonic at precisely 700 °C. This value coincides with the highest temperature applied for the activation of CNTs. In case of reactions 6.2 and 6.3, $\Delta_{\text{R}}G < 0$ is reached at around 750 °C.



In either case, the formation of elemental phosphorus on the surface is favored at 700 °C. Thus, although the samples were cooled down to ambient temperature in Argon, the

spontaneous reaction with environmental oxygen yielding phosphorus pentoxide cannot be avoided. Either in the course of this process or in the subsequent washing step with water, exothermic reactions take place thereby unavoidably leading to substantial oxygen incorporation. The latter is reflected by the specific CO concentrations listed in Table 6.2, which were derived from TPD experiments.

Table 6.2.: Calculated amounts of CO₂ and CO amounts calculated from TPD and characteristic quantities derived from potentiometric pH titrations.

Sample	CO ₂ [$\mu\text{mol}\cdot\text{g}_{\text{CNT}}^{-1}$]	CO	Initial pH	Acid sites [$\mu\text{mol}\cdot\text{g}_{\text{Sample}}^{-1}$]		Total	pK _{a1}	pK _{a2}
				Type I (pK _{a1})	Type II (pK _{a2})			
400-PCNT	205	1631	2.99	612	738	1350	3.3	6.8
500-PCNT	162	1669	3.27	311	372	683	3.6	6.8
600-PCNT	153	1842	4.12	150	102	252	4.4	6.3
700-PCNT	202	2928	3.78	250	130	380	4.1	6.7

6.3.3. Acidic properties of P-modified CNTs in the Aqueous Phase

Titration curves as shown in Figure 6.2 were recorded for the pristine and P-modified samples in order to track the changes of the acidic properties in water upon functionalization. C-CNT is characterized by a neutral surface lacking of neutralizable sites as indicated by a starting pH of nearly 7 in addition to the absence of an inflection point in the corresponding titration curve. A substantial increase in acidity, whose extent inversely correlates with the thermal treatment temperature, is observed after H₃PO₄ activation. The starting pH of 400-PCNT drops below 3, whereas an intermediate value of 3.3 is observed for 500-PCNT. Samples 600-PCNT and 700-PCNT exhibit the highest starting pH value at around 4. A further significant difference was found among the investigated samples in terms of titratable sites. 400-PCNT possesses a large concentration of acid centers in the range of 1350 $\mu\text{mol}\cdot\text{g}_{\text{Sample}}^{-1}$, which is reduced by a factor of five to 252 $\mu\text{mol}\cdot\text{g}_{\text{Sample}}^{-1}$ for 600-PCNT (Table 6.2). This observation is related to the reduction of phosphate species attached to the CNTs. The oxygen content drops from around 6 to 4 wt%, while the amount of phosphorus changes from 1.4 to 0.2 wt% (Table 1). Although carboxylic acid groups and cyclic anhydrides introduced into the carbon backbone during the H₂O₂ treatment contribute to the surface acidity, their existence on the P-modified samples can be excluded since their decomposition takes place in the course of the thermal treatment as this step is carried out at least at 400 °C [172]. This is further reflected in the CO₂ profiles obtained by TPD. In general, acidic O-containing functional groups give rise to characteristic features below 430 °C in CO₂ profiles derived from TPD experiments. Precisely these peaks are not detected for the P-modified CNTs as depicted in Figure 6.1. Consequently, phosphorus-containing species define the acidic properties of the surface.

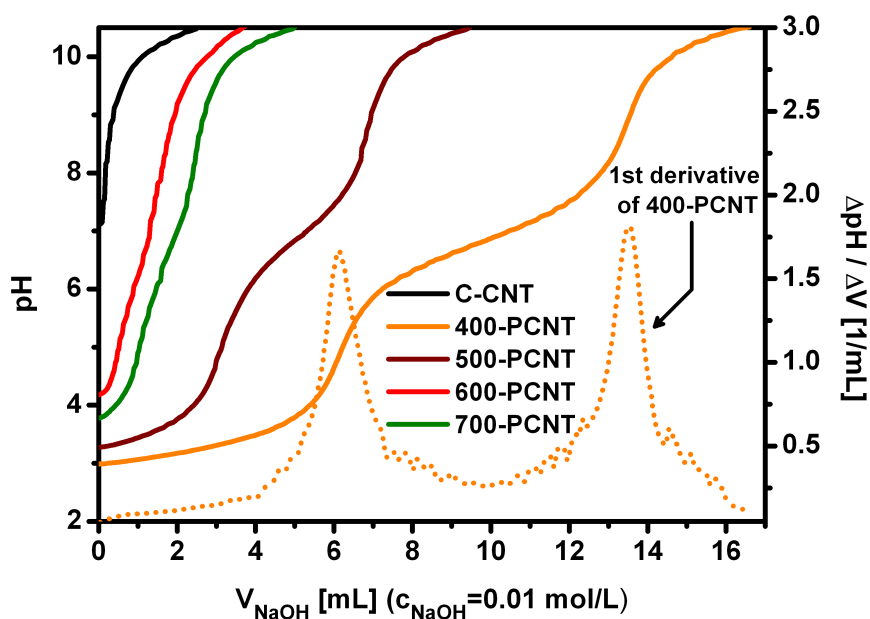


Figure 6.2.: Potentiometric pH-titration curves of the pristine and P-modified carbon nanotubes.

A common finding observed in the titration curves is the development of two well-defined equivalent points, which are more pronounced for 400-PCNT and 500-PCNT. Acid dissociation constants (pK_a), derived from the experimental data by determining the pH at the corresponding half-equivalent points, are summarized in Table 6.2. An excellent agreement among the modified samples can be found for pK_{a2} , which has a value of around 6.8. However, pK_{a1} adopts values between 3.3 and 4.4, which represents a deviation of around 1. This is rather associated with variations of acid sites concentrations that lead to initial pH values in the range from 3 to 4. In view of the low concentrations of acidic centers, the error of determination is considerably higher for 600-PCNT and 700-PCNT. Based on the more reliable values derived from 400-PCNT it can be stated that the herein investigated PCNTs possess a group of species with strong acidity ($pK_{a1} = 3.3$) and a second one with middle-strong acidity ($pK_{a2} = 6.8$). According to the calculated amounts of acid sites given in Table 6.2, around 45 to 65 % of them belong to the former category, while the rest falls into the latter one.

The acid dissociation constants are within the expectable range of phosphorus oxoacids. As observed in Table S6.1, phosphonic acid is characterized by the existence of two pK_a values at 2.0 and 6.6, whereas the triprotonic phosphoric acid forms three equilibria in aqueous solution with dissociation constants at 2.2, 7.2, and 12.7. The comparison of different phosphorus oxoacids clearly shows that the acidic strength depends on the amount of monomers constituting the molecule and on the oxidation state of the phosphorus. In spite of the well-defined equilibria observed for the modified CNTs in the aqueous phase, the configuration of the phosphorus attached to the carbon surface cannot be

unambiguously determined. In addition, electronic effects associated with the carbon nanostructure that influence the acidic properties of the functional groups are hard to elucidate. Nevertheless, the results obtained by means of potentiometric titration are in excellent agreement with the findings derived by NH_3 -TPD, NH_3 -microcalorimetry and the catalytic transformation of 2-propanol.

The hydrothermal stability of the generated phosphate species was titrimetrically evaluated over the samples exhibiting the highest extent of acidity. For this purpose, 400-PCNT was placed in an autoclave bomb together with water and heated to 200 °C. This temperature was maintained for 24 h prior to cooling down to ambient conditions. Thereafter the carbon sample was thoroughly washed and dried, before repeating the hydrothermal treatment for two more times. W1, W2, and W3 denote the corresponding washing cycle. As can be observed in Figure 6.3, the acid surface properties of 400-PCNT are strongly affected by the hydrothermal treatment. The first cycle is harsh enough in order to reduce the amount of acid sites by almost 90 %. During the second cycle, more than 90 % of the original concentration of acidic species is lost. However, the third cycle has no meaningful impact on the surface properties compared to the second one. Evidently, the surface phosphates are hydrolyzed under the applied conditions. Only a small fraction of the originally created functional groups withstands the hydrothermal treatment. This experiment shows that leaching is an important issue to be considered when working with solid acids in the liquid phase.

6.3.4. Investigation of gas-phase acidity by NH_3 microcalorimetry and NH_3 -TPD

Microcalorimetry was used to study the surface acidity through adsorption of ammonia over 400-PCNT and 500-CNT at 80 °C. Both samples exhibit a high extent of acidity as shown by potentiometric titration experiments (Figure 6.2). NH_3 adsorption isotherms of 400-PCNT during the 1st and 2nd adsorption cycle as a function of equilibrium pressure are shown in Figure 6.4a. The monolayer is fully developed at an equilibrium pressure below 3 mbar NH_3 , which corresponds to a saturation concentration of around 880 $\mu\text{mol}\cdot\text{g}_{\text{Sample}}^{-1}$. After degassing the sample and readsorption of the probe molecule under isothermal conditions at 80 °C, a considerable decrease of adsorption sites is observed as evidenced by the isotherm obtained during the 2nd cycle. In this case, the monolayer formation is recorded at an equilibrium pressure near 2.5 mbar. The resulting concentration is about 450 $\mu\text{mol}\cdot\text{g}_{\text{Sample}}^{-1}$. This finding is characteristic for partial irreversible adsorption that is associated with the formation of stable surface adsorption complexes. Nearly 430 $\mu\text{mol}\cdot\text{g}_{\text{Sample}}^{-1}$ of acid sites are lost due to strong interaction between ammonia and the modified carbon surface. Although differences are observed between gas-phase and

aqueous phase titration, the absolute amounts of sites determined by both methods are in a comparable range. Several phenomena like solvation effects in water and the proton affinity of ammonia in the gas phase give rise to the obtained discrepancies.

500-PCNT exhibits a substantial lower specific NH_3 uptake capacity as depicted in Figure 6.4b. An acid site concentration of $492 \mu\text{mol}\cdot\text{g}_{\text{Sample}}^{-1}$ was determined at monolayer coverage during the 1st cycle, which is formed at 2.5 mbar. Evidently, an increase of the treatment temperature from 400 to 500 °C reduces the amount of acidic centers by 45 %. The 2nd cycle reveals a partial irreversible NH_3 adsorption over 500-PCNT, whose extent is however lower than in 400-PCNT since 25 % and not 50 % of the surface sites are lost.

In addition to the monolayer coverage, the distribution and strength of acid centers present on the carbon surface can be analyzed based on the differential heats of NH_3 adsorption. This quantity is plotted for 400-PCNT in Figure 6.4b as a function of the amount of adsorbed probe molecule. The dashed line at $12 \text{ kJ}\cdot\text{mol}^{-1}$ marks the heat of condensation of ammonia [251]. During the 1st cycle, an initial differential heat of NH_3 adsorption of $117 \text{ kJ}\cdot\text{mol}^{-1}$ is obtained. This value remains constant up to a coverage of $88 \mu\text{mol}\cdot\text{g}_{\text{Sample}}^{-1}$ (region I). The differential heat of adsorption is thereafter reduced to $94 \text{ kJ}\cdot\text{mol}^{-1}$ and maintained over a coverage range of $298 \mu\text{mol}\cdot\text{g}_{\text{Sample}}^{-1}$ (region II). Both plateaus indicate the presence of two types of homogeneously distributed and energetically uniform adsorption centers. Although ammonia strongly chemisorbs on these surface sites,

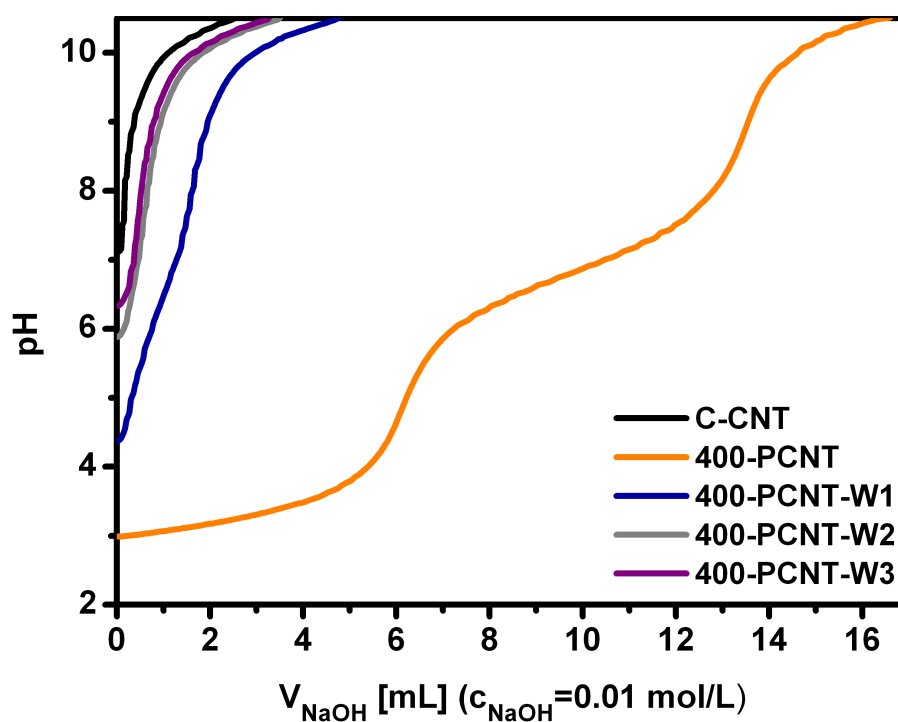


Figure 6.3.: Potentiometric pH-titration curves of as-prepared 400-PCNT and after up to 3 cycles (W1, W2, and W3) of hydrothermal treatment.

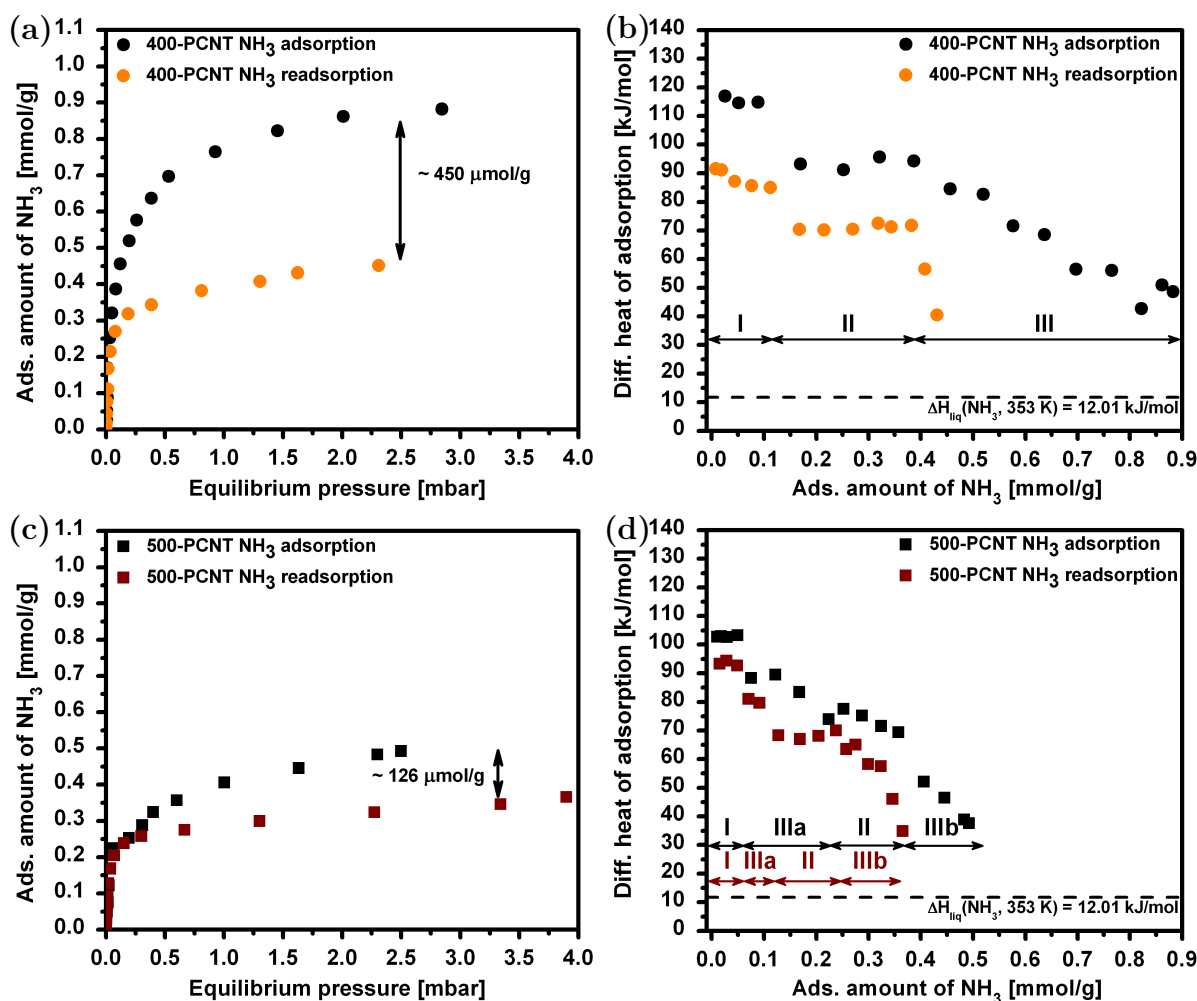


Figure 6.4.: Adsorption isotherms (a,c) and diff. heats as a function of coverage (b,d) derived from NH₃ microcalorimetry carried out at 80 °C after 1st and 2nd cycle over 400-PCNT and 500-PCNT.

a difference of $\sim 20 \text{ kJ}\cdot\text{mol}^{-1}$ is significant in terms of acid strength. At a coverage beyond $400 \mu\text{mol}\cdot\text{g}_{\text{Sample}}^{-1}$, the differential heat of adsorption steadily drops until a value of around $40 \text{ kJ}\cdot\text{mol}^{-1}$ is reached, which is typical for physisorption (region III). This linear decrease is characteristic for the presence of heterogeneous acid sites.

As was already stated in the discussion of the isotherms, an irreversible process is observed. One consequence is the reduction of the initial differential heat of NH₃ adsorption from 117 to $92 \text{ kJ}\cdot\text{mol}^{-1}$ for 400-PCNT. Interestingly, the plateau at low coverage is still present and spanned over a range of $112 \mu\text{mol}\cdot\text{g}_{\text{Sample}}^{-1}$. Similarly, region II exhibits a constant coverage interval of $270 \mu\text{mol}\cdot\text{g}_{\text{Sample}}^{-1}$ characterized by a differential heat of $71 \text{ kJ}\cdot\text{mol}^{-1}$. In regions I and II, the differential heats are respectively reduced by more than $20 \text{ kJ}\cdot\text{mol}^{-1}$, suggesting a decrease in terms of interaction between ammonia and the surface species indicating a loss in acid strength. However, the most prominent change is observed

in region III. Besides con-firming the heterogeneity of acid sites, the differential heat decreases significantly faster compared to the 1st adsorption. As shown in Figure S6.4a, the irreversibility can be quantified by comparing the sum of integral heats of adsorption with the overall integral heat of desorption. The former value is with 13.7 J nearly 84 % larger than the one obtained during the desorption step. In contrast, an analysis of these quantities after the 2nd cycle clearly shows that readsorption is a reversible process since the experimental values in the range of 6.5 J (Figure S6.4b) only differ by about 0.1 % among each other.

As depicted in Figure 6.4d, lower differential heats of NH₃ adsorption evidence the weaker acidic character of 500-PCNT. A value of 103 kJ·mol⁻¹ was recorded for the first plateau (region I), while the second one exhibits a differential heat of NH₃ adsorption amounting to 75 kJ·mol⁻¹ (region II), which is almost 20 kJ·mol⁻¹ below the corresponding quantity determined for 400-PCNT. In addition, between 40 to 50 % lower concentrations of acidic centers were determined for 500-PCNT in regions I (50 μmol·g_{Sample}⁻¹) and II (156 μmol·g_{Sample}⁻¹) compared to 400-PCNT. In contrast to the latter sample, the former shows the presence of two regimes characteristic for heterogeneously distributed and energetically unequal acid sites (regions IIIa and IIIb) that are indicative for a less defined surface acidity. A monotonic and linear decrease of -q_{diff} is respectively observed from 88-74 kJ·mol⁻¹ and from 69-38 kJ·mol⁻¹. In consequence of the previously discussed partial irreversible adsorption, the initial differential heat of NH₃ adsorption characteristic for region I falls by 10 kJ·mol⁻¹ to 93 kJ·mol⁻¹. The value in case of region II is reduced by 7 kJ·mol⁻¹ to 68 kJ·mol⁻¹. Interestingly, 400-PCNT and 500-PCNT exhibit comparable -q_{diff} values in regions I and II determined during readsorption, suggesting that similar final states of the surface sites are induced by the interaction with ammonia during the 1st cycle despite the obvious differences in acidic strength. Regions IIIa and IIIb are scarcely affected with respect to the differential heats as evidenced by similar values obtained during adsorption and readsorption, but in a stronger manner in terms of the amount of acid sites lost. Between 20 to 30 % lower concentrations of heterogeneous centers are determined during the 2nd adsorption cycle.

Based on the results derived from the differential heats of adsorption, two types of homogeneous sites have been identified, which coexist with a variety of heterogeneous centers. A simulation of the adsorption isotherms of 400-PCNT as presented Figure 6.4a using the Langmuir model is insofar inappropriate, since the assumptions [252] of energetically equivalent sites and the absence of interactions between adsorbate molecules on neighboring centers are not fulfilled. Even the higher order Langmuir isotherm is not suitable considering that the main difference with respect to the simple model is an adsorption associated with an activation process [253]. Similarly, the basic considerations

of the Temkin isotherm are not applicable for the herein investigated systems. According to this model, the heat of adsorbed molecules decreases linearly with the increase in coverage. Adsorption is furthermore characterized by a uniform distribution of binding energies reaching a given maximum value [254]. This is at most fulfilled in region III, where a steady decrease of differential heats is observed. Another fact that should be considered is that most likely not only adsorption, but also reaction takes place during exposure of the P-modified carbons to ammonia. These processes are not taken into consideration in any of the referred mathematical approaches. However, for the sake of completeness, the aforementioned models were applied for the description of the experimental results of 400-PCNT. The fitted isotherms are displayed in Figure S6.2 and the corresponding fitting parameters are listed in Table S6.2. As evidenced by the adjusted R^2 values, which lie between 0.9863 and 0.9907, all models describe the adsorption process during the 1st cycle with a comparable accuracy. This seems to be a mathematical effect, wherefore the physical meaning of the derived parameters is rather questionable. Upon ammonia readsorption, the coefficient of determination drops to values near 0.98 for the three models, suggesting a loss in fitting quality. These results are expectable since various types of acid centers present on the P-modified carbon nanotubes contribute to the adsorption properties to considerable different extents.

A crucial aspect to be analyzed is whether the phosphoric acid activation generates Lewis or Brønsted acid centers on the backbone of carbon nanotubes. Even the presence of both types of sites could be involved in the adsorption processes. Four types of regions have been identified in a typical calorimetric curve of differential heats of adsorption plotted as a function of coverage [255]. A steep decrease of high differential heats is characteristic for the existence of Lewis acid sites. Thereafter, the presence of at least one plateau with constant heats of adsorption is preferentially attributed to homogeneous Brønsted sites. At higher coverages, a second decrease is observed due to adsorption of the probe molecule on heterogeneous sites. Weak interactions in the last domain arise due to physisorption or hydrogen bonding between the probe and the investigated sample. An FTIR investigation of Bedia et al. [131] carried out on phosphoric acid impregnated and carbonized hemp stems at 450 °C in N_2 , which was carried out upon adsorption of pyridine and 2,6-dimethylpyridine, proposes that Lewis and Brønsted sites are present on the sample. However, it is questionable whether phosphate species have the ability of serving as Lewis acids, since the latter are per definition molecular entities capable of accepting an electron-pair. A rather plausible explanation is that coordinatively unsaturated metal cations, which might be present in the carbonized sample as a consequence of the inorganic residues already available in the used hemp stems, are responsible for adsorption of pyridine in the wavenumber region ascribable to Lewis acid sites. Therefore, the development of

two plateaus observed during microcalorimetric measurements might be associated with the presence of Brønsted acid sites.

NH₃-TPD was performed on the prepared P-modified CNTs. However, only 400-PCNT showed a significant ammonia uptake. This is partly related to the fact that NH₃-TPD experiments were carried out with 80 mg as commonly employed in other studies, corresponding to 2.5 times less amount of sample than used in the microcalorimetric measurements. In consequence, the absolute quantity of acid sites exposed to the probe molecule differs between both methods by the aforementioned factor. It should be pointed out that NH₃-TPD experiments were carried out up to 500 °C, since the thermal decomposition of acidic centers start beyond this value according to the TPD results presented in Figure 6.1b.

Figure 6.5a displays the NH₃-TPD profile of 400-PCNT after the 1st and 2nd ammonia adsorption cycle performed under isothermal conditions at 80 °C. Overall amounts of acid sites, which are listed in Table 6.3, are obtained by integration of the corresponding areas under the curves. Acid strength is related to the temperature at which the probe desorbs. With this respect, strong acid centers are characterized by ammonia evolution at high temperatures. Three different regions as indicated by arrows can be observed in the profile obtained during the 1st adsorption. This is in line with the previously discussed results derived from microcalorimetric measurements. According to NH₃-TPD, the amount of acid sites lies in the range of 315 $\mu\text{mol}\cdot\text{g}_{\text{Sample}}^{-1}$. Figure 6.5b shows the deconvoluted profile of 400-PCNT obtained during the 1st adsorption cycle. Three Gaussian peaks were used in order to fit the experimental data. They describe the distribution of sites with weak (< 225 °C), moderate (225 – 350 °C) and strong (> 350 °C) acidity. While the

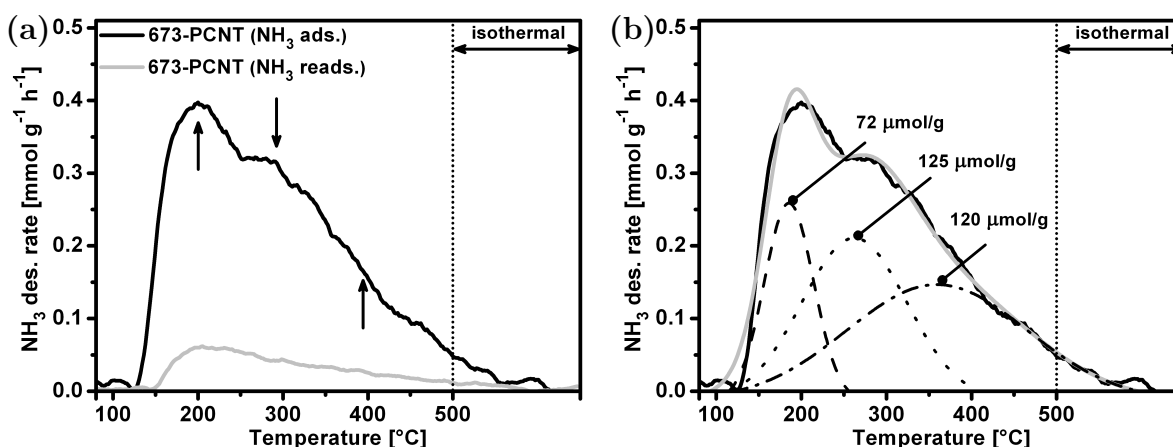


Figure 6.5.: (a) Analysis of gas-phase acidity and estimation of process reversibility by NH₃-TPD is shown for 400-PCNT. Arrows indicate regions with sites of different strength. (b) Deconvoluted profile of 1st NH₃ adsorption cycle on 400-PCNT according to the identified regions.

amounts of sites corresponding to the latter two regions are comparable to those obtained by NH₃-microcalorimetry, a notorious difference is encountered for the surface centers characterized by a weak acidity. Whereas NH₃-TPD suggests a specific concentration of 72 μmol·g_{sample}⁻¹, microcalorimetry indicates a larger fraction of around 496 μmol·g_{sample}⁻¹. This is most likely related to the specific differences between the methods. After the isothermal adsorption of ammonia, the system was thoroughly flushed with an inert gas stream. A consequence thereof is that a considerable quantity of physisorbed NH₃ molecules already desorb during this step. As opposed to this, microcalorimetric experiments are based on a stepwise dosing of the probe molecule into the chamber containing the sample until monolayer coverage is reached. Consequently, a higher adsorption capacity is recorded.

A considerable lower NH₃ adsorption is observed during the 2nd cycle as depicted in Figure 6.5a. This finding is indicative for irreversible interaction between the probe and the acidic carbon surface. Similar conclusions were drawn from microcalorimetry. Discrepancies in terms of acid site concentrations are noted between both methods. In this case, the results diverge by a factor of almost 10 as indicated in Table 6.3. Every region is strongly affected after the 1st desorption. In addition to the loss of physisorbed molecules, probably a large fraction of sites is still covered with ammonia despite the high temperatures. Since the desorption is driven by incrementing the temperature and not by pressure reduction as in the microcalorimetric cell, it is plausible that even higher temperatures are required in order to achieved a higher desorption amount. However, the thermal stability of surface species constraints the upper temperature limit. Irrespective of these differences, NH₃-TPD confirms the presence of acid sites as well as the irreversibility of the adsorption process.

Table 6.3.: Estimation of total acidity according to NH₃-TPD and NH₃ microcalorimetry (re)adsorption results of 400-PCNT and 500-PCNT performed at 80 °C

Sample	Amount of NH ₃ des. [μmol·g _{sample} ⁻¹]	-q _{ini} [kJ/mol]	-q _{ads} [kJ/mol]			n _{ads} [μmol·g _{sample} ⁻¹]			Total
			Region			Region			
			I	II	IIIa/IIIb/III	I	II	IIIa/IIIb/III	
400-PCNT-ads	315	117	115	94	-/-/85-50	88	298	-/-/496	882
400-PCNT-reads	45	92	88	71	-/-/71-41	112	270	-/-/49	431
500-PCNT-ads	n. d.	103	103	75	88-74/69-38/-	50	156	118/168/-	492
500-PCNT-reads	n. d.	93	93	68	81-68/68-35/-	49	110	79/128/-	366

6.3.5. Catalytic Transformation of 2-propanol

Titration experiments as well as calorimetric analysis using NH₃ as a basic probe molecule clearly evidenced the availability of highly acidic centers on the P-modified CNTs in different concentrations. Therefore, it is convenient to perform a complementary analysis

of the surface acidity by means of the catalytic transformation of 2-propanol. This test reaction exhibits a considerable sensitivity towards changes of the acid-base properties owing to the specificity of the reaction pathways. Conversion of the secondary alcohol on acid sites leads to the formation of propylene and diisopropyl ether, while dehydrogenation takes place over Lewis acid-base pairs yielding acetone [120].

Conversions and product selectivities as a function of time on stream obtained during the catalytic reaction are shown in Figure 6.6. 400-PCNT is by far the most active catalyst as evidenced by a stable conversion of nearly 50 % at 200 °C (Figure 6.6a). Increasing the temperature by 25 °C leads to an initial conversion of about 68 %, which thereafter gradually drops to 59 % over a period of 12 h. This evident deactivation becomes even more pronounced at 250 °C. An activity loss of more than 30 % is appreciated at this temperature. However, the most prominent deactivation is observed at 275 °C reflected by a decrease in conversion amounting to almost 40 %.

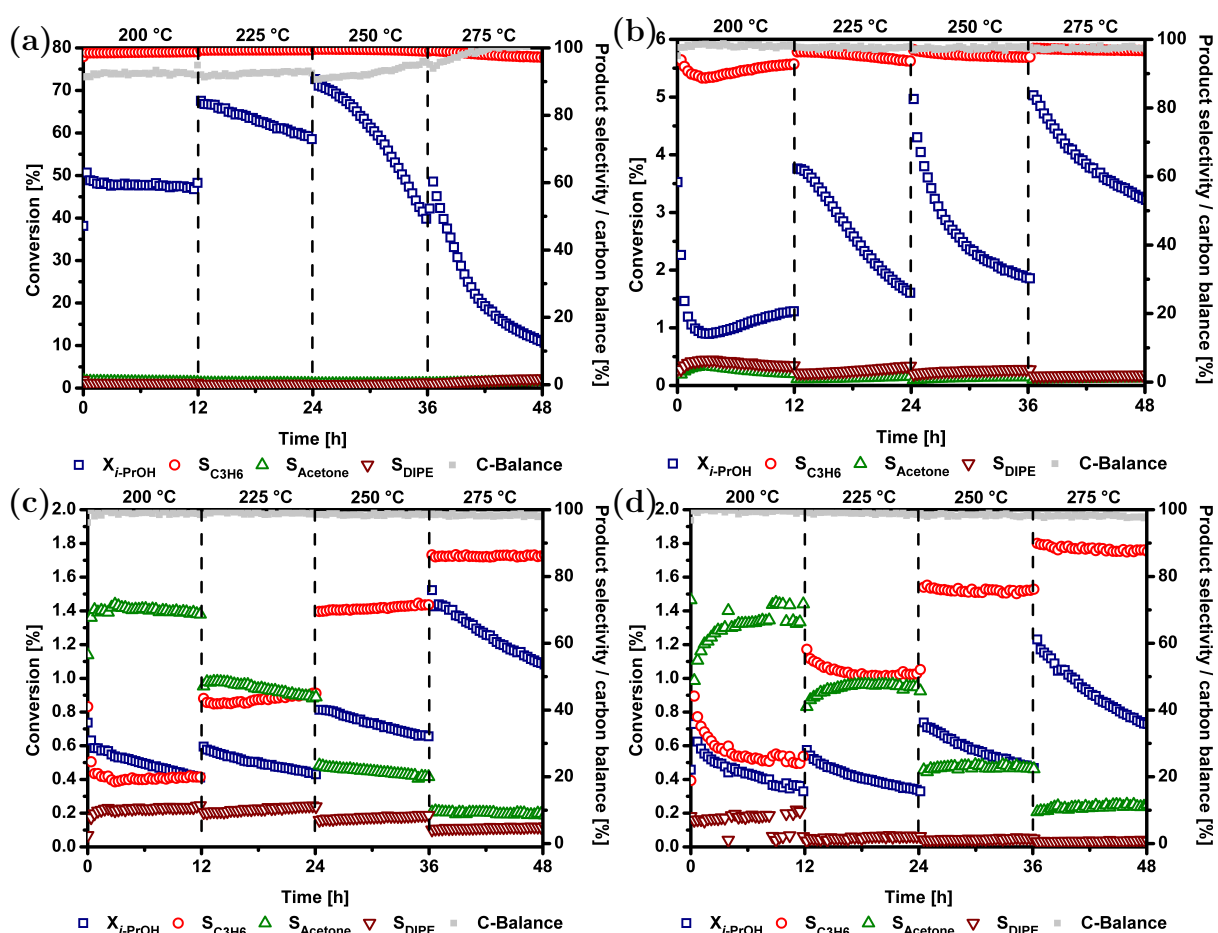


Figure 6.6.: Conversions and selectivities as a function of time on stream obtained at four different temperatures during the catalytic decomposition of 2-propanol on (a) 400-PCNT, (b) 500-PCNT, (c) 600-PCNT, and (d) 700-PCNT. Samples were previously treated at 350 °C in N_2 for 2h.

to 100 % with loss in activity. This implies that a fraction of 2-propanol is adsorbed at high conversions. The surface of 400-PCNT is undoubtedly highly acidic as reflected by selectivities towards dehydration products of 100 %. Propylene is predominantly formed with small amounts of diisopropyl ether detected at the highest reaction temperature after the strong deactivation phase.

500-PCNT is considerably less active than 400-PCNT (Figure 6.6b). The highest conversion, which was determined at the end of the deactivation period at a reaction temperature of 275 °C, is somewhat lower than 4 %. This sample also exhibits a high extent of acidity considering that propylene and diisopropyl ether are produced with more than 95 % selectivity. In contrast to 400-PCNT, a small fraction of 2-propanol is already converted to acetone. Although both samples produce dehydration products with high selectivities, an extreme difference is observed in terms of activity. 400-PCNT possesses twice as much acid centers as 500-PCNT according to pH titration experiments and NH_3 -microcalorimetry. This difference certainly plays a decisive role since a larger specific concentration of active sites is available for the turnover of 2-propanol. However, the catalytic activities differ by factors of up to 50. Not only the amount of sites, but also their strength are responsible for these observations. According to the microcalorimetric measurements, the differential heats of NH_3 adsorption in the range ascribed to Lewis acid sites differ between these samples by around 15 $\text{kJ}\cdot\text{mol}^{-1}$. Although this value is strictly valid for the basic probe, this finding already shows that sites of higher acid strength are available on 400-PCNT compared to 500-PCNT. Since the microcalorimetric measurements are carried out in the gas phase, the aforementioned observations are also applicable for adsorbent-adsorbate interactions between 2-propanol and the activated carbon surface. Thus, the surface acid properties of CNTs are strongly sensitive to the activation temperature in the presence of phosphoric acid, considering that 100 °C leads to such significant differences in terms of acidic properties.

According to the quantities derived from pH titrations, 600-PCNT and 700-PCNT exhibit comparable amounts of acid centers. The values determined by this means were the lowest within the series of prepared catalysts. Both facts are confirmed based on the results obtained from the catalytic transformation of 2-propanol (Figure 6.6c and d). Conversions are in the range between 0.4 and 1%, which are considerably lower than the values obtained for 500-PCNT and certainly for 400-PCNT. Even the selectivity patterns of both samples are similar. At lower temperatures, acetone is produced with nearly 70 % selectivity, which gradually decreases with increasing reaction temperature reaching 10 % at 275 °C. This is an evidence for the acid-base bifunctional character of the surface.

As can be observed in Figure 6.6, the conversion of 2-propanol pronouncedly decreases with time on stream especially at temperatures above 200 °C. Deactivation is generally

related to the loss of active sites during reaction and/or the irreversible adsorption of species on catalytic centers. Thus, PCNTs were analyzed by EDX after reaction in order to address this issue. The obtained results are listed in Table 6.4. A comparison with the elemental composition of the as-prepared samples reveals that 400-PCNT and 500-PCNT contain 64 and 22 per cent less phosphorus after reaction, respectively. According to microcalorimetry 400-PCNT contains more and stronger acid sites than 500-PCNT, which is reflected by significant differences in terms of catalytic activity. In view of this, the more pronounced decay of P-content in the former case has two implications: first, phosphate species are the active sites at which the turnover towards propylene takes place; second, the deactivation process is dominated by the destruction of phosphate species *via* hydrolysis. This is in line with titrimetric evaluation of the stability under hydrothermal conditions. As opposed to this, 600-PCNT-ar and 700-PCNT-ar exhibit comparable P-concentrations as the fresh samples. Due to lower conversion levels the feed is significantly less humid, thus avoiding hydrolysis of the active sites. In addition, dehydrogenation of the secondary also takes places. Deactivation in these cases most likely originates from the irreversible adsorption of educts, intermediates and/or products.

Table 6.4.: Elemental composition of PCNTs after catalytic decomposition of 2-propanol.

ID ^a	Sample	Elemental analysis [wt %] ^b		
		C	O	P
17886	400-PCNT-ar	96.3 ± 0.5	3.3 ± 0.4	0.5 ± 0.1
17887	500-PCNT-ar	95.8 ± 0.4	3.5 ± 0.3	0.7 ± 0.1
17888	600-PCNT-ar	96.8 ± 0.4	3.1 ± 0.4	0.2 ± 0.1
17889	700-PCNT-ar	97.0 ± 0.7	2.3 ± 0.8	0.7 ± 0.1

^a Internal sample number to distinguish reproductions of sample preparation ^b Elemental composition is the average of 7 measured EDX spectra

6.3.6. Oxidation resistance of P-modified CNTs

Phosphorus incorporation into the structure of carbon materials has been often applied in order to increase their oxidative stability. The role of this heteroatom has been enlightened by several studies [115, 231, 235, 256]. Accordingly, the enhancement in oxidative resistance arises from either the development of a protective diffusion layer resulting from the thermal decomposition of phosphorus precursors or the selective blockage of active sites present in the carbon structure at which combustion is initiated [235].

Irrespective of the type of phosphorus species present on the surface, whereby it has been proposed that the inhibition effect arises from the presence of C–O–PO₃ surface groups [231], activation of CNTs in the presence of H₃PO₄ leads to a significant increase of the oxidative stability. Figure 6.7a depicts the TG profiles of the pristine and modified CNTs

obtained during TPO in synthetic air. C-CNT exhibits the lowest resistance since it lacks of any phosphorus containing species. Both, the extrapolated onset temperature T_{Onset} and T_{50} , the temperature at which 50% of the mass has been fully oxidized, show similar values in the range of 610 °C. A significant increase is already observed for 600-PCNT that according to EDX measurements contains 0.2 wt% phosphorus. In this case, T_{Onset} is almost 40 °C higher than that encountered for C-CNT. An even stronger impact is observed for T_{50} , which amounts to 670 °C. Further improvement is observed for higher phosphorus contents. As shown in Figure 6.7b, T_{Onset} and T_{50} level off after surpassing a threshold value of 0.7 wt% at upper limits around 680 °C and 710 °C, respectively. Thus, phosphorus incorporation achieved by the herein presented approach leads to a shift in the oxidation resistance in the range of 40-70 °C and to an increase of the T_{50} value of 60-100 °C towards higher temperatures with respect to the pristine CNT material. These differences have the following two implications: phosphorus improves on the one hand the stability of the nanostructured carbon against thermal oxidation, and on the other hand, its presence lowers the combustion reaction rate. The latter is reflected by the slope change of the TG curves in the temperature interval where the oxidation takes place. This finding is fully in line with kinetic studies performed on pure and P-modified graphite [231, 256]. Although a combustion inhibition is observed upon phosphorus incorporation, the activation energy calculated for carbon oxidation remains unaffected. Such an observation was regarded as an implication that the basic mechanism is governed by a unique rate determining step. Thus, a decrease in reaction rates is related to changes in the preexponential factors.

DSC measurements were performed during TPO experiments in order to monitor heat changes associated with carbon oxidation. Molar enthalpies of oxidation $-\Delta H_{\text{Oxidation}}$ were derived from the DSC signals by integrating the peak between the experimental data and the sigmoidal baseline curve. The resulting values were plotted in Figure 6.7b

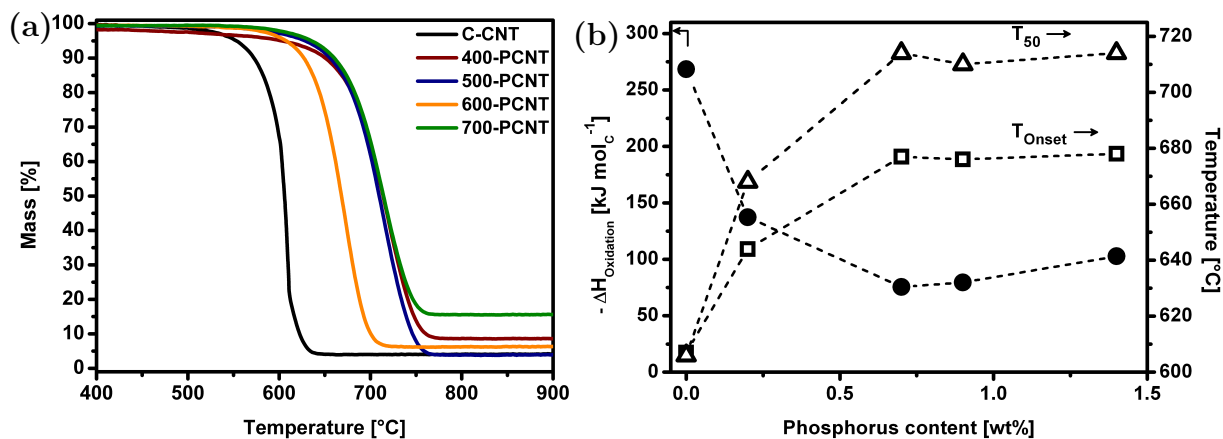


Figure 6.7.: (a) Thermogravimetric changes during TPO of pristine and P-modified CNTs in synthetic air (b) Dependency of $-\Delta H_{\text{Oxidation}}$, T_{Onset} and T_{50} on phosphorus content.

against the phosphorus content. Interestingly, $-\Delta H_{\text{Oxidation}}$ exhibits an opposite trend as compared to the T_{Onset} and T_{50} values. The highest specific enthalpy of oxidation, with a value of $\sim -270 \text{ kJ}\cdot\text{mol}_C^{-1}$, was obtained for C-CNT. A drastic decrease to $-137 \text{ kJ}\cdot\text{mol}_C^{-1}$ is observed for 600-PCNT, which further drops to a lower limit in the range of $-80 \text{ kJ}\cdot\text{mol}_C^{-1}$ for higher P contents. This is a further evidence for the inhibition effect arising from the presence of phosphorus species on the CNT surfaces. A significant reduction in heat release is most likely a consequence of an effectively blockage of highly reactive carbon sites.

6.4. Conclusions

Phosphorus modified CNTs were prepared *via* thermal treatment in the presence of H_3PO_4 at four different temperatures (400, 500, 600, and 700 °C) in Ar after previous incorporation of oxygen functional groups through oxidation in H_2O_2 . This modification approach yielded highly acidic surface species maintaining the mesoporous structure of the material without development of microporosity. As further evidenced by N_2 adsorption-desorption experiments, the BET surface area increases with decreasing treatment temperature. Since phosphoric acid is not an oxidizing agent, the initial increase in surface area is rather associated with the pretreatment in hydrogen peroxide.

CO evolution during TPD experiments evidenced the presence of two types of highly stable species on the CNT surface. Although CO starts to emerge at 500 °C, the main features dominating the profiles are encountered at 890 and 940 °C. In contrast to results obtained with activated carbons obtained through carbonization of impregnated precursors, an increase in treatment temperature reduces the P-content in posttreated nanostructured carbons. This trend is likewise observed for the specific concentration of acidic species, which according to potentiometric pH titrations decrease from 1350 to below $400 \mu\text{mol}\cdot\text{g}_{\text{Sample}}^{-1}$. In addition, two well-defined equivalent points were found. The acid sites exhibited characteristic pK_a values in the range of 3.3 and 6.8, which are comparable to those typical of oxoacids of phosphorus.

NH_3 microcalorimetry evidenced the existence of two types of homogeneously distributed and energetically equivalent acid sites as reflected by the development of two plateaus with distinct differential heats of NH_3 adsorption. Increasing the treatment temperature from 400 to 500 °C reduces the overall amount of centers, while simultaneously changing their acid strength. 400-PCNT possesses Lewis acid sites exhibiting differential heats of NH_3 adsorption in the range of $120 \text{ kJ}\cdot\text{mol}^{-1}$, whereas the value obtained for the corresponding centers in 500-PCNT is lowered by about $15 \text{ kJ}\cdot\text{mol}^{-1}$. Furthermore, the monolayer capacity of 400-PCNT is twice as large. Partial irreversible adsorption of ammonia decreases the

acid strength and the overall adsorption capacity. The latter was further confirmed by NH_3 -TPD performed over 400-PCNT. This sample showed a high conversion in the transformation of 2-propanol towards propylene. However, a strong deactivation was observed at reaction temperatures beyond 200 °C. 500-PCNT was considerably less active, yet leading to dehydration products with high selectivity. 600-PCNT and 700-PCNT showed the behavior of an acid-base bifunctional surface.

Phosphorus incorporation substantially enhances the oxidative stability as evidenced by a shift of the extrapolated onset temperature and the T_{50} value towards higher temperatures. The most pronounced variations with respect to the pristine material were respectively 70 and 100 °C. These values remained constant after a P-content of 0.7 wt%. As opposed to this, the molar heat of combustion was reduced from -280 to about -80 $\text{kJ}\cdot\text{mol}_\text{C}^{-1}$, which most likely arises from the effective blockage of reactive carbon sites.

As evidenced by the extensive investigation herein presented, a well-defined acidity and high resistance against thermal oxidation of CNTs can be easily achieved by surface modification with phosphorus species. In view of the excellent NH_3 uptake capacity of PCNTs, these mesoporous nanocarbons are suitable as solid adsorbents for compounds with basic properties. Furthermore, the presence of acid surface species with high thermal stability enable the potential of using these kind of nanomaterials as catalyst support even at elevated temperatures. Finally, the enhanced oxidative stability opens the possibility of employing PCNTs as electrode materials for a variety of electrochemical applications.

6.5. Supporting Information

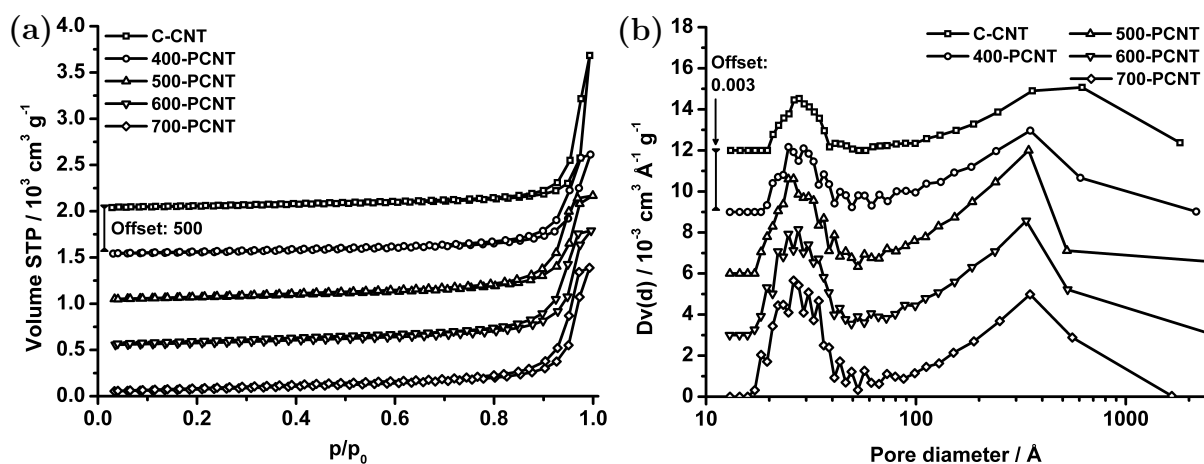


Figure S6.1.: (a) BET isotherms and (b) pore size distributions of pristine and functionalized carbon nanotubes.

Table S6.1.: pK_a values of selected oxoacids of phosphorus [257].

Formula	Name	pK_{a1}	pK_{a2}	pK_{a3}	pK_{a4}	pK_{a5}
H_3PO_2	Phosphinic acid	1.24	-	-	-	-
H_3PO_3	Phosphonic acid	2.00	6.59	-	-	-
H_3PO_4	Phosphoric acid	2.21	7.21	12.67	-	-
$H_4P_2O_6$	Hypophosphoric acid	2.2	2.8	7.3	10.0	-
$H_4P_2O_7$	Diphosphoric acid	0.85	1.49	5.77	8.22	-
$H_5P_3O_{10}$	Triphosphoric acid	≤ 0	0.89	4.09	6.98	9.93

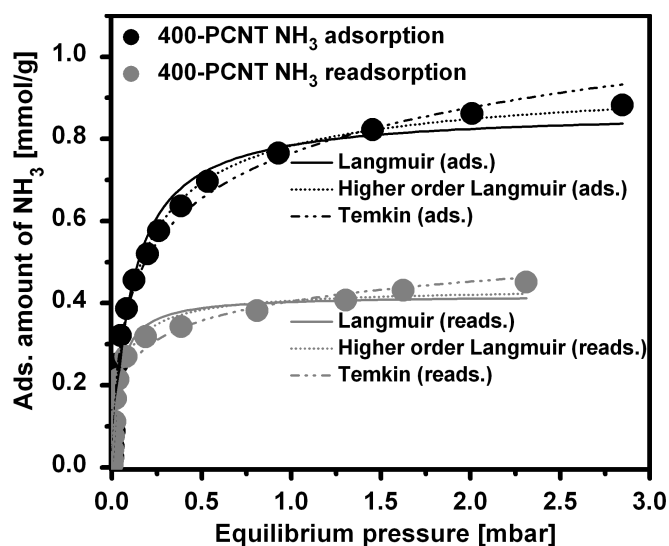


Figure S6.2.: Fit of adsorption isotherms obtained during 1st and 2nd ammonia adsorption at 80 °C over 400-PCNT. Langmuir, higher order Langmuir and Temkin models were applied in both cases.

Table S6.2.: Fitting parameters obtained for three different adsorption models derived from NH₃ microcalorimetry measurements performed over 400-PCNT at 80 °C.

Model	N _{mono} [μmol·g _{Sample} ⁻¹]	K [mbar ⁻¹]*	Order	R ²
Fit parameters for 1st adsorption				
Langmuir	868 ± 21	9.39 ± 0.92	1	0.9863
Higher Langmuir	961 ± 33	6.85 ± 0.86	1.29 ± 0.08	0.994
Temkin	4074 ± 160	4.19·10 ⁻⁹ ± 6.56·10 ⁻¹⁰	-	0.9907
Fit parameters for 2nd adsorption				
Langmuir	419 ± 11	24.72 ± 3.12	1	0.9804
Higher Langmuir	440 ± 20	20.11 ± 3.97	1.2 ± 0.15	0.9819
Temkin	1199 ± 76	2.82·10 ⁻⁹ ± 8.36·10 ⁻¹⁰	-	0.9748

* Characteristic fitting parameter (p*) of the Temkin model

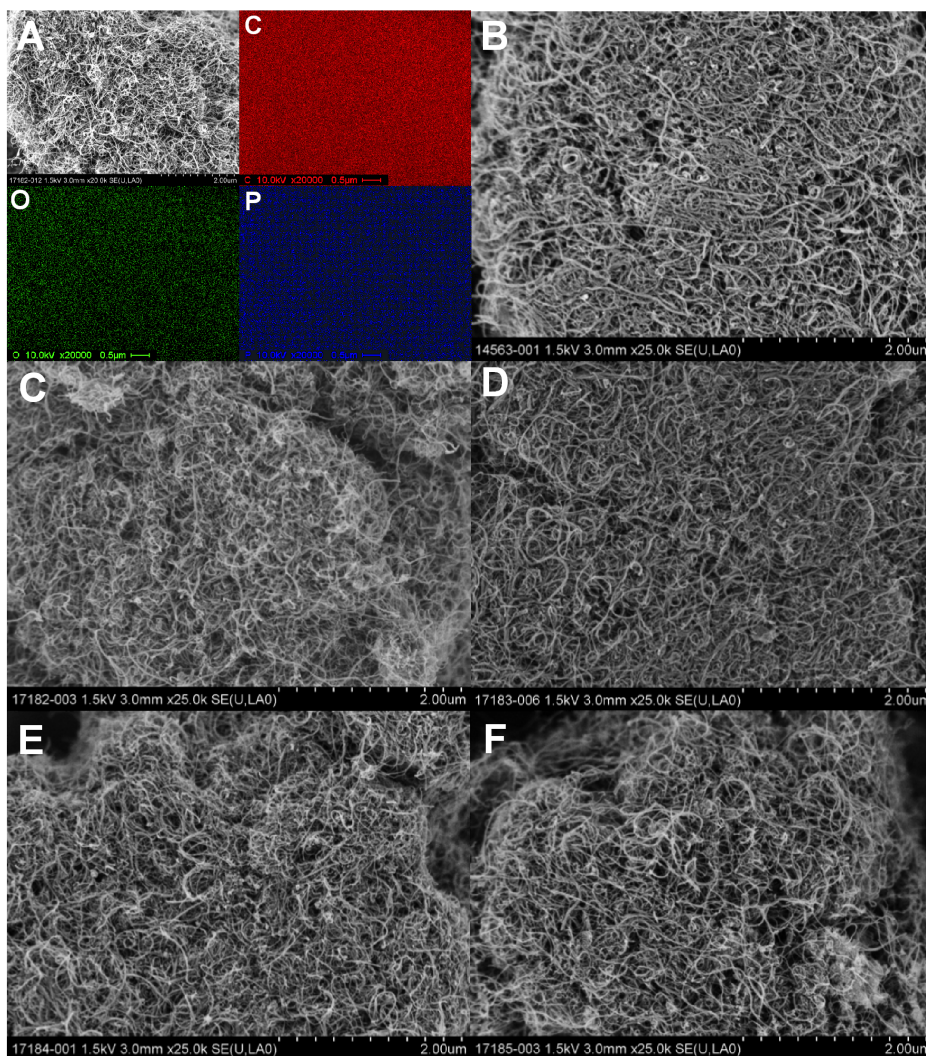


Figure S6.3.: Elemental distribution with corresponding SEM micrograph of 400-PCNT (A) and SEM micrographs of C-CNT (B), 400-PCNT (C), 500-PCNT (D), 600-PCNT (E), and 700-PCNT (F).

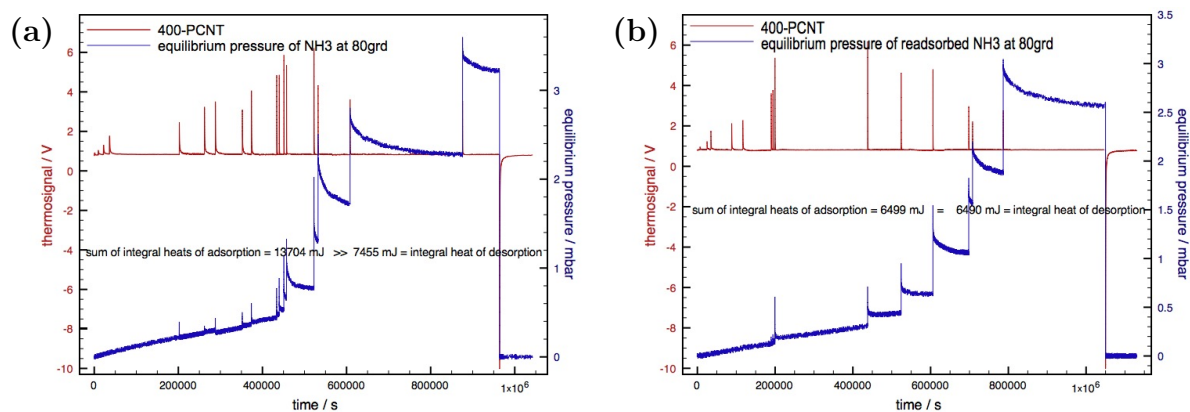


Figure S6.4.: Thermosignals at low coverage obtained for the 1st (a) and 2nd (b) NH₃ adsorption cycle over 400-PCNT. The corresponding equilibrium pressures in addition to the sum of integral heats of adsorption and overall integral heat of desorption are also shown.

7. Conclusion and outlook

Multiwalled carbon nanotubes have been chemically modified following various functionalization strategies in order to incorporate heteroatoms into the nanostructure. The aim thereby was to tailor the surface acid-base properties in a rational fashion and to understand the impact of the modification approaches on the adjusted characteristics. Oxygen, sulfur and phosphorus containing CNTs were prepared with the purpose of increasing the acidity, whereas nitrogen incorporation was carried out in order to enhance the basic properties. Deeper insights were gained through investigation of the resulting CNTs by a combination of various techniques including potentiometric pH titrations, elemental analysis, TPD, XPS, NH_3 -TPD, and NH_3 microcalorimetry.

A key method applied throughout the herein presented systematic work was the transformation of 2-propanol over the diversely functionalized CNTs. Its application was especially important for the analysis of the physicochemical properties of NCNTs, whose surface species can be either acidic or basic in nature. Variations cannot be tracked by potentiometric pH titration since the extent of acid-base strength of these moieties is rather low. This is reflected by the high resemblance of the experimental titration curves. However, results derived from the transformation of 2-propanol clearly show that amination at 300 °C leads to an acid-base bifunctional surface, while nitrogen incorporation at 500 °C already creates a basic surface. This becomes even more evident on the sample prepared at 700 °C, which under comparable conditions transforms the secondary alcohol at a higher rate to acetone with almost 100 % selectivity. Thus, the studies performed permit to draw the conclusion that the transformation of 2-propanol, typically applied to investigate inorganic compounds, is a robust and sensitive method that allows to analyze variations of the acid-base properties of nanostructured carbons irrespective of the chosen derivatization strategy.

However, it is indispensable to gather information about the nature of the functional groups in order to attempt to understand the origin of the surface acid-base properties. TPD experiments provided fundamental knowledge about the abundance and structure of the functional groups, which can be inferred from the gaseous compounds detected in the course of the thermal decomposition. For instance, SO_2 and H_2O are concomitantly formed as a consequence of the desulfonation of benzenesulfonic acid groups. CO_2 evolution is related to the degradation of carboxylic acids, cyclic anhydrides and lactones, whereas

CO is related to the decomposition of cyclic anhydrides, phenols, ethers and ketonic species. Moreover, CO is observed at temperatures beyond 750 °C as a consequence of the decomposition of phosphate species. With respect to N-containing species, the decomposition of imides, lactams, pyrrolic-N and pyridinic nitrogen results in the formation of HCN. The former two can be further identified by the evolution of HNCO. H₂ is related to the dehydrogenation of the carbon backbone and to the thermal depletion of pyrrolic-N and pyridinic nitrogen. Nitrogen functional groups may also decompose to N₂, which is indicative for the mobility of surface species.

Sulfur as part of benzenesulfonic acid entities was covalently attached to the system through diazotization of sulfanilic acid *via* a radical intermediate applying different precursor-to-carbon ratios in ODCB and water. Besides this efficient type of direct sidewall derivatization approach, amination of OCNTs by treating the preoxidized sample in NH₃ at 300, 500, and 700 °C was performed with the aim of creating nitrogen containing surface species. In addition, phosphorus modification was achieved by activation of OCNTs in the presence of phosphoric acid between 400 and 700 °C in Argon. Unquestionably, the acid-base properties of the herein investigated modified CNTs substantially differ from those of the pristine material, which exhibits a neutral behavior in view of the absence of heteratoms. In doing so, other important characteristics of the matter are affected, including wettability of the surface, dispersion capability in the liquid phase, defect density, local electronic structure and oxidative resistance. This is to a great extent associated with the nature of species present on the carbon surface.

Acidity is increased when carboxylic acids, cyclic anhydrides, benzenesulfonic acid groups and phosphates are tethered to the carbon nanostructure. The former two are simply created by contacting the unmodified sample with an oxidizing agent like nitric acid. However, this kind of approach presents some disadvantages. Besides the formation of the targeted species, a high variety of other functionalities including lactones, phenols, ethers and ketones are simultaneously created, which in consequence increases the degree of complexity of the system. Controlling the nature of surface species following this strategy is therefore not possible. In addition, the propensity towards the undesirable formation of higher reactive amorphous carbon layers on the surface augments, consequently lowering the oxidative stability of the sample in an oxygen containing atmosphere. Similarly, the wet-oxidative treatment creates larger quantities of structural defects, which are preferential sites at which combustion initiates. Higher functionalization temperatures and larger concentrations of the oxidizing agent are necessary when considerable amounts of O-containing moieties need to be created. Since this combination of parameters intensifies the oxidative power of the employed agent, the integrity of the nanocarbon cannot be maintained due to severe structural damages.

A great advantage of the applied diazotization approach is that the incorporation of acidic sites is certainly achieved in a controlled way. Variation of the precursor-to-carbon ratio allows to tailor the surface acidity by introducing aimed quantities of the targeted species. Moreover, the bare sample is not subjected to harsh conditions, therefore preventing structural degradation. An important aspect to be taken into account is that this method does not represent a trade-off in terms of thermal stability, since the covalently attached sulfonic acid entities exhibit comparable or even enhanced thermal resistance as carboxylic acid groups. Phosphates attached to the carbon surface formed during activation with phosphoric acid not only allows to incorporate substantial amounts of acidic species, leading to carbon materials with an outstanding adsorption capacity towards basic compounds as evidenced by a NH_3 uptake of up to almost $1 \text{ mmol}\cdot\text{g}^{-1}$, but also permits a significant improvement of the oxidation resistance. The presence of phosphorus is known to increase the O_2 activation barrier and suppress the formation of highly reactive oxygen radicals.

Increase in basicity is on the contrary achieved by incorporation of nitrogen into the carbon surface. Pyridinic species, which are created to a predominant extent at higher temperatures in the presence of ammonia, serve as Lewis-basic sites since they possess a free electron pair. This simultaneously changes the local electronic structure, which plays a crucial role whenever nanocarbons are employed as a support. For instance, supported catalysts with an improved stability can be obtained since the presence of N-containing species induce an enhancement of the metal-support interaction. Surface modifications by these means have an impact on the structure of the active phase, which in turn affects the catalytic behavior of the supported systems. In contrast to phosphorus, the thermal oxidation stability of nanocarbons are not improved *via* nitrogen functionalization. In fact, its presence can be even detrimental if the heteroatom is a constituent element of surface species instead of being directly incorporated into the carbon lattice. When functional groups like imides and lactams decorate the surface of the nanocarbon, the low thermal stability of these species plays a decisive role since a decomposition at early stages generates defect sites that are attacked by oxygen radicals accelerating the combustion process. As opposed to this, oxidation of carbonaceous materials containing pyrrole-like, pyridinic and quaternary nitrogen species, characterized by notorious higher thermal stabilities, is delayed. In consequence, the onset of combustion is shifted towards temperatures comparable to that of the unmodified sample. Obviously, nitrogen arranged as described before behaves in this regard similarly to sp^2 carbon atoms. These findings are compelling considering the gaining interest of utilizing N-doped CNTs as electrode material in electrochemical applications, where the resistance of carbon against corrosion plays a crucial role.

Although a large number of synthetic approaches have been reported in literature, one of the main problems remains the small amount of pristine carbon material that is commonly functionalized. As long as the focus essentially lies in demonstrating that the modification routine is suitable for altering their surface properties, this issue is not a problem. However, the scale-up capability of a specific method is crucial when it comes to real applications. For this reason, besides following the aim of attempting to understand the intrinsic properties of the modified samples, an important aspect was to functionalize quantities in the gram instead of milligram scale. Based on the obtained results, this goal was successfully accomplished for all modification routes.

Finally, it is highly desirable to develop derivatization approaches that are generic in nature, since they would allow to functionalize various types of nanostructured carbons. This is not straightforward considering that the propensity of nanocarbons towards chemical modification is determined by their specific morphology and structure. Curvature of the graphitic sheets, defect density, ratio of basal-to-edge sites, and crystallinity are some of the factors that have an influence on the reactivity. Future research work should therefore consider testing promising routines not only on carbon nanotubes, but also on graphite, soot, and carbon blacks. The latter are inexpensive carbon materials commonly used in industrial applications that should be regarded as benchmark systems.

Bibliography

- [1] H. W. Kroto, J. R. Heath, S. C. O'Brien, R. F. Curl, R. E. Smalley, *Nature* **1985**, *318*, 162–163.
- [2] S. Larsson, A. Volosov, A. Rosén, *Chem. Phys. Lett.* **1987**, *137*, 501–504.
- [3] S. Satpathy, *Chem. Phys. Lett.* **1986**, *130*, 545–550.
- [4] R. C. Haddon, L. E. Brus, K. Raghavachari, *Chem. Phys. Lett.* **1986**, *125*, 459–464.
- [5] V. Elser, R. C. Haddon, *Nature* **1987**, *325*, 792–794.
- [6] P. W. Fowler, P. Lazzeretti, R. Zanasi, *Chem. Phys. Lett.* **1990**, *165*, 79–86.
- [7] Z. C. Wu, D. A. Jelski, T. F. George, *Chem. Phys. Lett.* **1987**, *137*, 291–294.
- [8] D. E. Weeks, W. G. Harter, *Chem. Phys. Lett.* **1988**, *144*, 366–372.
- [9] R. E. Stanton, M. D. Newton, *J. Phys. Chem.* **1988**, *92*, 2141–2145.
- [10] D. E. Weeks, W. G. Harter, *J. Chem. Phys.* **1989**, *90*, 4744–4771.
- [11] W. Krätschmer, L. D. Lamb, K. Fostiropoulos, D. R. Huffman, *Nature* **1990**, *347*, 354–358.
- [12] S. Iijima, *Nature* **1991**, *354*, 56–58.
- [13] R. Bacon, *J. Appl. Phys.* **1960**, *31*, 283–290.
- [14] A. Oberlin, M. Endo, T. Koyama, *J. Cryst. Growth* **1976**, *32*, 335–349.
- [15] G. G. Tibbetts, *J. Cryst. Growth* **1984**, *66*, 632–638.
- [16] J. S. Speck, M. Endo, M. S. Dresselhaus, *J. Cryst. Growth* **1989**, *94*, 834–848.
- [17] D. H. Robertson, D. W. Brenner, J. W. Mintmire, *Phys. Rev. B* **1992**, *45*, 12592–12595.
- [18] J. W. Mintmire, B. I. Dunlap, C. T. White, *Phys. Rev. Lett.* **1992**, *68*, 631–634.

- [19] N. Hamada, S.-i. Sawada, A. Oshiyama, *Phys. Rev. Lett.* **1992**, *68*, 1579–1581.
- [20] S. Iijima, T. Ichihashi, *Nature* **1993**, *363*, 603–605.
- [21] D. S. Bethune, C. H. Klang, M. S. de Vries, G. Gorman, S. R., J. Vazquez, R. Beyers, *Nature* **1993**, *363*, 605–607.
- [22] J. W. G. Wildöer, L. C. Venema, A. G. Rinzler, R. E. Smalley, C. Dekker, *Nature* **1998**, *391*, 59–62.
- [23] T. W. Odom, J.-L. Huang, P. Kim, C. M. Lieber, *Nature* **1998**, *391*, 62–64.
- [24] A. K. Geim, K. S. Novoselov, *Nat. Mater.* **2007**, *6*, 183–191.
- [25] M. Dresselhaus, P. Avouris in *Carbon Nanotubes*, Vol. 80 of *Top. Appl. Phys.*, M. Dresselhaus, G. Dresselhaus, P. Avouris (Eds.), Springer Berlin / Heidelberg, **2001**, pp. 1–9.
- [26] R. H. Baughman, *Science* **2002**, *297*, 787–792.
- [27] A. T. Jung, Ph.D. thesis, Universitätsbibliothek der Universität Erlangen-Nürnberg, Erlangen, **2007**.
- [28] S. Reich, C. Thomsen, J. Maultzsch, *Carbon nanotubes: Basic concepts and physical properties 2nd ed.*, Wiley-VCH, Weinheim, **2005**.
- [29] A. G. de Souza Filho, F. S. Binotto, *Química Nova* **2007**, *30*, 1695–1703.
- [30] M. Dresselhaus, G. Dresselhaus, R. Saito, *Carbon* **1995**, *33*, 883–891.
- [31] S. Amelinckx, D. Bernaerts in *Supercarbon*, Vol. 33 of *Springer series in materials science*, S. Yoshimura, R. P. H. Chang (Eds.), Springer, Berlin, **1998**, pp. 51–80.
- [32] S. Amelinckx, D. Bernaerts, X. B. Zhang, G. van Tendeloo, J. van Landuyt, *Science* **1995**, *267*, 1334–1338.
- [33] M. Liu, J. M. Cowley, *Ultramicroscopy* **1994**, *53*, 333–342.
- [34] J.-P. Tessonnier, D. Rosenthal, T. W. Hansen, C. Hess, M. E. Schuster, R. Blume, G. Frank, N. Pfänder, O. Timpe, D. S. Su, R. Schlögl, *Carbon* **2009**, *47*, 1779–1798.
- [35] S. Blatt, Ph.D. thesis, Karlsruhe Institute of Technology, **2008**.

- [36] F. Hauke, A. Hirsch in *Carbon Nanotubes and Related Structures: Synthesis, Characterization, Functionalization, and Applications*, D. M. Guldi, N. Martín (Eds.), Wiley-VCH Verlag GmbH & Co. KGaA, **2010**, chapter 6, pp. 135–198.
- [37] M. Prato, *J. Mater. Chem.* **1997**, *7*, 1097–1109.
- [38] S. Niyogi, M. A. Hamon, H. Hu, B. Zhao, P. Bhowmik, R. Sen, M. E. Itkis, R. C. Haddon, *Acc. Chem. Res.* **2002**, *35*, 1105–1113.
- [39] A. Hirsch, O. Vostrowsky in *Functional Molecular Nanostructures*, Vol. 245 of *Topics in Current Chemistry*, A. D. Schlüter (Ed.), Springer Berlin / Heidelberg, **2005**, pp. 193–237.
- [40] R. C. Haddon, G. E. Scuseria, R. E. Smalley, *Chem. Phys. Lett.* **1997**, *272*, 38–42.
- [41] Z. Chen, W. Thiel, A. Hirsch, *ChemPhysChem* **2003**, *4*, 93–97.
- [42] M. Müller, J. Maultzsch, D. Wunderlich, A. Hirsch, C. Thomsen, *physica status solidi (b)* **2008**, *245*, 1957–1960.
- [43] N. Li, Y. Huang, F. Du, X. He, X. Lin, H. Gao, Y. Ma, F. Li, Y. Chen, P. C. Eklund, *Nano Lett.* **2006**, *6*, 1141–1145.
- [44] A. G. Rinzler, J. H. Hafner, P. Nikolaev, P. Nordlander, D. T. Colbert, R. E. Smalley, L. Lou, S. G. Kim, D. Tománek, *Science* **1995**, *269*, 1550–1553.
- [45] W. A. de Heer, A. Châtelain, D. Ugarte, *Science* **1995**, *270*, 1179–1180.
- [46] K. H. An, W. S. Kim, Y. S. Park, J.-M. Moon, D. J. Bae, S. C. Lim, Y. S. Lee, Y. H. Lee, *Adv. Funct. Mater.* **2001**, *11*, 387–392.
- [47] M. Hirscher, M. Becher, M. Haluska, A. Quintel, V. Skakalova, Y.-M. Choi, U. Dettlaff-Weglikowska, S. Roth, I. Stepanek, P. Bernier, A. Leonhardt, J. Fink, *J. Alloys Compd.* **2002**, *330-332*, 654–658.
- [48] P. G. Collins, K. Bradley, M. Ishigami, A. Zettl, *Science* **2000**, *287*, 1801–1804.
- [49] J. H. Hafner, C. L. Cheung, C. M. Lieber, *Nature* **1999**, *398*, 761–762.
- [50] K. D. Ausman, R. Piner, O. Lourie, R. S. Ruoff, M. Korobov, *J. Phys. Chem. B* **2000**, *104*, 8911–8915.

- [51] M. A. Herranz, N. Martín in *Carbon Nanotubes and Related Structures: Synthesis, Characterization Functionalization, and Applications*, D. M. Guldi, N. Martín (Eds.), Wiley-VCH Verlag GmbH & Co. KGaA, **2010**, chapter 5, pp. 103–134.
- [52] T. Fujigaya, N. Nakashima, *Polymer Journal* **2008**, *40*, 577–589.
- [53] M. J. O’Connell, S. M. Bachilo, C. B. Huffman, V. C. Moore, M. S. Strano, E. H. Haroz, K. L. Rialon, P. J. Boul, W. H. Noon, C. Kittrell, J. Ma, R. H. Hauge, R. B. Weisman, R. E. Smalley, *Science* **2002**, *297*, 593–596.
- [54] S. M. Bachilo, M. S. Strano, C. Kittrell, R. H. Hauge, R. E. Smalley, R. B. Weisman, *Science* **2002**, *298*, 2361–2366.
- [55] L. Jiang, L. Gao, J. Sun, *J. Colloid Interface Sci.* **2003**, *260*, 89–94.
- [56] V. C. Moore, M. S. Strano, E. H. Haroz, R. H. Hauge, R. E. Smalley, J. Schmidt, Y. Talmon, *Nano Lett.* **2003**, *3*, 1379–1382.
- [57] C. Richard, F. Balavoine, P. Schultz, T. W. Ebbesen, C. Mioskowski, *Science* **2003**, *300*, 775–778.
- [58] Y. Liu, L. Gao, J. Sun, *J. Phys. Chem. C* **2007**, *111*, 1223–1229.
- [59] M. F. Islam, E. Rojas, D. M. Bergey, A. T. Johnson, A. G. Yodh, *Nano Lett.* **2003**, *3*, 269–273.
- [60] D. Tasis, N. Tagmatarchis, A. Bianco, M. Prato, *Chem. Rev.* **2006**, *106*, 1105–1136.
- [61] D. Qian, E. C. Dickey, R. Andrews, T. Rantell, *Appl. Phys. Lett.* **2000**, *76*, 2868–2870.
- [62] M. López Manchado, L. Valentini, J. Biagiotti, J. Kenny, *Carbon* **2005**, *43*, 1499–1505.
- [63] B. Z. Tang, H. Xu, *Macromolecules* **1999**, *32*, 2569–2576.
- [64] S. A. Curran, P. M. Ajayan, W. J. Blau, D. L. Carroll, J. N. Coleman, A. B. Dalton, A. P. Davey, A. Drury, B. McCarthy, S. Maier, A. Strevens, *Adv. Mater.* **1998**, *10*, 1091–1093.
- [65] K. Besteman, J.-O. Lee, F. G. M. Wiertz, H. A. Heering, C. Dekker, *Nano Lett.* **2003**, *3*, 727–730.

- [66] L. Agüí, M. Eguílaz, C. Peña Farfal, P. Yáñez Sedeño, J. Pingarrón, *Electroanalysis* **2009**, *21*, 386–391.
- [67] J. Wang, A. Kawde, M. Musameh, *Analyst* **2003**, *128*, 912–916.
- [68] T. W. Chamberlain, M. d. C. Gimenez-Lopez, A. N. Khlobystov in *Carbon Nanotubes and Related Structures: Synthesis, Characterization Functionalization, and Applications*, D. M. Guldi, N. Martín (Eds.), Wiley-VCH Verlag GmbH & Co. KGaA, **2010**, chapter 12, pp. 349–384.
- [69] B. W. Smith, M. Monthieux, D. E. Luzzi, *Nature* **1998**, *396*, 323–324.
- [70] Y. Zhang, S. Iijima, Z. Shi, Z. Gu, *Philos. Mag. Lett.* **1999**, *79*, 473–479.
- [71] J. Sloan, R. E. Dunin-Borkowski, J. L. Hutchison, K. S. Coleman, V. C. Williams, J. B. Claridge, A. P. E. York, C. Xu, S. R. Bailey, G. Brown, S. Friedrichs, M. L. H. Green, *Chem. Phys. Lett.* **2000**, *316*, 191–198.
- [72] B. W. Smith, D. E. Luzzi, *Chem. Phys. Lett.* **2000**, *321*, 169–174.
- [73] H. Kataura, Y. Maniwa, T. Kodama, K. Kikuchi, K. Hirahara, K. Suenaga, S. Iijima, S. Suzuki, Y. Achiba, W. Krätschmer, *Synth. Met.* **2001**, *121*, 1195–1196.
- [74] H. Ulbricht, G. Moos, T. Hertel, *Phys. Rev. Lett.* **2003**, *90*, 095501.
- [75] K. Hirahara, S. Bandow, K. Suenaga, H. Kato, T. Okazaki, H. Shinohara, S. Iijima, *Phys. Rev. B* **2001**, *64*, 115420.
- [76] H. Kataura, Y. Maniwa, M. Abe, A. Fujiwara, T. Kodama, K. Kikuchi, H. Imahori, Y. Misaki, S. Suzuki, Y. Achiba, *Appl. Phys. A: Mater. Sci. Process.* **2002**, *74*, 349–354.
- [77] L. Kavan, L. Dunsch, H. Kataura, *Chem. Phys. Lett.* **2002**, *361*, 79–85.
- [78] M. Burghard, *Surf. Sci. Rep.* **2005**, *58*, 1–109.
- [79] D. J. Hornbaker, S.-J. Kahng, S. Misra, B. W. Smith, A. T. Johnson, E. J. Mele, D. E. Luzzi, A. Yazdani, *Science* **2002**, *295*, 828–831.
- [80] S. Banerjee, T. Hemraj-Benny, S. S. Wong, *Adv. Mater.* **2005**, *17*, 17–29.
- [81] W. Huang, Y. Wang, G. Luo, F. Wei, *Carbon* **2003**, *41*, 2585–2590.

- [82] J. Liu, A. G. Rinzler, H. Dai, J. H. Hafner, R. K. Bradley, P. J. Boul, A. Lu, T. Iverson, K. Shelimov, C. B. Huffman, F. Rodriguez-Macias, Y.-S. Shon, T. R. Lee, D. T. Colbert, R. E. Smalley, *Science* **1998**, *280*, 1253–1256.
- [83] J. Chen, M. A. Hamon, H. Hu, Y. Chen, A. M. Rao, P. C. Eklund, R. C. Haddon, *Science* **1998**, *282*, 95–98.
- [84] M. A. Hamon, J. Chen, H. Hu, Y. Chen, M. E. Itkis, A. M. Rao, P. C. Eklund, R. C. Haddon, *Adv. Mater.* **1999**, *11*, 834–840.
- [85] Y.-P. Sun, W. Huang, Y. Lin, K. Fu, A. Kitaygorodskiy, L. A. Riddle, Y. J. Yu, D. L. Carroll, *Chem. Mater.* **2001**, *13*, 2864–2869.
- [86] K. Fu, W. Huang, Y. Lin, L. A. Riddle, D. L. Carroll, Y.-P. Sun, *Nano Lett.* **2001**, *1*, 439–441.
- [87] K. Fu, A. Kitaygorodskiy, A. M. Rao, Y.-P. Sun, *Nano Lett.* **2002**, *2*, 1165–1168.
- [88] L. Qu, R. B. Martin, W. Huang, K. Fu, D. Zweifel, Y. Lin, Y.-P. Sun, C. E. Bunker, B. A. Harruff, J. R. Gord, L. F. Allard, *J. Chem. Phys.* **2002**, *117*, 8089–8094.
- [89] B. Li, Z. Shi, Y. Lian, Z. Gu, *Chem. Lett.* **2001**, *30*, 598–599.
- [90] N. Hu, G. Dang, H. Zhou, J. Jing, C. Chen, *Mater. Lett.* **2007**, *61*, 5285–5287.
- [91] W. E. Ford, A. Jung, A. Hirsch, R. Graupner, F. Scholz, A. Yasuda, J. M. Wessels, *Adv. Mater.* **2006**, *18*, 1193–1197.
- [92] T. J. Bandosz in *Carbon Materials for Catalysis*, John Wiley & Sons, Inc., **2008**, chapter 2, pp. 45–92.
- [93] C. A. León y León, J. M. Solar, V. Calemma, L. R. Radovic, *Carbon* **1992**, *30*, 797–811.
- [94] M. Montes-Morán, D. Suárez, J. Menéndez, E. Fuente, *Carbon* **2004**, *42*, 1219–1225.
- [95] S. van Dommele, A. Romero-Izquierdo, R. Brydson, K. P. de Jong, J. H. Bitter, *Carbon* **2008**, *46*, 138–148.
- [96] R. Arrigo, M. Havecker, R. Schlögl, D. S. Su, *Chem. Commun.* **2008**, 4891–4893.
- [97] R. Arrigo, M. Hävecker, S. Wrabetz, R. Blume, M. Lerch, J. McGregor, E. P. J. Parrott, J. A. Zeitler, L. F. Gladden, A. Knop-Gericke, R. Schlögl, D. S. Su, *J. Am. Chem. Soc.* **2010**, *132*, 9616–9630.

- [98] H. P. Boehm, *Carbon* **1994**, *32*, 759–769.
- [99] L. R. Radovic, F. Rodríguez-Reinoso in *Chemistry and Physics of Carbon*, Vol. 25, P. Thrower (Ed.), Dekker, New York, **1994**, pp. 243–358.
- [100] R. Schlögl in *Handbook of Heterogeneous Catalysis*, Wiley-VCH Verlag GmbH & Co. KGaA, **2008**.
- [101] F. Rodríguez-Reinoso, *Carbon* **1998**, *36*, 159–175.
- [102] L. R. Radovic, C. A. Leon y Leon in *Chemistry and Physics of Carbon*, Vol. 24, P. Thrower (Ed.), Dekker, New York, **1994**, pp. 213–310.
- [103] W. Schneider, W. Diller in *Ullmann's Encyclopedia of Industrial Chemistry*, Wiley-VCH Verlag GmbH & Co. KGaA, **2000**.
- [104] H. D. Lauss, W. Steffens in *Ullmann's Encyclopedia of Industrial Chemistry*, Wiley-VCH Verlag GmbH & Co. KGaA, **2000**.
- [105] J. Wieckowska, *Catal. Today* **1995**, *24*, 405–465.
- [106] T. G. Alkhazov, A. E. Lisovskii, Y. A. Ismailov, A. I. Kozharov, *Kinet. Catal.* **1978**, *19*, 482–485.
- [107] J. L. Figueiredo, M. F. R. Pereira, *Catal. Today* **2010**, *150*, 2–7.
- [108] T. G. Alkhazov, A. E. Lisovskii, T. K. Gulakhmedova, *React. Kinet. Catal. Lett.* **1979**, *12*, 189–193.
- [109] M. F. R. Pereira, J. J. M. Órfão, J. L. Figueiredo, *Appl. Catal., A* **1999**, *184*, 153–160.
- [110] D. S. Su, J. J. Delgado, X. Liu, D. Wang, R. Schlögl, L. Wang, Z. Zhang, Z. Shan, F. S. Xiao, *Chem. Asian J.* **2009**, *4*, 1108–1113.
- [111] T.-J. Zhao, W.-Z. Sun, X.-Y. Gu, M. Rønning, Chen, Y.-C. Dai, W.-K. Yuan, A. Holmen, *Appl. Catal., A* **2007**, *323*, 135–146.
- [112] R. S. Drago, K. Jurczyk, *Appl. Catal., A* **1994**, *112*, 117–124.
- [113] J. Delgado, X. Chen, J. Tessonnier, M. Schuster, E. D. Rio, R. Schlögl, D. Su, *Catal. Today* **2010**, *150*, 49–54.

- [114] A. Rinaldi, J. Zhang, B. Frank, D. S. Su, S. B. Abd Hamid, R. Schlögl, *ChemSusChem* **2010**, *3*, 254–260.
- [115] B. Frank, J. Zhang, R. Blume, R. Schlögl, D. S. Su, *Angew. Chem., Int. Ed.* **2009**, *48*, 6913–6917.
- [116] B. Frank, M. Morassutto, R. Schomäcker, R. Schlögl, D. S. Su, *ChemCatChem* **2010**, *2*, 644–648.
- [117] J. L. Figueiredo, M. F. R. Pereira in *Carbon Materials for Catalysis*, John Wiley & Sons, Inc., **2008**, chapter 4, pp. 177–217.
- [118] G. S. Szymański, G. Rychlicki, *Carbon* **1991**, *29*, 489–498.
- [119] G. S. Szymański, G. Rychlicki, *React. Kinet. Catal. Lett.* **1991**, *43*, 475–479.
- [120] G. S. Szymański, G. Rychlicki, *Carbon* **1993**, *31*, 247–257.
- [121] G. S. Szymański, G. Rychlicki, A. P. Terzyk, *Carbon* **1994**, *32*, 265–271.
- [122] F. Carrasco-Marín, A. Mueden, C. Moreno-Castilla, *J. Phys. Chem. B* **1998**, *102*, 9239–9244.
- [123] C. Moreno-Castilla, M. López-Ramón, M. Carrasco-Marín, *Carbon* **2000**, *38*, 1995–2001.
- [124] C. Moreno-Castilla, F. Carrasco-Marín, C. Parejo-Pérez, M. L. Ramón, *Carbon* **2001**, *39*, 869–875.
- [125] J. Zawadzki, M. Wiśniewski, J. Weber, O. Heintz, B. Azambre, *Carbon* **2001**, *39*, 187–192.
- [126] G. S. Szymański, Z. Karpiński, S. Biniak, A. Świątkowski, *Carbon* **2002**, *40*, 2627–2639.
- [127] A. F. Pérez-Cadenas, F. J. Maldonado-Hódar, M.-C. Carlos, *Carbon* **2003**, *41*, 473–478.
- [128] R. Rioux, M. Vannice, *J. Catal.* **2003**, *216*, 362–376.
- [129] E. Jasińska, B. Krzyżyńska, M. Kozłowski, *Catal. Lett.* **2008**, *125*, 145–153.
- [130] J. Bedia, J. M. Rosas, J. Márquez, J. Rodríguez-Mirasol, T. Cordero, *Carbon* **2009**, *47*, 286–294.

- [131] J. Bedia, R. Ruiz-Rosas, J. Rodríguez-Mirasol, T. Cordero, *J. Catal.* **2010**, *271*, 33–42.
- [132] J. Bedia, R. Ruiz-Rosas, J. Rodríguez-Mirasol, T. Cordero, *AIChE J.* **2010**, *56*, 1557–1568.
- [133] J. Bedia, J. Rosas, D. Vera, J. Rodríguez-Mirasol, T. Cordero, *Catal. Today* **2010**, *158*, 89–96.
- [134] J. Bedia, R. Barrionuevo, J. Rodríguez-Mirasol, T. Cordero, *Appl. Catal., B* **2011**, *103*, 302–310.
- [135] J. Jasińska, B. Krzyżyńska, M. Kozłowski, *Cent. Eur. J. Chem.* **2011**, *9*, 925–931.
- [136] R. T. Mayes, P. F. Fulvio, Z. Ma, S. Dai, *Phys. Chem. Chem. Phys.* **2011**, *13*, 2492–2494.
- [137] A. Corma, H. García, *Chem. Rev.* **2003**, *103*, 4307–4366.
- [138] C. Lucarelli, A. Vaccari, *Green Chem.* **2011**, *13*, 1941–1949.
- [139] K. Tanabe, W. F. Hölderich, *Appl. Catal., A* **1999**, *181*, 399–434.
- [140] S. Yan, C. DiMaggio, S. Mohan, M. Kim, S. O. Salley, K. Y. S. Ng, *Top. Catal.* **2010**, *53*, 721–736.
- [141] J. L. Bahr, J. M. Tour, *Chem. Mater.* **2001**, *13*, 3823–3824.
- [142] J. L. Bahr, E. T. Mickelson, M. J. Bronikowski, R. E. Smalley, J. M. Tour, *Chem. Commun.* **2001**, *0*, 193–194.
- [143] A. Hirsch, O. Vostrowsky in *Functional Molecular Nanostructures*, Vol. 245 of *Topics in Current Chemistry*, A. Schlüter (Ed.), Springer Berlin Heidelberg, **2005**, pp. 193–237.
- [144] I. D. Rosca, F. Watari, M. Uo, T. Akasaka, *Carbon* **2005**, *43*, 3124–3131.
- [145] H. Yu, Y. Jin, F. Peng, H. Wang, J. Yang, *J. Phys. Chem. C* **2008**, *112*, 6758–6763.
- [146] V. Likodimos, T. A. Steriotis, S. K. Papageorgiou, G. E. Romanos, R. R. Marques, R. P. Rocha, J. L. Faria, M. F. Pereira, J. L. Figueiredo, A. M. Silva, P. Falaras, *Carbon* **2014**, *69*, 311–326.

- [147] T. Shimada, H. Yanase, K. Morishita, J.-i. Hayashi, T. Chiba, *Carbon* **2004**, *42*, 1635–1639.
- [148] A. Fallah, Y. Nakayama, *Carbon* **2012**, *50*, 1879–1887.
- [149] Y.-R. Shin, I.-Y. Jeon, J.-B. Baek, *Carbon* **2012**, *50*, 1465–1476.
- [150] K. A. Wepasnick, B. A. Smith, K. E. Schrote, H. K. Wilson, S. R. Diegelmann, D. H. Fairbrother, *Carbon* **2011**, *49*, 24–36.
- [151] S. Santangelo, G. Messina, G. Faggio, S. H. Abdul Rahim, C. Milone, *J. Raman Spectrosc.* **2012**, *43*, 1432–1442.
- [152] P. Cañete Rosales, V. Ortega, A. Álvarez-Lueje, S. Bollo, M. González, A. Ansán, M. T. Martínez, *Electrochim. Acta* **2012**, *62*, 163–171.
- [153] B. K. Price, J. M. Tour, *J. Am. Chem. Soc.* **2006**, *128*, 12899–12904.
- [154] P. Lin, B. Li, J. Li, H. Wang, X. Bian, X. Wang, *Catal. Lett.* **2010**, *141*, 459–466.
- [155] D. R. Stellwagen, F. van der Klis, D. S. van Es, K. P. de Jong, J. H. Bitter, *ChemSusChem* **2013**, *6*, 1668–1672.
- [156] S. Brunauer, P. H. Emmett, E. Teller, *J. Am. Chem. Soc.* **1938**, *60*, 309–319.
- [157] E. P. Barrett, L. G. Joyner, P. P. Halenda, *J. Am. Chem. Soc.* **1951**, *73*, 373–380.
- [158] R. Mikhail, S. Brunauer, E. Bodor, *J. Colloid Interface Sci.* **1968**, *26*, 45–53.
- [159] C. A. Dyke, M. P. Stewart, F. Maya, J. M. Tour, *Synlett* **2004**, 155–160.
- [160] S. Campidelli, B. Ballesteros, A. Filoramo, D. Díaz Díaz, G. de la Torre, T. Torres, G. M. A. Rahman, C. Ehli, D. Kiessling, F. Werner, V. Sgobba, D. M. Guldi, C. Cioffi, M. Prato, J.-P. Bourgoïn, *J. Am. Chem. Soc.* **2008**, *130*, 11503–11509.
- [161] J. M. González-Domínguez, M. González, A. Ansón-Casaos, A. M. Díez-Pascual, M. A. Gómez, M. T. Martínez, *J. Phys. Chem. C* **2011**, *115*, 7238–7248.
- [162] C. Ménard-Moyon, C. Fabbro, M. Prato, A. Bianco, *Chem. Eur. J.* **2011**, *17*, 3222–3227.
- [163] H. Leinonen, M. Lajunen, *J. Nanopart. Res.* **2012**, *14*, 1–12.
- [164] H. R. Darabi, M. Jafar Tehrani, K. Aghapoor, F. Mohsenzadeh, R. Malekfar, *Appl. Surf. Sci.* **2012**, *258*, 8953–8958.

- [165] P. Luksirikul, K. Tedsree, M. G. Moloney, M. L. H. Green, S. C. E. Tsang, *Angew. Chem., Int. Ed.* **2012**, *51*, 6998–7001.
- [166] F. Wang, K.-J. Deng, L. Zhou, J.-B. Zhao, X.-H. Ke, L.-L. Wen, *J. Inorg. Organomet. Polym. Mater.* **2012**, *22*, 1182–1188.
- [167] S. A. Farokhi, S. T. Nandibewoor, *Tetrahedron* **2003**, *59*, 7595–7602.
- [168] K. S. W. Sing, *Pure Appl. Chem.* **1985**, *57*, 603–619.
- [169] G. Cheng, T. Hasell, A. Trewin, D. J. Adams, A. I. Cooper, *Angew. Chem., Int. Ed.* **2012**, *51*, 12727–12731.
- [170] J. L. Culshaw, G. Cheng, M. Schmidtman, T. Hasell, M. Liu, D. J. Adams, A. I. Cooper, *J. Am. Chem. Soc.* **2013**, *135*, 10007–10010.
- [171] G. Giambastiani, S. Cicchi, A. Giannasi, L. Luconi, A. Rossin, F. Mercuri, C. Bianchini, A. Brandi, M. Melucci, G. Ghini, P. Stagnaro, L. Conzatti, E. Passaglia, M. Zoppi, T. Montini, P. Fornasiero, *Chem. Mater.* **2011**, *23*, 1923–1938.
- [172] J. Figueiredo, M. Pereira, M. Freitas, J. Órfão, *Carbon* **1999**, *37*, 1379–1389.
- [173] A. P. Terzyk, *J. Colloid Interface Sci.* **2003**, *268*, 301–329.
- [174] H. T. Gomes, S. M. Miranda, M. J. Sampaio, A. M. Silva, J. L. Faria, *Catal. Today* **2010**, *151*, 153–158.
- [175] D.-Q. Yang, J.-F. Rochette, E. Sacher, *J. Phys. Chem. B* **2005**, *109*, 7788–7794.
- [176] Y. G. Adewuyi, *Ind. Eng. Chem. Res.* **2001**, *40*, 4681–4715.
- [177] Z.-P. Sun, X.-G. Zhang, R.-L. Liu, Y.-Y. Liang, H.-L. Li, *J. Power Sources* **2008**, *185*, 801–806.
- [178] X. Liu, B. Frank, W. Zhang, T. P. Cotter, R. Schlögl, D. S. Su, *Angew. Chem., Int. Ed.* **2011**, *50*, 3318–3322.
- [179] J. J. Delgado, X.-W. Chen, B. Frank, D. S. Su, R. Schlögl, *Catal. Today* **2012**, *186*, 93–98.
- [180] X. Chen, *J. Catal.* **2001**, *197*, 292–302.
- [181] R. Liu, X. Wang, X. Zhao, P. Feng, *Carbon* **2008**, *46*, 1664–1669.

- [182] W. Zhao, B. Yang, C. Yi, Z. Lei, J. Xu, *Ind. Eng. Chem. Res.* **2010**, *49*, 12399–12404.
- [183] B. Philip, J. Xie, A. Chandrasekhar, J. Abraham, V. K. Varadan, *Smart Mater. Struct.* **2004**, *13*, 295–298.
- [184] D. Yan, G. Yang, *J. Appl. Polym. Sci.* **2009**, *112*, 3620–3626.
- [185] S. van Dommele, K. P. de Jong, J. H. Bitter, *Chem. Commun.* **2006**, 4859–4861.
- [186] C. Chen, J. Zhang, B. Zhang, C. Yu, F. Peng, D. Su, *Chem. Commun.* **2013**, *49*, 8151–8153.
- [187] S. Kundu, T. C. Nagaiah, W. Xia, Y. Wang, S. V. Dommele, J. H. Bitter, M. Santa, G. Grundmeier, M. Bron, W. Schuhmann, M. Muhler, *J. Phys. Chem. C* **2009**, *113*, 14302–14310.
- [188] R. Arrigo, S. Wrabetz, M. E. Schuster, D. Wang, A. Villa, D. Rosenthal, F. Girsgdies, G. Weinberg, L. Prati, R. Schlögl, D. S. Su, *Phys. Chem. Chem. Phys.* **2012**, *14*, 10523–10532.
- [189] A. Villa, D. Wang, P. Spontoni, R. Arrigo, D. Su, L. Prati, *Catal. Today* **2010**, *157*, 89–93.
- [190] S. Kundu, W. Xia, W. Busser, M. Becker, D. A. Schmidt, M. Havenith, M. Muhler, *Phys. Chem. Chem. Phys.* **2010**, *12*, 4351–4359.
- [191] B. Stöhr, H. Boehm, R. Schlögl, *Carbon* **1991**, *29*, 707–720.
- [192] N. Fairley, A. Carrick, *The Casa cookbook*, Acolyte Science, Cheshire, **2005**.
- [193] A. Proctor, P. M. Sherwood, *J. Electron Spectrosc. Relat. Phenom.* **1982**, *27*, 39–56.
- [194] A. Proctor, P. M. A. Sherwood, *Anal. Chem.* **1982**, *54*, 13–19.
- [195] D. Shirley, *Phys. Rev. B* **1972**, *5*, 4709–4714.
- [196] J. Yeh, I. Lindau, *At. Data Nucl. Data Tables* **1985**, *32*, 1–155.
- [197] H. Boehm, G. Mair, T. Stoehr, A. R. De Rincón, B. Tereczki, *Fuel* **1984**, *63*, 1061–1063.
- [198] J. A. Menéndez, J. Phillips, B. Xia, L. R. Radovic, *Langmuir* **1996**, *12*, 4404–4410.
- [199] M. S. Shafeeyan, W. M. A. W. Daud, A. Houshmand, A. Arami-Niya, *Appl. Surf. Sci.* **2011**, *257*, 3936–3942.

- [200] S. Haydar, C. Moreno-Castilla, M. Ferro-García, F. Carrasco-Marín, J. Rivera-Utrilla, A. Perrard, J. Joly, *Carbon* **2000**, *38*, 1297–1308.
- [201] E. K. Fields, S. Meyerson, *Chem. Commun.* **1965**, 474–476.
- [202] K. Chen, J. C. Mackie, D. Wojtalewicz, E. M. Kennedy, B. Z. Dlugogorski, *J. Hazard. Mater.* **2011**, *187*, 407–412.
- [203] S.-T. Etemad-Rad, E. Metcalfe, *Fire Mater.* **1993**, *17*, 33–37.
- [204] G. Choudhary, A. M. Cameron, R. A. Back, *J. Phys. Chem.* **1968**, *72*, 2289–2292.
- [205] C. W. Hand, D. J. Bogan, *J. Phys. Chem.* **1971**, *75*, 1532–1536.
- [206] K.-M. Hansson, J. Samuelsson, L.-E. Åmand, C. Tullin, *Fuel* **2003**, *82*, 2163–2172.
- [207] X. Hong, L. Zhang, T. Zhang, F. Qi, *J. Phys. Chem. A* **2009**, *113*, 5397–5405.
- [208] E. Ikeda, J. C. Mackie, *J. Anal. Appl. Pyrolysis* **1995**, *34*, 47–63.
- [209] B. Xiao, J. P. Boudou, K. M. Thomas, *Langmuir* **2005**, *21*, 3400–3409.
- [210] J. M. Jones, A. W. Harding, S. D. Brown, K. Thomas, *Carbon* **1995**, *33*, 833–843.
- [211] F. Matthias Bickelhaupt, R. H. Fokkens, L. J. De Koning, N. M. Nibbering, E. J. Baerends, S. J. Goede, F. Bickelhaupt, *Int. J. Mass Spectrom. Ion Processes* **1991**, *103*, 157–168.
- [212] J. Casanovas, J. M. Ricart, J. Rubio, F. Illas, J. M. Jiménez-Mateos, *J. Am. Chem. Soc.* **1996**, *118*, 8071–8076.
- [213] R. Jansen, H. van Bekkum, *Carbon* **1995**, *33*, 1021–1027.
- [214] R. Graupner, J. Abraham, A. Vencelová, T. Seyller, F. Hennrich, M. M. Kappes, A. Hirsch, L. Ley, *Phys. Chem. Chem. Phys.* **2003**, *5*, 5472–5476.
- [215] J. Pels, F. Kapteijn, J. Moulijn, Q. Zhu, K. Thomas, *Carbon* **1995**, *33*, 1641–1653.
- [216] C. Kozłowski, P. M. Sherwood, *J. Chem. Soc. Faraday Trans. 1* **1985**, *81*, 2745–2756.
- [217] B. Marchon, J. Carrazza, H. Heinemann, G. Somorjai, *Carbon* **1988**, *26*, 507–514.
- [218] D. Rosenthal, M. Ruta, R. Schlögl, L. Kiwi-Minsker, *Carbon* **2010**, *48*, 1835–1843.
- [219] T. Ohta, M. Yamada, H. Kuroda, *Bull. Chem. Soc. Jpn.* **1974**, *47*, 1158–1161.

- [220] T. Takahagi, I. Shimada, M. Fukuhara, K. Morita, A. Ishitani, *J. Polym. Sci., Part A: Polym. Chem.* **1986**, *24*, 3101–3107.
- [221] M. Ai, *J. Catal.* **1975**, *40*, 318–326.
- [222] J. A. Fuwape, *Agrofor. Syst.* **1993**, *22*, 175–179.
- [223] F. Emmerich, C. Luengo, *Biomass Bioenergy* **1996**, *10*, 41–44.
- [224] P. K. Gallagher, Z. Zhong, *J. Therm. Anal.* **1992**, *38*, 2247–2255.
- [225] W. M. Haynes, C. R. Company, *CRC handbook of chemistry and physics*, CRC Press, Boca Raton, Fla.; London, **2013**.
- [226] B. Frank, J. Zhang, R. Blume, R. Schlögl, D. S. Su, *Angew. Chem., Int. Ed.* **2009**, *48*, 6913–6917.
- [227] J. Rakszawski, W. Parker, *Carbon* **1964**, *2*, 53–63.
- [228] T. Đurkić, A. Perić, M. Laušević, A. Dekanski, O. Nešković, M. Veljković, Z. Laušević, *Carbon* **1997**, *35*, 1567–1572.
- [229] Y.-J. Lee, L. R. Radovic, *Carbon* **2003**, *41*, 1987–1997.
- [230] D. Savchenko, A. Serdan, V. Morozov, G. Van Tendeloo, S. Ionov, *New Carbon Mater.* **2012**, *27*, 12–18.
- [231] D. McKee, C. Spiro, E. Lamby, *Carbon* **1984**, *22*, 285–290.
- [232] S. Labruquère, R. Pailler, R. Naslain, B. Desbat, *J. Eur. Ceram. Soc.* **1998**, *18*, 1953–1960.
- [233] X. Wu, L. R. Radovic, *Carbon* **2006**, *44*, 141–151.
- [234] J. Rosas, J. Bedia, J. Rodríguez-Mirasol, T. Cordero, *Fuel* **2009**, *88*, 19–26.
- [235] J. M. Rosas, R. Ruiz-Rosas, J. Rodríguez-Mirasol, T. Cordero, *Carbon* **2012**, *50*, 1523–1537.
- [236] A. Seron, H. Benaddi, F. Beguin, E. Frackowiak, J. Bretelle, M. Thiry, T. Bandosz, J. Jagiello, J. Schwarz, *Carbon* **1996**, *34*, 481–487.
- [237] V. Strelko Jr, M. Streat, O. Kozynchenko, *React. Funct. Polym.* **1999**, *41*, 245–253.

- [238] A. M. Puziy, O. I. Poddubnaya, A. Martínez-Alonso, A. Castro-Muñiz, F. Suárez-García, T. J. M. D., *Carbon* **2007**, *45*, 1941–1950.
- [239] Z. Jin, Z. Sun, L. J. Simpson, K. J. O'Neil, P. A. Parilla, Y. Li, N. P. Stadie, C. C. Ahn, C. Kittrell, J. M. Tour, *J. Am. Chem. Soc.* **2010**, *132*, 15246–15251.
- [240] A. M. Puzii, *Theor. Exp. Chem.* **2011**, *47*, 277–291.
- [241] M. Solum, R. Pugmire, M. Jagtoyen, F. Derbyshire, *Carbon* **1995**, *33*, 1247–1254.
- [242] A. M. Puziy, O. I. Poddubnaya, A. Martínez-Alonso, F. Suárez-García, J. M. Tascón, *Carbon* **2002**, *40*, 1493–1505.
- [243] A. M. Puziy, O. I. Poddubnaya, A. Martínez-Alonso, F. Suárez-García, J. M. Tascón, *Carbon* **2003**, *41*, 1181–1191.
- [244] A. M. Puziy, O. I. Poddubnaya, A. Martínez-Alonso, F. Suárez-García, J. M. Tascón, *Carbon* **2005**, *43*, 2857–2868.
- [245] L. C. Jozefowicz, H. G. Karge, E. N. Coker, *J. Phys. Chem.* **1994**, *98*, 8053–8060.
- [246] C. Li, D. Wang, T. Liang, X. Wang, L. Ji, *Mater. Lett.* **2004**, *58*, 3774–3777.
- [247] G. Wang, Y. Ling, F. Qian, X. Yang, X.-X. Liu, Y. Li, *J. Power Sources* **2011**, *196*, 5209–5214.
- [248] A. M. Puziy, O. I. Poddubnaya, R. P. Socha, J. Gurgul, W. M., *Carbon* **2008**, *46*, 2113–2123.
- [249] J. M. Rosas, J. Bedia, J. Rodríguez-Mirasol, T. Cordero, *Ind. Eng. Chem. Res.* **2008**, *47*, 1288–1296.
- [250] P. J. Hall, J. M. Calo, *Energy Fuels* **1989**, *3*, 370–376.
- [251] L. Haar, J. S. Gallagher, *J. Phys. Chem. Ref. Data* **1978**, *7*, 635–792.
- [252] I. Langmuir, *J. Am. Chem. Soc.* **1916**, *38*, 2221–2295.
- [253] S. Wrabetz, X. Yang, G. Tzolova-Müller, R. Schlögl, F. C. Jentoft, *J. Catal.* **2010**, *269*, 351–358.
- [254] K. Foo, B. Hameed, *Chem. Eng. J.* **2010**, *156*, 2–10.
- [255] S. Bennici, A. Auroux in *Metal Oxide Catalysis*, S. D. Jackson, J. S. J. Hargreaves (Eds.), Wiley-VCH Verlag GmbH & Co. KGaA, Weinheim, Germany, pp. 391–441.

- [256] C. R. Maier, L. E. Jones, *Carbon* **2005**, *43*, 2272–2276.
- [257] C. E. Housecroft, *Inorganic chemistry 2nd ed.*, Pearson Prentice Hall, Upper Saddle River, N.J, **2005**.

Klaus Friedel

PhD student at the Fritz Haber Institute of the Max Planck Society

Personal Information

Surname(s) Friedel Ortega
Name(s) Klaus Dieter
Nationality Venezuelan
E-mail friedel.klaus@googlemail.com
LinkedIn <http://www.linkedin.com/pub/klaus-friedel/46/42a/b91>

Education

09.2010-07.2014 **PhD studies** Fritz Haber Institute of the Max Planck Society, Berlin
Title: "Insights into the Acid-Base Properties of Functionalized Multiwall Carbon Nanotubes"

04.2005-06.2010 **University studies: Engineering Management** Technical University of Berlin, Berlin
Specialization in Technical Chemistry
University degree: Diplom-Ingenieur (equiv. to Master of Engineering)
Final mark: 1.6
Diploma thesis under supervision of Prof. Dr. Reinhard Schomäcker: "Comparison of activity and selectivity of modified and unmodified VO_x/SBA-15 catalysts for the ODP" - *submitted in German*

09.1999-11.2004 **Middle School and High School** Colegio Alexander von Humboldt, Lima
Abitur (equiv. to A-level), Final mark: 1.4

08.1995-07.1999 **Elementary School and Middle School** Colegio Alexander von Humboldt, Norte, Mexico City

1992-07.1995 **Elementary School** Colegio Humboldt Caracas, Caracas

Professional Experience

02.2009-04.2009 **Internship** BASF SE, Ludwigshafen
Planning of a CRM system and implementation of a customer sample database for the Business Unit "Engineering Plastics Europe"

10.2008-02.2009 **Working student position** BASF Services Europe GmbH, Berlin
IT-based administration and organization of training events for German and Belgian companies belonging to the BASF Group

04.2007-07.2007 **Internship** G-Elit Hartstoffe, Berlin
Material testing and quality control of green shapes for the production of carbide tools

Language Skills

German (native), **Spanish** (native), **English** (fluent)

Construction Projects

06.2012-10.2012 Concept development and CAD design of a high temperature laboratory furnace (up to 1050 °C) with the purpose of performing catalytic gas-phase reactions and temperature programmed experiments (TPD/TPO)
Fritz Haber Institute of the Max Planck Society

03.2008-10.2008 Thermodynamic dimensioning, design, and construction of a small absorption chiller within the scope of a student research project (together with Dipl.-Ing. Marc Dünow) under supervision of Prof. Dr.-Ing. Felix Ziegler Institute of Energy Engineering - Technical University of Berlin

Awards and Distinctions

- 25.09.2013 **Poster prize**
5th International Conference on Carbon for Energy Storage / Conversion and Environment Protection (CESEP)
- 09.2010-07.2014 **Research grant for PhD studies**
Max Planck Society
- 10.2005-06.2010 **Stipend program "Deutsche Auslandsschulen"**
German Academic Exchange Service (DAAD)
Full grant awarded for higher education studies at the Technical University of Berlin

Conference Contributions

- 03.2014 **Poster** Weimar
47. Jahrestreffen Deutscher Katalytiker
Title: Catalytic conversion of 2-propanol as a sensitive tool for understanding the acid-base properties of N-doped carbon nanotubes
- 09.2013 **Poster** Mülheim an der Ruhr
5th International Conference on Carbon for Energy Storage / Conversion and Environment Protection (CESEP)
Title: Probing the basicity of nitrogen functionalized carbon nanotubes by TPD and catalytic decomposition of 2-propanol
- 02.2013 **Poster** Fellbach
Inno.CNT Jahreskongress 2013
Title: Modification of carbon nanotubes via in situ generated diazo compounds: radical addition of benzenesulfonic acid - *presented in German*
- 02.2012 **Poster** Weimar
45. Jahrestreffen Deutscher Katalytiker
Title: Diazonium-based derivatization of highly graphitic carbon nanofibers: a selective route towards a solid acid catalyst

Publications

Influence of thermal treatment on surface and oxidation properties of P-modified carbon nanotubes

Klaus Friedel Ortega, Sabine Wrabetz, Annette Trunschke, Robert Schlögl
to be submitted

Insights into the intrinsic acid-base properties of N-doped carbon nanotubes: a combined TPD, XPS and 2-propanol reaction investigation

Klaus Friedel Ortega, Rosa Arrigo, Benjamin Frank, Annette Trunschke, Robert Schlögl
to be submitted

Tailoring the acidity of carbon nanotubes through addition of in situ generated benzenesulfonic acid radicals

Klaus Friedel Ortega, Benjamin Frank, Annette Trunschke, Robert Schlögl
to be submitted

CNT-Supported Mo_xC Catalysts: Effect of Loading and Carburization Parameters

Benjamin Frank, Klaus Friedel, Frank Girgsdies, Xing Huang, Robert Schlögl, Annette Trunschke
ChemCatChem 2013, 5(8), S. 2296–2305